ERUPTION RECORD AND ASPECTS OF MAGMA GENESIS AND EVOLUTION FOR THE VOLCANOES OF THE SOUTHERNMOST ANDEAN SOUTHERN VOLCANIC ZONE, CHILE

by

DEREK JAMES WELLER

B.A., University of Colorado, 2010

M.S., University of Colorado, 2015

A thesis submitted to the

Faculty of the Graduate School of the

University of Colorado in partial fulfillment

of the requirement for the degree of

Doctor of Philosophy

Department of Geological Sciences

2017

This thesis entitled:
Eruption Record and Aspects of Magma Genesis and Evolution for Volcanoes of the Southernmost Andean Southern Volcanic Zone, Chile
written by Derek James Weller
has been approved for the Department of Geological Sciences

Charles R. Stern

G. Lang Farmer

Thomas M. Marchitto

Brian M. Hynek

Suzanne P. Anderson

Date

The final copy of this thesis has been examined by the signatories, and we find that both the content and the form meet acceptable presentation standards of scholarly work in the above mentioned discipline.

Weller, Derek James (Ph.D., Geological Sciences)

Eruption record and aspects of magma genesis and evolution for volcanoes of the southernmost Andean Southern Volcanic Zone, Chile

Thesis directed by Professor Charles R. Stern

Sediment cores from twelve lakes located to the east of the volcanic front of the southernmost portion of the Andean Southern Volcanic Zone (SSVZ) preserve greater than 75 late Pleistocene to Holocene tephras derived from different explosive eruptions of volcanoes in this region. Correlation of the tephra deposits and source volcano identification are based on the stratigraphic position of the tephra within the cores, tephra lithostratigraphic data (deposit thickness, grain size) and petrochemistry. Only 7 of these tephra have been previously identified in outcrops, indicating the importance of lake cores for identifying smaller eruptions. The suggested source volcanoes for these tephra include Hudson (33 events), Mentolat (18 events), Melimoyu, (4 events), and either Macá, Cay, Yanteles, or some of the many minor monogenetic eruptive centers (20 events) in the area. Hudson has been the most active volcano in SSVZ, producing greater than 45 km^3 of eruptive material since the late Pleistocene. Radiocarbon age determinations on the lacustrine sediments allow for tephra age estimates using a Bayesian approach. The tephra records preserved in the lake cores and the age constraints indicate that there is no significant temporal change in the frequency of explosive eruptions associated with deglaciaiton. They also constrain changes in sedimentation rate in each lake through time, an important paleoclimate indicator.

For the four southernmost volcanoes along the volcanic front in the SSVZ (Melimoyu, Mentolat, Macá and Hudson) glass compositions of melt inclusion from olivine phenocrysts found

in the tephras are used to constrain primitive magma compositions and melt generation parameters such as slab surface temperatures, fraction of mantle melting and mantle water content. The results indicate that magma compositions and melting parameters are similar along the arc front below Melimoyu, Macá, and Hudson, but distinct below Mentolat. These differences may be generated at the source region above the subducted slab, and in the case of Mentolat, may be related to a subducted Nazca Plate fracture zone that projects beneath this center and can transport greater amounts of hydrous phases, seawater and sediments into the sub-arc mantle.

Acknowledgments

First and foremost, I would like to thank my advisor, Chuck Stern. I am incredibly grateful for his support, dedication and mentorship throughout the course of my PhD. With your guidance, I have developed as a scientist, researcher and a writer so thank you for all of your support through this process. I would like to thank my committee member Tom Marchitto for his guidance in my early development as a scientist, his unwavering support throughout my graduate studies and his willingness to accommodate my research goals by granting me access to his laboratory facilities. I would also like to thank Lang Farmer for his continual support during his tenure as department chair and afterword for allowing me access to his laboratory facilities. I would like to thank Brian Hynek and Suzanne Anderson for their commitment to my thesis and providing an interesting perspective on my research. I owe much to my friend and mentor Garry Zabel for stimulating my interest in geology and encouraging me to further my education as a geoscientist.

I would also like to thank all of the individuals who have helped me with my laboratory work including Julien Allaz, Emily Verplank, Jim Metcalf, and Paul Boni. I would also like to thank Dan Mitchell for his assistance on countless computer repairs and for his good company.

Additionally, I would like to thank my friends here in the department for their encouragement throughout these last 6 years. You have helped me to grow professionally as a researcher, and I cannot thank you enough. I would like to personally thank Phil Orlandini and Danny Feucht for assistance with my defense preparation. Also, I would like to thank my office

mates for the office comradery and Aaron Hantsche, Jon Oulton, Rhiana Henry for their contributions in making the Mineralogy and Petrology classes a fun and enjoyable experience.

Finally, I am eternally grateful for the unwavering support of my family. I could not have completed this without you and thank you for encouraging me to follow my dreams. You guys have been my inspiration for so many years and I dedicate this thesis to you. I would also like to thank Kristine Johnson for being the most patient and understanding individual I know. Your dedication, compassion and support will not be forgotten.

Contents

Chapters

Tables

Figures

Chapter 1

Introduction

1.1 Tephrochronology

When a volcano erupts, it will often eject solid particles of volcanic glass, crystals, pumice and rock fragments into the atmosphere. These materials, known as tephra, are the constituents of eruption plumes during violent explosive eruptions. The size of the particles that fall out of the plume are largest near the volcano and gets progressively smaller with distance from the edifice. Similarly, the thickness of the deposits generally decreases moving further away from the volcanic center. For large eruptions, these tephra plumes can disperse material over very large areas and are deposited nearly instantaneously, in a matter of days, weeks or months, but not years. Unless it has been reworked after deposition, a tephra layer from an explosive eruption has essentially an identical age and therefore can be considered an isochron (Lowe 2011).

Once identified, the deposits which represent individual volcanic eruptions must be characterized or 'fingerprinted' using distinguishing physical properties identified in the field, such as tephra thickness and color, or other properties obtained from laboratory analysis, including tephra grain size, mineral content and chemistry, volcanic glass and bulk-tephra chemistry. Where a tephra deposit has been dated, this age can be transferred to other localities where the same tephra has been newly identified. These principles are the foundation for the field of tephrochronology, which stated simply, is a stratigraphic method for linking, dating and synchronizing geological, paleoenvironmental, paleoclimatic, or archaeological sequences of events and can provide a linkage between terrestrial, marine and ice records (Lowe, 2011).

1.2 Background on Andean Volcanology

The west coast of South America is a convergent margin where subduction of the Nazca and Antarctic Plates beneath the South American continent generates a chain of volcanoes consisting of over 200 Pleistocene and Holocene volcanoes (Fig. 1.1; Stern 2004). This volcanic chain is subdivided into four distinct volcanic zones named Northern Volcanic Zone (NVZ; 2°N-5°S), Central Volcanic Zone (CVZ; 14°S-28°S), Southern Volcanic Zone (33°S-46°S) and Austral Volcanic Zone (AVZ; 49°S-55°S). Pleistocene and Holocene volcanoes in the Chilean Andeans provide a natural laboratory to study subduction related volcanism, magma genesis and evolution due to the wide variety of subduction parameters that change along the length of the arc. Volcanoes of the CVZ and the SVZ occur where the angle of subduction is relatively steep (>25°) while gaps in the active volcanism occur where the slab angle becomes relatively flat (<10°). The thickness of the continental crust changes dramatically along the length of the arc with crustal thickness estimates up to ~65 km below the CVZ in the north of Chile, and thinning to ~30 km below the southern SVZ in the south of Chile (Hildrith and Moorbath 1988).

The Southern Volcanic Zone alone consists of ~60 Pleistocene to Holocene stratovolcanoes, more than 3 giant caldera complexes, and numerous small monogenetic eruptive centers (MEC; Stern 2004). It is further divided into four segments based on broad changes in the composition and petrographic features of the eruptive products (Tormey et al. 1991; López-Escobar et al. 1993; 1995, Sellés et al. 2004; Völker et al. 2011). Major centers of the Northern SVZ (33-34.5°S) are predominately hornblende-bearing andesites and occur over thick continental crust while stratovolcanoes of the Transitional SVZ (34.5-37°S), where the crustal thickness decreases, are composed predominately of basaltic andesites. The Central (37.0-41.5°S) and Southern (41.5-46°S) SVZ, below which the crust has thinned to <35 km, have volcanoes that

Figure 1.1. Map of South America showing the relative convergence rates of the subducting Nazca and Antarctic Plates and the distribution of the volcanoes along the western coast of South America. The volcanoes are grouped into 4 volcanic zones named the Northern (NVZ), Central (CVZ), Southern (SVZ), and Austral Volcanic Zones (AVZ; Stern 2004). The four major volcanoes of the SSVZ (Fig. 1.2), which are the focus of this thesis, are located at the southern tip of the SVZ.

erupt mainly basalts to basaltic andesites (López-Escobar et al. 1995; Tormey et al. 1991).

This study focuses on the five volcanoes that form the volcanic front of the southernmost SVZ: Melimoyu, Mentolat, Macá, Cay, and Hudson (Fig. 1.2). Melimoyu and Hudson are both large volcanic centers (142 km^3 and 147 km^3 respectively), while Macá (39 km^3), Cay (48 km^3) and Mentolat (31 km^3) are relatively small (Völker et al. 2011). In addition to the differences in their sizes, which is related to extrusion rates and thus rates of magma production, these volcanoes are also diverse in their magma petrochemistry and mineral assemblages (Lopez-Escobar et al. 1993, 1995). This compositional diversity is an important property that can be used to identify source volcanoes for tephras identified from the region (Naranjo and Stern, 1998, 2004, Stern 2008, Stern et al. 2015; 2016) and is also the focus for the later chapters of this dissertation.

1.3 Dissertation outline and results

This dissertation is divided into two different parts, the first part involves the assembly of a tephro-chrono-stratigraphic framework for the SSVZ volcanoes. This first portion of the dissertation expands upon the studies of Narjano and Stern (1998, 2004) with a focus on identifying previously unrecognized eruptions preserved as tephra layers in sediment cores from 12 small lake located to the east and southeast of the volcanic front of the SSVZ (Fig. 1.2). In the second part of this dissertation, I investigate aspects of magma genesis and evolution at the SSVZ centers Each chapter is presented as a stand-alone manuscript intended for journal publications, including figures, tables, references, and supplementary material.

1.3.1 Tephrochronology Chapters 2-4

Chapter 2, which has already been published in the *Bulletin of Volcanology* (Weller et al., 2015; Bull Vol 77:107-131), presents a detailed record of explosive eruptions preserved within

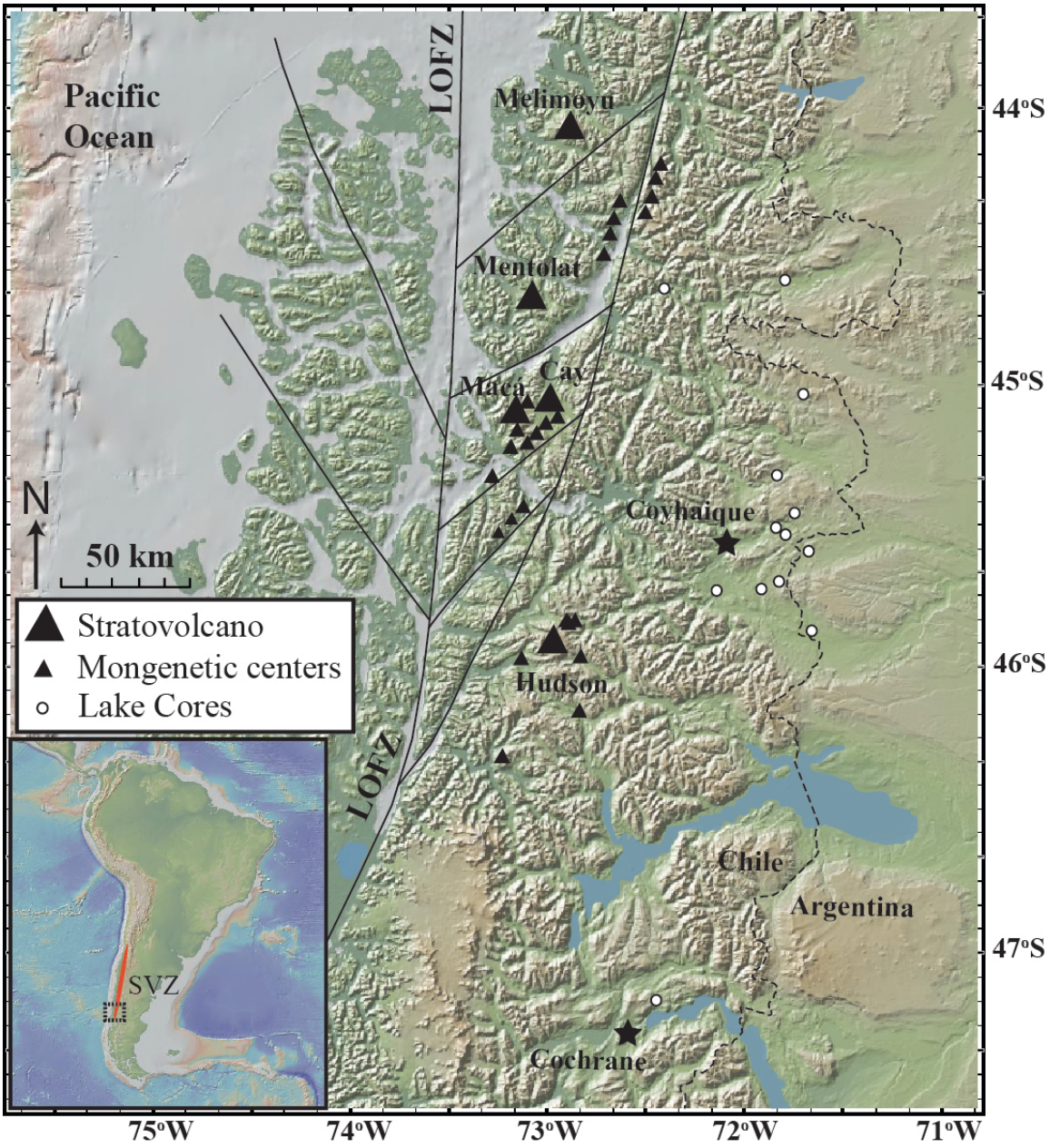

Figure 1.2. Map of the Southernmost Andeans Southern Volcanic Zone (SSVZ) showing the location of the major centers and some of the monogenetic eruptive centers located along the Liquiñe-Ofqui Fault Zone (LOFZ). Open circles show are the location of tephra-bearing lake cores obtained for this study.

eight lake sediment cores from near the town of Coyhaique (Fig. 1.2). The lake cores were obtained at 1 meter intervals and photographed using transmitted x-rays to aid in the identification of the tephra layers (Fig. 1.3). The tephras are the white layers, or the denser lithologies compared to the predominately organic matter-rich lacustrine sediments they are preserved within. Each correlated tephra is named from A to Z with tephra A1, located near the top of core section 1, being the youngest observed in the sedimentary record while tephra MENo, located near the base of core section 9, is one of the oldest. The suggested source volcanoes for tephra from the Unco and other sediment core from the region include Hudson (33 events), Mentolat (18 events), Melimoyu, (4 events), and either Macá, Cay, Yanteles, or some of the many minor monogenetic eruptive centers (MEC's; 20 events) in the area. Only 7 of these tephras have been identified in tephra outcrops indicating the importance of lake cores for identifying smaller eruptions.

Chapter 3, a manuscript now under review for publication in the *Bulletin of Volcanology*, expands upon the work done in Chapter 2 with a new data set of radiocarbon age dates obtained from a new lake core just north of the study area for Chapter 2. Pervious age constraints were limited to radiocarbon age dates near the base of the lake cores with limited age controls within the sedimentary record. The new age estimates are distributed throughout the lacustrine record and are used to create an age model for the new lake core (Fig. 1.4) and the lake cores described in Chapter 2 to generate age estimates for each tephra (Table 1.1). The results from these two chapters indicate that while outcrop based studies of Naranjo and Stern (1998; 2004) are able to identify the larger eruptions, lake cores provide exceptional stratigraphic and chronologic control allowing for the identification of even small eruption. Additionally, the eruption record and age constraints indicate that there has been no significant change in the frequency of explosive eruptions associated with deglaciation (Fig. 1.5).

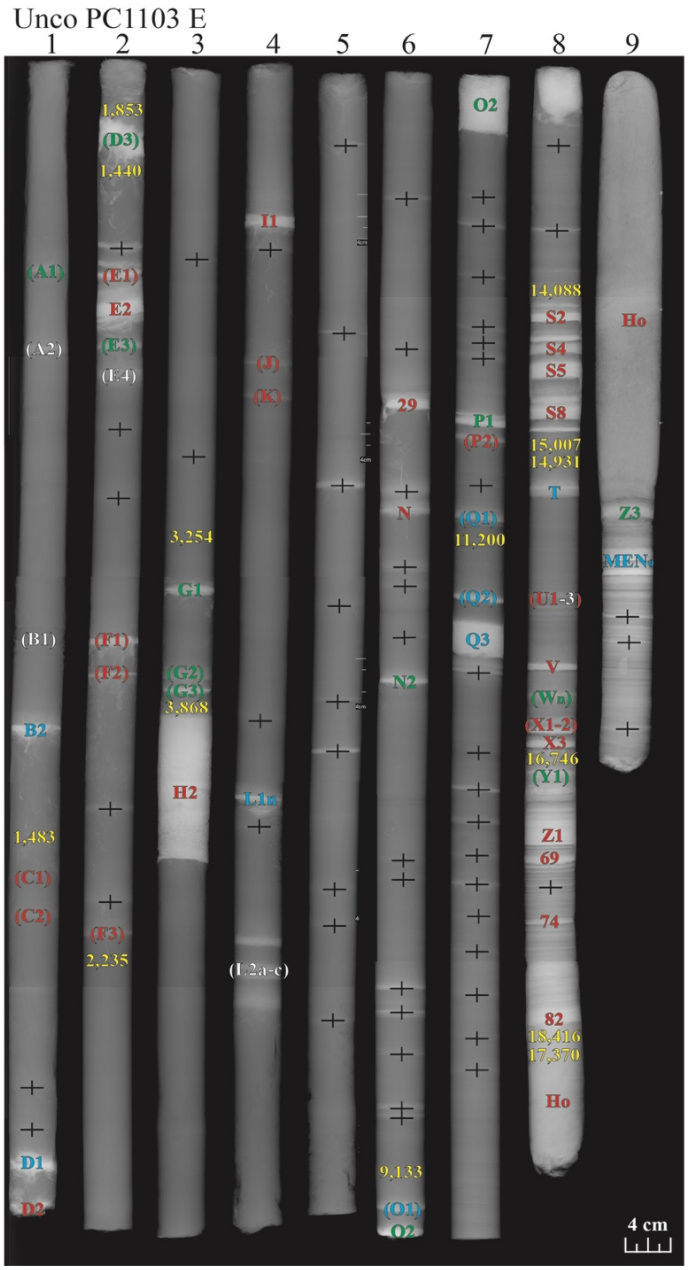

Figure 1.3. Transmitted x-ray photograph of the 8.5-meter-long lake sediment core from lake Unco. The tephra in this core appear as white layers due to their higher density compared to the predominantly organic lake sediments in which they are preserved. Sampled and unsampled (in parentheses) tephra that have been correlated with tephra in other lake sediment cores from near Coyhaique are labeled from A to Z, and numerous thin unsampled dense layers, most probably tephra, are indicated by a + symbol. The tephra labels have been color coded according to the source volcano (red tephra from Hudson, blue from Mentolat, and green from either Macá, Cay, or a monogenetic eruptive centers). Tephra with white labels were not sampled from either the Unco core or the other cores from near Coyhaique, but are correlated based on stratigraphic relations. New and previously published radiocarbon age dates are shown in yellow.

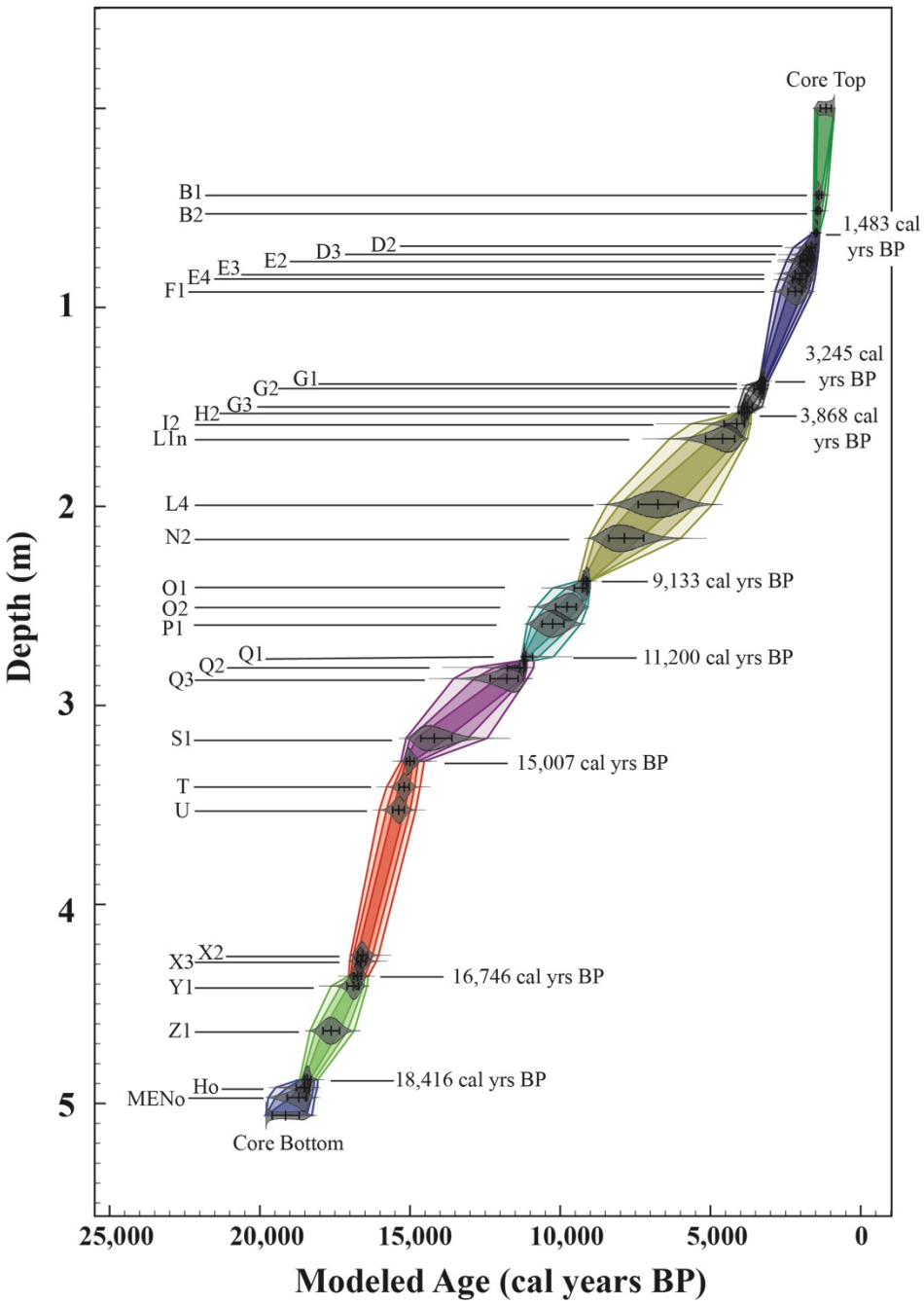

Figure 1.4. Age versus depth model for the tephra in the Laguna La Trapananda sediment core (LLT). The seven ages from the LLT core and for the Hudson H2 eruption (Naranjo and Stern 1998, 2004) that control the model are indicated on the right of the curve, and the ages of all the tephra are tabulated in table 1.1. Colored fields represent different sections of each core bound on each end by the radiocarbon age determinations. Within the colored fields are the 68% (darker inner field), 95%, and 99.7% (lightest outer field) highest probability density envelopes with the modeled Gaussian age distribution (grey) including the median (middle black tick mark) and the 1-sigma on the mean for the modeled age estimates (black bars).

Table 1.1. Average modeled age in cal years BP for tephra observed in the lake cores near Coyhaique.

Tephra	Source	Age	1σ	Tephra	Source	Age	1σ
A1	**M/C/MEC**	793	1031	**N**	**Hudson**	8233	541
A2	**-**	1021	820	**N2**	**M/C/MEC**	8864	347
B1	**-**	1340	427	**O1**	**Mentolat**	9261	210
B2	**Mentolat**	1426	367	**O2**	**M/C/MEC**	9417	280
C1	**Hudson**	1532	109	**P1**	**M/C/MEC**	10613	388
C2	**Hudson**	1612	156	**P2**	**Hudson**	10724	360
D1	**Mentolat**	1774	216	**Q1**	**Mentolat**	11142	248
D2	**Hudson**	1872	203	**Q2**	**Mentolat**	11378	275
D3	**Macá**	1922	215	**Q3**	**Mentolat**	11407	339
E1	**Hudson**	1900	239	**S1**	**Hudson**	14647	386
E2	**Hudson**	1965	240	**S10**	**Hudson**	14967	249
E3	**M/C/MEC**	1956	231	**T**	**Mentolat**	15120	224
E4	**-**	2058	260	**U1**	**Hudson**	15473	349
F1	**Hudson**	2211	274	**U2**	**-**	15487	399
F2	**Hudson**	2235	269	**U3**	**-**	15750	360
F3	**Hudson**	2494	278	**V**	**Hudson**	15956	443
G1	**M/C/MEC**	3314	159	**Wn**	**M/C/MEC**	16437	296
G2	**M/C/MEC**	3614	197	**Ws**	**Hudson**	16210	613
G3	**M/C/MEC**	3771	170	**X1**	**Hudson**	16608	310
H2	**Hudson**	3868	84	**X2**	**Hudson**	16654	205
I1	**Hudson**	4528	469	**X3**	**Hudson**	16695	181
I2	**Mentolat**	4793	596	**Y1**	**M/C/MEC**	16878	226
J	**Hudson**	5337	609	**Y2**	**-**	17467	318
L1n	**Mentolat**	5372	637	**Z1**	**Hudson**	17575	315
K	**Hudson**	5434	619	**Ho**	**Hudson**	18459	205
L1s	**M/C/MEC**	6450	611	**Z3**	**M/C/MEC**	18497	258
L4	**Mentolat**	6747	665	**MENo**	**Mentolat**	18672	459
M	**Hudson**	8139	558	**Z5**	**M/C/MEC**	18844	524

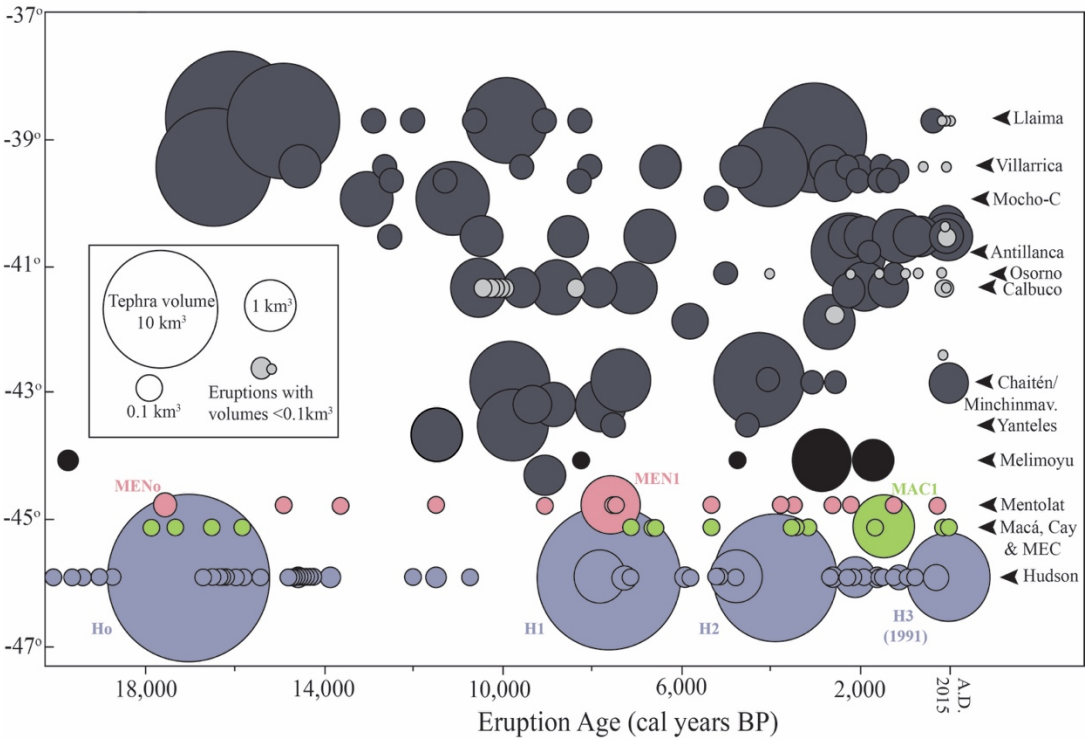

Figure 1.5. Eruption volumes for volcanic centers of the SVZ between 37°S and 47°S from Late-glacial and Holocene time. Modified from Watt et al. (2013a) to include the eruptions from Hudson, Mentolat and either Macá, Cay or one of the MEC documented in this study.

Chapter 4, submitted and under review for publication in the journal *Andean Geology*, is a separate tephrochronology study from a different drainage basin located further north in the SSVZ, that focuses on two sediment cores from lakes located directly east of Mentolat. The eruptions identified in these lake cores are important because they allow for better characterization of the Mentolat and Melimoyu derived tephras.

1.3.2 Petrogenesis Chapter 5

In the previous chapters, the source volcanoes for all the eruptions were determined in part by the tephra petrochemistry. This petrochemical diversity is the focus for the subsequent chapters with the goal of better constraining the processes contributing to this variability. The following chapters utilize material from these explosive eruptions to investigate different aspects of magma genesis and evolution at the SSVZ centers.

In Chapter 5, to be submitted to the journal *Lithos*, I compare the compositions of primitive magmas and the estimated conditions during melt generation at four of the arc front volcanoes. Primitive magmas are estimated using glass compositions observed as melt inclusion in olivines phenocryst from these eruptions. The glass compositions are then back-calculated to primitive magma compositions (Fig. 1.6). This study revealed that primitive magmas and melt generation parameters are relatively uniform at Melimoyu, Macá, and Hudson. However, primitive magmas from Mentolat have unusually low TiO_2, MgO, K_2O (Fig. 1.6), and high volatiles (S, Cl, and H_2O) and are generated by higher degree of partial melting of a relatively water-rich mantle that occur at lower pressures, temperatures and slab surface temperatures than the other centers. I conclude that these primitive magma petrochemical differences are generated in the source region above the subducting slab beneath these centers and in the case of Mentolat, is possibly related to a subducted

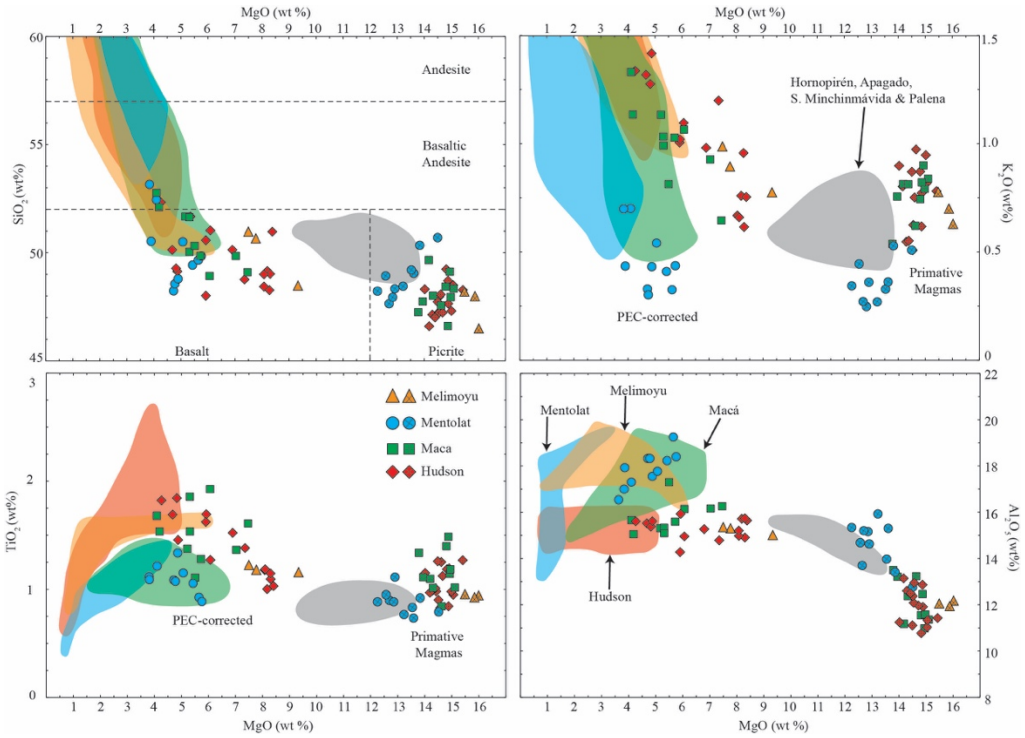

Figure 1.6. Major element variation diagrams for the primitive magmas (symbols with cross or plus sign) and the PEC-corrected melt inclusion (open symbols). Also shown are the fields for bulk rock and glass analysis for each center illustrating the petrochemical variability observed in the primitive magmas, the PEC-corrected magmas, and the more evolved eruptive products. Mentolat generally has much lower K_2O, TiO_2, MgO, and higher Al_2O_3 than the other centers that generally overlap in their magma compositions. Included for comparison are the primitive magma compositions determined for Hornopirén, and the mafic monogenetic centers north of the SSVZ centers (Watt et al. 2013b)

Nazca Plate fracture zone that projects beneath this center.

1.3.3 Trace Element Method Chapter 6

The focus of Chapter 6 is to present the development and results of a method to decompose mafic to felsic geologic samples and to simultaneously analyze 36 minor and trace elements using ICP-MS techniques. Included in this chapter is a laboratory comparison from ACME, LEGS, and the method developed as part of this study (Fig. 1.7). Analysis of the 36 trace and minor elements developed in this method are in generally good agreement with recommended values for the international reference material (BHVO-1) that range across more than five orders of magnitude in concentration. Accuracy of the results was generally better than 10% (in % deviation of recommended values for BHVO-1 and VMD (Valmont Dike)) for most elements and can reproduce results from the alkali glass fusion method utilized by ACME laboratory (Fig. 1.7).

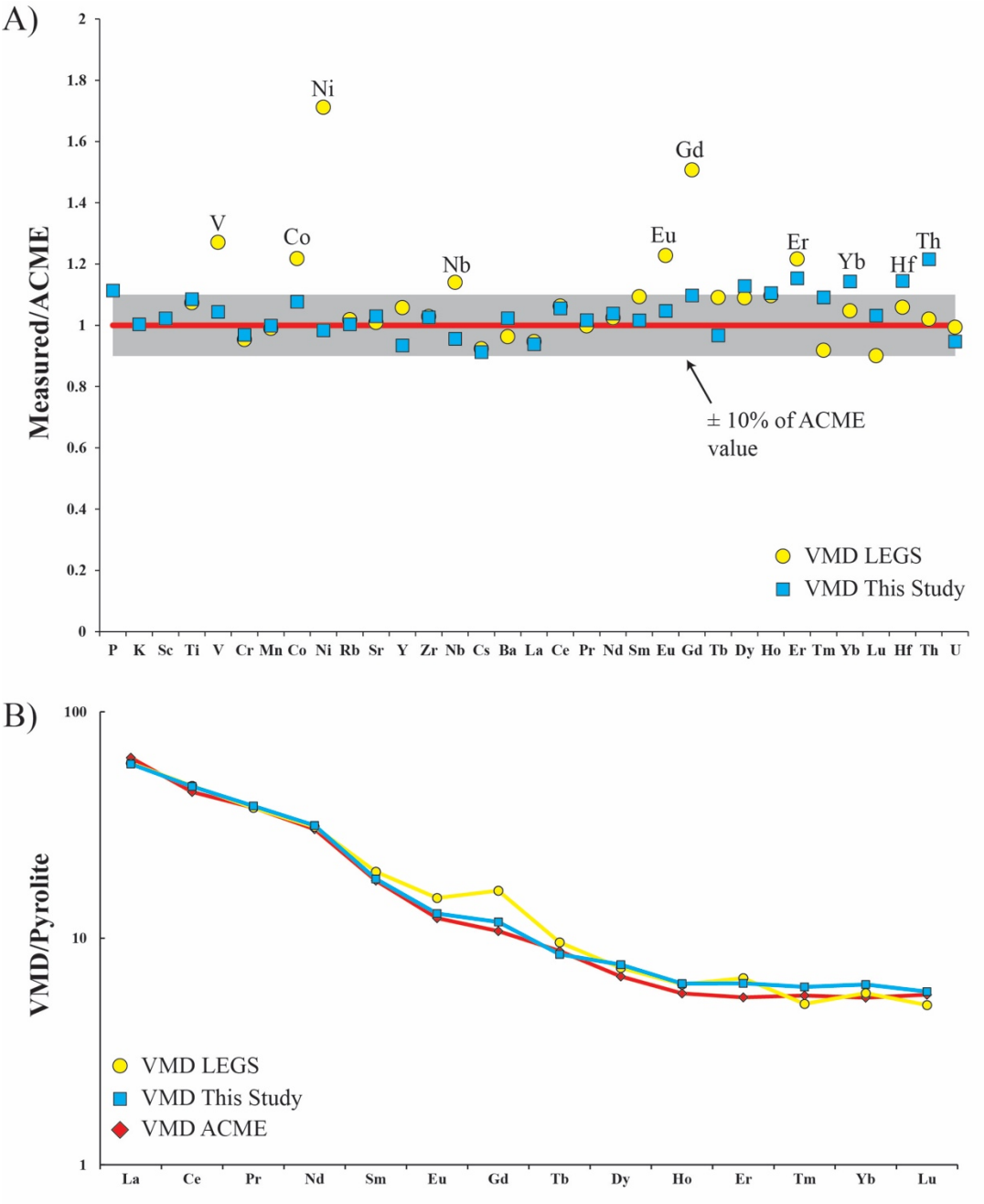

Figure 1.7. **A)** The recovery yield for 36 elements normalized to the VMD values reported from the ACME lab showing the ±10% field (grey) for the ACME values. Most elements are generally better than ±10% of the reported values. The LEGS analysis are generally within the ±10% field except V, Co, Ni, Nb, Eu, Gd and Er. **B)** Pyrolite normalized REE diagram for the Valmont Dike from three laboratories, ACME (red), LEGS (yellow), and this study (blue). The values from this study show good agreement with ACME analysis and produce generally smooth REE trends. Some heavy REE from this study are slightly elevated compared to the ACME data, but the differences are much less than LEGS data.

1.4 References

Hildreth W, Moorbath S (1988) Crustal contributions to arc magmatism in the Andes of Central Chile. Contrib Mineral Petrol 98:455-489

López-Escobar L, Kilian R, Kempton P, Tagiri M (l993) Petrology and geochemistry of Quaternary rocks from the southern volcanic zone of the Andes between 41°30' and 46°00'S, Chile. Rev Geol Chile 20: 33–55

López-Escobar L, Cembrano J, Moreno H, (1995) Geochemistry and tectonics of the chilean Southern Andes basaltic Quaternary volcanism (37-46ºS). Revista Geológica de Chile 22 (2): 219-234

Lowe DJ (2011) Tephrochronology and its application: A review. Quat Geol. 6: 107-153

Naranjo JA, Stern CR (1998) Holocene explosive activity of Hudson Volcano, southern Andes. Bull Volcanol 59(4): 291–306

Naranjo JA, Stern CR (2004) Holocene tephrochronology of the southernmost part (42°30'-45°S) of the Andean Southern Volcanic Zone. Rev Geol Chile 31(2): 225–240

Sellés D, Rodríguez AC, Dungan MA, Naranjo JA, Gardeweg M (2004) Geochemistry of Nevado de Longaví (36.2°S): a compositionally atypical volcano in the Southerrn Volcanic Zone of the Andes. Rev Geol Chile 31(2): 293-315

Stern CR (2004) Active Andean Volcanism: its geologic and tectonic setting. Rev Geol Chile 31(2): 161-206

Stern CR (2008) Holocene tephrochronology record of large explosive eruptions in the southernmost Patagonian Andes. Bull Volcanol 70(4): 435–454

Stern CR, de Porras ME, Maldonado A (2015) Tephrochronology of the upper Río Cisnes valley (44°S), southern Chile. Andean Geol 42(2): 173-192

Stern CR, Moreno PI, Henrique WI, Villa-Martinez RP, Sagredo E, Aravena JC, De Pol-Holz R (2016) Holocene tephrochronolgy in the area around Cochrane, southern Chile. Andean Geol 43(1): 1-19

Tormey DR, Hickey-Vargas R, Frey FA, López-Escobar L (1991) Recent lavas from the Andean volcanic front (33 to 42^{o}S): Interpretations of along-arc compositional variations. Geol Soc Spec Pap 265

Watt SFL, Pyle DM, Mather TA (2013a) The volcanic response to deglaciation: evidence from glaciated arcs and a reassessment of global eruption records. Earth Sci Rev 122: 77-102

Watt SFL, Pyle DM, Mather TA, Naranjo JA (2013b) Arc magma compositions controlled by linked thermal and chemical gradients above the subducting slab. Geophs Res Lett 40(11): 2550-2556

Völker D, Kutterolf S, Wehrmann H (2011) Comparative mass balance of volcanic edifices at the southern volcanic zone of the Andes between 33^{o}S and 46^{o}S. J Volcanol Geotherm Res. 205: 114-129

Chapter 2

Tephrochronology of the southernmost Andean Southern Volcanic Zone, Chile

Published in *Bulletin of Volcanology*, 2015

Coauthors: Carmen G. Miranda[2], Patricio I. Moreno[2], Rodrigo Villa-Martinez[3], Charles R. Stern[1]

[1]Department of Geological Sciences, University of Colorado, Boulder, CO, USA

[2]Instituto de Ecología y Biodiversidad, Departamento of Ciencias Ecológicas, Universidad de Chile, Santiago, Chile

[3]Gaia-Antartica, Universidad de Magallanes, Punta Arenas, Chile

2.1 Abstract

Correlations among and identification of the source volcanoes for over 60 Late-Glacial and Holocene tephra preserved in eight lacustrine sediment cores taken from small lakes near Coyhaique, Chile (46°S), were made based on the stratigraphic position of the tephra in the cores, lithostratigraphic data (tephra layer thickness and grain size), and tephra petrochemistry (glass color and morphology, phenocryst phases, and bulk-tephra trace-element contents determined by ICP-MS). The cores preserve a record of explosive eruptions, since ~17,800 cal yrs BP, of the volcanoes of the southernmost Andean Southern Volcanic Zone (SSVZ). Suggested source volcanoes for 55 of these tephra include Hudson (32 events), Mentolat (10 events), and either Macá, Cay or some of the many minor monogenetic eruptive centers (MEC; 13 events) in the area. Only four of these eruptions had been previously identified in tephra outcrops in the region, indicating the value of lake cores for identifying smaller eruptions in tephrochronologic studies. The tephra records preserved in these lake cores, combined with those in marine cores, which extend these records back to 20,000 cal yrs BP, prior to the Last Glacial Maximum, suggest that that no significant temporal change in the frequency of explosive eruptions was associated with deglaciation. Over this time period, Hudson volcano, one of the largest and longest lived volcanoes in the southern Andes, has had >55 eruptions, four of them very large, and has produced >45 km^3 of pyroclastic material, making it also one of the most active volcanoes in the SVZ in terms of both frequency and volume of explosive eruptions.

2.2 Introduction

The southernmost portion of the Andean Southern Volcanic Zone (SSVZ) consists of the five large volcanic centers Melimoyu, Mentolat, Macá, Cay, and Hudson (Fig. 2.1; Stern 2004;

Völker et al. 2011), as well as numerous small monogenetic eruptive centers (MEC) located either along the Liquiñe-Ofqui Fault System (LOFS) or surrounding the larger volcanoes (López-Escobar et al. 1995; D'Orazio et al. 2003; Gutiérrez et al. 2005; Vargas et al. 2013). The Holocene tephrochronology of this region has been studied from outcrops to the east and southeast of the major volcanic centers (Naranjo and Stern 1998, 2004; Mella et al. 2012), from sediment cores taken in bogs and lakes located to the east (de Porras et al. 2012; Stern et al. 2015), southeast (Markgraf et al. 2007; Elbert et al. 2013; Stern et al. 2016) and the west (Haberle and Lumley 1998), as well as in some Pacific Ocean marine cores (Siani et al. 2010, 2013; Carel et al. 2011). These previous studies were limited by the lack of long cores from southeast of the arc, which due to the prevailing wind patterns is the location most favorable for preserving airborne eruptive products.

This paper presents a high-resolution tephrochronology of explosive eruptions of southernmost Andean Southern Volcanic Zone (SSVZ) volcanoes since the beginning of the last glacial termination based on the tephra record preserved in lacustrine sediment cores collected from eight small lakes to the southeast of the SSVZ volcanoes near the town of Coyhaique (Fig. 2.1; Fig. A2.1 in the appendix). This portion of the Andes was heavily glaciated during the last glaciation. Retreat of the glaciers, beginning at approximately 17,800 cal yrs BP as indicated by the ages of the deepest organic sediment layers in each core (Table A2.1 in the appendix; Miranda et al. 2013), generated many small shallow lakes with limited catchment areas in the semi-arid region to the southeast of the volcanic arc. These lakes provide favorable environments for the preservation of the tephra produced by explosive eruptions of the southernmost SSVZ volcanoes extending back into the Late-Glacial period.

Tephra from a very large Late-Glacial age explosive eruption (Ho) of the Hudson volcano

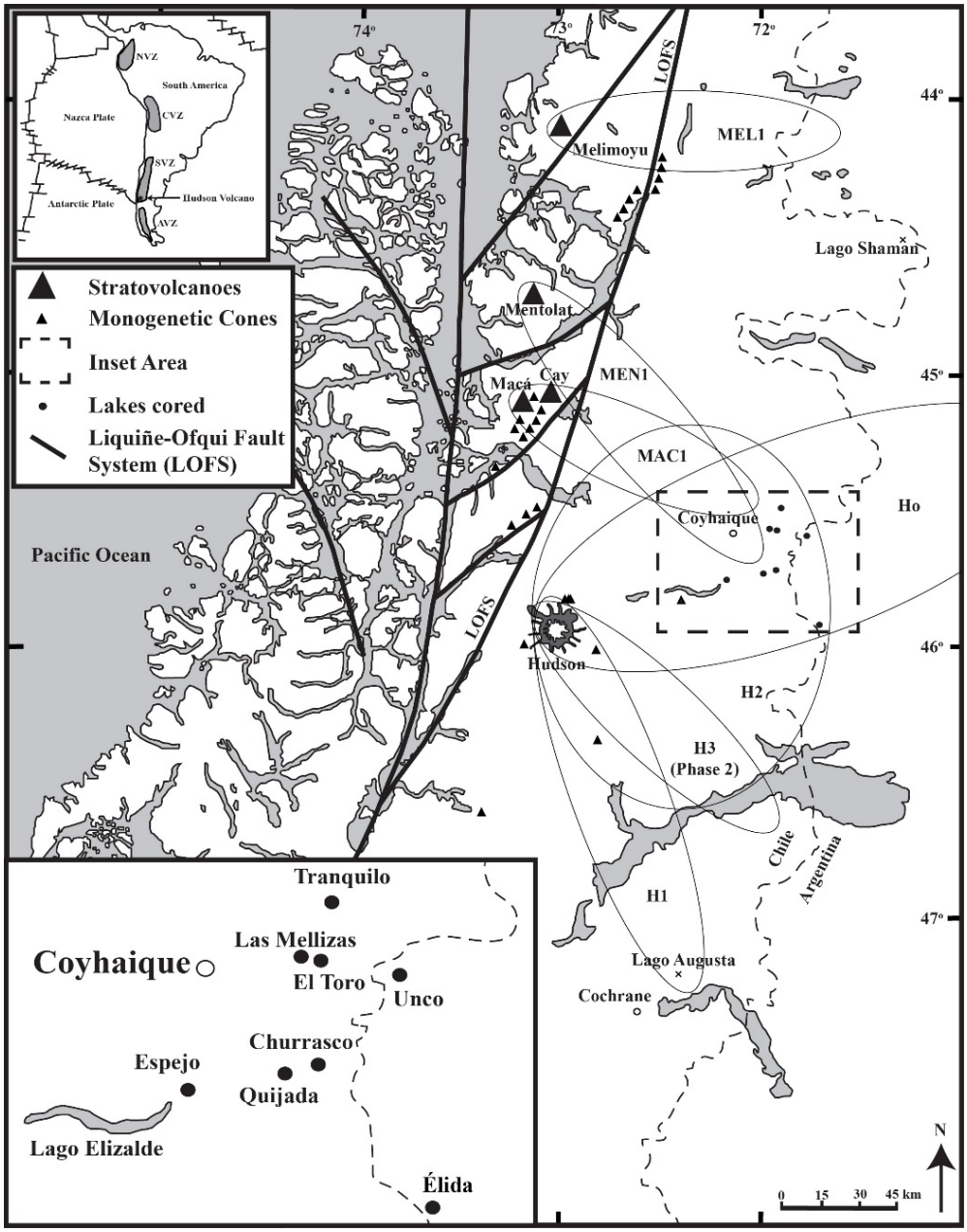

Figure 2.1. Map of the southernmost portion of the Andean SVZ showing the location of the major volcanoes and some of the minor monogenetic eruptive centers (MEC) along the Liquiñe-Ofqui Fault System (LOFS) and surrounding Hudson, Macá and Cay (Gutiérrez et al. 2005, Vargas et al. 2013). The dashed box shows the area of the inset map locating the lakes near Coyhaique from which tephra-bearing cores were obtained for this study. Also indicated are the locations of other lakes (x's) to the north (Shaman; de Porras et al. 2012; Stern et al. 2015a) and south (Augusta; Villa-Martínez et al. 2012; Stern et al. 2013, 2015b) from which tephra from SSVZ volcanoes have previously been reported. The 10 cm isopachs for some of the previously documented medium to large Holocene and Late-Glacial eruptions of SSVZ volcanoes (MEL1; MEN1; MAC1 and Hudson Ho, H1, H2 and H3 Phase 2) are taken from Scasso et al. (1994), Naranjo and Stern (1998; 2004), Weller et al. (2014) and Stern et al. (2016).

was previously recognized in these same cores (Weller et al. 2014). This study identifies. and characterizes lithostratigraphic and petrochemical information for the tephra from many more (>60; Fig. 2.2; Tables 2.1 and 2.2) previously undocumented smaller explosive eruptions of Hudson, Mentolat, Macá and possibly either Cay or one of the many minor monogentic eruptive centers (MEC) in the region. These results constrain a better understanding of both the eruption frequency of these volcanoes through time, and the variability in their volcanic products. They provide isochrons (tephra horizons of equal age; Lowe 2011; Fontijn et al. 2014) which can be utilized, at least in the cases of the larger eruptions, to constrain the age of tephra in palaeoclimatic, palaeoecologic and archaeologic records in the region, as well as allowing for synchronization of terrestrial tephra airfall outcrop studies with lacustrine and oceanic records. They are also significant for evaluating the volcanic risk for local population centers, such as Coyhaique, one of the fastest growing cities in Chile.

2.3 Geologic Background

The Andean SVZ results from the subduction of the Nazca Plate beneath the Southern American Plate (Fig 1; Stern 2004). Hudson, the southernmost volcanic center in the SVZ, sits ~280 km to the east of the Chile Rise-Trench triple junction, an active spreading center that separates the Antarctic and Nazca Plates. Over the last 15-20 Ma, the triple junction has migrated northward along the continental margin as a result of the oblique collision between the ridge and the trench (Cande and Leslie 1986; Nelson et al. 1994). Just to the south of Hudson there is a gap in volcanic activity that separates the SVZ from the Austral Volcanic Zone (AVZ; Stern and Kilian 1996; Stern 2004). The major volcanic centers of the SSVZ occur just to the east and west of the arc-parallel LOFS (Cembrano et al. 1996; D'Orazio et al. 2003; Vargas et al. 2013). This fault system originated in response to the impingement of the Chile Rise against the continent and the

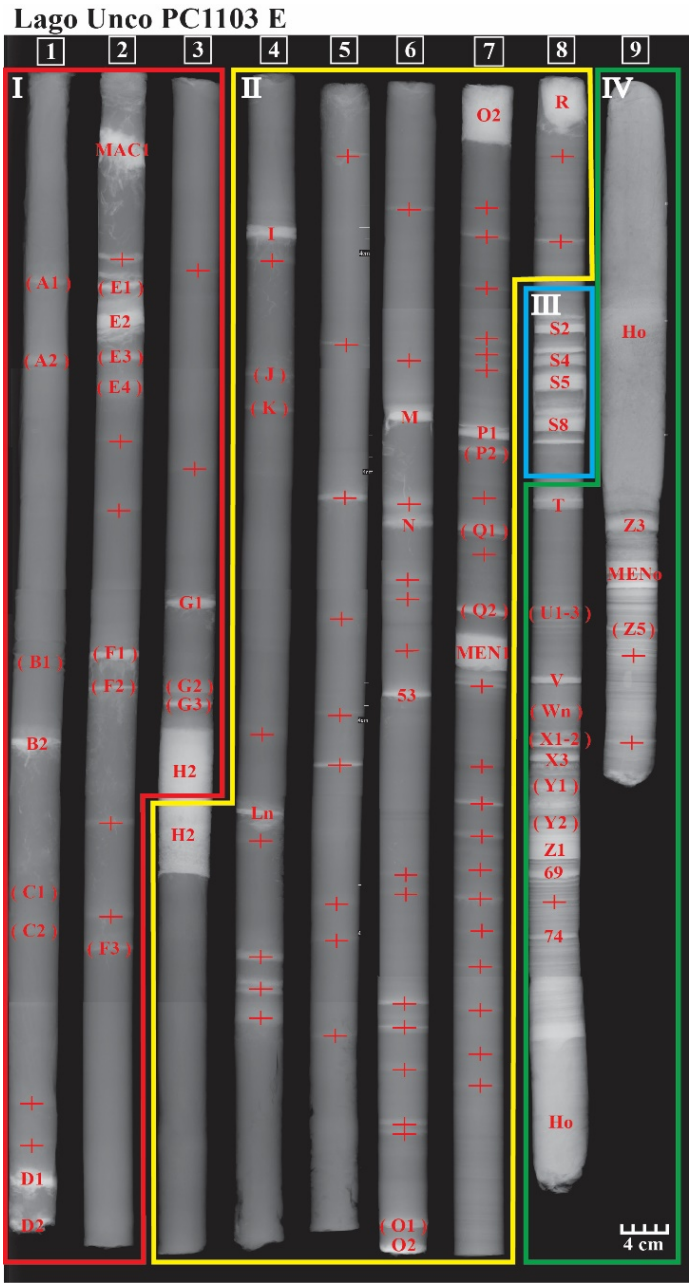

Figure 2.2. X-ray image of the 8.5 x 1 meter sections of the core from Lago Unco. The >70 different tephra in this core appear as white layers due to their higher density compared to the predominantly organic lake sediments in which they are preserved. Sampled and unsampled (in parentheses) tephra from 59 eruptions that have been correlated with tephra in other cores are labeled A1 through Z3 (Table 2.1). Samples of three tephra not correlated with tephra in other cores are labeled by their cm depth in each section (T1-9) of the core (T6-53, T8-69 and T8-74), and numerous thin unsampled dense layers, most probably tephra, are indicated by a + symbol. The core has been divided into four zones (Zone I from the top to tephra H2; Zone II from tephra H2 to the top of the sequence of 10 tephra S1-10; Zone III the sequence S1-10; Zone IV from S10 to the bottom of the core) for the purpose of describing the different tephra.

Table 2.1a. Thickness (cm) of 61 tephra correlated in cores from multiple lakes

		Chem		Southern Lakes				Northern Lakes				Age (cal yrs BP)
	Tephra	Type	Source	LE	LQ	LC	LEl	LU	LM	LT	LTr	
Zone I	A1	LAM	M/C/MEC	Tr	Tr	-	-	Tr	Tr	1	Tr	
	A2	-	-	Tr	Tr	-	-	Tr	Tr	Tr	Tr	
	B1	-	-	Tr	Tr	Tr	-	Tr	Tr	-	-	
	B2	LAF	MEN	Tr	Tr	Tr	-	1	Tr	1	4	
	C1	HA	HUD	3	1	1	-	Tr	3	<1	<1	
	C2	HA	HUD	<1	<1	1	-	Tr	-	1	1	
	D1	LAF	MEN	-	-	<1	-	1	<1	<1	-	
	D2	HA	HUD	-	-	1	-	1	<1	1	1	
	D3=MAC1	LAM	MACA	2	2	1	-	1	8	7	8	1,440 ± 60
	E1	HA	HUD	1	-	-	-	<1	-	<1	1	
	E2	HA	HUD	3	1	2	-	1	3	3	2	
	E3	LAM	M/C/MEC	2	-	-	-	1	-	<1	1	
	E4	-	-	<1	<1	Tr	-	Tr	-	1	<1	
	F1	HA	HUD	<1	1	1	1	1	1	1	1	
	F2	HA	HUD	1	<1	1	>1	<1	Tr	Tr	-	
	F3=T6	HA	HUD	1	<1	1	-	<1	Tr	Tr	-	
	G1	LAM	M/C/MEC	1	<1	1	1	1	2	1	1	
	G2	LAM	M/C/MEC	2	1	<1	Tr	Tr	Tr	<1	<1	
	G3	LAM	M/C/MEC	1	-	1	1	1	<1	<1	Tr	
	H2	HA	HUD	53	24	24	14	12	14	8	11	4,000 ± 50
Zone II	I	HA	HUD	2	Tr	Tr	2	1	-	-	-	
	J	HA	HUD	1	1	1	1	Tr	-	-	-	
	K	HA	HUD	1	<1	1	1	Tr	-	-	-	
	Ls	LAM	M/C/MEC	-	-	1	1	-	-	-	-	
	Ln	LAF	MEN	-	-	-	-	1	-	1	1	
	M	HA	HUD	2	1	2	1	Tr	-	-	-	
	N	HA	HUD	5	5	3	4	1	-	-	-	
	O1	LAF	MEN	Tr	-	Tr	<1	<1	1	<1	-	
	O2	LAM	M/C/MEC	-	-	1	Tr	6	5	5	-	
	P1	LAM	M/C/MEC	Tr	1	1	1	1	5	<1	-	
	P2	HA	HUD	1	1	1	1	<1	-	<1	-	
	Q1	LAF	MEN	<1	Tr	2	<1	<1	1	<1	9	
	Q2	LAF	MEN	-	-	-	-	1	-	3	6	
	MEN1	LAF	MEN	<1	1	1	1	3	2	3	4	7,670 ± 60
	R	LAF	MEN	<1	<1	<1	<1	3	4	-	1	

*** MAC1 and MEN1 ages from Naranjo and Stern, 2004; H2 age from Naranjo and Stern, 1998; Ho age from Weller et al. 2014, all other ages from Miranda et al. 2013**

Tr trace (<0.5 cm); HUD Hudson; MEN Mentolat; M/C/MEC Macá, Cay, and/or minor eruptive centers; HA high abundance; LAM low-abundance mafic; LAF low-abundance felsic

LE-Espejo; LQ-Quijada; LC-Churrasco; LEl-Élida; LU-Unco; LM-Las Mellizas; LT-El Toro; LTr-Tranquilo

Table 2.1b. Thickness (cm) of 61 tephra correlated in cores from multiple lakes

		Chem		Southern Lakes				Northern Lakes				Age (cal yrs BP)
	Tephra	Type	Source	LE	LQ	LC	LEl	LU	LM	LT	LTr	
Zone III	S1	HA	HUD	1	1	<1	-	<1	-	2	1	<14,088 ± 40
	S2	HA	HUD	1	1	1	1	1	1	1	1	
	S3	HA	HUD	1	1	1	1	<1	<1	<1	1	
	S4	HA	HUD	2	1	3	1	1	1	1	<1	
	S5	HA	HUD	3	2	1	1	2	2	1	1	
	S6	HA	HUD	1	<1	<1	<1	Tr	Tr	<1	Tr	
	S7	HA	HUD	1	<1	1	1	<1	<1	<1	<1	
	S8	HA	HUD	2	2	2	1	1	<1	<1	<1	
	S9	HA	HUD	1	>1	-	1	<1	<1	<1	-	
	S10	HA	HUD	<1	1	-	1	Tr	-	<1	Tr	14,931 ± 30
Zone IV	T	LAF	MEN	-	-	-	-	1	1	1	1	
	U1	-	-	<1	<1	Tr	1	<1	<1	<1	<1	
	U2	-	-	1	<1	Tr	1	Tr	<1	-	-	
	U3	-	-	<1	<1	-	-	Tr	Tr	-	-	
	V	HA	HUD	1	1	1	<1	1	1	1	1	
	Ws	HA	HUD	2	<1	<1	<1	-	-	-	-	
	Wn	LAM	M/C/MEC		-	-	-	Tr	<1	1	-	
	X1	HA	HUD		<1	<1	-	Tr	<1	<1	Tr	
	X2	HA	HUD		1	1	1	<1	<1	1	1	
	X3	HA	HUD		1	1	1	1	1	<1	<1	
	Y1	LAM	M/C/MEC		1	1	1	<1	<1	1	<1	
	Y2	-	-		<1	-	-	-	<1	<1	-	
	Z1	HA	HUD		9	2	-	3	4	3	4	
	H0	HA	HUD		88	64	19	58	68	32	61	17,370 ±70
	Z3	LAM	M/C/MEC		1	1	-	1	2	1	10	
	Z4=MENo	LAF	MEN		-	-	-	3	3	1	-	
	Z5	LAM	M/C/MEC		-	-	-	-	1	1	-	< 17,445 ± 45

*** MAC1 and MEN1 ages from Naranjo and Stern, 2004; H2 age from Naranjo and Stern, 1998; Ho age from Weller et al. 2014, all other ages from Miranda et al. 2013**

Tr trace (<0.5 cm); HUD Hudson; MEN Mentolat; M/C/MEC Macá, Cay, and/or minor eruptive centers; HA high abundance; LAM low-abundance mafic; LAF low-abundance felsic

LE-Espejo; LQ-Quijada; LC-Churrasco; LEl-Élida; LU-Unco; LM-Las Mellizas; LT-el Toro; LTr-Tranquilo

Table 2.2a. Maximum grain size (mm) of tephras in cores from multiple lakes

	Tephra	Source	Southern lakes				Northern lakes			
			LE	LQ	LC	LEl	LU	LM	LT	LTr
Zone I	**A1**	**M/C/MEC**	–	–	–	–	–	–	0.6	–
	B2	**MEN**	–	–	–	–	0.6	–	0.6	1
	C1	**HUD**	0.8	0.8	0.6	–	–	0.2	–	–
	C2	**HUD**	–	–	0.3	–	–	–	0.2	0.2
	D1	**MEN**	–	–	–	–	1.2	–	–	–
	D2	**HUD**	–	–	0.6	–	0.6	–	–	0.4
	D3=MAC1	**MACA**	1	1	1.2	–	1.2	1.2	1.4	1
	E1	**HUD**	0.4	–	–	–	–	–	–	0.4
	E2	**HUD**	0.8	0.8	0.6	–	0.6	0.5	0.6	0.4
	E3	**M/C/MEC**	0.5	–	–	–	0.5	–	–	0.5
	F1	**HUD**	0.8	0.6	0.3	1	–	0.3	0.3	0.1
	F2	**HUD**	0.5	–	–	–	–	–	–	–
	F3=T6	**HUD**	0.5	–	0.4	–	–	–	–	–
	G1	**M/C/MEC**	0.6	–	0.6	0.8	1	0.8	0.8	0.8
	G2	**M/C/MEC**	0.6	0.7	–	–	–	–	–	–
	G3	**M/C/MEC**	0.6	–	0.8	0.4	–	–	–	–
	H2	**HUD**	24	20	16	–	7	5	5	5
Zone II	**I**	**HUD**	0.4	–	–	0.6	0.3	–	–	–
	J	**HUD**	0.2	0.3	0.4	0.5	–	–	–	–
	K	**HUD**	0.8	–	0.9	0.6	–	–	–	–
	Ls	**M/C/MEC**	–	–	0.4	0.6	–	–	–	–
	Ln	**MEN**	–	–	–	–	0.6	–	0.6	0.8
	M	**HUD**	0.6	0.8	1	0.6	0.4	–	–	–
	N	**HUD**	1	0.8	0.6	0.8	0.4	–	–	–
	O1	**MEN**	–	–	–	–	–	0.6	–	–
	O2	**M/C/MEC**	–	–	1	–	0.8	–	0.8	–
	P1	**M/C/MEC**	–	0.3	0.2	0.3	0.2	0.8	–	–
	P2	**HUD**	0.6	0.6	0.5	0.9	–	–	–	–
	Q1	**MEN**	–	–	0.4	–	–	0.6	–	2.5
	Q2	**MEN**	–	–	–	–	–	–	2.7	3
	MEN1	**MEN**	–	0.6	0.8	1	1	1.4	2	2.4
	R	**MEN**	–	–	–	–	2	2	–	1.5

LE-Espejo; LQ-Quijada; LC-Churrasco; LEl-Élida; LU-Unco; LM-Las Mellizas; LT-el Toro; LTr-Tranquilo

Table 2.2b. Maximum grain size (mm) of tephras in cores from multiple lakes

	Tephra	Source	Southern lakes				Northern lakes			
			LE	LQ	LC	LEl	LU	LM	LT	LTr
Zone III	**S1**	**HUD**	0.8	0.6	–	–	–	–	0.8	0.8
	S2	**HUD**	0.4	0.4	0.4	0.6	0.3	0.3	0.4	0.3
	S3	**HUD**	0.8	0.8	0.6	–	–	–	0.6	
	S4	**HUD**	0.6	0.5	0.6	0.4	1.2	1.2	1.4	–
	S5	**HUD**	0.6	0.6	0.5	0.4	0.5	0.5	0.6	0.3
	S6	**HUD**	0.6	–	–	–	–	–	–	–
	S7	**HUD**	–	–	–	0.5	–	–	–	–
	S8	**HUD**	0.4	0.4	0.5	–	–	–	–	–
	S9	**HUD**	0.6	–	–	–	–	–	–	–
	S10	**HUD**	–	–	–	0.8	–	–	–	–
Zone IV	**T**	**MEN**	–	–	–	–	0.5	0.6	0.8	0.8
	V	**HUD**	0.6	0.6	0.6	–	0.4	0.4	0.4	0.2
	Ws	**HUD**	0.4	–	–	–	–	–	–	–
	Wn	**M/C/MEC**	–	–	–	–	–	0.3	0.4	–
	X1	**HUD**	–	–	0.3	–	–	–	–	–
	X2	**HUD**	–	0.3	0.3	0.4	–	–	0.4	0.3
	X3	**HUD**	–	0.6	–	0.6	0.5	0.2	–	0.3
	Y1	**M/C/MEC**	–	–	0.2	0.3	–	–	0.4	–
	Z1	**HUD**	–	0.8	0.6	–	0.6	0.6	0.6	0.4
	Z3	**M/C/MEC**	–	–	0.4	–	0.3	0.4	0.3	0.6
	Z4=MENo	**MEN**	–	–	–	–	0.6	0.8	0.8	–
	Z5	**M/C/MEC**	–	–	–	–	–	0.6	0.5	–

LE-Espejo; LQ-Quijada; LC-Churrasco; LEl-Élida; LU-Unco; LM-Las Mellizas; LT-el Toro; LTr-Tranquilo

oblique subduction of the Nazca Plate underneath South America (Nelson et al. 1994; Cembrano et al. 1996).

According to Völker et al. (2011), average volcanic extrusion rates in the Andean arc decrease southwards from 9.9 km^3/km in the Central SVZ north of 41°S, to only 2.2 km^3/km in the southernmost part of the SVZ south of where the Guafo Fracture Zone enters the Chile Trench at ~44°S. Despite this southward regional reduction in the estimated average extrusion rate, the Hudson volcano is larger (147 km^3) than average SVZ volcanic edifices (~100 km^3). Hudson, with a documented history of over 1 million years (Orihashi et al., 2004), is also older than average SVZ centers. Nevertheless, Hudson volcano, which is the only volcano in the southernmost SSVZ to have had historic activity (González-Ferrán 1994), has erupted a large volume of pyroclastic material since the beginning of glacial retreat (>45 km^3; Weller et al. 2014) and as a result has a high proportion (~30%) of pyroclastic material not included in the estimate of its total volume made by Völker et al. (2011). Therefore, the Holocene activity of Hudson has clearly been anomalous compared to other volcanoes in the SVZ. In contrast, Völker et al. (2011) estimate the volumes of the Mentolat, Cay and Macá volcanoes, which, like Hudson, might be much older than Holocene, as between only 40-50 km^3 each, and the numerous Holocene minor eruptive centers (MEC) in this zone have an even smaller volume (<<10 km^3 total).

Melimoyu volcano (Fig. 2.1), which is formed by basalts, andesites and dacites (López-Escobar et al. 1993; Naranjo and Stern 2004), has had two large and a number of smaller Holocene explosive eruptions (Naranjo and Stern 2004; Stern et al. 2015), but there is no evidence of Melimoyu tephras dispersed as far to the south as Coyhaique. Mentolat is formed by basaltic andesite and andesite lavas (López-Escobar et al. 1993) capped by a summit crater filled with an ice covered dome (see Fig. 2.13 in Naranjo and Stern 2004). A light grey andesitic tephra deposit

(MEN1; Fig. 2.1), dated at approximately 7,690 ± 60 cal yrs BP (Stern et al. 2016), has been observed in outcrops northwest of Coyhaique (Naranjo and Stern 2004), and also in cores from both Lago Shaman (Fig. 2.1) east of the volcano (de Porras et al. 2012; Stern et al. 2015) and from other small lakes, such as Augusta (Fig. 2.1), and trenches in bogs south of Coyhaique near the town of Cochrane (Fig. 2.1; Villa-Martínez et al. 2012; Stern et al. 2013, 2016). Two other younger tephra which crop out in the vicinity of the Mentolat volcano have been attributed to eruptions of this volcano at <2,560 and 4,320 cal yrs BP, respectively (Mella et al. 2012), and tephra from these events, as well as six tephra derived from other eruptions of Mentolat, have been observed in cores from Lago Shaman (Fig 1) and Mallín el Embudo east of the volcano (de Porras et al. 2012; 2014; Stern et al. 2015).

45 km south of Mentolat, Cay is a highly eroded stratovolcano formed by basalts, basaltic andesites and dacites (Futa and Stern 1988; López-Escobar et al. 1993; D'Orazio et al. 2003). There are no previous observations of Holocene tephra deposits attributed to this volcano. Macá, located at the northwest end of a prominent NW-SE trending volcanic ridge 15 km to the west of Cay, is a partially eroded stratovolcano composed of basalts and basaltic andesites (Futa and Stern 1988; López-Escobar et al. 1993; D'Orazio et al. 2003; Gutiérrez et al. 2005). Outcrops northwest of Coyhaique of basaltic-andesite MAC1 tephra (Fig. 2.1), dated at 1,440 ± 40 cal yrs BP, have been attributed to a medium size explosive eruption of this volcano (Naranjo and Stern 2004). Surrounding Macá and Cay volcanoes are numerous monogenetic cones that have erupted mostly basalts, but in some cases basaltic andesites and andesites (D'Orazio et al. 2003; Gutiérrez et al. 2005; Vargas et al. 2013).

Hudson, the southernmost volcano of the SVZ, contains a 10 km in diameter ice-filled caldera (Naranjo and Stern 1998; Gutiérrez et al. 2005). Several historic eruptions from Hudson

have been observed, including a small Plinian eruption in 1971 AD that melted a part of the caldera ice fill and generated a large lahar (Best 1992), and the larger explosive H3 event in 1991 AD (>4 km^3; Naranjo 1991; Scasso et al. 1994; Kratzmann et al. 2009, 2010; Wilson et al. 2011, 2012). Additionally, evidence for multiple large explosive Late-Glacial and Holocene eruptions from Hudson are preserved as tephra deposits observed in both outcrops and lacustrine sediment cores over a large region of southernmost Patagonia (Fig. 2.1), as far west as the Pacific coast (Haberle and Lumley 1998), east to the Atlantic coast and as far south as Tierra del Fuego (Stern 1991, 2008; Naranjo and Stern 1998) and Isla de los Estados (Unkel et al. 2010; Björck et al. 2012), as well as in Pacific oceanic sediment cores (Siani et al. 2010, 2013; Carel et al. 2011). These eruptions include the ~17,370 ± 70 cal yrs BP Ho event (>20 km^3; Weller et al. 2014), the 8,170 ± 60 cal yrs BP H1 eruption (>18 km^3; Stern 1991, 2008; Naranjo and Stern 1998; Stern et al. 2016), and the 4,000 ± 50 cal yrs BP H2 eruption (>5 km^3; Naranjo and Stern 1998). Tephra from several other smaller Holocene eruptions of Hudson within excavated trenches, including a distinctive mafic tephra T6 dated as 2,235 ± 120 cal yrs BP, have also been observed southeast of this volcano (Naranjo and Stern 1998).

Lavas and tephra from the southernmost SSVZ volcanoes fall in two distinguishable chemical groups which have been termed Low Abundance (LA) and High Abundance (HA) type samples (Fig. 2.3; López-Escobar et al. 1993, 1995). Samples of lavas and tephras derived from Mentolat, Macá, Cay and MEC volcanoes south of Mentolat are all LA types, while Hudson has erupted only HA lavas and tephra with distinctly higher incompatible large-ion-lithophile (LIL; Cs, Rb, Ba, Sr, K, Th), rare-earth-element (REE) and high-field-strength element (HFSE; Ti, Zr, Nb, Hf, U) contents. For the Hudson volcano, Carel et al. (2011) have demonstrated that Hudson's HA chemical characteristics are reflected in both bulk lava, tephra and tephra glass

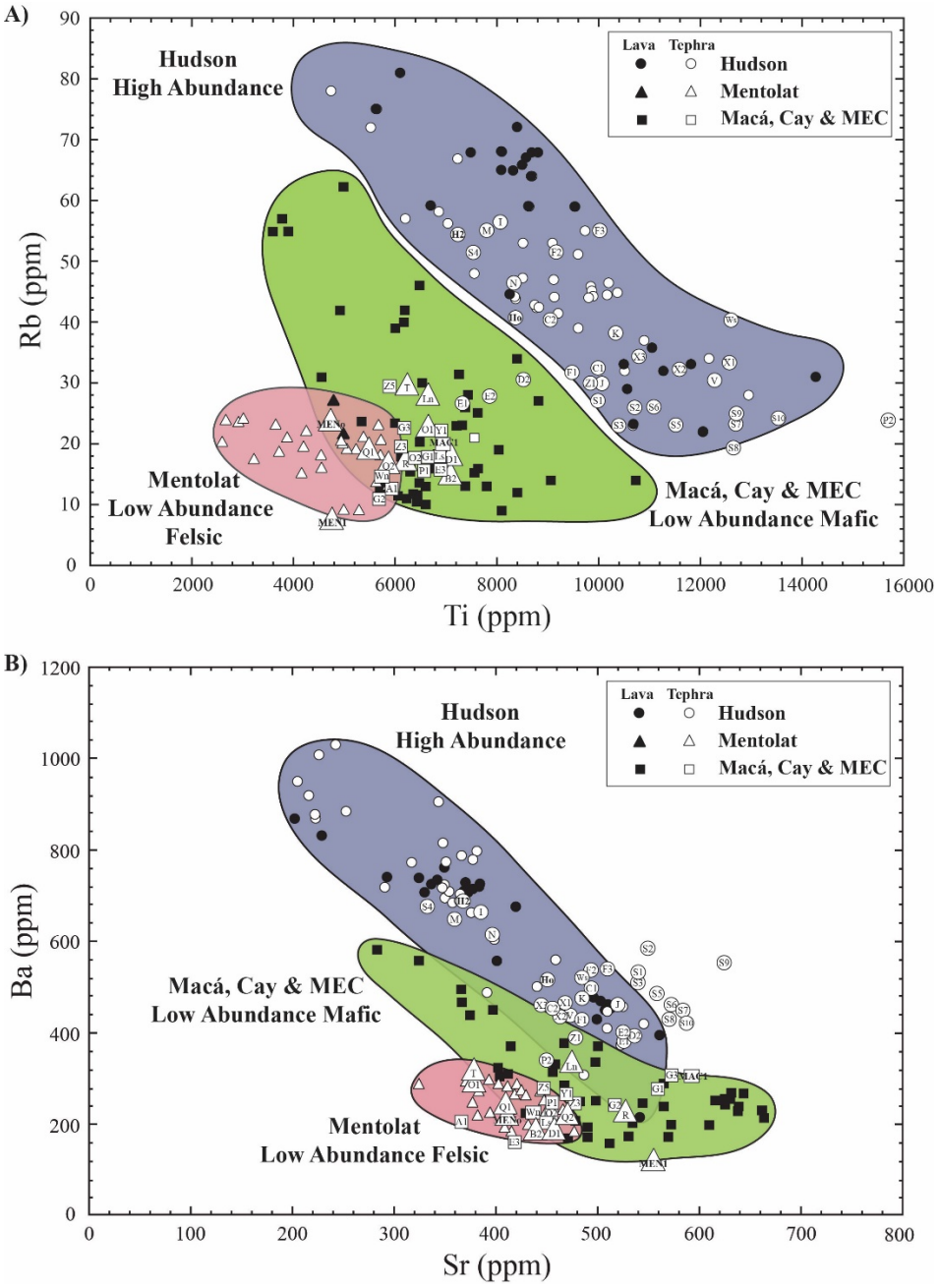

Figure 2.3. A. Ti versus Rb; and B. Sr versus Ba concentrations, in parts-per-million (ppm), for published data of lavas (small solid symbols) and tephras (small open symbols) from Hudson, Mentolat, Macá, Cay and MEC (Futa and Stern 1988; López-Escobar et al. 1993; 1995; Naranjo and Stern 1998, 2004; D'Orazio et al. 2003; Gutiérrez et al. 2005; Stern et al. 2015a, 2015b), and bulk tephra from this study (larger labeled open symbols; Tables 2.2-2.5). The Hudson samples are all High Abundance (HA) types which contain generally higher Ti, Rb, and Ba than both the Low Abundance Mafic samples from Macá, Cay and MEC, and the Low Abundance Felsic samples, which contain amphibole and clear glass (Fig. 2.4), from Mentolat.

chemical analysis

Among the volcanoes characterized by the eruption of LA magmas, Mentolat andesites have, at any given SiO_2, lower K_2O (López-Escobar et al. 1993; Naranjo and Stern 2004; Stern et al. 2016) and other LIL element (Fig. 2.3) concentrations than Maca, Cay and MEC basalts and basaltic andesites. In this respect they are similar to andesites erupted from other volcanoes further north along the SVZ volcanic front such as Huequi (Watt et al. 2011), Calbuco (López-Escobar et al. 1995) and Nevado de Longaví (Sellés et al. 2004), which like Mentolat all have amphibole as a phenocryst phase (Fig. 2.4).

These chemical differences, along with petrographic characteristic and spatial distribution, have been used in the past to identify the SSVZ source volcanoes of specific tephra (Stern 1991; 2008; Naranjo and Stern 2004; Carel et al. 2011; Stern et al. 2013, 2015, 2016; Weller et al. 2014). They are also used in this paper as a guide to the possible source volcanoes of tephra found in the sediment cores from the lakes near Coyhaique (Fig. 2.3).

2.4 Methods

Eight lakes were cored as part of a project to understand the paleoclimatic evolution of this region of southern Patagonia (Miranda et al. 2013). These lakes, all formed by glacial scouring of the bedrock, were selected for sampling because of their small size (<800 meter maximum diameter; <1 km^2 surface area), shallow depth (<10 meters), and the limited area of their drainage catchments (<10 km^2), which minimizes the volume of clastic sedimentary input from streams. They are all significantly smaller than other lakes in the region, such as Castor and Escondida (Fig. A2.1 in the appendix; Elbert et al. 2013), from which cores with tephra have been reported previously. Multiple sediment cores from each lake, which are stored in a refrigerator at the Universidad de Chile in Santiago, were obtained over a three year period using a 5 cm modified Livingston Piston Corer. The cores were collected at one meter length intervals

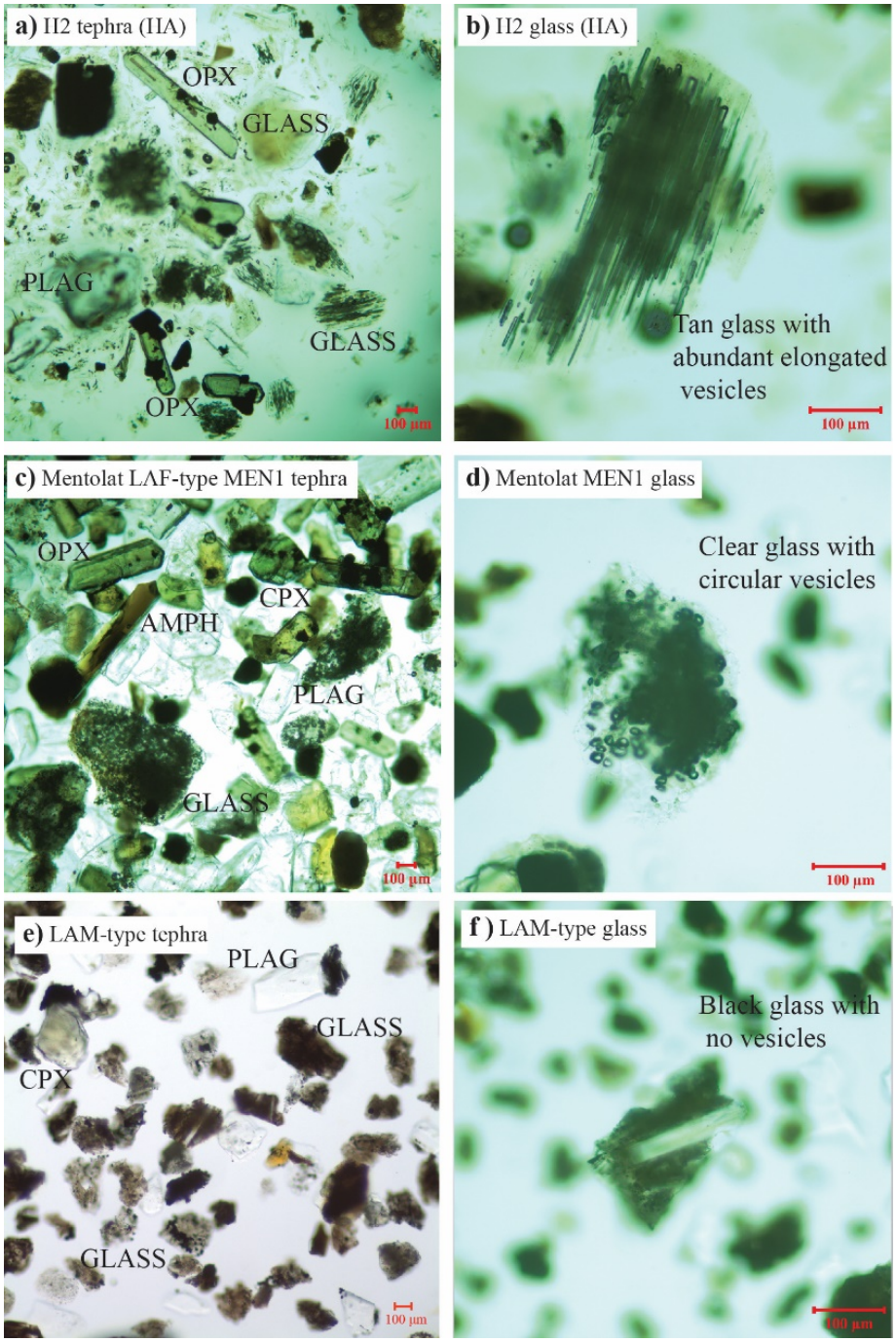

Figure 2.4. Photomicrographs of petrochemical distinct types of tephra from different source volcanoes. **A and B.** Hudson-derived H2 tephra containing light brown glass with elongate cylindrical vesicles and phenocrysts of plagioclase, clinopyroxene and orthopyroxene. **C and D.** Mentolat-derived MEN1 phenocryst-rich tephra containing plagioclase, clino and orthopyroxene, brown amphibole and colorless glass with abundant undeformed vesicles and no mineral microlites. **E and F.** MAC1 tephra, derived from Macá, containing black glass with abundant mineral microlites and no visible vesicles.

until sediments transitioned from predominately organic-matter-rich lacustrine to sand- and clay-rich glacial sediments. The length of the sediment record for each lake is unique and is controlled by the duration since the glacial retreat and the sediment accumulation rate since that time. A preliminary chronology of some of the different tephra identified in the cores, specifically Ho (Weller et al. 2014) and the S1 to S10 sequence of tephra (Fig. 2.2), as well as the age of the earliest organic rich sediment near the base of the cores, has been controlled by AMS radiocarbon dates of organic material in the sediments above and below these tephra (Table A2.1 in the appendix; Miranda et al. 2013; Weller et al. 2014). Radiocarbon dates were converted to calendar years before present (cal yrs BP) using the CALIB 7 program and the SHCal13 data set (Stuiver et al. 1998). The age of other tephra (D3=MAC1 from Maca, F3=T6 and H2 from Hudson volcano, and MEN1 from Mentolat; Table 2.1) are controlled by previously determined ages from outcrops (Naranjo and Stern 1998, 2004) and other cores in the region (Elbert et al. 2013; Stern et al. 2016). The ages of all the other previously unknown tephra in these cores have not been determined directly, but can be roughly estimated based their depth in the cores relative to these five dated tephra.

Each core segment was imaged using transmitted X-rays to aid in the identification of the tephra deposits. Figure 2.2 shows the X-ray images for the approximately 8.5 meters of sediment cored from Lago Unco (core #PC1103E). The darker layers are the less dense organic material rich post-glacial lacustrine sediments, while the white layers within the cores are denser lithologies, generally tephra deposits, but also including sands in the deeper parts of the cores deposited during late-glacial and/or glacial times. The X-ray image of the other seven lakes are contained in the appendix (Figs. A2.2-A2.8 in the appendix).

Thicker, visually identifiable tephra layers were removed from the lake cores with a knife. Over 400 tephra samples were collected from the cores over a three year period, but many of the very thin dense layers observed in the X-ray images of the cores were not sampled. Tephra were washed in water and acetone to remove organic matter. A portion of each tephra sample was mounted on a slide and examined under a petrographic microscope to characterize its grain size (Table 2.2) and petrography (Fig. 2.4; Table A2.2 in the appendix). A total of 290 bulk tephra samples were powdered in a tungsten-moly shatter box and dissolved at 95°C in a mixture of HF, HCl and HNO_3 acids for trace-element analysis using an ELAN D CR ICP-MS. Repeated analysis of internal lab standards, including a basalt, andesite and rhyolite, were used to determine precision, which is generally better than 10% at the concentration levels of the tephra, and analysis of basalts samples BHVO1 and NIST2711 were used to monitor accuracy (Table A2.11 of the appendix; Saadat and Stern 2011). Analyses of individual tephra from the different cores are presented in Tables A2.3-A2.10 of the appendix, and the average of specific tephra correlated across the cores are presented in Tables 2.3-2.6.

2.5 Results

The results include a description of tephra thickness (Table 2.1), maximum grain size (Table 2.2), petrography (Table A2.2 in the appendix) and trace-element chemistry (averages for specific tephra in Tables 2.3-2.6; all the data for the each tephra in every core in Tables A2.3-A2.10 of the appendix), as well as correlations of tephra among cores and source volcano identification (Table 2.1; Figs. 2.2 and 2.5-2.8; Figs. A2.2-A2.8 in the appendix). To simplify the presentation of the results, each core has been subdivided into four zones which are bound by tephra from distinctive well-constrained eruptions or eruption sequences (Fig. 2.2). Zone I begins

at the top of the cores and extends to the tephra derived from the 4,000 ± 50 cal yrs BP late Holocene H2 eruption of the Hudson volcano (Naranjo and Stern 1998), which was identified in every core based on its thickness and petrography. Zone II consist of all the tephra between the H2 eruption and the sequence of 10 closely spaced tephra S1 to S10 observed in every core. Zone III consist only of this sequence of these 10 eruptions (S1 through S10), while Zone IV consist of all of the sediments and volcanic products below this sequence and extending back to the predominately clay and sand-rich glacial-lacustrine sediments at the bottom of the cores. In each of these zones, groups of tephra which have similar stratigraphic relations, with relatively small separations among themselves and greater separations from the tephra in other groups, have been identified in multiple cores. These tephra groups, which have been correlated across multiple cores by both their stratigraphic relations and petrochemical characteristics, have been named A though H2 in Zone I, I though R in Zone II, S1 through S10 in Zone III, and T though Z in Zone IV (Figs. 2.2 and 2.5-2.8; Table 2.1). Many of these groups have multiple tephra layers, labeled as for example S1 through S10. In some cases not all the tephra in any group (for example tephra A2 in group A, or any of the U1-3 tephra) were sampled, but they are labeled and included in Table 2.1 because they appear in multiple cores in regular stratigraphic relations with other tephra. Also, the tephra within any one group may have different sources (for example group D; Table 2.1), because the different groups were identified based on their consistent internal stratigraphic relations, not their source volcanoes.

Lagos Tranquilo, El Toro, Las Mellizas and Unco are located in the northern portion of the study area, while Espejo, Quijada, Churrasco and Élida are further to the south (Fig. 2.1). A northern and southern division of the lakes (Table 2.1; Figs 2.5-2.8) based on this geographic separation is useful because the cores from the northern four lakes have fewer, thinner and finer

grained deposits of Hudson-derived tephra, and more frequent, somewhat thicker, and coarser deposits of Mentolat-derived tephra.

2.5.1 Correlations and source volcano identification

Correlation of the tephra deposits (Table 2.1; Figs. 2.2 and 2.5-2.8; Figs. A2.2-A2.8 in the appendix) are based on three criteria: 1) the stratigraphic position of the tephra in the cores; 2) bulk-tephra trace-element compositions (Fig. 2.3 Tables 2.2-2.5; Tables A2.3-2.10 in the appendix); and 3) the color, morphology (Fig. 2.4) and abundance of their volcanic glass along with the identity and abundance of mineral microlites and phenocrysts (Table A2.2 in the appendix). Tentative identifications of the source volcanoes of tephra are also based on bulk-tephra chemistry and petrology as outlined below.

2.5.2 Hudson tephra

All published analyses of lavas and tephra derived from explosive eruptions of Hudson volcano, which range from basaltic to dacitic in composition, are High Abundance (HA) chemical types (Fig. 2.3), and thus all tephra with HA chemistry in the cores from the lakes near Coyhaique are considered to be derived from the Hudson volcano. These HA tephra (Table 2.1) are generally thicker and coarser grained (Table 2.2) in the southern lakes compared to the northern ones consistent with the location of Hudson volcano (Fig. 2.1). Tephra derived from previously documented explosive eruptions of Hudson also have other distinctive morphologic and petrologic characteristics used to distinguish the smaller eruptions from Hudson observed within the cores. Specifically, tephra produced by Phase 2 of the H3 (1991 AD) eruption, as well as H2 and Ho tephra, are all characterized by the presence of pale orange-brown, vesicle-rich glass, which generally lacks plagioclase microlites (Figs. 2.4A and 2.4B). The vesicles are often highly deformed into elongated cylindrical shape reflecting the rapid extrusion of magma during these

explosive eruptions. Most all the HA chemical type of tephras attributed to eruptions of the Hudson volcano have this type of pale orange-brown, vesicle-rich tephra glass. However, darker, vesicle-poor and microlite-rich glass also occurs in many of the tephra with HA chemistry (Fig. 2.4A). Mafic glasses with similar morphology are associated with both Phase I of the H3 (Kratzmann et al. 2009) and the Ho (Weller et al. 2014) eruptions. Thus Hudson tephra color and morphology is variable and the overall chemistry of tephra glasses from Hudson eruptions varies from basaltic to dacitic, as do Hudson lavas, although all are HA chemical types (Fig. 2.3). Minor plagioclase feldspar, clinopyroxene, orthopyroxene, and small amounts of olivine phenocrysts are present in Hudson-derived tephra deposits, but not amphibole (Table A2.2 in the appendix).

2.5.3 Mentolat tephra

In contrast, Mentolat lavas (López-Escobar et al. 1993) and MEN1 tephra (Naranjo and Stern 2004; Stern et al. 2013, 2015, 2016) are Low Abundance (LA) chemical types (Fig. 2.3), with relatively low LIL (K, Rb, Ba) for intermediate (Ti <6000 ppm; Fig. 2.3) compositions compared even to other LA type basalts (López-Escobar et. 1993; Naranjo and Stern 2004; Watt et al. 2011). MEN1 tephra is characterized by the presence of colorless rhyolitic (Stern et al. 2016) glass with abundant circular undeformed vesicles and no mineral microlites (Figs. 2.4C and 2.4D). Other tephras in the cores with LA character and containing clear colorless glass are referred to as Low Abundance Felsic petrochemical types (LAF) and interpreted as being derived from the Mentolat volcano. However, the MEN1 eruption, like those of Hudson, as well as Melimoyu MEL1 and Chaitén CHA1 further north in the SSVZ (Naranjo and Stern 2004), was also heterogeneous, grading upwards in proximal outcrops into a more mafic composition, so that darker vesicle-poor, microlite-rich glass also occurs in this and other LAF-type tephra. These other LAF chemical type tephra layers, interpreted to have been produced by Mentolat (Table 2.1),

which are thicker and more frequent in the northern lakes, have, as does MEN1 tephra, abundant plagioclase, clinopyroxene and highly pleochroic orthopyroxene (hypersthene) phenocrysts (Fig. 2.4C), minor olivine, along with variable amounts of dark brown amphibole and in two cases (tephras O1 and R) biotite. López-Escobar et al. (1993) also recognized biotite in one Mentolat lava sample.

2.5.4 Macá, Cay and MEC derived tephra

Many of the tephra deposits within the sediment cores are LA chemical types, but are petrographically distinct from Mentolat tephras. These have dark brown to black glass with low to moderate vesicle abundances and often high abundances of microlites, but lack any clear vesicle-rich glass (Fig. 2.4E and 4F). The most abundant mineral phenocryst are plagioclase with minor clinopyroxene, orthopyroxene and trace olivine. Amphibole is absent. These tephras with LA character with dark glass, but no clear glass or amphibole, which are referred to as Low Abundance Mafic petrochemical types (LAM), are chemically and petrologically similar to MAC1 tephra derived from the Macá volcano (Naranjo and Stern 2004), but they may also have been derived from Cay volcano or one of the many small Holocene minor eruptive centers (MEC) in the region, which both also erupted LAM type magmas. These tephra are not assigned to a specific one of these possible sources, with the exception of the one tephra in group D (D3) which is correlated directly with MAC1 (Table 2.1).

2.5.5 General

An important point is that for these lake deposits no internal eruption-related lithostratigraphic variations have been observed within individual tephra layers, even for the thickest deposits such as Ho (Weller et al. 2014) and H2. This is because deposition of the tephra from the air to the bottom of even these small lakes involves processes of mixing and

homogenization such as settling, bioturbation or lake currents that eliminates the stratigraphic segregation of sequentially variable eruptive phases often preserved in outcrop deposits of tephra airfall (Bertrand et al. 2014). The bulk tephra in the cores represent the end product of these mixing processes that, we suggest, are likely to have been generally similar in all the spatially related small lakes from which the tephra have been sampled, thus rendering the chemical compositions of the bulk tephra comparable. For this reason we consider the approach of comparing bulk trace-element chemical analysis of tephra from different cores to be a useful technique for correlation of the tephra among the cores in this relatively restricted area of southern Chile, despite the fact that it is clear that all the tephra are heterogeneous mixtures of mineral grains and glasses of variable compositions that may be mechanically separated in different proportions during deposition, thus affecting the final bulk composition of the tephra. Nevertheless, the trace element data (Tables 2.3-2.6) preserve the High Abundance compared to Low Abundance characteristics of tephra associated with the specific petrographic features described above, such as, for example, amphibole and clear glass in the LAF type tephra interpreted to have been derived from Mentolat (Figs. 2.4C and 2.4D), and stretched-vesicle-rich, pale brown, microlite-free glasses in HA type tephra interpreted to have been derived from Hudson volcano (Figs. 2.4A and 2.4B).

2.5.6 Zone 1; core tops to H2 (Fig. 2.5; Table 2.3)

Tephra group A

Tephra group A consists of two thin deposits, a few centimeters apart, each recognized in two of the southern and four of the northern cores (Table 2.1). Tephra A1 has a LAM type chemical composition. It consists of blocky black to dark brown glass with minor small spherical vesicles and high abundance of plagioclase microlites. Plagioclase phenocrysts are common

Table 2.3a. Average trace element concentrations (ppm) of tephras in zone I from the core top to the H2 eruption

	Tephra Name								
	A1	**B2**	**C1**	**C2**	**D1**	**D2**	**D3= MAC1**	**E1**	**E2**
	Chemical Type								
	LAM	**LAF**	**HA**	**HA**	**LAF**	**HA**	**LAM**	**HA**	**HA**
	Source Volcano								
	M/C/ MEC	**MEN**	**HUD**	**HUD**	**MEN**	**HUD**	**MACA**	**HUD**	**HUD**
	n								
	1	**3**	**4**	**3**	**1**	**2**	**7**	**2**	**7**
Ti	5905	7069	9964	9027	6901	8503	6820	7282	7867
V	97	299	287	241	334	307	222	258	256
Cr	11	18	15	13	17	29	102	55	51
Mn	1086	1452	1319	1181	1418	1220	1110	1158	1173
Co	22	34	42	31	44	43	45	37	41
Ni	31	32	32	32	38	41	84	55	48
Cu	73	71	70	126	86	136	92	98	78
Zn	109	133	120	121	130	126	98	116	112
Rb	13	15	32	40	17	31	19	27	28
Sr	367	442	493	456	455	531	580	526	528
Y	20	20	31	31	21	29	20	23	24
Zr	91	87	209	206	93	187	157	190	195
Nb	3	4	9	10	2	8	7	9	10
Cs	-	0.4	0.5	0.7	0.7	0.7	0.2	0.6	0.4
Ba	199	186	495	448	190	391	308	382	390
La	9.1	8.3	28.5	28.7	8.5	23.5	19.5	24.2	25.1
Ce	22.2	19.9	65.2	65.4	20.8	53.2	44.8	54.4	55.9
Pr	2.8	2.7	8.5	8.3	2.86	6.8	5.6	6.7	6.9
Nd	14.0	13.3	36.9	35.9	14.2	29.6	23.9	28.4	29.3
Sm	3.96	3.47	7.61	7.56	3.41	6.36	5.00	5.91	6.05
Eu	1.08	1.09	2.26	2.11	0.93	1.86	1.50	1.72	1.75
Gd	4.4	4.2	8.9	8.8	4.25	7.5	5.8	6.7	6.9
Tb	0.52	0.54	1.08	0.99	0.47	0.81	0.65	0.77	0.80
Dy	3.66	3.41	6.24	6.08	3.68	5.18	3.98	4.58	4.73
Ho	0.59	0.62	1.18	1.06	0.66	0.95	0.72	0.86	0.86
Er	2.20	2.20	3.65	3.53	2.29	3.03	2.28	2.68	2.78
Tm	0.13	0.20	0.41	0.38	0.20	0.32	0.22	0.32	0.30
Yb	1.83	1.99	3.07	3.03	1.96	2.64	2.03	2.27	2.46
Lu	-	0.14	0.32	0.26	0.21	0.32	0.17	0.32	0.26
Hf	2.5	2.7	5.0	4.8	1.9	4.1	3.7	4.6	4.9
Pb	7.0	5.3	6.9	8.2	4.8	6.5	5.3	6.8	6.9
Th	1.2	1.9	3.6	4.3	0.6	2.9	2.5	3.9	4.1
U	0.4	0.3	0.8	0.9	0.3	0.6	0.5	0.7	0.8

Table 2.3b. Average trace element concentrations (ppm) of tephras in zone I from the core top to the H2 eruption

	Tephra Name							
	E3	**F1**	**F2**	**F3**	**G1**	**G2**	**G3**	**H2**
	Chemical Type							
	LAM	**HA**	**HA**	**HA**	**LAM**	**LAM**	**LAM**	**HA**
	Source Volcano							
	M/C/ MEC	**HUD**	**HUD**	**HUD**	**M/C/ MEC**	**M/C/ MEC**	**M/C/ MEC**	**HUD**
	n							
	1	**7**	**1**	**1**	**7**	**2**	**3**	**10**
Ti	6888	9468	9157	9993	6617	5656	6146	7221
V	386	261	274	348	234	221	232	146
Cr	38	27	14	14	92	76	92	13
Mn	1395	1218	1311	1280	1037	1007	930	1147
Co	45	34	38	33	39	43	37	20
Ni	39	39	34	35	61	53	59	26
Cu	127	98	46	133	85	66	97	55
Zn	135	117	112	113	97	86	84	110
Rb	16	32	51	55	17	11	23	54
Sr	419	483	492	509	561	521	580	368
Y	16	30	31	33	21	16	20	37
Zr	83	218	199	209	136	93	127	349
Nb	3	9	11	8	8	4	6	17
Cs	0.8	0.4	1.2	1.0	0.2	0.3	0.5	0.9
Ba	156	428	532	539	274	245	310	688
La	6.4	27.3	28.0	31.6	17.0	11.8	17.5	38.7
Ce	17.3	62.6	64.0	69.7	39.3	27.2	38.9	84.7
Pr	2.2	8.0	8.3	9.3	5.0	3.5	5.0	10.2
Nd	11.7	34.0	34.4	38.9	21.7	15.7	20.9	41.1
Sm	2.76	7.32	7.35	7.94	4.64	3.50	4.52	8.59
Eu	0.87	2.10	2.26	2.27	1.50	1.13	1.41	2.49
Gd	3.7	8.5	8.5	9.2	5.3	4.1	5.3	10.0
Tb	0.39	0.98	1.17	1.10	0.60	0.31	0.65	1.20
Dy	3.03	5.89	6.20	6.46	3.77	3.19	3.83	6.93
Ho	0.54	1.07	1.22	1.23	0.67	0.34	0.73	1.32
Er	1.78	3.45	3.46	3.79	2.24	1.77	2.27	4.27
Tm	0.18	0.37	0.43	0.44	0.21	0.12	0.26	0.50
Yb	1.61	2.98	3.05	3.52	1.93	1.59	1.91	3.95
Lu	0.17	0.29	0.45	0.48	0.20	0.12	0.23	0.49
Hf	2.2	4.9	6.1	5.0	3.9	2.5	2.8	8.0
Pb	5.0	7.1	7.2	9.0	4.3	4.1	4.7	11.2
Th	1.1	3.5	7.0	4.3	2.8	1.2	2.3	6.0
U	0.4	0.8	1.0	1.0	0.4	0.3	0.5	1.4

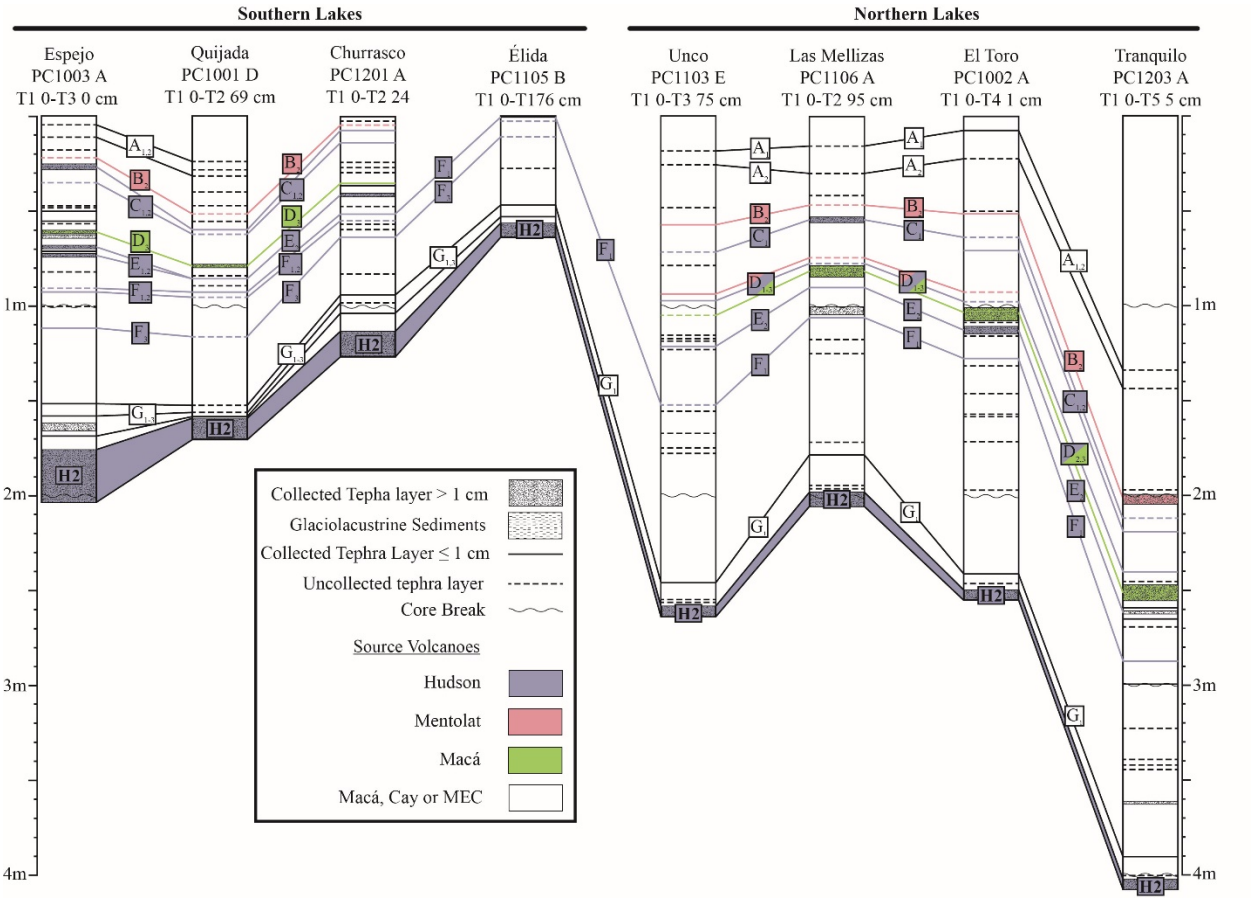

Figure 2.5. Stratigraphic sections for the eight lake cores for Zone 1, from the top of the cores to the H2 Hudson tephra, showing the correlations for tephras A to H2 (Table 2.1) among the different cores.

in this tephra. Based on its chemistry and petrography, its source volcano may be either Macá, Cay or one of the MEC. No samples were taken of A2 from any of the cores.Tephra Group B

Tephra group B consists of two thin deposits in three of the southern cores and thicker (up to 4 cm) layers in the northern lakes (Table 2.1). No samples were taken of tephra B1. Tephra B2 is a LAF petrochemical type characterized by both abundant black and less abundant colorless glass, the latter with high abundances of spherical vesicles and no mineral microlites. Phenocrysts include abundant plagioclase, clinopyroxene, orthopyroxene and small to moderate abundances of both olivine and dark brown amphibole. Based on its LAF type petrochemistry, and the presence of both clear glass and amphibole, we suggest that its source was Mentolat volcano.

Tephra Group C

Tephra group C generally occurs as two deposits. Tephra C1, the thicker (up to 3 cm) of the two, which was sampled from four of the lake cores, is a HA chemical type which consists of both black and dark brown glass with no or minor spherical vesicles and abundant plagioclase microlites. Phenocrysts include plagioclase along with minor pyroxenes and trace olivine. C2 is thinner, but has similar HA chemical and petrologic characteristics. Based on their HA chemistry, both tephra are interpreted as having been derived from the Hudson volcano.

Tephra Group D

Tephra group D contains three distinct deposits. Tephras D1 and D2 are generally 1 cm or less in thickness, while tephra D3 is up to 8 cm thick. Tephra D1 is a LAF petrochemical type characterized by two distinct glass types; one is black in color with no visible vesicles and the other clear with moderate abundances of undeformed spherical vesicles. Phenocrysts in D1 include plagioclase, minor clinopyroxene, orthopyroxene, olivine, and trace amphibole. These features together suggest that D1 tephra was derived from Mentolat.

Tephra D2 is a HA chemical type, and thus likely to have been derived from Hudson volcano, although its Ti content is somewhat low compared to other Hudson samples (Fig. 2.3). It consists of dark orange-brown glass color containing a moderate abundances of undeformed spherical vesicles and high abundance of mineral microlites. Phenocrysts include plagioclase and clinopyroxene.

Tephra D3 is a LAM chemical type with blocky dark orange-brown to black glass containing few or no spherical vesicles and lacking microlites. This tephra contains plagioclase phenocrysts along with minor clinopyroxene and trace olivine. We correlate this tephra with the MAC1 eruption dated as 1,440 cal yrs BP (Table 2.1) based on its LAM trace-element chemistry and thickness, which is consistent with the 10 cm isopach (Fig. 2.1) as estimated by Naranjo and Stern (2004), and its stratigraphic position in the cores, which is consistent with an age similar to that of MAC1. Therefore, we suggest that this is equivalent to tephra T3 in Castor and Escondido lakes (Fig. A1 in the appendix) identified by Elbert et al. (2013), which is one of the thickest of the eight tephra they identify, and has essentially the same bulk chemistry as MAC1 determined by Naranjo and Stern (2004). Although their bulk sediment age for this tephra (160 AD) is 500 years older than that of MAC1, Bertrand et al. (2012) have shown that lake sediment ^{14}C ages may be significantly older than true ages because of the input from the surrounding drainage basin of older organic material into a lake.

Tephra Group E

Tephra group E contains up to 4 different deposits. Tephra E1 and E4 range in thickness only up to 1 cm, while E3 is up to 2 cm and E2 up to 3 cm (Table 2.1). E4 was too thin to sample. E1 and E2 (Fig. 2.4) are HA chemical types, suggesting that Hudson was the source of these two tephra, although both have low Ti compared to other HA samples (Fig. 2.3). They consist of dark

orange to pale brown glass containing moderate abundances of circular vesicles and moderate to high microlite abundances. The dominant phenocrysts within these deposits are plagioclase, but orthopyroxene and clinopyroxene also occur.

Tephra E3 is a LAM chemical type with both black and brown glass with no or few visible vesicles and abundant microlites. Plagioclase is the only phenocryst observed. This tephra may be sourced from either Macá, Cay or one of the MEC.

Tephra Group F

Tephra group F contains three deposits all of which are 1 cm or less in thickness and HA chemical types, and therefore all are considered to be derived from Hudson volcano (Table 2.1). They are characterized by both black and orange-brown glass, the latter with moderate to low abundances of weakly deformed vesicles and moderate to high abundances of microlites. Plagioclase and trace orthopyroxene occur as phenocrysts. Based on its stratigraphic position in the cores and its HA trace-element character, we correlate tephra F3 with the 2,235 ± 120 cal yrs BP mafic Hudson tephra T6 described by Naranjo and Stern (1998). Elbert et al. (2013) also correlate their tephra T6 (300 BC) with that described by Naranjo and Stern (2004), as both have similar age and chemistry.

Tephra Group G

Tephra group G consists of three LAM chemical type deposits (Table 2.1), suggesting that they may be sourced from either Macá, Cay or one of the MEC. We correlate G1, which is the thickest (up to 2 cm), with tephra T7 (1,700 BC) of Elbert et al. (2013) on the basis of its stratigraphic positon just above H2. The glass in these three deposits is either black, with no or few visible microlites or vesicles, or brown with a moderate to low abundances of spherical

vesicles and abundant microlites. Phenocrysts include plagioclase and clinopyroxenes, orthopyroxene, and trace amounts of olivine.

Tephra H2

The bottom of Zone I corresponds to the 8 to >50 cm thick tephra produced by the HA chemical type Hudson H2 eruption at 4,000±50 cal yrs BP (Naranjo and Stern 1998). This is tephra T8 of Elbert et al. (2013), estimated by them as 4,060 cal yrs BP based on an extrapolation assuming a constant sedimentation rate during the 700 years before their oldest date at 3,348±100 cal yrs BP, and tephra HW5 of Haberle and Lumley (1998), estimated by them as 3,850 cal yrs BP also based on extrapolation assuming a constant sedimentation rates from after an older age of 4,250±35 cal yrs BP from deeper in the core. It contains vesicle-rich, pale orange-brown glass and phenocrysts of plagioclase and orthopyroxene.

2.5.7 Zone 2; H2 to top of the S1-10 sequence (Fig. 2.6; Table 2.4)

Tephra I

Tephra I is a HA chemical type with a broad spectrum of glass morphologies that range from dark brown mafic glass with minor microlites and few spherical vesicles to pale brown glass with moderate abundances of stretched vesicles that grade into light tan to clear glass with high abundances of stretched vesicles. Phenocrysts include minor amounts of pyroxenes and plagioclase. Based on its HA chemistry, we suggest that this tephra, which is thicker in the southern lake cores (up to 2 cm), is derived from the Hudson volcano. The trace-element chemistry for the proximal deposit (Lago Espejo; Table A3 in the appendix) is overall more mafic in composition (higher Ti, Mn, Sr and lower Rb, Ba and Zr) than the two distal deposits (Lago Élida and Lago

Table 2.4a. Average trace element compositions (ppm) of tephras in zone II from the H2 eruption to the top of the sequence of tephras S1-10

	Tephra Name						
	I	**J**	**K**	**Ls**	**Ln**	**M**	**N**
	Chemical Type						
	HA	**HA**	**HA**	**LAM**	**LAF**	**HA**	**HA**
	Source Volcano						
	HUD	**HUD**	**HUD**	**M/C/MEC**	**MEN**	**HUD**	**HUD**
	n						
	3	**4**	**3**	**2**	**3**	**3**	**9**
Ti	8084	10010	10342	6830	6639	7813	8304
V	172	306	282	339	224	165	170
Cr	9	16	16	25	23	18	23
Mn	1292	1236	1171	1160	1077	1126	1246
Co	22	33	29	37	28	20	33
Ni	30	34	36	36	38	35	38
Cu	74	108	85	127	79	97	66
Zn	125	123	123	110	118	114	121
Rb	57	30	38	18	28	55	46
Sr	385	521	484	447	474	360	397
Y	39	30	32	21	23	42	39
Zr	343	222	207	83	128	388	346
Nb	16	13	11	2	4	17	16
Cs	1.2	0.5	0.9	0.9	0.5	1.3	0.8
Ba	661	459	473	197	334	649	612
La	39.0	30.8	32.1	9.5	15.4	42.0	38.2
Ce	85.4	69.3	70.0	21.7	36.1	93.0	85.7
Pr	10.31	8.88	9.11	3.08	4.66	11.4	10.62
Nd	42.2	36.2	37.0	13.8	21.5	45.6	42.4
Sm	8.49	7.65	7.92	3.59	4.88	9.44	8.94
Eu	2.35	2.20	2.27	1.14	1.35	2.51	2.53
Gd	9.64	8.90	9.13	4.47	5.75	10.5	10.12
Tb	1.16	1.03	1.11	0.57	0.65	1.35	1.26
Dy	6.88	5.82	6.12	3.77	4.36	7.56	7.35
Ho	1.33	1.08	1.19	0.75	0.75	1.52	1.39
Er	4.21	3.37	3.75	2.27	2.61	4.77	4.39
Tm	0.53	0.38	0.46	0.26	0.19	0.63	0.55
Yb	3.82	2.95	3.16	2.02	2.35	4.41	4.15
Lu	0.53	0.30	0.43	0.28	0.18	0.67	0.53
Hf	7.1	5.6	5.0	2.0	3.0	8.5	7.7
Pb	10.1	8.0	7.8	5.9	7.0	12.6	10.5
Th	5.2	3.9	4.6	1.1	2.2	6.2	5.2
U	1.4	0.8	1.0	0.5	0.7	1.5	1.2

Table 2.4b. Average trace element compositions (ppm) of tephras in zone II from the H2 eruption to the top of the sequence of tephras S1-10

	Tephra Name							
	O_1	**O_2**	**P_1**	**P_2**	**Q_1**	**Q_2**	**MEN1**	**R**
Chemical Type	**LAF**	**LAM**	**LAM**	**HA**	**LAF**	**LAF**	**LAF**	**LAF**
Source Volcano	**MEN**	**M/C/MEC**	**M/C/MEC**	**HUD**	**MEN**	**MEN**	**MEN**	**MEN**
n	**1**	**5**	**8**	**5**	**3**	**2**	**7**	**3**
Ti	6627	6230	6524	15661	5478	5875	4761	6199
V	157	204	213	321	190	176	185	249
Cr	56	18	22	13	16	18	22	18
Mn	1162	1078	1122	1596	1092	1175	1607	1364
Co	71	29	34	36	27	29	34	33
Ni	46	32	35	39	34	34	30	37
Cu	78	69	91	103	120	48	22	40
Zn	116	107	115	145	117	114	117	119
Rb	22	17	16	24	19	16	7	17
Sr	378	452	452	450	409	472	556	528
Y	28	21	20	38	22	20	12	19
Zr	108	86	78	201	104	84	49	86
Nb	5	4	4	9	4	3	2	3
Cs	0.4	0.5	0.5	0.5	0.9	0.4	0.2	0.5
Ba	289	229	224	337	231	218	113	223
La	14.1	9.6	9.5	26.2	11.1	9.3	5.5	10.6
Ce	32.5	22.9	22.8	63.6	25.5	22.3	13.7	24.8
Pr	4.3	3.08	3.12	8.69	3.47	2.92	1.87	3.19
Nd	20.3	14.5	14.0	39.5	16.0	14.0	9.0	14.9
Sm	4.82	3.73	3.69	8.72	3.77	3.68	2.16	3.69
Eu	1.54	1.17	1.23	2.69	1.21	1.08	0.88	1.21
Gd	6.0	4.45	4.43	10.25	4.59	4.45	2.70	4.30
Tb	0.69	0.56	0.57	1.29	0.52	0.50	0.31	0.50
Dy	4.74	3.71	3.71	7.23	3.62	3.56	2.21	3.61
Ho	0.92	0.67	0.74	1.37	0.67	0.62	0.35	0.65
Er	2.93	2.28	2.22	4.18	2.25	2.42	1.32	2.12
Tm	0.31	0.21	0.28	0.50	0.24	0.20	0.14	0.21
Yb	2.79	1.99	2.11	3.52	2.07	2.02	1.25	1.95
Lu	0.31	0.14	0.24	0.46	0.25	0.10	0.09	0.21
Hf	2.8	2.4	2.6	4.5	2.7	2.1	1.4	2.1
Pb	9.1	6.7	6.8	5.6	8.0	6.2	3.2	5.9
Th	2.3	1.4	1.9	2.6	1.8	1.1	0.6	1.2
U	0.6	0.5	0.4	0.6	0.5	0.4	0.1	0.4

Unco; Tables A2.6 and A2.7 in the appendix), and the Lago Espejo deposit contains a larger proportion of dark brown compared to pale brown glass. We interpret this to result from variable wind directions during its eruption such as also occurred during the 1991 AD Hudson eruption, which distributed Phase 1 basaltic tephra to the north and Phase 2 trachyandesitic to the southeast (Scasso et al. 1994; Kratzmann et al. 2009).

Tephras J and K

Tephras J and K are HA chemical types, and both are up to 1 cm in thickness in the southern cores. Both consist predominantly of black and brown glass with minor undeformed spherical vesicles and a high abundance of microlites. Plagioclaseis the dominant phenocrysts, and pyroxenes are also present in these deposits. Based on their HA type chemistry, both tephras were derived from the Hudson volcano.

Tephras Ls and Ln

Tephras Ls and Ln are two thin tephra deposits in similar stratigraphic position in the southern (Ls) and northern (Ln) lakes, but with different petrochemistry and source volcanoes. Ls is a LAM petrochemical type which contains abundant black to dark brown glass with minor undeformed spherical vesicles and microlites. Plagioclase phenocrysts occur along with trace amounts of pyroxenes. This tephra may have been sourced from either Macá, Cay or one of the MEC. Ln in contrast is a LAF petrochemical type which has clear microlite-free glass with abundant spherical vesicles. Plagioclase, pyroxenes, olivine and abundant amphibole occur in this Ln tephra, which is similar to MEN1 tephra (Fig. 2.4) and, we therefore suggest, is derived from Mentolat.

Tephras M and N

Tephras M and N are only observed in the southern lakes where they have thicknesses up

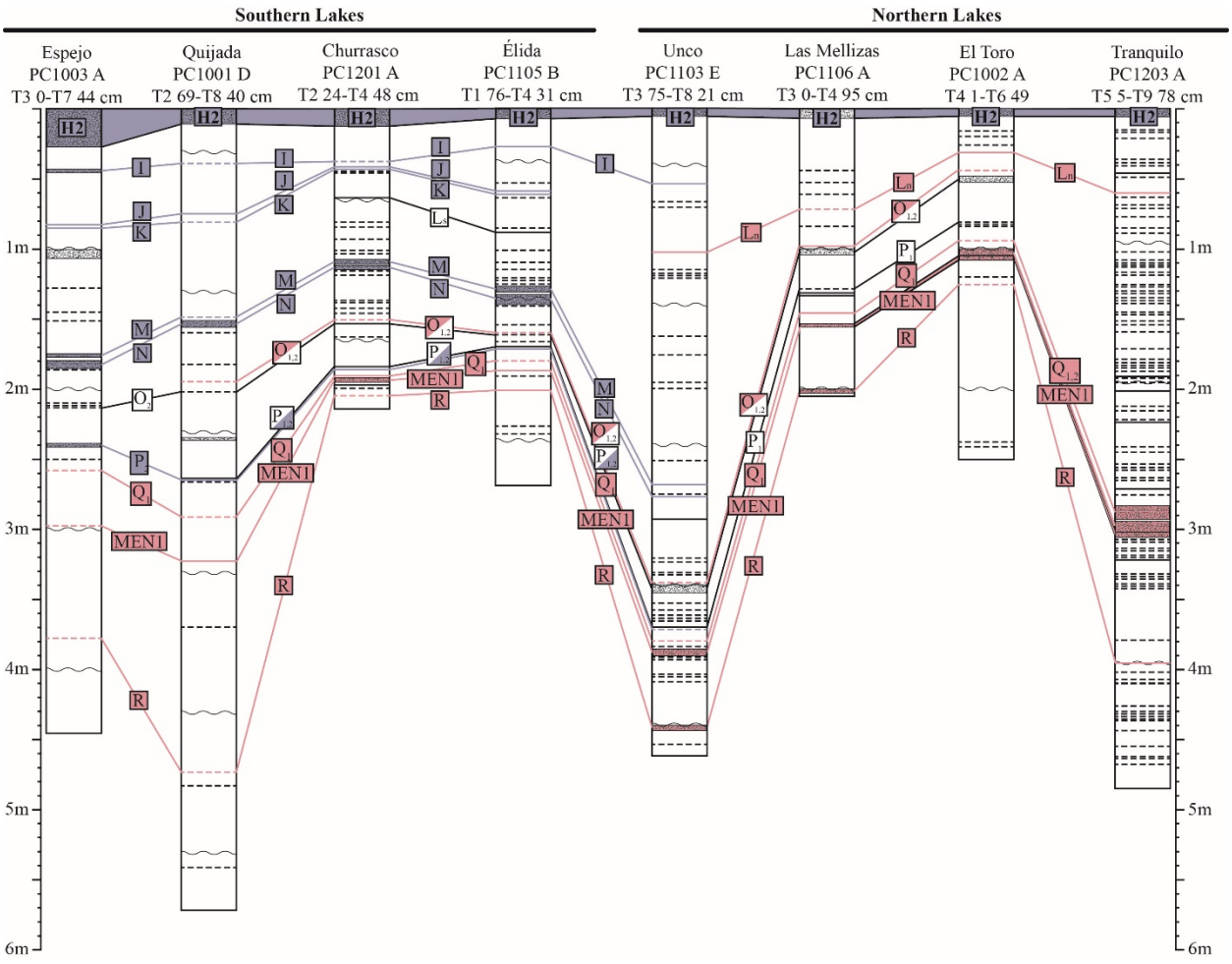

Figure 2.6. Stratigraphic sections for the eight lake cores for Zone 2, from the H2 Hudson tephra to the top of the S1-10 sequence of tephra, showing the correlations from tephras H2 to R among the different cores.

to 2 cm and 5 cm respectively. Both are HA chemical types, and we therefore suggest are from Hudson volcano. They contain pale brown glass lacking microlites, but with abundant stretched vesicles similar to H2 glass (Fig. 2.4b). Phenocrysts include plagioclase, clinopyroxene and orthopyroxene.

Tephra Group O

Tephra O1 is a LAF petrochemical type tephra deposits, containing dark vesicle-poor but microlite-rich glass along with clear glass. It contains abundant plagioclase and pyroxene phenocrysts, olivine, as well as both brown and green amphiboles and biotite, and we therefore suggest that it was derived from Mentolat volcano. Tephra O2 is a LAM petrochemical type which is up to 6 cm thick in the northern cores. O2 is characterized by black, vesicle-poor glass with a high abundance of mineral microlites. Phenocrysts include low abundances of plagioclase and clinopyroxene. This tephra may have been derived from either Macá, Cay or one of the MEC.

Tephra Group P

Group P comprises two tephra deposits. The younger one (P1) is a LAM chemical type is up to 5 cm in thickness and is characterized by abundant blocky black glass with moderate amounts of mineral microlites, few vesicles, abundant plagioclase, along with trace amounts of pyroxenes. It was derived from either Macá, Cay or one of the MEC. The older P2 is a HA chemical type, with distinctive high Ti content (Fig. 2.3; Table 2.4), containing stretched vesicle-rich orange glass with few mineral microlites and only a small proportion of plagioclase and pyroxene phenocrysts. Based on these petrochemical characteristics we suggest that this tephra was derived from Hudson volcano.

Tephra Group Q

Tephra group Q consists of two LAF petrochemical type tephra, containing both dark brown glass with spherical to moderately deformed oval vesicles and with few microlites, and also clear glass with abundant circular vesicles. Phenocrysts include plagioclase, clinopyroxene, orthopyroxene, olivine and amphibole, and we suggest that both these tephra were derived from Mentolat.

Tephra MEN1

MEN1 tephra ranges in thickness between <1 to 4 cm and is thicker in the northern lakes. It is a LAF chemical type with abundant colorless glass containing undeformed circular vesicles (Fig. 2.4). Plagioclase, clinopyroxene, orthopyroxene, olivine and amphibole occur as phenocrysts. This tephra is correlated with the 7,710 cal yrs BP MEN1 tephra (Fig. 2.1) observed in outcrop west and north of Coyhaique (Naranjo and Stern 2004), as well as in cores from Lago Shaman to the northeast (Fig. 2.1; de Porres et al. 2012; Stern et al. 2015), from small lakes further south near Cochrane such as Lago Augusta (Fig. 2.1; Villa-Martínez et al. 2012; Stern et al. 2013, 2016), and bog cores to the southeast in Argentina (McCulloch et al. 2014).

Tephra R

This is a LAF petrochemical type tephra, with clear and minor black glass, with plagioclase, clinopyroxene, orthopyroxene, olivine, amphibole and biotite phenocrysts, which we suggest based on its petrochemistry is derived from Mentolat volcano. It is thicker to the north.

2.5.8 Zone III; S1-S10 tephra sequence (Fig. 2.7; Table 2.5)

Zone III consists of a sequence of 10 closely spaced tephra which has been dated as between >14,080 to <14,910 cal yrs BP (Fig. 2.7; Table A2.1 in the appendix; Miranda et al., 2013). Five of the cores contain all 10 of these clearly distinct tephra layers separated by lacustrine

sediments (Espejo, Quijada, Churrasco, Élida, Unco), whereas in the other three northern lakes (Las Mellizas, El Toro, Tranquilo) tephras S1-S5 are clearly present, but not all of S6-S10 are definitive. The thickness of each deposit in the different lakes is variable, but only by a small amount (from 3 to <1 cm).

Tephra S1-S3 and S5-S10 are all HA chemical types, which consist of mafic dark brown volcanic glass with spherical non-stretched vesicles, abundant plagioclase microlites, but few mineral phenocrysts (Fig 4). Chemically, these nine tephra are similar to mafic magmas erupted from Hudson volcano (Table 2.5), either as lavas (HV-107; Gutiérrez et al. 2005), tephra such as Phase 1 in the H3 event (Kraztmann et al. 2009, 2010), or the mafic components of the Late Glacial Ho eruption (Weller et al. 2014).

S4, in contrast, is clearly distinguishable from the other tephra by its light brown glass with abundant stretched vesicles, common plagioclase and pyroxene phenocrysts, and trace element chemistry indicating a more felsic tephra (Table 2.5). The fact that the S4 tephra is morphologically and petrochemically distinct from the others establishes a definitive stratigraphic marker that allows for the correlation of the other nine S deposits. S4 tephra has glass color, morphology and HA chemical composition characteristic of other intermediate to silicic tephra derived from Hudson volcano such as H2.

The entire S1-S10 sequence overlaps in age the oldest 14,560 cal yrs BP Hudson-derived tephra (HW1) identified from the Pacific coast by Haberle and Lumley (1998) and tephra TL5 at 800 cm depth in Pacific Ocean core MD07-3088 (Siani et al. 2010; Carel et al. 2011).

2.5.9 Zone IV: S10 through the base of the cores (Fig. 2.8; Table 2.6)

Tephra T

Table 2.5a. Average trace element concentrations (ppm) of the S1-10 tephra in zone III

	Tephra Name						
	S1	**S2**	**S3**	**S4**	**S5**	**S6**	**S7**
	Chemical Type						
	HAM	**HAM**	**HAM**	**HA**	**HAM**	**HAM**	**HAM**
	Source Volcano						
	HUD	**HUD**	**HUD**	**HUD**	**HUD**	**HUD**	**HUD**
	n						
	4	**10**	**4**	**7**	**8**	**1**	**1**
Ti	9976	10692	10406	7542	11515	11097	12689
V	237	253	261	102	253	288	285
Cr	23	19	18	6	17	25	18
Mn	1302	1326	1326	1320	1413	1395	1487
Co	37	38	35	36	32	36	30
Ni	34	30	30	20	30	46	27
Cu	89	111	93	91	90	49	86
Zn	122	120	121	123	125	122	126
Rb	27	26	23	51	23	26	23
Sr	540	552	540	332	558	575	580
Y	31	35	35	45	37	36	40
Zr	233	252	256	418	263	263	268
Nb	14	13	13	20	15	12	13
Cs	0.3	0.6	0.5	0.8	0.4	0.8	0.5
Ba	523	578	511	674	486	457	449
La	32.9	34.2	34.0	42.1	34.6	32.7	36.5
Ce	75.2	78.9	78.7	95.0	80.7	76.1	86.3
Pr	9.47	10.09	10.07	11.57	10.53	9.84	10.91
Nd	40.8	42.1	42.2	46.9	44.4	41.3	48.0
Sm	8.32	8.81	8.77	9.78	9.25	8.92	10.01
Eu	2.47	2.59	2.56	2.73	2.71	2.69	2.93
Gd	9.05	9.61	9.68	10.75	10.19	10.12	10.45
Tb	1.08	1.21	1.24	1.41	1.30	1.29	1.38
Dy	6.31	6.71	6.64	8.22	7.05	7.26	7.71
Ho	1.13	1.27	1.27	1.62	1.34	1.27	1.51
Er	3.54	3.85	3.89	4.98	4.07	3.86	4.33
Tm	0.36	0.48	0.47	0.69	0.53	0.48	0.57
Yb	3.01	3.39	3.35	4.81	3.48	3.32	3.42
Lu	0.23	0.44	0.37	0.70	0.45	0.53	0.55
Hf	5.4	5.6	5.7	9.4	6.5	5.5	5.7
Pb	10.8	6.2	6.4	11.5	6.0	7.4	4.3
Th	4.7	3.6	3.8	7.8	4.4	3.5	4.1
U	0.6	0.7	0.6	1.6	0.7	0.7	0.8

Table 2.5b. Average trace-element concentrations (ppm) of the S1-10 tephra in zone III

	Tephra Name					
	S8	S9	S10	**P1 1991AD***	**94T-59C***	**HV-107***
	Chemical Type					
	HAM	**HAM**	**HAM**	**HA**	**HA**	**HA**
	Source Volcano					
	HUD	**HUD**	**HUD**	**HUD**	**HUD**	**HUD**
	n					
	3	**1**	**1**	**2**	**1**	**1**
Ti	12668	12702	13528	12529	10502	11810
V	291	301	280	331	-	258
Cr	17	27	19	26	-	52
Mn	1540	1461	1431	1472	1242	1394
Co	38	49	51	32	-	20
Ni	37	49	25	12	-	3
Cu	77	56	77	48	-	27
Zn	125	135	117	104	-	-
Rb	19	25	24	30	29	33
Sr	571	625	586	535	578	504
Y	38	38	41	37	28	40
Zr	266	255	229	183	194	228
Nb	11	11	12	8	9	10
Cs	0.3	0.8	0.5	-	0.7	1
Ba	434	548	421	405	405	466
La	35.2	36.7	35.0	-	29.2	30.1
Ce	84.7	84.5	80.5	-	62.8	71.0
Pr	10.99	10.9	10.8	-	8.16	9.50
Nd	47.1	49.2	46.5	-	33.4	40.0
Sm	9.84	9.78	9.81	-	7.04	8.60
Eu	2.92	3.04	2.97	-	1.99	2.71
Gd	12.08	11.02	10.6	-	8.03	8.20
Tb	1.38	1.35	1.37	-	0.95	1.23
Dy	7.52	7.50	7.38	-	5.58	7.30
Ho	1.36	1.40	1.46	-	1.04	1.55
Er	4.14	4.39	4.12	-	3.40	4.00
Tm	0.51	0.55	0.54	-	0.38	0.59
Yb	3.58	3.65	3.54	-	2.90	3.60
Lu	0.48	0.52	0.56	-	0.39	0.55
Hf	5.7	5.5	5.0	-	4.5	5.4
Pb	6.0	7.2	4.5	-	7.1	7.0
Th	3.1	3.8	4.5	-	5.5	3.7
U	0.6	0.7	0.7	-	1.0	0.9

[a]Kratzmann et al. (2009); [b] Naranjo and Stern (1998); [c]Gutiérrez et al. (2005)

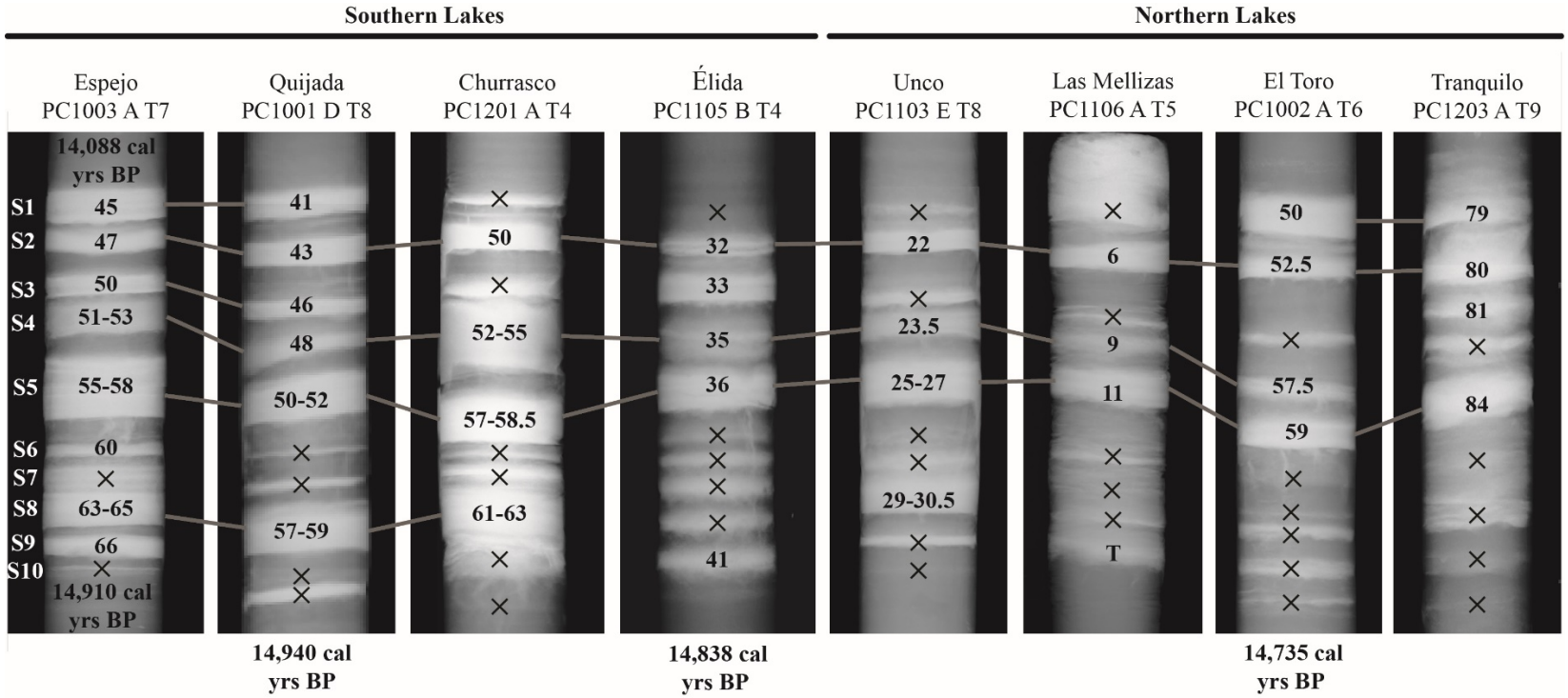

Figure 2.7. Images of Zone 3, the S1-10 sequence of closely spaced eruptions within the eight lake cores. Analyzed samples are marked with the depth from the top of the indicated core section and the unsampled tephra are marked with an 'X'. Some images were stretched in order to line up the correlated tephras, but all cores are 4 cm wide, and the depth in cm to each layer provide a measure of the actual vertical scale for each image. All deposits within the sequence are HA chemical types derived from Hudson. The S4 tephra contains light brown glass with elongated vesicles, and lower Ti and Sr and higher Rb, Ba, Zr and La contents, and is clearly more intermediate in composition that the other nine tephra, which all contain dark brown glass with few spherical vesicles and abundant mineral microlites. Radiocarbon dates are labeled in their respective cores (Table A2.2 in Appendix; Miranda et al. 2013). The width of each core is approximately 4 cm and deposits without a depth range are 1 cm or less in thicknes

Tephra T is a LAF petrochemical type only observed in the northern cores (Table 2.1). This tephra is characterized by clear glass with abundant circular vesicles. It contains phenocrysts of plagioclase, clinopyroxene, orthopyroxene and minor amounts of weakly pleochroic brown amphibole, and for these reasons we suggest that it was derived from the Mentolat volcano.

Tephra Group U

Tephra group U consists of two to three thin but well-defined deposits observed in most of the cores, none of which were sampled because they were all too thin.

Tephra V

Tephra V is observed in all of the lakes as an approximately 1 cm deposit. It is a HA chemical type and therefore we suggest is derived from the Hudson volcano. Tephra V is characterized by dark brown glass with a blocky morphology, high abundances of microlites, low abundances of undeformed vesicles, and minor plagioclase and pyroxene phenocryst.

Tephras Ws and Wn

Tephras Ws and Wn are two chemically and morphologically distinct tephra deposits that occur in about the same stratigraphic position. Tephra Wn is up to 1 cm in thickness in the northern lakes, while tephra Ws is up to 2 cm in thickness in the southern lakes. Tephra Wn is a LAM chemical type containing dark brown microlite rich glass with spherical vesicles and moderate abundances of plagioclase and minor pyroxenes phenocrysts. This tephra may have been sourced from either Macá, Cay or one of the MEC. Tephra Ws in the southern lakes is a HA chemical type, derived from Hudson volcano, with dark orange to brown microlite-rich glass and moderate amounts of plagioclase and pyroxene phenocrysts.

Tephra Group X

Tephra Group X generally consists of three deposits all of which are 1 cm or less in

Table 2.6a. Average trace element compositions (ppm) of the tephras in zone IV from the bottom of the S1-10 sequence to the bottom of the core

	Tephra Name						
	T	**V**	**Ws**	**Wn**	**X1**	**X2**	**X3**
	Chemical Type						
	LAF	**HAM**	**HAM**	**LAM**	**HAM**	**HAM**	**HAM**
	Source Volcano						
	MEN	**HUD**	**HUD**	**M/C/MEC**	**HUD**	**HUD**	**HUD**
	n						
	8	**11**	**1**	**2**	**1**	**4**	**7**
Ti	6228	12266	12586	5807	12557	11568	10794
V	161	311	256	260	246	245	229
Cr	14	16	9	24	9	7	11
Mn	1104	1272	1487	873	1369	1331	1294
Co	47	38	81	35	21	26	38
Ni	20	27	39	26	19	15	19
Cu	137	133	43	325	143	102	81
Zn	118	122	131	98	122	121	119
Rb	29	30	40	16	33	32	34
Sr	377	471	486	443	462	462	444
Y	26	36	44	17	42	41	37
Zr	128	231	298	69	270	268	260
Nb	5	11	12	2	10	12	11
Cs	1.3	0.5	1.3	0.4	0.8	0.8	0.6
Ba	310	437	515	199	438	437	454
La	13.7	30.1	32.6	9.8	31.1	30.2	30.3
Ce	32.6	70.3	77.1	22.2	73.3	70.7	70.4
Pr	4.3	9.2	10.3	2.9	9.7	9.5	9.0
Nd	19.4	39.8	45.1	12.9	42.4	40.4	39.1
Sm	4.97	8.80	9.88	3.30	9.25	8.97	8.57
Eu	1.55	2.68	2.97	1.10	2.79	2.80	2.58
Gd	5.92	10.19	11.15	4.12	10.0	10.05	9.98
Tb	0.80	1.29	1.46	0.52	1.37	1.37	1.24
Dy	4.81	6.95	8.32	3.18	7.86	7.53	6.98
Ho	0.94	1.32	1.64	0.57	1.57	1.50	1.32
Er	2.96	4.07	4.91	1.90	4.63	4.39	4.16
Tm	0.35	0.50	0.62	0.12	0.57	0.57	0.51
Yb	2.74	3.46	3.96	1.80	4.19	3.99	3.59
Lu	0.33	0.48	0.66	0.13	0.58	0.58	0.51
Hf	3.7	5.5	6.5	2.0	5.8	6.7	5.9
Pb	9.6	6.9	8.8	8.1	5.5	6.2	6.9
Th	3.2	3.5	4.4	2.0	3.7	4.7	4.4
U	0.9	0.7	0.9	0.5	1.0	0.9	0.9

Table 2.6b. Average trace element compositions (ppm) of the tephras in zone IV from the bottom of the S1-10 sequence to the bottom of the core

	Tephra Name					
	Y1	**Z1**	**H0**	**Z3**	**MEN0**	**Z5**
	Chemical Type					
	LAM	**HAM**	**HUD**	**LAM**	**LAF**	**LAM**
	Source Volcano					
	M/C/MEC	**HUD**	**HUD**	**M/C/MEC**	**MEN**	**M/C/MEC**
	n					
	5	**16**	**22**	**7**	**7**	**4**
Ti	6740	9846	8350	6091	4728	5864
V	261	306	208	236	208	245
Cr	18	35	18	9	21	22
Mn	1153	1179	1134	1067	1030	1146
Co	35	38	33	28	30	29
Ni	21	29	25	20	24	29
Cu	125	108	231	119	69	125
Zn	110	108	108	101	87	110
Rb	21	30	41	19	23	29
Sr	470	478	451	475	411	446
Y	23	29	31	20	16	21
Zr	99	183	226	79	73	78
Nb	4	9	13	4	3	3
Cs	1.0	0.8	1.1	0.9	1.4	1.6
Ba	259	386	514	242	206	277
La	12.8	23.6	28.6	9.5	8.4	11.2
Ce	29.4	53.8	63.4	22.3	19.1	25.4
Pr	3.9	6.9	7.9	3.0	2.5	3.3
Nd	17.4	29.4	33.1	14.2	11.2	15.0
Sm	4.29	6.51	7.19	3.69	2.83	3.78
Eu	1.39	2.07	2.17	1.28	0.98	1.25
Gd	5.13	7.56	8.23	4.41	3.36	4.70
Tb	0.70	0.98	1.04	0.59	0.38	0.58
Dy	4.12	5.49	5.82	3.74	2.77	3.64
Ho	0.83	1.07	1.12	0.72	0.54	0.70
Er	2.52	3.29	3.43	2.27	1.79	2.28
Tm	0.30	0.41	0.41	0.29	0.19	0.24
Yb	2.26	2.88	3.09	2.06	1.65	2.06
Lu	0.29	0.40	0.39	0.29	0.20	0.22
Hf	2.8	4.4	5.6	2.6	2.2	2.3
Pb	7.3	5.6	8.5	5.8	6.2	9.1
Th	2.9	4.0	5.3	2.1	2.2	2.7
U	0.7	0.8	1.2	0.6	0.8	1.3

thickness, although in some cores tephra X1 is missing or very thin. All are HA chemical types, derived from Hudson volcano, with dark to pale orange-brown blocky glass containing both circular and elongated vesicles and few microlites. Plagioclase and pyroxene phenocrysts are present.

Tephra Group Y

Tephra Group Y includes two tephra. Y1 is a 1 cm or less LAM chemical type tephra characterized by a low abundance of pale brown glass with moderate to high microlite abundances and minor circular vesicles. It contains plagioclase and minor pyroxene phenocryts. This tephra may have been sourced from either Macá, Cay or one of the MEC. Tephra Y2 was not sampled.

Tephra Group Z

Tephra group Z generally consists of five deposits. Tephra Z1 was sampled from six of the lake cores and is a HA chemical type that ranges in thickness from 2-9 cm. It is characterized by pale brown blocky glass with minor microlites and vesicles that range from circular to moderately elongated. Plagioclase phenocrysts exist along with minor amounts of pyroxenes. Z1 was derived from Hudson.

Tephra Z2, or Ho (Fig. 2.3), described by Weller et al. (2014), was produced by a very large late-glacial eruption from Hudson bracketed in age between 17,300 and 17,440 cal yrs BP. Based on its age and thickness this corresponds to the 42 cm thick tephra observed by Markgraf et al. (2007) between 1109 and 1151 cm depth from a core in Mallín Pollux (Fig. A1 in the appendix).

Tephra Z3 is a LAM chemical type that is approximately 1-2 cm thick in three of the northern lakes. It is characterized by microlite-rich pale brown to orange-brown glass withfew spherical vesicles, and, abundant plagioclase and minor pyroxene phenocrysts. Z3 was derived from either Macá, Cay or one of the MEC.

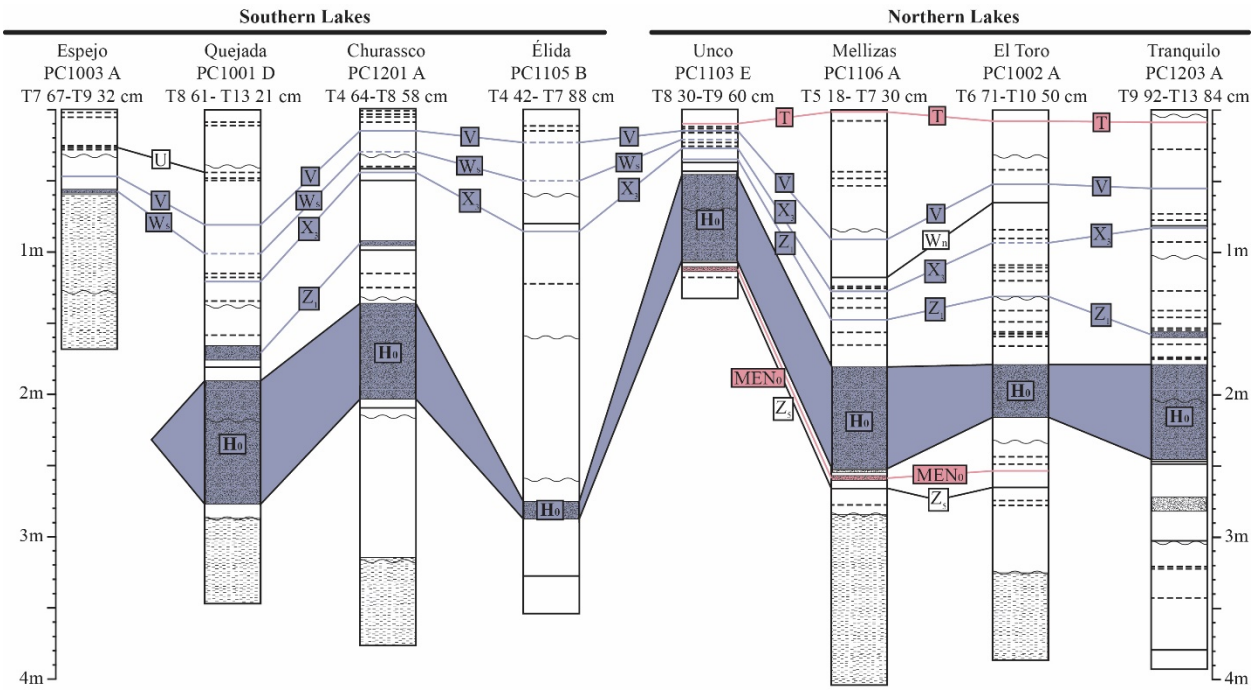

Figure 2.8. Stratigraphic sections for the eight lakes for Zone 4, from the S1-10 sequence of tephra to the base of the cores which generally occurs where predominately organic rich lake sediments end and glacio-lacustrine clay-rich sediments begin. Shown are the correlations of tephras T through Z which includes the large Late-Glacial Ho eruption from Hudson (Weller et al. 2014).

Z4, or MENo, is a LAF petrochemical type tephra characterized by colorless glass that lacks microlites and contains abundant small undeformed circular vesicles. It contains abundant plagioclase and orthopyroxene phenocrysts, as well as minor clinopyroxene, olivine and dark brown amphibole. It is observed in three of the northern lake and is derived from Mentolat volcano. It also occurs in Lago Shaman (de Porras et al. 2012; Stern et al. 2015).

Z5 tephra is a LAM chemical type that is approximately 1 cm in thickness and only occurs in two northern lake cores. It is characterized by its black irregularly shaped glass with abundant large microlites (Fig 4), and contains abundant plagioclase phenocrysts and minor pyroxenes. Z5 was derived from either Macá, Cay or one of the MEC.

2.6 Discussion and Conclusion

Some of the many dense layers observed as white bands in the X-ray images (Fig. 2.2) of the multiple lakes cores from near Coyhaique, Chile, may be sands or re-worked tephra, but the >60 tephra listed in Table 2.1 all occur in similar stratigraphic relations to each other in multiple cores (Figs. 2.5-2.8), and we therefore consider them to be derived from independent eruptions. The chemistry and petrology of 55 of these >60 tephra are consistent with and support the correlations based on stratigraphy alone. We therefore conclude that >60 explosive eruptions of various sizes of southernmost SSVZ volcanoes, including possibly the Minor Eruptive Cones (MEC) have occurred since glacial retreat at approximately 17,800 cal yrs BP.

Most of the eruptions observed in these cores must have been small (<0.1 km^3), since they are thin (Table 2.1) and fine grained (Table 2.2). Only four of the tephra preserved in these lakes (D3=MAC1; H2, F3=Hudson T6, and MEN1) have been correlated with tephra previously reported in outcrops in the region and these form the thickest (Table 2.1) and coarsest grained

(Table 2.2) deposits in the cores, with the exception of Ho which has not been observed in outcrop. Nevertheless, it is clear that although tephrochronology studies based solely on outcrops, such as those of Naranjo and Stern (1998, 2004), are satisfactory for identifying large eruptions, they are only seeing a minor proportion with regard to all eruptions, a conclusion also reached by Moreno et al. (2015) for the Chaitén volcano further north in the Andean SSVZ. On the other hand, it is also significant to note that tephra from one of the largest Holocene eruptions of Hudson, the H1 event at 8,170 ± 60 cal yrs BP, nor the more recent H3 (1991 Phase 2) eruption (Stern 1991, 2008; Naranjo and Stern 1998; Kratzmann et al. 2009; Prieto et al. 2013; Stern et al. 2016), do not occur in any of these cores because they were not distributed towards the northeast of the volcano (Fig. 2.1).

The northern lakes contain higher proportion of tephra that are similar in morphology and chemistry to previously identified tephra derived from Mentolat (10 in total), whereas the southern lakes preserve a larger proportion of tephra chemically and petrologically similar to previously described tephra derived from Hudson (32 in total; Table 2.1). Thirteen tephra are considered to be derived from either Macá, Cay or MEC, with one of these correlated with tephra MAC1 from Macá. Seven tephra identified in multiple cores, and a number not correlated across cores, have not been sampled.

The majority of the analyzed deposits lay within the chemical fields defined using previously published data for the eruptive products from the SSVZ volcanic centers (Fig. 2.3). Three deposits petrographically similar to Hudson-derived tephra have lower Ti than other Hudson samples, but are in other ways similar chemically to Hudson-derived rocks. Several sample that are attributed to the Mentolat volcano also lie within the Macá, Cay or MEC fields, with higher Ti at a given Rb content than Mentolat lavas, but these tephras contain clear volcanic glass and brown

amphibole, similar to the volcanic products from the previously documented MEN1 eruption (Naranjo and Stern 2004; Stern et al. 2015, 2016). They also contain mafic components such as microlite–rich and vesicle-poor dark mafic volcanic glass and olivine. These different glass components likely represent different phases of the eruptions similar to the range in tephra chemistry and petrology observed in outcrops of the MEN1 eruption (Naranjo and Stern 2004), and in the products of other chemically heterogeneous SSVZ explosive eruptions.

The large number of eruptions documented from the lake cores near Coyhaique represent a significant contribution to the record of eruptions from volcanoes in this region during Late-Glacial and Holocene times (Fig. 2.9). These new results indicate that although explosive eruptions within the SSVZ are episodic, they have on the average been regularly repetitive throughout Late-Glacial to historic times without any significant change in the frequency. This conclusion extends back to 20,000 cal yrs BP, before the Last Glacial Maximum, when the tephra from Pacific Ocean marine cores are also considered (Carel et al. 2011), and suggests that deglaciation did not enhance the rates of explosive eruptions.

The new information, combined with previously published data concerning tephra derived from the Hudson volcano (Naranjo and Stern 1998; Haberle and Lumley 1998; Carel et al. 2011; Weller et al. 2014) indicate that this volcano has had >55 explosive eruptions since 20,000 cal yrs BP (Fig. 2.9). These eruptions have produced >45 km^3 of pyroclastic material based on previously published volume estimates of its larger eruptions (Weller et al. 2014). This makes Hudson one of the most active volcanoes in the SSVZ in terms of both frequency frequency and volume of explosive eruptions, comparable to Volcán Mocho-Choshuenco (Rawson et al. 2015), perhaps as a result of its location just east of the Chile Rise-Trench triple junction. Nevertheless the tephra record indicates that local population centers such as Coyhaique (Fig. 2.1) could also be

Figu

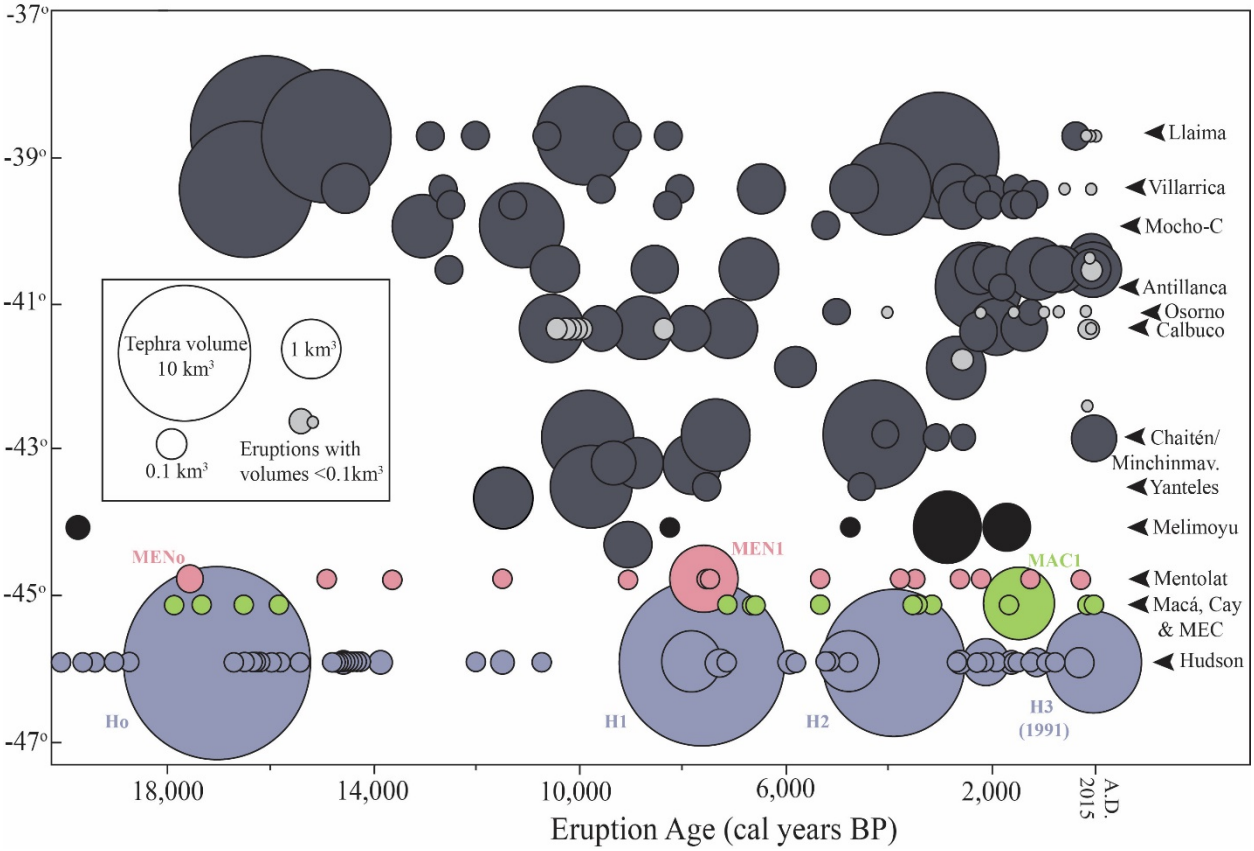

re 2.9. Eruption volumes for volcanic centers of the SVZ between 37°S and 47°S from Late-Glacial and Holocene time. Modified from Watt et al. (2013) to include the many small volume (<<1 km^3) eruptions from Hudson, Mentolat and either Macá, Cay or one of the MEC documented in this study, and the eruptions identified by Stern et al. (2015a) in Lago Shaman and Mallín el Embudo east of the arc (Fig. 2.1), by Haberle and Lumley (1998) along the western coast and by Siani et al. (2010, 2013) and Carel et al. (2011) in Pacific Ocean marine cores.

profoundly affected by future eruptions from Macá and Mentolat volcanoes similar in magnitude to those that occurred in the past.

Using the radiocarbon ages of the S2.1-2.10 tephra (Fig. 2.7; Miranda et al. 2013) and of previously dated eruptions (MAC1; H2, MEN1; Ho; Naranjo and Stern, 2004; Weller et al. 2014; Stern et al. 2016), depth versus age sedimentation profiles for the eight lake cores are compared to each other and to profiles from other lakes in the region (Fig. 2.10), including Mallín Pollux (Markgraf et al. 2007) and Augusta (Fig. 2.1; Villa-Martínez et al. 2012). The profiles all exhibit intervals of both slower and more rapid accumulation of material within the lakes. Significantly, the cores show similar patterns, with relatively rapid sedimentation rates between 18,000 to 15,000 cal yrs BP, followed by slower rates up to 7,500 cal yrs BP, after which relatively more rapid sedimentation rates prevail. A similar conclusion was reached previously for Lago Augusta (Villa-Martínez et al. 2012) and Mallín Pollux (Markgraf et al. 2007) based on a greater number of internally consistent age dates. However, significantly different explanations, involving changes in precipitation and temperature, have been proposed to explain these changes in these two lakes. Resolving these differences, which require other data such as identification of pollen types at different depths in the cores, is beyond the scope of this paper. Nevertheless, the profiles illustrate the power of tephrochronology for constraining temporal correlations among core records over a relatively large region, and the data suggest that these changes in sedimentation rates were produced by regional environmental changes that affected the lakes located both in the semi-arid region to the east of the current drainage divide (Unco and Élida), as well as in the wetter region more to the west (Espejo).

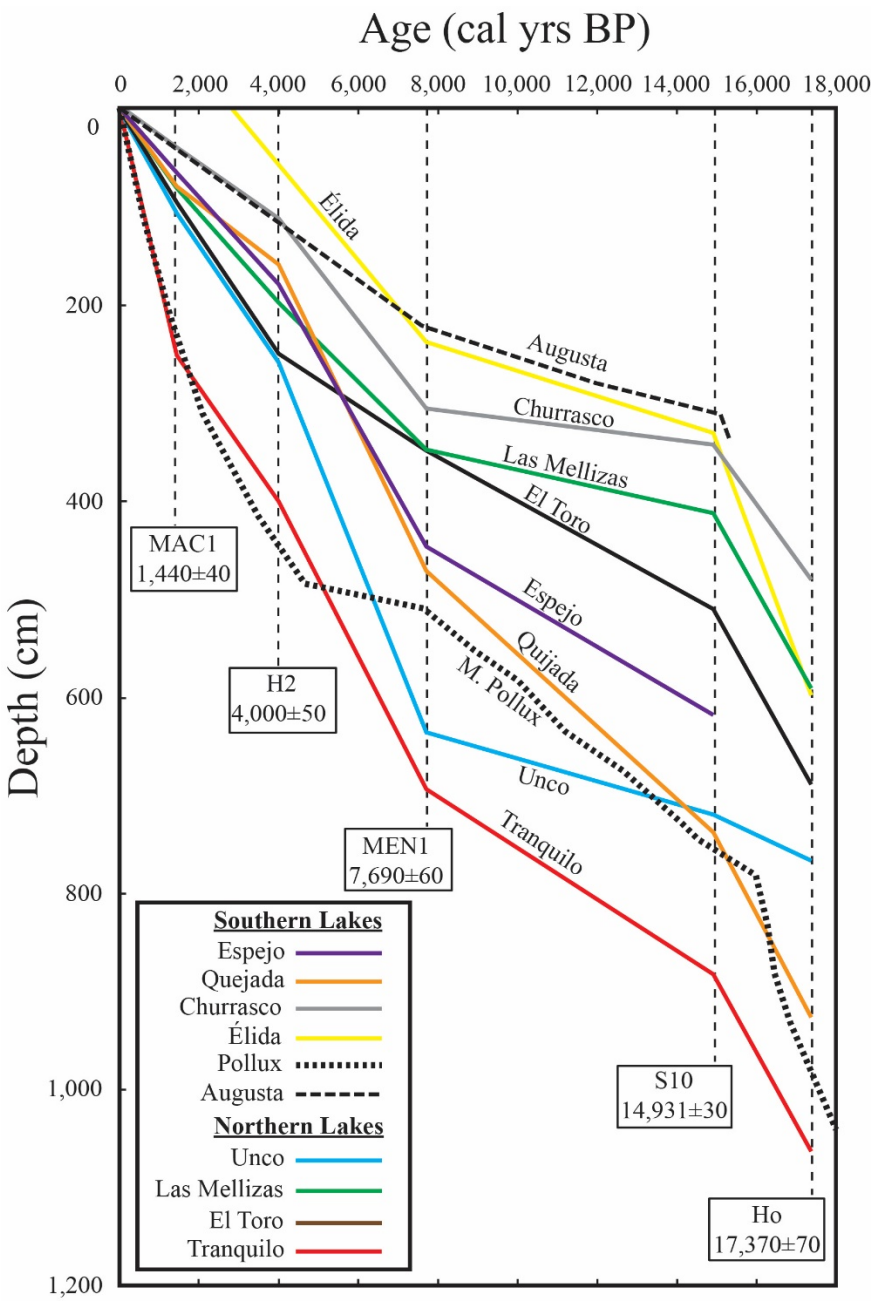

Figure 2.10. Sedimentation profiles for the eight lake cores, from the surface to the top of the Ho tephra, using the ages of previously dated large explosive eruptions from Hudson (H2, Ho), Mentolat (MEN1) and Macá (MAC1) (Table 2.1; Naranjo and Stern 1998, 2004; Weller et al. 2014), including two previously published profiles, based on independent sets of internal age dates, from Mallín Pollux (Markgraf et al. 2007) and Lago Augusta (Villa-Martínez et al. 2012). The thickness of the H2 tephra, which ranges from 8 to 53 cm (Table 2.1), has been subtracted from the total integrated length of the sediment in the cores, but other tephra layers, which are about the same thickness in every core, have not.

2.7 References

Bertrand S, Araneda A, Vargas P, Jana P, Fagel N, Urrutia R (2012). Using the N/C ratio to correct bulk radiocarbon ages from lake sediments: Insights from Chilean Patagonia. Quat Geochron 12: 23-29

Bertrand S, Daga R, Bedert, R, Fontijn K (2014) Deposition of the 2011-2012 Cordon Caulle tephra (Chile, 40°S) in lake sediments: implications for tephrochronology and volcanology. J Geophys Res 119: 2555-2573

Best JL (1992) Sedimentology and event timing of a catastrophic volcaniclastic mass flow, Volcán Hudson, southern Chile. Bull Volcanol 54: 299–318

Björck S, Rundgren M, Ljung K, Unkel I, Wallin A (2012) Multi-proxy analyses of a peat bog on Isla de los Estados, easternmost Tierra del Fuego: a unique record of the variable Southern Hemisphere Westerlies since the last deglaciation. Quat Sci Rev 42: 1-14

Cande SC, Leslie RB (1986) Late Cenozoic Tectonics of the Southern Chile Trench. J Geophys Res 91(B1): 471–496

Carel M, Siani G, Delpech G (2011) Tephrostratigrapy of a deep-sea sediment sequence off the south Chilean margin: New insight into the Hudson volcanic activity since the last glacial period. J Volcanol Geotherm Res. 208: 99-111

Cembrano J, Hervé F, Lavenu A (l996) The Liquiñe-Ofqui fault zone: long-lived intra-arc fault system in southern Chile. Tectonophys 259: 55–66

de Porras ME, Maldonado A, Abarzúa AM, Cárdenas ML, Francois JP, Martel-Cea A, Stern, CR (2012) Postglacial vegetation, fire and climate dynamics at Central Chilean Patagonia (Lake Shaman, 44°S). Quat Sci Revs 50: 71–85

de Porras ME, Maldonado A, Quintana FA, Martel-Cea1 JO, Reyes O, Méndez C (2014) Environmental and climatic changes in Central Chilean Patagonia since the Late Glacial (Mallín El Embudo, 44°S). Climates of the Past 10: 1063–1078

D'Orazio M, Innocenti F, Manetti P, Tamponi M, Tonarini S, González-Ferrán O, Lahsen A (2003) The Quaternary calc-alkaline volcanism of the Patagonian Andes close to the Chile triple junction: geochemistry and petrogenesis of volcanic rocks from the Cay and Maca volcanoes (~45°S, Chile). J S Amer Earth Sci 16(4): 219–242

Elbert J, Wartenburg R, von Gunten L, Urrutia R, Fisher D, Fujak M, Hamann Y, Greber ND, Grosjean M (2013) Late Holocene air temperature variability reconstructed from the sediments of Laguna Escondida, Patagonia Chile. Palaeogeog Palaeoclimat Palaeoecol 396: 482-492

Fontijn K, Lachowycz SM, Rawson H, Pyle DM, Mather TA, Naranjo JA, Moreno-Roa H (2014) Late Quaternary tephrostratigraphy of southern Chile and Argentina. Quat Sci Revs 89: 70-84

Futa K, Stern CR (l988) Sr and Nd isotopic and trace element compositions of Quaternary volcanic centers of the southern Andes. Earth Planet Sci Lett 88: 253–262

Gutiérrez F, Gioncada A, González-Ferrán O, Lahsen A, Mazzuoli R (2005) The Hudson volcano and surrounding monogenetic centres (Chilean Patagonia): an example of volcanism associated with ridge-trench collision environment. J Volcanol Geotherm Res 145: 207–233

Gonzáles-Ferrán O (1994) Volcanes de Chile. Instituto Geografico Militar, Santiago, 640 p

Haberle SG, Lumley SH (1998) Age and origin of tephras recorded in postglacial lake sediments to the west of the southern Andes, 44^{o}S to 47^{o}S. J Volcanol Geotherm Res. 84: 238-256

Kratzmann DJ, Carey S, Scasso RA, Naranjo JA (2009) Compositional variations and magma mixing in the 1991 eruptions of Hudson volcano, Chile. Bull Volcanol 71(4): 419–439

Kratzmann DJ, Carey S, Scasso RA, Naranjo JA (2010) Role of cryptic amphibole crystallization in magma differentiation at Hudson volcano, Southern Volcanic Zone, Chile. Contrib Mineral Petrol 159: 237–264

López-Escobar L, Kilian R, Kempton P, Tagiri M (l993) Petrology and geochemistry of Quaternary rocks from the southern volcanic zone of the Andes between 41°30’ and 46°00’S, Chile. Rev Geol Chile 20: 33–55

López-Escobar L, Parada MA, Hickey-Vargas R, Frey FA, Kempton P, Moreno H (1995) Calbuco Volcano and minor eruptive centers distributed along thLiquifie-Ofqui Fault Zone, Chile (41°S) contrasting origin of andesitic and basaltic magmain the Southern Volcanic Zone of the Andes. Contr Mineral Petrol 119: 345-361

Lowe DJ (2011) Tephrochronology and its application: A review. Quat Geol. 6: 107-153

Markgraf V, Whitlock C, Haberle S (2007) Vegetation and fire history during the last 18,000 cal yr B.P. in Southern Patagonia: Mallín Pollux, Coyhaique, Province Aisén (45^{o}41'30", 71^{o}50'30"W, 640 m elevation). Palaeogeogr Palaeoclimatol Palaeoecol 254: 492-507

McCulloch R, Figuerero MJ, Mengoni GL, Barclay R (2014) Un registro Holoceníco de cambios ambientales dinamicos y cronología cultural de Monte Zeballos-Paso Roballos, Santa Cruz, Patagonia central. Libro de Resumenes, IX Jornadas de Arqueología de la Patagonia, Coyhaique, p. 4

Mella M, Ramos A, Kraus S, Duhart P (2012) Tefroestratigrafía, magnitud y geoquímica de erupciones holocenas mayores del volcán Mentolat, Andes del Sur (44º40’S), Chile. Actas, Congreso Geológico Chileno, No. 13, Antofagasta.

Miranda CG, Moreno PI, Vilanova I, Villa-Martínez RP (2013) Glacial fluctuations in the Coyhaique-Balmaceda sector of central Patagonia (45°S-46°S) during the last glacial termination. Bollettino di Geofisica 54: 268-271

Moreno P, Alloway BV, Villarosa G, Outes V, Henríquez WI, De Pol-Holz R, Pearce NJG (2015) A past-millennium maximum in postglacial activity from Volcán Chaitén, southern Chile. Geology 43: 47-50

Naranjo JA (l991) Nueva erupción del volcán Hudson. Rev Geol Chile 18: 183–184

Naranjo JA, Stern CR (1998) Holocene explosive activity of Hudson Volcano, southern Andes. Bull Volcanol 59(4): 291–306

Naranjo JA, Stern CR (2004) Holocene tephrochronology of the southernmost part (42°30'-45°S) of the Andean Southern Volcanic Zone. Rev Geol Chile 31(2): 225–240

Nelson E, Forsythe R, Arit I (1994) Ridge collision tectonics in terrane development. J S Amer Earth Sci 7(3-4): 271–278

Orihashi Y, Naranjo JA, Motoki A, Sumino H, Hirata D, Anma R, Nago K (2004) Quaternary volcanic activity of Hudson and Lautaro volcanoes, Chilean Patagonia: New constraints from K-Ar ages. Rev Geol Chile 31: 207–224

Prieto A, Stern CR, Esterves J (2013) The peopling of the Fuego-Patagonian fjords by littoral hunter-gatherers after the mid-Holocene H1 eruption of Hudson volcano. Quat Internat 317: 3-13

Rawson H, Naranjo JA, Smith, V, Fontijn K, Pyle DM, Mather TA, Moreno H (2015) The frequency and magnitude of post-glacial explosive eruptions at Volcán Mocho Choshuenco, southern Chile. J Volcanol Geotherm Res 299: 103-129

Saadat S, CR Stern (2011) Petrochemistry and genesis of olivine basalts from small monogenetic parasitic cones of Bazman stratovolcano, Makran arc, southeastern Iran. Lithos 125: 609-617

Scasso RA, Corbella H, Tiberi P (l994) Sedimentological analysis of the tephra from the 12–15 August l991 eruption of Hudson volcano. Bull Volcanol 56: 121–132

Sellés D, Rodríguez AC, Dungan MA, Naranjo JA, Gardeweg M (2004) Geochemistry of Nevado de Longaví (36.2°S): a compositionally atypical volcano in the Southerrn Volcanic Zone of the Andes. Rev Geol Chile 31(2): 293-315

Siani G, Colin C, Mechel E, Carel M, Richter T, Kissel C, Dewilde F (2010) Late Glacial to Holocene terrigenous sediment record in the Northern Patagonian margin: paleoclimate implications. Palaeogeogr Palaeoclimatol Palaeoecol 297: 26-36

Siani G, Michel E, De Pol-Holz R, DeVries T, Lamy F, Carel M, Isguder G, Dewilde F, Lourantou A (2013) Carbon isotope records reveal precise timing of enhanced Southern Ocean upwelling during the last deglaciation. Nature Communications 4: 2758 DOI: 10.1038/ncomms3758

Stern CR (l991) Mid-Holocene tephra on Tierra del Fuego (54°S) derived from the Hudson volcano (46^{o}S): evidence for a large explosive eruption. Rev Geol Chile 18: 139–146

Stern CR (2004) Active Andean Volcanism: its geologic and tectonic setting. Rev Geol Chile 31(2): 161-206

Stern CR (2008) Holocene tephrochronology record of large explosive eruptions in the southernmost Patagonian Andes. Bull Volcanol 70(4): 435–454

Stern CR, Kilian R (l996) Role of the subducted slab, mantle wedge and continental crust in the generation of adakites from the Andean austral volcanic zone. Contrib Mineral Petrol 123: 263–281

Stern CR, Moreno PI, Henrique WI, Villa-Martinez RP, Sagredo E, Aravena JC (2013) Tephrochronology in the area around Cochrane, southern Chile. Bollettino di Geofisica 54: 199-202

Stern CR, de Porras ME, Maldonado A (2015) Tephrochronology of the upper Río Cisnes valley (44°S), southern Chile. Andean Geol 42(2): 173-192

Stern CR, Moreno PI, Henrique WI, Villa-Martinez RP, Sagredo E, Aravena JC, De Pol-Holz R (2016) Holocene tephrochronolgy in the area around Cochrane, southern Chile. Andean Geol 42(3): 2016

Stuiver M, Reimer PJ, Braziunas TF (1998) High-precision radiocarbon age calibration for terrestrial and marine samples. Radiocarbon 40(3): 1127–1151

Unkel I, Fernandez M, Björck S, Ljung K, Wohlfarth B (2010) Records of environmental changes during the Holocene from Isla de los Estados (54.4^{o}S), southern Tierra del Fuego. Global Planet Change 74: 99-113

Vargas G, Rebolledo S, Sepúlveda SA, Lahsen A, Thiele R, Townley B, Padilla C, Rauld R, Herrera MJ, Lara M (2013) Submarine earthquake rupture, active faulting and volcanism along the major Liquiñe-Ofque Fault Zone and implications for seismic hazard assessment in the Patagonian Andes. Andean Geol 40: 141-171

Villa-Martínez R, Moreno PI, Valenzuela MA (2012) Deglacial and postglacial vegetation changes on the eastern slopes of the central Patagonian Andes (47^{o}S). Quat Sci Rev 32: 86-99

Völker D, Kutterolf S, Wehrmann H (2011) Comparative mass balance of volcanic edifices at the southern volcanic zone of the Andes between 33^{o}S and 46^{o}S. J Volcanol Geotherm Res. 205: 114-129

Watt SFL, Pyle DM, Mather TA (2011) Geology, petrology and geochemistry of the dome complex of Huequi volcano, southern Chile. Andean Geol 38(2): 335-348

Watt SFL, Pyle DM, Mather TA (2013) The volcanic response to deglaciation: evidence from glaciated arcs and a reassessment of global eruption records. Earth Sci Rev 122: 77-102

Weller DJ, Miranda CG, Moreno PI, Villa-Martínez RP, Stern CR (2014) A large late-glacial Ho eruption fo the Hudson volcano, southern Chile. Bull Volcanol 76: 831-849

Wilson T M, Cole JW, Stewart C, Cronin SJ, Johnston DM (2011) Ash storms: impacts of wind-remobilised volcanic ash on rural communities and agriculture following the 1991 Hudson eruption, southern Patagonia, Chile. Bull Volcanol 73: 223–239

Wilson T, Cole J, Johnston D, Cronin S, Stewart C, Dantas A (2012) Short-and long-term evacuation of people and livestock during a volcanic crisis: lessons from the 1991 eruption of Volcan Hudson, Chile. J Applied Volcanol 1: 2

Chapter 3

New age controls on the tephrochronology of the southernmost Andean Southern Volcanic Zone, Chile

Submitted to *Bulletin of Volcanology*, 2017

Coauthors: ME de Porras[2], A Maldonado[2,3], C Méndez[4], Charles R. Stern[1]

[1]Department of Geological Sciences, University of Colorado, Boulder, CO, USA

[2]Centro de Estudios Avanzados en Zonas Áridas (CEAZA), Universidad de La Serena, Casilla 599, La Serena, Chile

[3]Departamento de Biología Marina, Universidad Católica del Norte, Coquimbo, Chile

[4]Departamento de Antropología, Universidad de Chile, Santiago, Chile

3.1 Abstract

The chronology of over 50 tephra layers preserved in a sediment core from Laguna La Trapananda (LLT) in the southern portion of the Andean Southern Volcanic Zone (SSVZ), Chile, is constrained by seven new radiocarbon age determinations, which span the period since glacial retreat to the late Holocene. These tephra, which are attributed to small to medium sized eruptions from volcanoes of the SSVZ, including Mentolat, Hudson, Macá, and potentially Cay, or one of the many monogenetic eruptive centers (MEC) located along the Liquiñe-Ofqui Fault Zone (LOFZ) or surrounding the major volcanoes, are correlative with tephra previously described from other lake cores in the region. The ages of the tephra in the LLT core, and from these other different lake cores, are estimated by a Bayesian statistical method using the seven new ages from the LLT core along with one for the widely dispersed H2 tephra which was produced by a large mid-Holocene eruption of the Hudson volcano and which occurs in all the lake cores from this region. The results provid isochrons (surfaces of equal age) that can be used to constrain the frequency of eruptions of the different volcanic centers in the SSVZ, the complex depositional histories of these small lacustrine systems of southern Chile, and the age of corresponding tephra observed in other paleoclimatic, paleoecologic, and archaeologic studies in the region.

3.2 Introduction

Lakes and bogs from the southern portion of the Andean Southern Volcanic Zone (SSVZ; Fig. 3.1) preserve exceptional records of late glacial and Holocene explosive volcanism because of their nearly continuous record of sedimentation, which allows for the preservation of tephra from both small and large explosive eruptions (Weller et al. 2014, 2015; Stern et al. 2015, 2016). The detail of these records are unrivaled by outcrops, which rarely contain records with the same

exceptional stratigraphic and chronological control observed in lake sediment cores. Lakes and bogs downwind of the volcanic arc are therefore the ideal environments to examine late glacial and Holocene records of volcanic activity in this region. Once tephra layers are characterized lithostratigraphically and petrochemically, they can be correlated with one another in different sediment cores or outcrops over a wide region and used as time-synchronous horizons, which can be important for linking regional paloeclimatic, archaeologic, and geologic archives (Lowe, 2011; Fontijn et al. 2014).

A sediment core taken from the small Laguna La Trapananda (LLT; Fig. 3.1), which has a limited internally drained catchment size, preserves over 50 tephra layers (Fig. 3.2) derived from explosive eruptions of volcanoes of the southernmost portion of the Andean Southern Volcanic Zone (SSVZ). The tephra from this lake can be correlated to those in other lake sediment cores previously described from the region (Fig. 3.1 and Figs. S1 to S8 of the Appendix; Weller et al. 2015) based on both their stratigraphic positions within the cores and their bulk tephra petrochemisty (Fig. 3.3). The ages of the tephra in the LLT core have been constrained by seven new radiocarbon dates (Table 3.1). Here we present a refined tephrochronology for the multiple lake cores from near Coyhaique based on these new and previously published radiocarbon age estimates, which range from throughout the Holocene and back into late glacial time. The age of the greater than 50 tephra from both Laguna La Trapananda and the eight other lake sediment cores from near the town of Coyhaique in southern Chile (Fig. 3.1), are then estimated by Bayesian age modeling using the OXCAL program using the Southern Hemisphere radiocarbon calibration data (Hogg et al. 2013).

3.3 Background

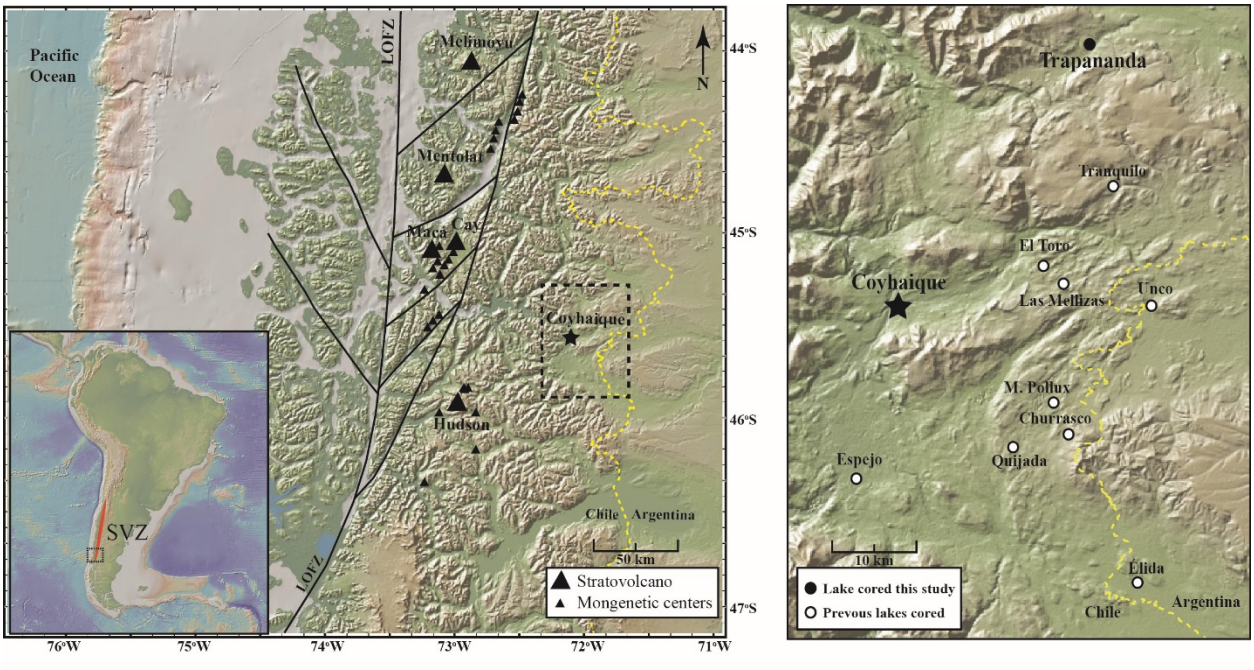

Figure 3.1. Map (on the left) of the southernmost portion of the Andean SVZ showing the location of the major volcanoes and some of the minor monogenetic eruptive centers (MEC) along the Liquiñe-Ofqui Fault Zone (LOFZ) and surrounding Hudson, Macá and Cay (Lopez-Escobar et al. 1993; Gutiérrez et al. 2005; Vargas et al. 2013). The dashed box shows the area of the map (on the right) locating Laguna La Trapananda (solid circle) and the other lakes from which sediment cores have been extracted and tephra identified near Coyhaique (Weller et al. 2015). Also indicated is the locations of Mallín el Pollux (Markgraf et al. 2007). Map constructed using GeoMapApp (http://www.geomapapp.org).

Table 3.1. Radiocarbon age dates from Laguna La Trapananda

Lake	Laboratory No.	Core	Section	Depth	14C years BP	1σ error	Cal year BP	1σ error
LLT	D-AMS 013305	0115A	AT2	28-29	1636	29	1483	39
LLT	D-AMS 017342	0115A	AT3	24-25	3082	22	3245	56
LLT	D-AMS 017343	0115A	AT4	28-29	8229	38	9133	76
LLT	D-AMS 017344	0115A	AT4	78-79	9804	38	11,200	45
LLT	D-AMS 013304	0115A	AT5	34-35	12668	47	15,007	128
LLT	D-AMS 017345	0115A	AT6	53-54	13878	43	16,746	124
LLT	D-AMS 013303	0115A	AT7	17-18	15192	59	18,416	98

The Andean SVZ (Fig. 3.1 inset) consists of ~60 Pleistocene and Holocene composite stratovolcanoes, as well as numerous minor monogenetic eruptive centers (MEC; Stern 2004). This 1400 km long volcanic chain has been divided into the Northern SVZ (NSVZ; 33^{o}S-34.5^{o}S), the Transitional SVZ (TSVZ; 34.5^{o}S-37^{o}S), the Central SVZ (CSVZ; 37^{o}S-41.5^{o}S) and the southernmost portion of the SVZ (SSVZ; 41.5^{o}S-46^{o}S) based on the geometry of the arc and the petrochemical characteristics of the erupted rocks.

This study focuses on tephra produced by eruptions of the volcanoes of the southernmost part of the SSVZ, which according to Völker et al. (2011) consists of 5 volcanic centers: Melimoyu, Mentolat, Macá, Cay, and Hudson (Fig.1), and many minor eruptive centers (MEC) located around the major centers and along the Liquiñe-Ofqui Fault Zone (Fig. 3.1; LOFZ; López-Escobar et al. 1993; D'Orazio et al. 2003; Gutiérrez et al. 2005; Vargas et al. 2013). Based on whole rock petrochemical characteristics, López-Escobar et al. (1993, 1995a, 1995b) classified the basalt of the Andean SVZ into two petrochemical groups, termed Type-1 and Type-2, distinguished by the relative abundance K_2O and incompatible trace elements such as large ion-lithophile elements (LILE; Rb, Cs, Ba, Y, Th, and U), high-field strength elements, (HFSE; Ti, Zr, Hf, Ta) and rare earth elements (REE).

Among the volcanoes of the SSVZ, Hudson, and Melimoyu have produced lavas and tephra with relatively high concentrations of incompatible trace elements such as LILE, HFSE and REE, and have been termed High Abundance (HA) petrochemical types (Stern et al. 2015, 2016; Weller et al. 2015) that correspond to the Type-2 chemical classification of López-Escobar et al. (1993, 1995a, 1995b). Mentolat, Macá, Cay and the MEC have produced lavas and tephra that have relatively low concentrations of LILE, HFSE and REE (Fig. 3.3), which have been termed Low Abundance (LA) petrochemical types and correspond to the Type-1 chemical classification of

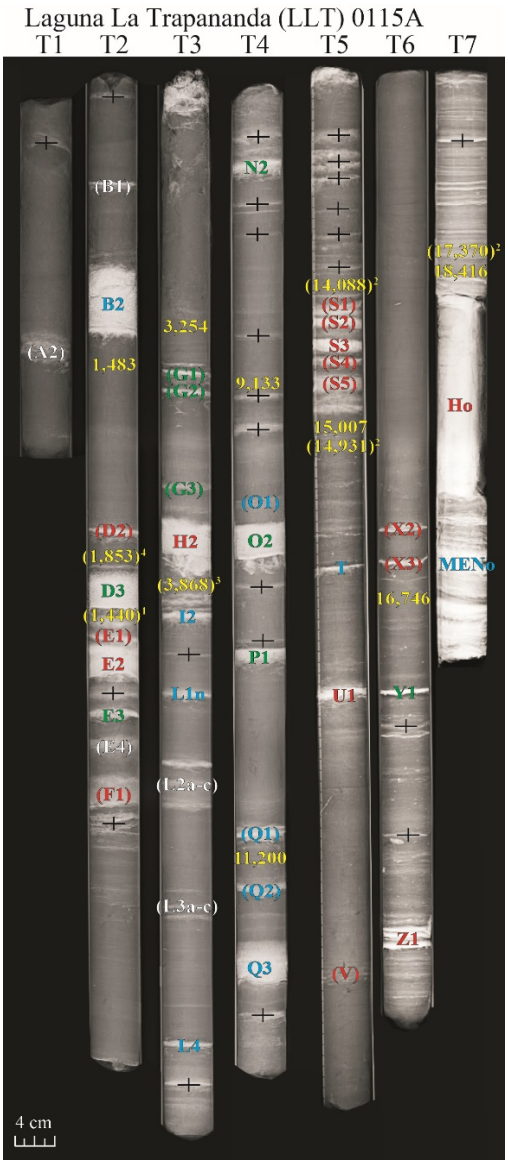

Figure 3.2. Transmitted X-ray image of the lake sediment core from Laguna La Trapananda (LLT). The tephra in this core appear as white layers due to their higher density compared to the predominantly organic lake sediments in which they are preserved. Sampled and unsampled (in parentheses) tephra that have been correlated with tephra in other lake sediment cores from near Coyhaique are labeled with the same nomenclature used in Weller et al. (2015), and numerous thin unsampled dense layers, most probably tephra, are indicated by a + symbol. The tephra labels have been color coded according to the source volcano (red tephra from Hudson, blue from Mentolat, and green from either Macá, Cay, or a monogenetic eruptive centers (MEC)) Tephra with white labels were never sampled from the LLT core or the cores from near Coyhaique but are correlated based on the stratigraphic relations between the cores. New and previously published (Naranjo and Stern 1998[3], 2004[1]; Elbert et al. 2013[4]; Weller et al. 2015[2]) radiocarbon age dates are shown in yellow.

López-Escobar et al. (1993, 1995a, 1995b).

A further division among the Type-1 or LA type centers has been made to distinguish the eruptive products from Mentolat, which produces amphibole bearing andesitic and dacitic lavas and tephra with unusually low concentrations of LILE, HFSE and REE (Fig. 3.3), and has been termed a Very Low Abundance (VLA) or Low Abundance Felsic (LAF) petrochemical type center (Stern et al. 2015, 2016; Weller et al. 2015). Mentolat is similar to some other centers in the SVZ such as Nevado de Longaví (Sellés et al. 2004; Rodríguez et al. 2007), Huequi (Watt et al. 2011), and Calbuco (López-Escobar et al. 1995b), which also have erupted amphibole-bearing products with VLA type chemistry.

Previous tephrochronologic studies of the SSVZ have relied both on these petrochemical differences as well as lithostratigraphic data (age, tephra grain size, etc) to correlate tephra observed in lake and ocean sediment cores amongst themselves and to other tephra described in outcrop (Haberle and Lumley 1998; Naranjo and Stern 2004; Carel et al. 2011; Elbert et al. 2013; Stern 1991, 2008; Stern et al. 2015, 2016; Weller et al. 2014, 2015). The same criteria are used here, where tephra correlation is done by comparing the stratigraphic relations of the tephra amongst the lake sediment cores and the sequential stacking of petrochemically and petrographically distinct eruptions. Based on these correlations, the new radiocarbon age determinations are also correlated amongst the tephra observed in other lake sediment cores taken from the region (Weller et al. 2015).

3.4 Methods

The ~6m long LLT sediment core (Fig. 3.2) was obtained using a modified piston corer

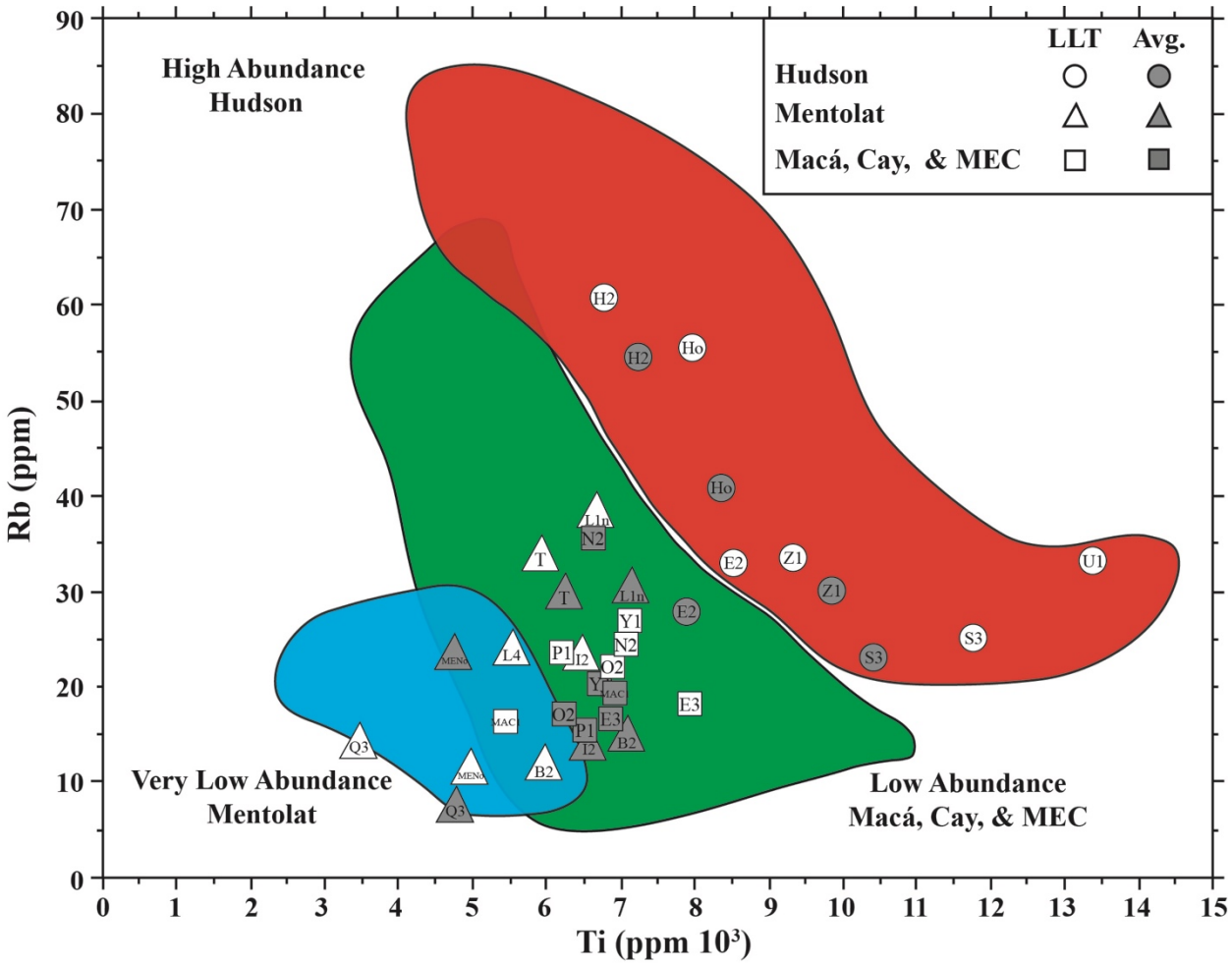

Figure 3.3. Ti versus Rb concentrations, in parts-per-million (ppm) illustrating the High Abundance (HA; red), Low Abundance (LA; green), and Very Low Abundance (VLA; blue) compositional fields for SSVZ centers created using published data of lavas and tephra from Hudson, Mentolat, Macá, Cay and MEC (Futa and Stern 1988; López-Escobar et al. 1993, 1995; Naranjo and Stern 1998, 2004; D'Orazio et al. 2003; Gutiérrez et al. 2005; Weller et al. 2014, 2015; Stern et al. 2015, 2016). Bulk tephra from this study are indicated by open symbols and the average composition of the same tephra are indicated by grey symbols (Tables 3.2-3.4). The Hudson samples are all High Abundance (HA) petrochemical types, which contain generally higher Ti and Rb, than both the Low Abundance (LA) samples from Macá, Cay and MEC, and the Very Low Abundance (VLA) samples from Mentolat.

(Wright 1967). This lake, located 1,160 masl at 45°20'22.85"S and 71°50'11.49"W (Fig. 3.1), was selected because of its small size (<0.1 km^2) and limited basin catchment (<2 km^2) to reduce the amount of clastic input into the lacustrine system. The core was extracted at 1-meter intervals until the sediments transitioned from predominately organic-matter-rich lacustrine sediments to fine-grained glaciolacustrine sands and clays. The core was photographed using transmitted x-rays to aid in the identification of the tephra (Fig. 3.2). The dark material in the photo is the less dense organic matter rich lacustrine sediments and the white layers are the denser lithologies, which are often tephra deposits except in the deepest parts of the cores where fine-grained glaciolacustrine sands and clays occur.

The >50 tephra in the LLT core can in almost all cases be correlated, based simply on their stratigraphic position, with the tephra in other lake cores (Fig. 3.1 and Appendix Figs. S1-S8) previously described from the Coyhaique area by Weller et al. (2015). The A to Z nomenclature used for tephra in these other cores has also been used for the tephra in this new core (Fig. 3.2). However, to confirm these correlations, and to characterize some tephra only observed in the LLT core, a subset of 19 of the deposits greater than 1 cm in thickness were sampled for trace element analysis and petrographic description. A portion of these 19 tephra were removed from the core using a knife and washed in water and acetone to remove organic matter. A part of the cleaned sample was powdered in a moly-tungsten shatter box and dissolved in a mixture of HF, HNO_3 and HCl for trace element analysis using an ELAN D CR ICP-MS. Based on repeat analysis of internal standards with known compositions (Saadat and Stern 2011), these analyses are accurate to ±10% at the concentration levels in these tephra. Another part of the sample was mounted on a petrographic slide to describe features such a tephra glass color, vesicle morphology, microlite

type and abundance, as well as the presence and identity of mineral pheonocrysts (Table A3.1 of the Appendix).

Seven AMS radiocarbon ages (Table 3.1) were determined, by DirectAMS Radiocarbon Dating Services (Brothwell, Washington, USA), on organic matter in bulk sediment samples within the core, and these were converted to calendar years before present (cal years BP) by applying the ShCall 13 curve (Hogg et al. 2013) to the CALIB 7.0.4 program (Stuiver et al. 1998, 2013). The seven new age determinations (Table 3.1), as well as a previously determined age for the large H2 eruption of the Hudson volcano (Naranjo and Stern 1998), were used to control the chronology of the tephra in the LLT (Fig. 3.4) and other cores (Fig. 3.5; Table 3.5).

The average age of the undated tephra in the LLT core and the other cores from near Coyhaique (Tables 3.5 and A3.2 of the Appendix) were estimated with the OXCAL program using the Southern Hemisphere radiocarbon calibration data (Hogg et al. 2013). The OXCAL program uses a Bayesian method, which incorporates information on both the depth and ordering of the tephra deposits and the available radiocarbon ages (Bronk Ramsey 2008). This information was used to determine a representative set of possible ages for each tephra in the sedimentary record (Fig. 3.4; Bronk Ramsey 2008). For this analysis, the P sequence mode was applied with a k parameter (Table A3.2 of the Appendix) calculated with the method outlined in Bronk Ramsey (2008) using three distinct horizons observed in every lake core; the H2 eruption of Hudson, the Q3 eruption of Mentolat and the base of the Hudson derived sequence of 10 closely spaced eruptions (S1-S10; Fig 2). The tephra layers with thicknesses greater than 1 cm were all subtracted from the total integrated thickness of each core for these calculations.

3.5 Results

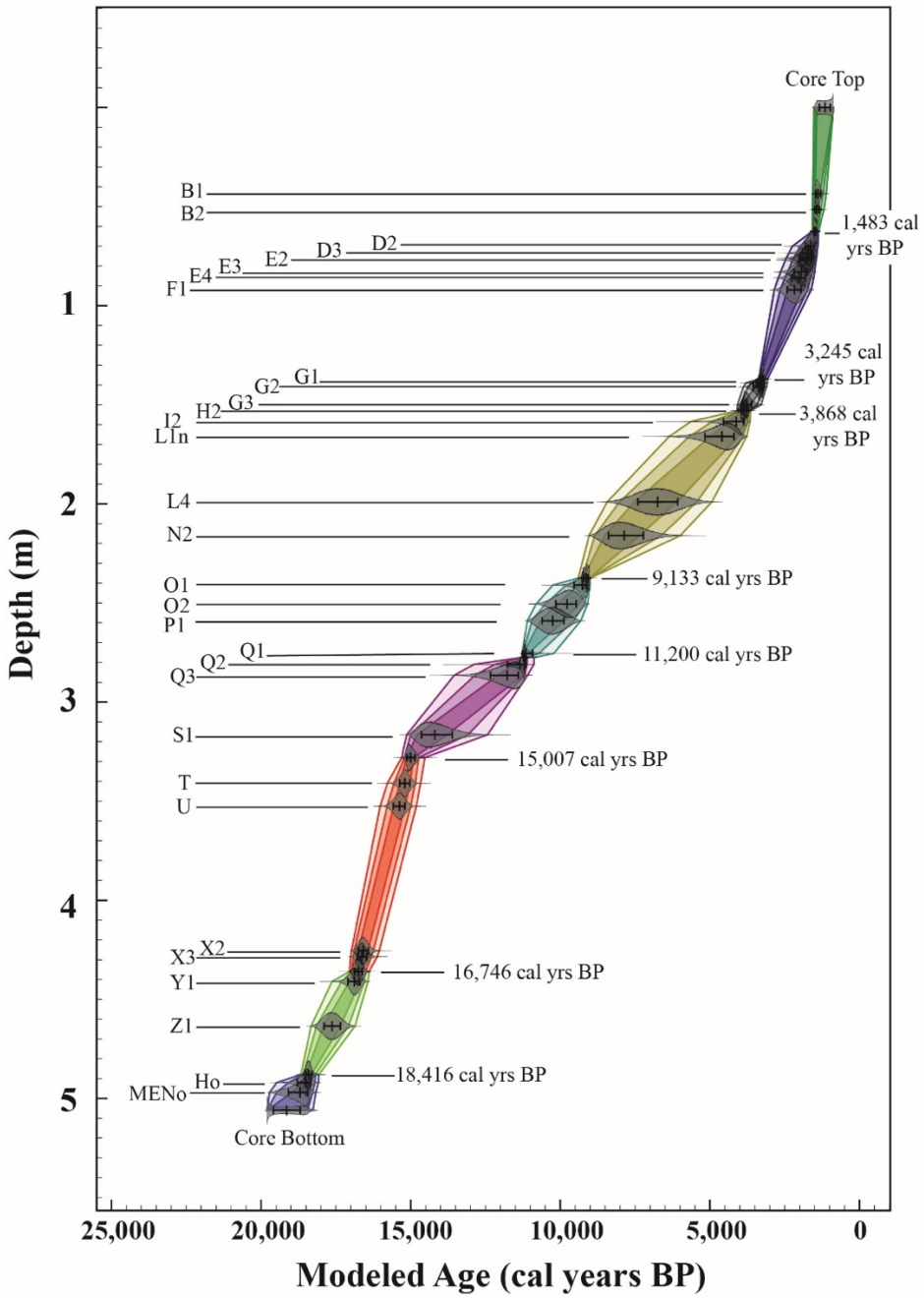

Figure 3.4. Age versus depth model for the tephra in the Laguna La Trapananda sediment core, calculated using OXCAL 4.2 (Bronk Ramsey, 2008) with the Southern Hemisphere radiocarbon calibration data SHCal13 (Hogg et al. 2013). The seven ages from the LLT core (Table 3.1) and for the Hudson H2 eruption (Naranjo and Stern 1998, 2004) that control the model are indicated on the right of the curve, and the ages of all the tephra are tabulated in Table A3.3 of the Appendix. Colored fields represent different sections of each core bound on each end by the radiocarbon age determinations. Within the colored fields are the 68% (darker inner field), 95%, and 99.7% (lightest outer field) highest probability density envelopes with the modeled Gaussian age distribution (grey) including the median (middle black tick mark) and the 1-sigma on the mean for the modeled age estimates (black bars).

Table 3.2a. Trace element concentrations (ppm) of the Hudson derived tephra form LLT and other cores from near Coyhaique

Lake	**LLT**	**Avg***	**LLT**	**Avg***	**LLT**	**Avg***
Section	**T2**	**-**	**T3**	**-**	**T5**	**-**
Depth	**52-55**	**-**	**40-45**	**-**	**24-25**	**-**
Chem. Type	**HA**	**HA**	**HA**	**HA**	**HA**	**HA**
Source	**Hudson**	**Hudson**	**Hudson**	**HUD**	**Hudson**	**Hudson**
Tephra	**E2**	**E2**	**H2**	**H2**	**S3**	**S3**
Lab No.	**DW15-03**	**-**	**DW15-06**	**-**	**DW15-15**	**-**
n	**1**	**7**	**1**	**10**	**1**	**4**
Ti	8538	7867	6767	7221	11785	10406
V	302	256	184	146	344	261
Cr	46	51	17	13	24	18
Mn	1191	1173	1066	1147	1210	1326
Co	41	41	40	20	38	35
Ni	55	48	38	26	52	30
Cu	52	78	17	55	48	93
Zn	139	112	132	110	162	121
Rb	33	28	61	54	25	23
Sr	598	528	392	368	660	540
Y	29	24	38	37	34	35
Zr	226	195	364	349	270	256
Nb	14	10	19	17	14	13
Cs	1.0	0.4	1.6	1.3	0.9	0.5
Ba	453	390	702	688	504	511
La	28.6	25.1	39.3	38.7	35.1	34.0
Ce	65.7	55.9	88.7	84.7	81.7	78.7
Pr	8.09	6.9	10.47	10.22	10.34	10.1
Nd	32.8	29.3	41.2	41.1	44.3	42.2
Sm	7.44	6.05	9.81	8.59	9.49	8.77
Eu	2.68	1.75	3.33	2.49	3.22	2.56
Gd	10.54	6.9	13.19	9.97	13.35	9.7
Tb	1.18	0.80	1.42	1.20	1.31	1.24
Dy	5.54	4.73	7.09	6.93	6.97	6.64
Ho	1.08	0.86	1.26	1.32	1.21	1.27
Er	3.24	2.78	4.39	4.27	4.01	3.89
Tm	0.39	0.30	0.51	0.50	0.36	0.47
Yb	2.76	2.46	3.85	3.95	3.09	3.35
Lu	0.38	0.26	0.52	0.55	0.40	0.37
Hf	5.0	4.9	7.7	8.0	5.3	5.7
Pb	6.9	6.9	10.7	11.2	6.6	6.4
Th	1.9	4.1	3.3	6.0	1.6	3.8
U	0.9	0.8	1.5	1.4	0.8	0.6

*** Average or single tephra trace element contents from Weller et al. (2015)**

Table 3.2b. Trace element concentrations (ppm) of the Hudson derived tephra form LLT and other cores from near Coyhaique

Lake	**LLT**	**LLT**	**Avg***	**LLT**	**Avg***
Section	**T5**	**T6**	**-**	**T7**	**-**
Depth	**57**	**79-81**	**-**	**20-40**	**-**
Chem. Type	**HA**	**LA**		**HA**	**HA**
Source	**Hudson**	**Hudson**	**Hudson**	**Hudson**	**Hudson**
Tephra	**U**	**Z1**	**Z1**	**Ho**	**Ho**
Lab No.	**DW15-17**	**DW15-19**	**-**	**DW15-20**	**-**
n	**1**	**1**	**16**	**1**	**22**
Ti	13387	9318	9846	7998	8350
V	369	340	306	232	208
Cr	19	53	35	DL	18
Mn	1239	1165	1179	1119	1134
Co	79	34	38	41	33
Ni	48	59	29	39	25
Cu	49	43	108	33	231
Zn	155	132	108	147	108
Rb	33	33	30	56	41
Sr	554	562	478	402	451
Y	35	28	29	35	31
Zr	227	165	183	296	226
Nb	11	8	9	19	13
Cs	1.1	2.1	0.8	2.8	1.1
Ba	469	408	386	617	514
La	28.6	22.6	23.6	34.5	28.6
Ce	68.9	52.5	53.8	77.5	63.4
Pr	8.84	6.63	6.9	9.3	7.94
Nd	38.4	28.1	29.4	38.4	33.1
Sm	9.09	6.77	6.51	9.36	7.19
Eu	3.06	2.42	2.07	3.02	2.17
Gd	12.42	9.09	7.6	12.2	8.23
Tb	1.34	1.01	0.98	1.33	1.04
Dy	7.25	5.31	5.49	6.74	5.82
Ho	1.24	0.95	1.07	1.24	1.12
Er	3.93	3.15	3.29	4.25	3.43
Tm	0.40	0.28	0.41	0.47	0.41
Yb	3.23	2.74	2.88	3.45	3.09
Lu	0.37	0.28	0.40	0.46	0.39
Hf	4.6	3.7	4.4	9.1	5.6
Pb	6.7	6.4	5.6	11.3	8.5
Th	1.7	2.0	4.0	3.0	5.3
U	0.9	1.0	0.8	1.5	1.2

*** Average or single tephra trace element contents from Weller et al. (2015)**

Table 3.3a. Trace element concentrations (ppm) of the Mentolat derived tephra form LLT and other cores from near Coyhaique

Lake	**LLT**	**Avg***	**LLT**	**LTr***	**LLT**	**Avg***	**LLT**
Section	**T2**	**-**	**T3**	**AT5**	**T3**	**-**	**T3**
Depth	**17-25**	**-**	**49-49.5**	**49**	**56-56.5**	**-**	**89-89.5**
Chem.Type	**VLA**	**VLA**	**VLA**	**VLA**	**VLA**	**VLA**	**VLA**
Source	**Mentolat**	**Mentolat**	**Mentolat**	**Mentolat**	**Mentolat**	**Mentolat**	**Mentolat**
Tephra	**B2**	**B2**	**I2**	**I2**	**L1n**	**L1n**	**L4**
Lab No.	**DW15-01**	**-**	**DW15-07**	**CS 4112**	**DW15-08**	**-**	**DW15-09**
n	**1**	**4**	**1**	**1**	**1**	**2**	**1**
Ti	5937	7069	6456	6560	6639	7137	5566
V	279	299	320	360	215	270	269
Cr	14	18	21	16	24	17	24
Mn	1478	1452	1210	1581	1032	1164	1325
Co	39	34	57	45	72	31	115
Ni	36	32	45	37	50	35	47
Cu	32	71	43	73	31	71	44
Zn	137	133	142	129	134	131	138
Rb	11	15	23	14	38	30	23
Sr	529	442	478	442	488	505	513
Y	19	20	23	18	28	24	21
Zr	76	87	123	107	166	133	109
Nb	27	4	5	3	7	4	5
Cs	0.9	0.7	1.9	0.5	1.4	0.7	2.6
Ba	155	186	254	173	452	355	240
La	7.0	8.3	13.1	8.5	22.3	16.6	13.8
Ce	16.9	19.9	31.0	20.7	50.9	38.9	31.8
Pr	2.3	2.67	3.9	2.7	6.42	5.0	4.30
Nd	11.1	13.3	17.5	13.7	27.1	22.9	18.9
Sm	3.06	3.47	4.39	3.17	6.56	5.17	4.46
Eu	1.34	1.09	1.62	0.84	2.24	1.42	1.60
Gd	4.1	4.17	6.0	4.3	8.68	6.2	5.97
Tb	0.59	0.54	0.70	0.46	0.97	0.69	0.65
Dy	3.10	3.41	4.17	3.38	5.07	4.61	3.72
Ho	0.65	0.62	0.78	0.56	1.00	0.81	0.71
Er	1.94	2.20	2.55	2.04	3.08	2.76	2.30
Tm	0.25	0.20	0.26	0.20	0.34	0.28	0.23
Yb	1.82	1.99	2.23	2.01	2.76	2.46	2.03
Lu	0.27	0.21	0.28	0.20	0.32	0.27	0.22
Hf	3.5	2.7	2.8	2.5	3.8	3.0	2.5
Pb	4.0	5.3	6.2	4.0	9.1	6.9	6.4
Th	0.4	1.9	1.0	0.8	1.7	2.1	1.0
U	0.3	0.3	0.6	0.3	1.1	0.7	0.7

*** Average or single tephra trace element contents from Weller et al. (2015)**

Table 3.3b. Trace element concentrations (ppm) of the Mentolat derived tephra form LLT and other cores from near Coyhaique

Lake	**LLT**	**Avg***	**LLT**	**Avg***	**LLT**	**Avg***
Section	**T4**	**-**	**T5**	**-**	**T7**	**-**
Depth	**79-82.5**	**-**	**46**	**-**	**44-46**	**-**
Chem.Type	**VLA**	**VLA**	**VLA**	**VLA**	**VLA**	**VLA**
Source	**Mentolat**	**Mentolat**	**Mentolat**	**Mentolat**	**Mentolat**	**Mentolat**
Tephra	**Q3**	**Q3**	**T**	**T**	**MENo**	**MENo**
Lab No.	**DW15-13**	**-**	**DW15-16**	**-**	**DW15-21**	**-**
n	**1**	**7**	**1**	**8**	**1**	**7**
Ti	3448	4761	5920	6228	4945	4728
V	184	185	211	161	281	208
Cr	DL	22	25	14	24	21
Mn	1127	1607	1043	1104	1148	1030
Co	26	34	80	47	35	30
Ni	50	30	50	20	51	24
Cu	16	22	33	137	22	69
Zn	101	117	121	118	109	87
Rb	14	7	33	29	11	23
Sr	616	556	497	377	517	411
Y	16	12	23	26	14	16
Zr	83	49	104	128	55	73
Nb	3	2	4	5	2	3
Cs	0.9	0.2	4.0	1.3	0.9	1.4
Ba	184	113	322	310	134	206
La	8.0	5.5	13.1	13.7	5.4	8.4
Ce	19.2	13.7	30.6	32.6	13.4	19.1
Pr	2.59	1.9	3.85	4.3	1.73	2.5
Nd	12.1	9.0	17.3	19.4	8.5	11.2
Sm	3.08	2.16	4.64	4.97	2.41	2.83
Eu	1.28	0.88	1.79	1.55	0.91	0.98
Gd	3.92	2.7	6.04	5.9	3.25	3.4
Tb	0.44	0.31	0.69	0.80	0.33	0.38
Dy	2.66	2.21	3.95	4.81	2.42	2.77
Ho	0.43	0.35	0.76	0.94	0.41	0.54
Er	1.72	1.32	2.53	2.96	1.46	1.79
Tm	0.11	0.14	0.25	0.35	0.09	0.19
Yb	1.56	1.25	2.32	2.74	1.27	1.65
Lu	0.14	0.09	0.24	0.33	0.11	0.20
Hf	2.0	1.4	2.6	3.7	1.4	2.2
Pb	4.8	3.2	8.9	9.6	3.9	6.2
Th	0.5	0.6	1.9	3.2	0.4	2.2
U	0.4	0.1	1.1	0.9	0.3	0.8

*** Average or single tephra trace element contents from Weller et al. (2015)**

Table 3.4a. Trace element concentrations (ppm) of the Macá, Cay, or MEC derived tephra form LLT and other cores from near Coyhaique

Lake	**LLT**	**Avg***	**LLT**	**Avg***	**LLT**	**LU***
Section	**T2**	**-**	**T2**	**-**	**T4**	**ET6**
Depth	**46-49**	**-**	**58.5-59**	**-**	**7-8**	**53**
Chem.Type	**LA**	**LA**	**LA**	**LA**	**LA**	**LA**
Source	**Macá**	**Macá**	**M/C/MEC**	**M/C/MEC**	**M/C/MEC**	**M/C/MEC**
Tephra	**MAC1/D3**	**MAC1/D3**	**E3**	**E3**	**N2**	**N2**
Lab No.	**DW15-02**	**-**	**DW15-04**	**CS 4106**	**DW15-10**	**CS 4133**
n	**1**	**7**	**1**	**1**	**1**	**1**
Ti	5481	6820	7931	6888	7048	6617
V	236	222	394	386	270	292
Cr	120	102	55	38	19	38
Mn	944	1110	1290	1395	1199	1065
Co	56	45	155	45	53	30
Ni	101	84	58	39	51	40
Cu	35	92	74	127	37	140
Zn	104	98	142	135	145	103
Rb	16	19	18	16	24	37
Sr	688	580	522	419	516	477
Y	18	20	24	16	25	23
Zr	120	157	91	83	109	142
Nb	12	7	7	3	9	3
Cs	0.6	0.2	1.4	0.8	1.4	1.0
Ba	245	308	214	156	273	351
La	14.9	19.5	10.4	6.4	12.4	15.5
Ce	35.1	44.8	25.8	17.3	29.5	35.3
Pr	4.53	5.6	3.56	2.2	3.83	4.61
Nd	19.4	23.9	16.2	11.7	18.1	20.0
Sm	4.37	5.00	4.32	2.76	4.93	4.62
Eu	1.61	1.50	1.67	0.87	1.79	1.15
Gd	6.05	5.8	5.93	3.7	6.62	5.45
Tb	0.69	0.65	0.82	0.39	0.79	0.62
Dy	3.35	3.98	4.26	3.03	4.35	4.10
Ho	0.63	0.72	0.85	0.54	0.84	0.76
Er	1.99	2.28	2.46	1.78	2.70	2.56
Tm	0.22	0.22	0.29	0.18	0.28	0.27
Yb	1.71	2.03	2.22	1.61	2.44	2.38
Lu	0.21	0.17	0.31	0.17	0.26	0.31
Hf	3.0	3.7	2.4	2.2	6.2	3.3
Pb	3.5	5.3	5.9	5.0	7.5	7.6
Th	0.8	2.5	0.7	1.1	0.9	2.7
U	0.4	0.5	0.6	0.4	0.7	0.8

*** Average or single tephra trace element contents from Weller et al. (2015)**

Table 3.4b. Trace element concentrations (ppm) of the Macá, Cay, or MEC derived tephra form LLT and other cores from near Coyhaique

Lake	**LLT**	**Avg***	**LLT**	**Avg***	**LLT**	**Avg***
Section	**T4**	**-**	**T4**	**-**	**T6**	**-**
Depth	**40-43**	**-**	**51-53**	**-**	**58**	**-**
Chem.Type	**LA**	**LA**	**LA**	**LA**	**LA**	**LA**
Source	**M/C/MEC**	**M/C/MEC**	**M/C/MEC**	**M/C/MEC**	**M/C/MEC**	**M/C/MEC**
Tephra	**O2**	**O2**	**P1**	**P1**	**Y1**	**Y1**
Lab No.	**DW15-11**	**-**	**DW15-12**	**-**	**DW15-18**	**-**
n	**1**	**5**	**1**	**8**	**1**	**5**
Ti	6861	6230	6208	6524	7127	6740
V	244	204	218	213	265	261
Cr	17	18	19	22	24	18
Mn	1226	1078	1052	1122	1278	1153
Co	27	29	33	34	62	35
Ni	50	32	50	35	48	21
Cu	31	69	19	91	33	125
Zn	143	107	124	115	149	110
Rb	22	17	23	16	27	21
Sr	496	452	552	452	535	470
Y	25	21	23	20	26	23
Zr	98	86	109	78	113	99
Nb	4	4	4	4	4	4
Cs	1.4	0.5	1.0	0.5	2.4	1.0
Ba	274	229	293	224	301	259
La	11.4	9.6	13.4	9.5	14.3	12.8
Ce	26.7	22.9	31.6	22.8	34.0	29.4
Pr	3.72	3.1	4.07	3.1	4.42	3.9
Nd	17.5	14.5	18.5	14.0	20.3	17.4
Sm	4.84	3.73	4.87	3.69	5.06	4.29
Eu	1.79	1.17	1.84	1.23	1.78	1.39
Gd	6.19	4.5	6.55	4.4	7.04	5.1
Tb	0.76	0.56	0.73	0.57	0.81	0.70
Dy	4.51	3.71	4.34	3.71	4.73	4.12
Ho	0.81	0.67	0.80	0.74	0.83	0.83
Er	2.66	2.28	2.53	2.22	2.89	2.52
Tm	0.26	0.21	0.24	0.28	0.27	0.30
Yb	2.42	1.99	2.22	2.11	2.56	2.26
Lu	0.28	0.14	0.25	0.24	0.31	0.29
Hf	2.6	2.4	2.5	2.6	2.7	2.8
Pb	7.3	6.7	6.0	6.8	8.4	7.3
Th	0.8	1.4	1.1	1.9	1.6	2.9
U	0.6	0.5	0.6	0.4	0.9	0.7

*** Average or single tephra trace element contents from Weller et al. (2015)**

3.5.1 General

The results include a lithostratigraphic description (Table A3.1 of the Appendix) and a summary of the trace-element chemistry (Tables 3.2-3.4) of the 19 tephra sampled, the correlation of the tephra observed in other lake cores from the region (Fig. 3.2), source volcano identification, as well as the modeled average age for 56 tephra observed in both the LLT core and some or all of the other cores from near Coyhaique (Table 3.5).

3.5.2 Tephra correlations

Correlation of the tephra between the cores and source volcano identification is done based on three criteria: 1) bulk tephra trace element chemistries as compared against published trace element contents of lavas and tephra from the volcanoes of the SSVZ (Fig. 3.3, Tables 3.2-3.4); 2) the stratigraphic relationship between the cores; and 3) tephra lithostratigraphic characteristics such as glass color and morphology, vesicle abundance and morphology, the presence of mineral microlite, and the identity and abundance of mineral phenocrysts (Table A3.1 of the Appendix). For a more complete discussion of the petrochemical differences and tephra characteristic of tephra derived from SSVZ volcanoes see Weller et al. (2015) and Stern et al. (2016).

Among the 19 tephra layers sampled from Laguna Las Trapananda, seven eruptions are attributed to small to medium sized eruptions of Mentolat (Table 3.2), two of which (I2 and L4) were not previously recognized in the other lake cores from near Coyhaique. Six eruptions are attributed to explosive eruptions of Hudson volcano (Table 3.3), one of which (U1) was observed in the lake cores near Coyhaique, but was not previously sampled. One tephra (D3) is attributed to a medium sized explosive eruption of Macá (Table 3.4), and source volcanoes for five other tephra may be either Macá, Cay, or one of the MEC.

3.5.3 Mentolat Tephra

Seven of the sampled tephra are attributed to eruptions of Mentolat (Table 3.2). Five of these (B2, L1n, Q3 (previously MEN1), T and MENo) correspond to tephra observed in other lake cores near Coyhaique (Weller et al. 2014, 2015). All of these tephra contain white volcanic glass with rounded vesicles, but lacking mineral microlites, and have abundant phenocrysts of plagioclase, clino and orthopyroxene, amphibole, and minor olivine. All of these tephra are light grey in -color with abundant fine white pumice lapilli and a smaller amount of dark grey to black mafic components. These tephra are all VLA petrochemical types (Fig. 3.3; Table 3.2) which generally fall within the fields defined by previously reported analyses of Mentolat derived tephra and lavas.

Two other sampled tephra (I2 and L4), which are both VLA petrochemical type deposits (Fig. 3.3; Table 3.2) with tephra glass and mineral characteristics similar to the other Mentolat derived tephra (Table A3.1 of the Appendix) are also tentatively attributed to eruptions from Mentolat volcano. One deposit, tephra I2, is similar to a previously uncorrelated deposit from Lago Tranquilo (Fig. S7 of the Appendix; Weller et al. 2015). The other tephra (L4) is not observed in the other lake cores from the region. It underlies two distinctive sequences of three tephra each called L2a-c and L3a-c, but these have not been sampled.

Most significantly, the new age determinations indicate that the Mentolat-derived tephra previously identified as MEN1 in the eight other cores from near Coyhaique (Weller et al 2014, 2015) is older than the MEN1 tephra deposit described in outcrop by Naranjo and Stern (2004) and in lake cores further south by Stern et al. (2016) and McCulloch et al. (2016), and its name has been changed accordingly to Q3.

3.5.4 Hudson Tephra

Six tephra deposits (E2, H2, S3, U1, Z1 and Ho) from LLT are attributed to explosive eruptions from Hudson (Table 3.3). These tephras include the ~3,900 cal years BP H2 eruption (Naranjo and Stern 1998), the large late glacial Ho eruption previously dated at ~17,400 cal years BP from lake cores near Coyhaique (Weller et al. 2014, 2015), and several smaller eruptions including tephra S3 of the sequence of 10 (S1-S10) closely spaced Hudson-derived eruptions dated at approximately ≤15,000 cal years BP. Tephra U of the LLT lake core corresponds to the youngest of the three tephra U1-U3 from near Coyhaique, which were not previously sampled.

These tephra are all HA petrochemical type deposits (Fig. 3.3; Table 3.3), and are all generally similar in appearance and color to other Hudson derived tephra, including the Ho tephra, which contains a mixture of both dark mafic material and less abundant light brown to tan pumice lapilli. These deposits consist of either tan volcanic glass with no mineral microlites and abundant elongated vesicles or dark brown glass with few circular vesicles and variable amounts of mineral microlites. Commonly observed phenocrysts include plagioclase, clinopyroxene, orthopyroxene, but not amphibole.

3.5.5 Macá, Cay, and Minor Eruptive Centers (MEC) Tephra

Tephra D3 (Fig. 3.2), which is attributed to the small to medium sized explosive MAC1 eruption of Macá (Naranjo and Stern 2004; Weller et al. 2015), is also observed in the LLT core. Five additional LA petrochemical type tephra could be sourced from either Macá, Cay, or one of the MEC (Table 3.4). Four of these tephra (E3, O2, P1, and Y1; Weller et al. 2015) correspond to previously described eruptions. One tephra, N2, occurs in the same stratigraphic position and has similar LA-type petrochemistry to a previously uncorrelated tephra from Lago Unco (Fig. S8 of the Appendix). All of the LA petrochemical type eruptions consist of dark grey to black material

with glass that is dark brown in color and contains variable amounts of mineral microlites and circular vesicles. Common phenocrysts include olivine, clinopyroxene, and plagioclase with less common orthopyroxene, and in a few cases a small amount of amphibole.

3.5.6 Tephra Ages

The seven new radiocarbon age dates are reported in Table 3.1. The lowermost radiocarbon age in the LLT core (18,416±98 cal yrs BP; Fig. 3.2), which was sampled directly above the late glacial Ho eruption of Hudson, is similar to the ages of Ho determined in a core from Lago Castor (Fig. 3.1) just south of LLT (17,500-18,410 cal yrs BP; Van Daele et al., 2016) and estimated in one core from further north in the Cisnes river valley (18,820 yrs BP; Stern et al. 2015), but ~1000 years older than the previous determination of the age of this tephra in the eight cores from near Coyhaique (17,370±70 cal yrs BP; Miranda et al. 2012; Weller et al. 2014). The new age (15,007±128 cal yrs BP; Table 3.2) determined just below the S1-S10 sequence of tephra (at 34 cm depth in section T5; Fig. 3.2) is similar to the age (14,932 cal yrs BP; Weller et al., 2015) previously estimated for the beginning of this sequence of tephra (Fig. 3.2).

The average age estimates from the Bayesian modeling of the 56 tephra found in the LLT core and in each of the other eight lake cores from near Coyhaique are reported in Table A3.3 of the Appendix, and the average age of each of these 56 tephra found in some or all the lake sediment cores from near Coyhaique are reported in Table 3.5. In some few instances, the average model age of stratigraphically older tephra are calculated to have younger ages than the overlying tephra deposit. This is the result of some tephra being observed in all the lake cores, while other tephra are only preserved in a few lakes and their age estimate is biased towards those modeled ages. However, the age estimates for these tephra are all within the error estimates of the stratigraphically associated tephra.

Table 3.5. Average modeled age in cal years BP for tephra observed in the lake cores near Coyhaique

Tephra	Source	Age (cal years BP)	1σ	Tephra	Source	Age (cal years BP)	1σ
A1	**M/C/MEC**	793	1031	**N**	**Hudson**	8233	541
A2	**-**	1021	820	**N2**	**M/C/MEC**	8864	347
B1	**-**	1340	427	**O1**	**Mentolat**	9261	210
B2	**Mentolat**	1426	367	**O2**	**M/C/MEC**	9417	280
C1	**Hudson**	1532	109	**P1**	**M/C/MEC**	10613	388
C2	**Hudson**	1612	156	**P2**	**Hudson**	10724	360
D1	**Mentolat**	1774	216	**Q1**	**Mentolat**	11142	248
D2	**Hudson**	1872	203	**Q2**	**Mentolat**	11378	275
D3	**Macá**	1922	215	**Q3**	**Mentolat**	11407	339
E1	**Hudson**	1900	239	**S1**	**Hudson**	14647	386
E2	**Hudson**	1965	240	**S10**	**Hudson**	14967	249
E3	**M/C/MEC**	1956	231	**T**	**Mentolat**	15120	224
E4	**-**	2058	260	**U1**	**Hudson**	15473	349
F1	**Hudson**	2211	274	**U2**	**-**	15487	399
F2	**Hudson**	2235	269	**U3**	**-**	15750	360
F3	**Hudson**	2494	278	**V**	**Hudson**	15956	443
G1	**M/C/MEC**	3314	159	**Wn**	**M/C/MEC**	16437	296
G2	**M/C/MEC**	3614	197	**Ws**	**Hudson**	16210	613
G3	**M/C/MEC**	3771	170	**X1**	**Hudson**	16608	310
H2	**Hudson**	3868	84	**X2**	**Hudson**	16654	205
I1	**Hudson**	4528	469	**X3**	**Hudson**	16695	181
I2	**Mentolat**	4793	596	**Y1**	**M/C/MEC**	16878	226
J	**Hudson**	5337	609	**Y2**	**-**	17467	318
L1n	**Mentolat**	5372	637	**Z1**	**Hudson**	17575	315
K	**Hudson**	5434	619	**Ho**	**Hudson**	18459	205
L1s	**M/C/MEC**	6450	611	**Z3**	**M/C/MEC**	18497	258
L4	**Mentolat**	6747	665	**MENo**	**Mentolat**	18672	459
M	**Hudson**	8139	558	**Z5**	**M/C/MEC**	18844	524

3.6 Discussion

Most of the tephra from the Laguna La Trapananda sediment core are similar petrochemically, petrographically, and share similar stratigraphic relations with other tephra observed in other lake cores to the south (Weller et al. 2015). Seven of the tephra are similar to Mentolat derived tephra, six are similar to the eruptive products of Hudson, and six are similar to previously reported tephras derived from either Macá, Cay, or one of the MEC. Four of these tephra represent previously unrecognized or unsampled eruptions from volcanoes of the SSVZ, including two from Mentolat (I2 and L4), one from Hudson (U1), and one (N2) from either Macá, Cay, or one of the many MEC located along the LOFZ or surrounding the major centers.

The new radiocarbon ages confirm that Mentolat, Hudson, Macá and possibly Cay or one of the MEC have produced regionally widespread tephra since the late Pleistocene deglaciation of the region (Miranda et al. 2012) and throughout the Holocene. The ages confirm the conclusion that eruption rates of volcanoes in the southern SSVZ were essentially uniform since late glacial times, with no clear post-glacial increase in volcanic activity and no clear episodic concentrations of activity in specific periods since deglaciation of the region. Hudson volcano, located just north of the Chile Rise-Trench triple junction, has been the most active in terms of both volume and frequency (Table 3.5) of explosive eruptions (Weller et al. 2015).

Concerning specific tephra, the modeled age for tephra D3 (1,922±215 cal yrs BP; Table 3.5), which Weller et al. (2015) attributed to the late Holocene MAC1 eruption of Macá, is similar to the radiocarbon age date of tephra T3 (1,860±30 cal yrs BP; Elbert et al. 2013) from Lago Castor (Fig. 3.2), and older than the age estimate obtained from a proximal outcrop of this tephra (1,440±60 cal yrs BP; Narnajo and Stern 2004). The new radiocarbon age determinations also indicate that the tephra previously correlated with the MEN1 eruption of Mentolat from the eight

other lake cores near Coyhaique (Weller et al., 2015) is too old to correspond the 7,690±60 cal years BP outcrop deposit described by Naranjo and Stern (2004) and the distal MEN1 tephra deposit observed further south in lake cores near the town of Cochrane (Stern et al. 2016; McCulloch et al. 2016). This tephra, now named Q3, represents an older early-Holocene eruption of Mentolat volcano.

The estimated ages of the 56 tephra in the LLT sediment core provide a potentially significant tool for correlating with tephra in other cores from which ages, but not petrochemical characteristics, of tephra have been published. For example, the 9 tephra observed and dated in the lake sediment core from Castor lake (Fig. 3.1) by Elbert et al. (2013), can be correlated with the tephra in the LLT core based on their ages, and their sources thus identified. The ages suggest that the tephra identified by Elbert et al. (2013) as CAS-T9 (3,900 cal yrs BP) corresponds to H2, CAS-T8 (3,710 cal yrs BP) to G3, CAS-T6 (2,320 cal yrs BP) to one of the F tephra, CAS-T5 (2,070 cal yrs BP) to E4, CAS-T4 (1,930 cal yrs BP) to E2, CAS-T3 (1,850 cal yrs BP) to D3 (MAC1), CAS-T2 (1,620 cal yrs BP) to C2, and CAS-T1 (1,070 cal yrs BP) to A2.

The new age estimates can also be used as a tool for constraining sedimentation rates in lake cores obtained for paleoclimate studies. Based on the age estimates presented in Table 3.5, depth versus age sedimentation profiles were generated for the LLT core (Fig. 3.4) and for other lake sediment cores from the Coyhaique area (Fig. 3.5; Weller et al. 2015). These sedimentation profiles indicate that on each lake there have been intervals of relatively rapid and slower sediment accumulation. However, the timing of the sedimentation rate changes clearly varies amongst the lakes. For example, many of the lakes experience rapid accumulation of material after deglaciation until approximately 15,000 cal years BP, but decreasing rates of sediment accumulation doesn't take place until much later, at approximately 10,000 cal years BP, for several lakes such as

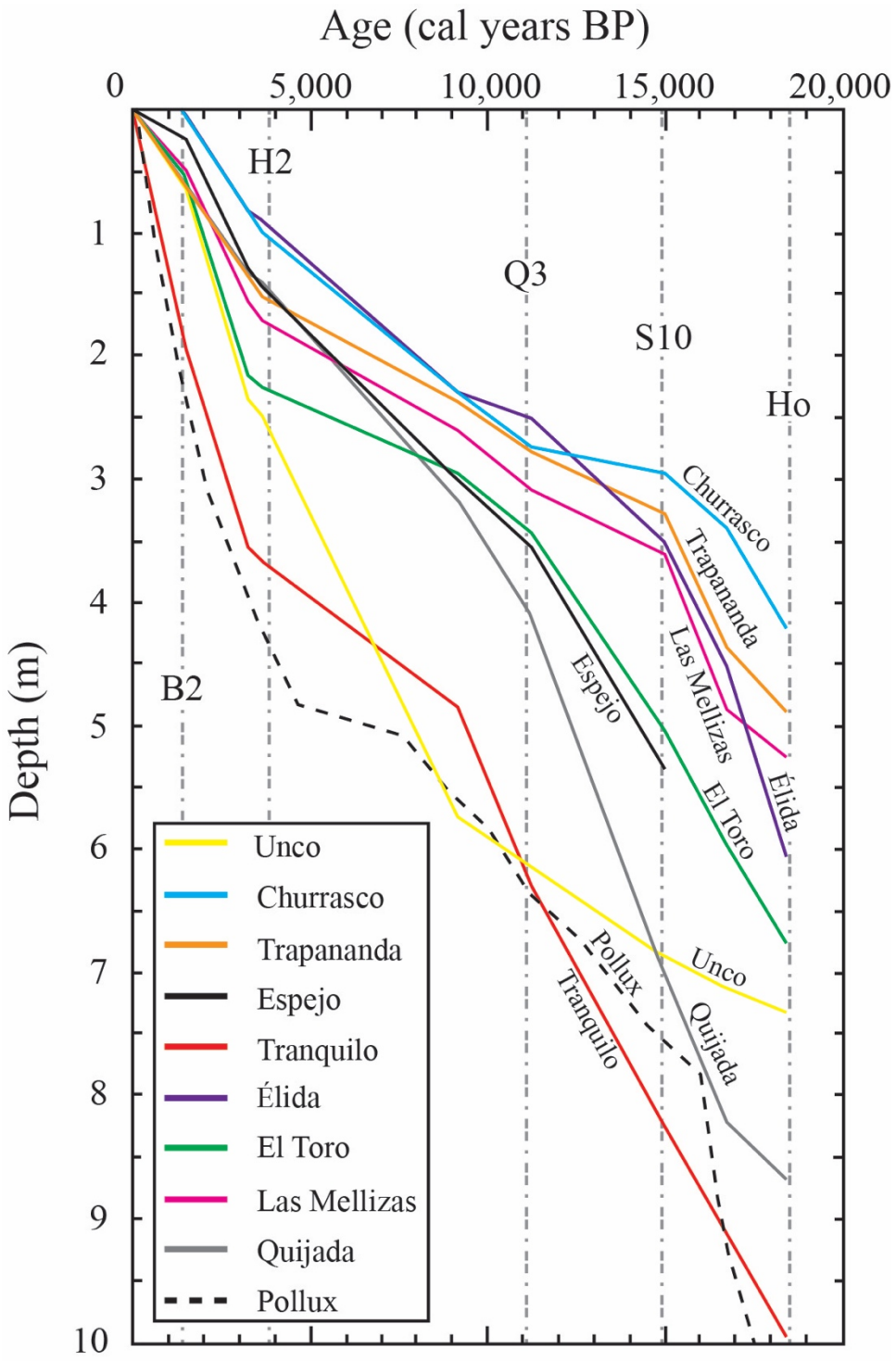

Figure 3.5. Sedimentation profiles for Laguna La Trapananda and the other eight lake cores from near Coyhaique (Weller et al. 2015), from the surface to the base of each core, using the new radiocarbon age estimates (Tables 3.5 and Table A3.3 of the Appendix). The figure includes one previously published profile, based on an independent sets of internal age ages, from Mallín el Pollux (Markgraf et al. 2007). Tephra with a thickness of 1 cm or greater have been subtracted from the total integrated length of the sediments in the cores.

Tranquilo and El Toro. Therefore the uniformity in the timing of the sedimentation rate changes previously suggested by Weller et al. (2015) is absent, indicating that each lake has its own complex sedimentation history that may be influenced by a number of factors such as lake elevation, timing of glacial retreat, connectivity to larger proglacial lakes, changes in regional vegetation cover, etc. The details of these complex histories are beyond the scope of this paper.

However, the early Holocene decrease in the sediment accumulation rate is followed by a more rapid sedimentation rate starting in all the cores after the H2 eruption at approximately 3,900 cal years BP. This rapid change in the sedimentation profiles is also observed in Mallín el Pollux (Markgraf et al. 2007) with an independent chronology, suggesting that this mid-Holocene change was regional and affected all the small lacustrine systems located in the relatively restricted region of southern Chile. Alternatively, this may merely reflect less compaction in the shallow parts of each core, but Weller et al. (2014) concluded that H2 and Ho tephra were not compacted to different degrees in thicker relative to shorter cores from different lakes with very different sedimentation rates.

3.7 Conclusions

Seven new radiocarbon ages from with a sediment core from the Laguna La Trapananda in southern Chile allow for the estimation of the ages of 56 tephra (Table 3.5) observed in this and other lake cores from the region. These age estimates provide a tool for 1) evaluating eruption rates in this region, which are found to be essentially uniform since late glacial times, 2) correlating tephra in the LLT core with those identified and dated in other lake cores for which petrochemical data has not been obtained, and 3) as isochrons for determining sedimentation rates, which are found to be both variable through time and different amongst the other lakes which have been

cored for paleoclimate and paleoecologic studies in the region. Further application and refinements of this tephrochronology tool is expected in the future both because the region is of interest to volcanologists due to its proximity to the Chile Rise-Trench triple junction and to paleoclimatologists due to its preservation of late glacial to recent climate change records in the southern hemisphere.

3.8 References

Bronk Ramsey, C (2008) Deposition models for chronological records. Quat Sci Rev 27: 42-60

Carel M, Siani G, Delpech G (2011) Tephrostratigrapy of a deep-sea sediment sequence off the south Chilean margin: New insight into the Hudson volcanic activity since the last glacial period. J Volcanol Geotherm Res 208: 99-111

D'Orazio M, Innocenti F, Manetti P, Tamponi M, Tonarini S, González-Ferrán O, Lahsen A (2003) The Quaternary calc-alkaline volcanism of the Patagonian Andes close to the Chile triple junction: geochemistry and petrogenesis of volcanic rocks from the Cay and Maca volcanoes (~45°S, Chile). J S Amer Earth Sci 16(4): 219–242

Elbert J, Wartenburg R, von Gunten L, Urrutia R, Fisher D, Fujak M, Hamann Y, Greber ND, Grosjean M (2013) Late Holocene air temperature variability reconstructed from the sediments of Laguna Escondida, Patagonia Chile. Palaeogeog Palaeoclimat Palaeoecol 396: 482-492

Fontijn K, Lachowycz SM, Rawson H, Pyle DM, Mather TA, Naranjo JA, Moreno-Roa H (2014) Late Quaternary tephrostratigraphy of southern Chile and Argentina. Quat Sci Revs 89: 70-84

Futa K, Stern CR (l988) Sr and Nd isotopic and trace element compositions of Quaternary volcanic centers of the southern Andes. Earth Planet Sci Lett 88: 253–262

Gutiérrez F, Gioncada A, González-Ferrán O, Lahsen A, Mazzuoli R (2005) The Hudson volcano and surrounding monogenetic centres (Chilean Patagonia): an example of volcanism associated with ridge-trench collision environment. J Volcanol Geotherm Res 145: 207–233

Haberle SG, Lumley SH (1998) Age and origin of tephras recorded in postglacial lake sediments to the west of the southern Andes, 44°S to 47°S. J Volcanol Geotherm Res 84: 238-256

Hickey RL, Frey FA, Gerlach DC (1986) Multiple sources for basaltic arc rocks from the Southern Volcanic Zone of the Andes (34-41°S): Trace element and isotopic evidence for contributions from subducted oceanic crust, mantle, and continental crust. J Geoph Res 91: 5963-5983.

Hickey-Vargas RL, Moreno-Roa H, López-Escobar L, Frey FA (1989) Geochemical variations in Andean basaltic and silicic lavas from the Villarrica-Lanín volcanic chain (39.5°S): an evaluation of source heterogeneity, fractional crystallization and crustal assimilation. Contrib Mineral Petrol 103: 361-386

Hickey-Vargas RL, Sun M, López-Escobar L, Moreno-Roa H, Reagan MK, Morris JD, Ryan JG (2003) Multiple subduction components in the mantle wedge: evidence from eruptive centers in the Central Southern volcanic zone, Chile. Geology 30 (3): 199-202.

Hogg A, Hua Q, Blackwell P, Niu M, Buck C, Guilderson T, Heaton TJ, Palmer JG, Paula JR, Reimer RW, Turney CSM, Zimmerman SRH (2013). SHCAL13 Southern Hemisphere Calibration, 0-50,000 years CAL BP. Radiocarbon 55(4): 1889-1903.

Kratzmann DJ, Carey S, Scasso RA, Naranjo JA (2009) Compositional variations and magma mixing in the 1991 eruptions of Hudson volcano, Chile. Bull Volcanol 71(4): 419–439

Kratzmann DJ, Carey S, Scasso RA, Naranjo JA (2010) Role of cryptic amphibole crystallization in magma differentiation at Hudson volcano, Southern Volcanic Zone, Chile. Contrib Mineral Petrol 159: 237–264

López-Escobar L, Kilian R, Kempton P, Tagiri M (l993) Petrology and geochemistry of Quaternary rocks from the southern volcanic zone of the Andes between 41°30’ and 46°00’S, Chile. Rev Geol Chile 20: 33–55

López-Escobar L, Cembrano J, Moreno H, (1995a) Geochemistry and tectonics of the chilean Southern Andes basaltic Quaternary volcanism (37-46ºS). Revista Geológica de Chile 22 (2): 219-234

López-Escobar L, Parada MA, Hickey-Vargas R, Frey FA, Kempton P, Moreno H (1995b) Calbuco Volcano and minor eruptive centers distributed along the Liquiñe-Ofqui Fault Zone, Chile (41°S) contrasting origin of andesitic and basaltic magmain the Southern Volcanic Zone of the Andes. Contr Mineral Petrol 119: 345-361

Lowe DJ (2011) Tephrochronology and its application: A review. Quat Geol. 6: 107-153

Markgraf V, Whitlock C, Haberle S (2007) Vegetation and fire history during the last 18,000 cal yr B.P. in Southern Patagonia: Mallín Pollux, Coyhaique, Province Aisén (45^{o}41'30", 71^{o}50'30"W, 640 m elevation). Palaeogeogr Palaeoclimatol Palaeoecol 254: 492-507

McCulloch RD, Figuerero MJ, Mengoni GL, Barclay R, Mansilla C (2016) A Holocene record of environmental change from Río Zeballos, central Patagonia. The Holocene DOI: 10.1177/0959683616678460

Miranda CG, Moreno PI, Vilanova I, Villa-Martínez RP (2013) Glacial fluctuations in the Coyhaique-Balmaceda sector of central Patagonia (45°S-46°S) during the last glacial termination. Bollettino di Geofisica 54: 268-271

Naranjo JA (l991) Nueva erupción del volcán Hudson. Rev Geol Chile 18: 183–184

Naranjo JA, Moreno HR, Banks NG (1993) La Eruptión del Volcán Hudson en 1991 (46°S), Regieón XI, Aisén, Chile. Servicio Nacional de Geologia y Mineria 44: 1-50

Naranjo JA, Stern CR (1998) Holocene explosive activity of Hudson Volcano, southern Andes. Bull Volcanol 59(4): 291–306

Naranjo JA, Stern CR (2004) Holocene tephrochronology of the southernmost part (42°30'-45°S) of the Andean Southern Volcanic Zone. Rev Geol Chile 31(2): 225–240

Rodríguez C, Sellés D, Dungan M, Langmuir C, Leeman W, (2007) Adikitic dacites formed by intracrustal crystal fractionation of water-rich parent magmas at Nevado de Longaví (36.2°S; Andean Southern Volcanic Zone, Central Chile). J Petrol 48(11): 2033-2061

Saadat S, CR Stern (2011) Petrochemistry and genesis of olivine basalts from small monogenetic parasitic cones of Bazman stratovolcano, Makran arc, southeastern Iran. Lithos 125: 609-617

Scasso RA, Corbella H, Tiberi P (l994) Sedimentological analysis of the tephra from the 12–15 August l991 eruption of Hudson volcano. Bull Volcanol 56: 121–132

Sellés D, Rodríguez AC, Dungan MA, Naranjo JA, Gardeweg M (2004) Geochemistry of Nevado de Longaví (36.2°S): a compositionally atypical volcano in the Southerrn Volcanic Zone of the Andes. Rev Geol Chile 31(2): 293-315

Stern CR (l991) Mid-Holocene tephra on Tierra del Fuego (54°S) derived from the Hudson volcano (46°S): evidence for a large explosive eruption. Rev Geol Chile 18: 139–146

Stern CR (2004) Active Andean Volcanism: its geologic and tectonic setting. Rev Geol Chile 31(2): 161-206

Stern CR (2008) Holocene tephrochronology record of large explosive eruptions in the southernmost Patagonian Andes. Bull Volcanol 70(4): 435–454

Stern CR, de Porras ME, Maldonado A (2015) Tephrochronology of the upper Río Cisnes valley (44°S), southern Chile. Andean Geol 42(2): 173-192

Stern CR, Moreno PI, Henrique WI, Villa-Martinez RP, Sagredo E, Aravena JC, De Pol-Holz R (2016) Holocene tephrochronolgy in the area around Cochrane, southern Chile. Andean Geol 42(3): 1-19

Stuiver M, Reimer PJ, Braziunas TF (1998) High-precision radiocarbon age calibration for terrestrial and marine samples. Radiocarbon 40(3): 1127–1151

Van Daele M, Bertrand S, Meyer I, Moernaut J, Vandoorne W, Siani G, Tanghe N, Ghazoui Z, Pino M, Urrutia R, De Batist M (2016) Late Quaternary evolution of Lago Castor (Chile, 45.6°S): Timing of the deglaciation in northern Patagonia and evolution of the southern westerlies during the last 17 kyr. Quat Sci Rev 133: 130-146

Vargas G, Rebolledo S, Sepúlveda SA, Lahsen A, Thiele R, Townley B, Padilla C, Rauld R, Herrera MJ, Lara M (2013) Submarine earthquake rupture, active faulting and volcanism along the major Liquiñe-Ofque Fault Zone and implications for seismic hazard assessment in the Patagonian Andes. Andean Geol 40: 141-171

Völker D, Kutterolf S, Wehrmann H (2011) Comparative mass balance of volcanic edifices at the southern volcanic zone of the Andes between 33^{o}S and 46^{o}S. J Volcanol Geotherm Res 205: 114-129

Watt SFL, Pyle DM, Mather TA (2011) Geology, petrology and geochemistry of the dome complex of Huequi volcano, southern Chile. Andean Geol 38(2): 335-348

Weller DJ, Miranda CG, Moreno PI, Villa-Martínez RP, Stern CR (2014) A large late-glacial Ho eruption fo the Hudson volcano, southern Chile. Bull Volcanol 76: 831-849

Weller DJ, Miranda CG, Moreno PI, Villa-Martínez RP, Stern CR (2015) Tephrochronology of the Andean Southern Volanic Zone, Chile. Bull Volcanol 76: 831-849

Wright HE Jr, (1967) A square-rod piston sampler for lake sediments. J Sed Petrol 37: 975–976

Chapter 4

Holocene Tephrochronology of the lower Río Cisnes valley, southern Chile

Submitted to *Andean Geology*, 2017

Coauthors: ME de Porras[2], A Maldonado[2,3], C Méndez[4], Charles R. Stern[1]

[1]Department of Geological Sciences, University of Colorado, Boulder, CO, USA

[2]Centro de Estudios Avanzados en Zonas Áridas (CEAZA), Universidad de La Serena, Casilla 599, La Serena, Chile

[3]Departamento de Biología Marina, Universidad Católica del Norte, Coquimbo, Chile

[4]Departamento de Antropología, Universidad de Chile, Santiago, Chile

4.1 Abstract

Sediment cores from lakes and bogs in the Río Cisnes valley contain tephra from explosive eruptions of volcanoes in the southern part of the Andean Southern Volcanic Zone (SSVZ). These tephra, which thicken and coarsen to the west, are attributed to eruptions from Melimoyu, Mentolat, Hudson, and potentially either Macá, Cay or one of the many minor eruptive centers (MEC) located both along the Liquiñe-Ofqui Fault Zone (LOFZ) and surrounding the major volcanoes. Correlation of the tephra between two new cores in the lower Río Cisnes valley, and amongst other cores previously described from the region, and source volcano identification for the tephra, has been done using lithostratigraphic data (tephra layer thickness and grain size), petrology (tephra glass color, vesicle morphology, and type and abundance of phenocryst phases), and by comparison of bulk tephra trace-element characteristics with previously published whole-rock and bulk tephra chemical analysis. Four tephras in these cores are attributed to eruptions of Mentolat, four to eruptions from Melimoyu, one possibly to Hudson, and six cannot be assigned to a specific source volcano. Some of these tephra correspond to pyroclastic tephra fall deposits previously observed in outcrop, including the MEL2 eruption of Melimoyu and the MEN1 eruption of Mentolat. However, others have not been previously observed and represent the products of newly identified small to medium sized eruptions from volcanoes of the SSVZ. These results provide new information concerning the frequency and magnitude of explosive eruption of SSVZ volcanoes and contribute to the evaluation of volcanic hazards in the region.

4.2 Introduction

Tephra produced by explosive eruptions can disperse over large distances in a very short period of time. Once characterized chemically, physically and morphologically, tephras provide

chronological time horizons, or isochrons, that can be correlated from one locality to the next (Lowel, 2011; Fontijn, 2014). Tephras deposited in lakes and bogs preserve exceptional records of volcanic activity, which provide insight into the frequency and magnitude of explosive eruptions, because of the relatively continuous record of sedimentation in these depositional environments.

Two recently retrieved cores from the lower Río Cisnes valley (Fig. 4.1), one from Laguna Las Mellizas (LLM) and one from Laguna Junco (LJU; Fig. 4.2), contain a record of tephra deposit derived from volcanoes of the southernmost part of the Andean Southern Volcanic Zone (SSVZ). Based on radiocarbon dating of organic matter from near the base of these cores (Table 4.1), where the lithology transitions upwards from finely-laminated glacial-lacustrine clays and fine-grained sands to predominately organic matter-rich material (Figs. 4.2 and 4.3), and from other lake cores taken from the region (de Porras et al. 2012, 2014; Stern et al. 2015), the present day lacustrine system was established at least by ~12,230 cal years BP and 16,816 cal years BP, the basal ages in the LLM and LJU cores respectively (Table 4.1), following retreat of the mountain glaciers from the region (Miranda et al. 2012). Since glacial retreat, numerous tephra were deposited within these two small lakes, each with limited drainage catchments. Here, we use the bulk trace-element chemistry, lithostratigraphic data, and petrologic features to characterize each tephra, to identify potential source volcanoes, and correlate these deposits with other tephra previously identified in both outcrops and in other lake cores from the region (Naranjo and Stern, 2004; Stern et al. 2015, 2016; Weller et al. 2014, 2015).

4.3 Geologic Background

The Andean Southern Volcanic Zone (SVZ; Fig. 4.1), a volcanic chain stretching from

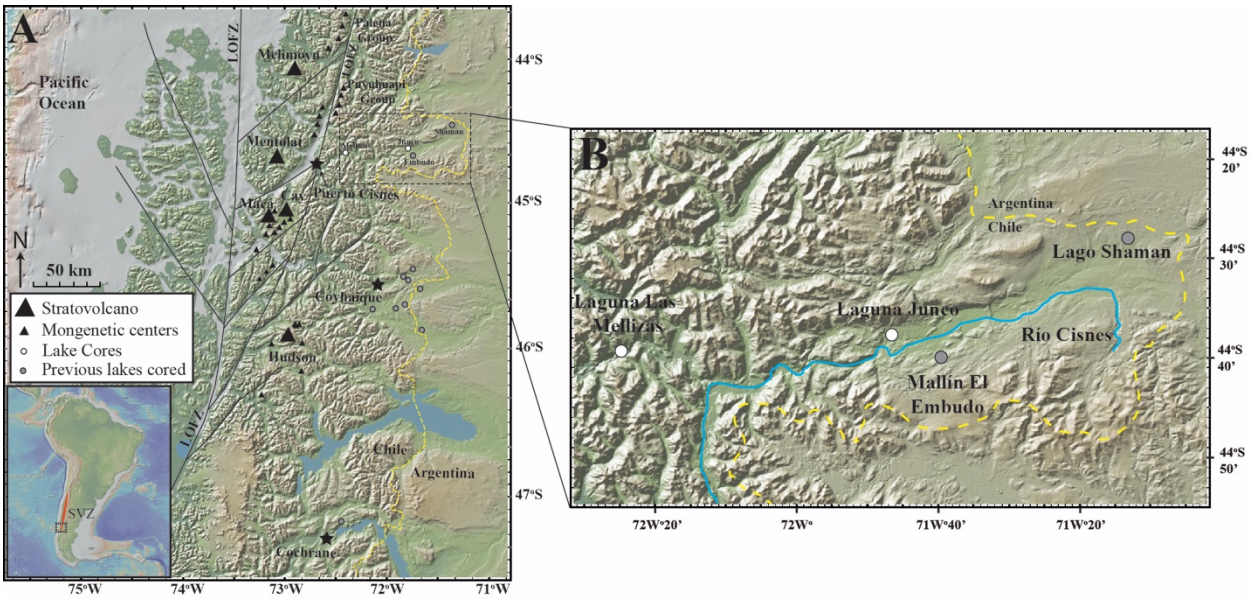

Figure 4.1. A. Map showing the location of Laguna Las Mellizas (LLM) and Laguna Junco (LJU) from which tephra bearing cores were obtained and the location of the major volcanic centers of the SSVZ and minor eruptive centers (MEC) located along the Liquiñe-Ofqui fault zone (LOFZ) and surrounding Hudson (Gutiérrez et al. 2005; Vargas et al. 2013), Macá, and Cay (López-Escobar et al. 1995a; D'Orazio et al. 2003). The dashed box shows the location of map B. **B.** Map of the Río Cisnes valley showing the location of LLM and LJU, and the location for other lakes from which tephra from SSVZ volcanoes have been previously reported (Lago Shaman and Mallín El Embudo; de Porras et al. 2012, 2014; Stern et al. 2015)

Table 4.1. Depth in centimeters (cm) of tephra and 14C age dates (cal yr BP) from Laguna Las Mellizas and Laguna Junco Cores

LLM 0115 B			LJU 0115 B		Shaman				
Tephra	**Section**	**Depth (cm)**	**Section**	**Depth (cm)**	**Tephra**	**Source**	**Outcrop Tephra**	**New Ages**	**Other Ages**
-	-	-	T2	78-79	-	-	-	1,438±24	-
C	T2	46-49	T3	53-55	a	Melimoyu	MEL2[1]	-	<1,680[1]
D	T2	94-96	-	-	c	Mentolat	-	-	2,490[2]
E	T3	0-3	-	-	-	Melimoyu	-	-	-
F	T3	49.5-50	-	-	-	M/C/M	-	-	-
G	T3	71-77	T5	71-72	d	Mentolat	MEN-1[3]	-	3,720[2]
-	-	-	T5	82-83	-	-	-	5,151±35	-
H	-	-	T5	83.5-85	-	M/C/MEC	-	-	-
I	T3	86-92	T5	92-93	e	Mentolat	-	-	3,880[2]
L	T4	15-15.5	-	-	-	Hudson	-	-	-
M	T4	33.5-34.5	T6	38-39	-	Melimoyu	-	-	-
N	T4	67-68	T7	10.5-11	i	Mentolat	MEN1[1]	-	7,690[1]
O	T4	71-72	T7	16-16.5	-	Melimoyu	-	-	-
P	T4	74-76	T7	19-20	-	M/C/M	-	-	-
Q	T5	19-21	-	-	-	M/C/M	-	-	-
R	T5	35-37	-	-	-	M/C/M	-	-	-
S	T5	51-52	-	-	-	M/C/M	-	-	-
-	T5	56-57	-	-	-	-	-	12,227±38	-
-	-	-	T9	7-8	-	-	-	16,816±68	-

[1]Naranjo and Stern, 2004; [2]Stern et al. 2015; [3]Mella et al. 2012

33°S to 46°S in Chile and Argentina, is generated by the subduction of the Nazca oceanic plate beneath the South American continent (Stern, 2004). The southern end of this zone is defined by the subduction of the Chile Rise, an active spreading center separating the Nazca and Antarctic Plates. This study is focused on the southernmost part of the SVZ, specifically the five large volcanic centers Melimoyu, Mentolat, Macá, Cay and Hudson, as well as numerous monogenetic minor eruptive centers (MEC) located along the Liquiñe-Ofqui Fault Zone (LOFZ) or surrounding Macá, Cay, and Hudson (Fig. 4.1; López -Escobar et al. 1993, 1995a; D'Orazio et al. 2003; Gutiérrez et al. 2005).

Melimoyu, the northernmost volcano, has a larger than average edifice compared to other SSVZ centers (~142 km^3; Völker et al. 2011), and is constructed of basalt, andesite and dacite lava flows (López-Escobar et al. 1993) with a small 1 km wide summit crater (Naranjo and Stern, 2004). Two Holocene tephras (MEL1 and MEL2) observed in outcrops directly east of the volcano (Naranjo and Stern, 2004) and in lake cores in the upper Río Cisnes valley southeast of the volcano (Stern et al. 2015), have been attributed to explosive eruptions from Melimoyu volcano. They have been dated at 2,765±70 and 1,680±80 cal years BP, respectively. Stern et al. (2015) also identified a number of other Holocene and one Late-Glacial tephra derived from Melimoyu in a core from Lago Shaman and an outcrop in the upper valley of the Río Cisnes (Fig. 4.1).

Mentolat volcano, which is a relatively small edifice (~36 km^3; Völker et al. 2011), with a snow and ice covered dome filling *a summit caldera (Naranjo and* Stern, 2004), is formed of basaltic andesite and andesitic lava flows (López-Escobar et al. 1993). Naranjo and Stern (2004) observed a light gray andesitic tephra (MEN1) in outcrops to the southeast of the volcanic center which has been dated at 7690±60 cal years BP (Stern et al. 2016), and Mella et al. (2012) described a younger tephra (MEN-1) from near Puerto Cisnes which have been dated as >2,614±87and

Figure 4.2. X-ray image of the ~5.5 1 meter sections of the core from LLM (0115 B). The tephra layers are white because they are denser lithologies than the organic matter-rich sediments they are preserved within. Sampled and unsampled (parentheses) tephras are labeled A through S. Tephras are color-coded to their source volcano: Red (Melimoyu), Orange (Hudson), Blue (Mentolat), Green (Macá, Cay, or one of the MEC), white no source identified. Also shown are the location and age of carbon-14 samples taken from the cores. Each core sections is approximately 1 m in length and 4 cm in diameter.

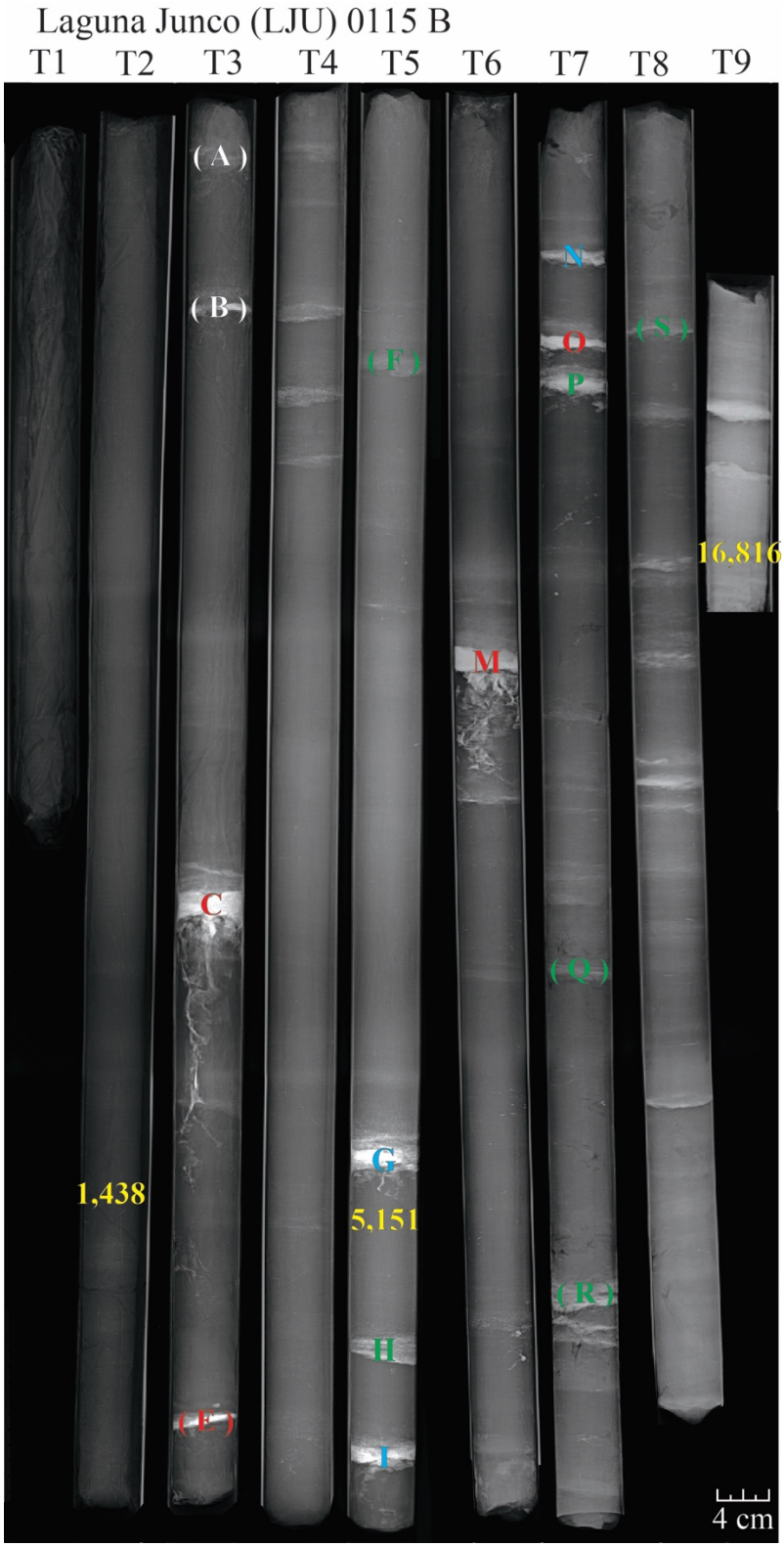

Figure 4.3. X-ray image of the LJU core (0115 B). Details as in Fig. 4.2.

4,336±56 cal years BP. Additionally, a Late-Glacial (MENo) and many other Holocene tephras derived from Mentolat, including MEN1, have been documented in lake cores from Lago Shaman and Mallín El Embudo (Fig. 4.1; Stern et al. 2015) in the upper Río Cisnes valley and from lake cores near Coyhaique (Weller et al. 2014, 2015) and Cochrane (Stern et al. 2016).

Macá and Cay are both relatively small centers located to the south of Mentolat (~39 and ~49 km^3 respectively; Völker et al. 2011). Macá is formed of basalt and basaltic andesite lavas (Futa and Stern, 1988; López -Escobar et al. 1993; D'Orazio et al. 2003). One Holocene tephra observed in outcrop, MAC1 (Naranjo and Stern, 2004), and in lake cores from near Coyhaique (tephra D3; Weller et al. 2015), has been attributed to a medium-sized eruption of this volcano dated at 1440±40 cal years BP. Cay volcano is a highly eroded edifice which is constructed of basalts, basaltic andesites, and dacites. No previous observations of Holocene deposits have been attributed to this volcano and the highly eroded nature of this center suggest a quiescent eruptive history throughout the Holocene.

Hudson volcano is a larger than average SSVZ volcano (~147 km^3; Völker et al. 2011), which has a ~10 km wide summit caldera and is formed by lavas with a wide range of compositions including basalt, basaltic andesites, andesites, and dacites (Futa and Stern, 1988; Gutierrez et al. 2005). Hudson had minor eruptions in 2011 AD and 1971 AD and a larger one in 1991 AD (Naranjo et al. 1993; Kratzmann et al. 2009; Wilson et al. 2011, 2012), as well as numerous pre-historic Holocene and Late-Glacial explosive eruptions producing tephra observed in lake cores and outcrops, including the 4000±50 cal years BP H2 eruption, the 8170±60 cal years BP H1 eruption, the 17,370±70 cal years BP Ho eruption, and multiple other small volume eruptions observed in lacustrine core and excavated trenches (Haberle and Lumley, 1998; Naranjo and Stern, 2004; Stern et al. 2015, 2016; Weller et al. 2014, 2015). The volume of explosively erupted

material, which exceeds ~45 km^3 (Weller et al. 2014), is not included in the estimate of the volume of its eruptive products made by Völker et al. (2011). Hudson is clearly one of the most active volcanoes in the SSVZ in terms of both the volume of material erupted and the frequency of eruptions (Weller et al. 2014, 2015).

There is significant along-strike petrochemical variability among the SSVZ centers. Based on whole rock chemical analysis, López -Escobar et al. (1993, 1995a) identified petrochemically distinct basalts and basaltic andesites which they termed Type-1 and Type-2 basalts. Type-1, depleted, or Low Abundance (LA) basalts, have medium to low-K_2O with relatively low concentrations of large-ion-lithophile elements (Fig. 4.4; LILE; Rb, CS, Ba, Y, Th and U), high-field-strength elements (HFSE; Ti, Zr, Hf), and rare-earth elements (REE) compared to the Type-2, enriched, or High Abundance (HA) basalts. HA basalts are characterized by high-K_2O with distinctively higher concentrations of HFSE, LILE, and REE (Fig. 4.4; Hickey et al. 1986; Hickey –Vargas et al. 1989, 2003; López -Escobar et al. 1993, 1995a, 1995b).

Among the SVZ volcanoes, Hudson, Melimoyu, and the Puyuhuapi group MEC are Type-2 or HA centers, while Macá, Cay, Mentolat and the Palena group MEC are Type-1 or LA volcanoes (López -Escobar et al. 1993, 1995a; D'Orazio et al. 2003; Gutiérrez et al. 2005; Carel et al. 2011; Watt et al. 2011, Stern et al. 2015, 2016; Weller et al. 2015). However, a further subdivision within the Type-1 or Low Abundance group has also been made to distinguish eruptive products from Mentolat, which produces lava and tephra with distinctively lower concentrations over a wide range of SiO_2 contents of incompatible LILE, HFSE, and REE than other Type-1 LA centers (López -Escobar et al. 1993; Stern et al. 2015, Weller et al. 2015). These Low Abundance Felsic (Weller et al. 2015) or Very Low Abundance (VLA; Stern et al. 2015) tephra can be distinguished from the other LA centers not only by their distinctively lower concentrations of

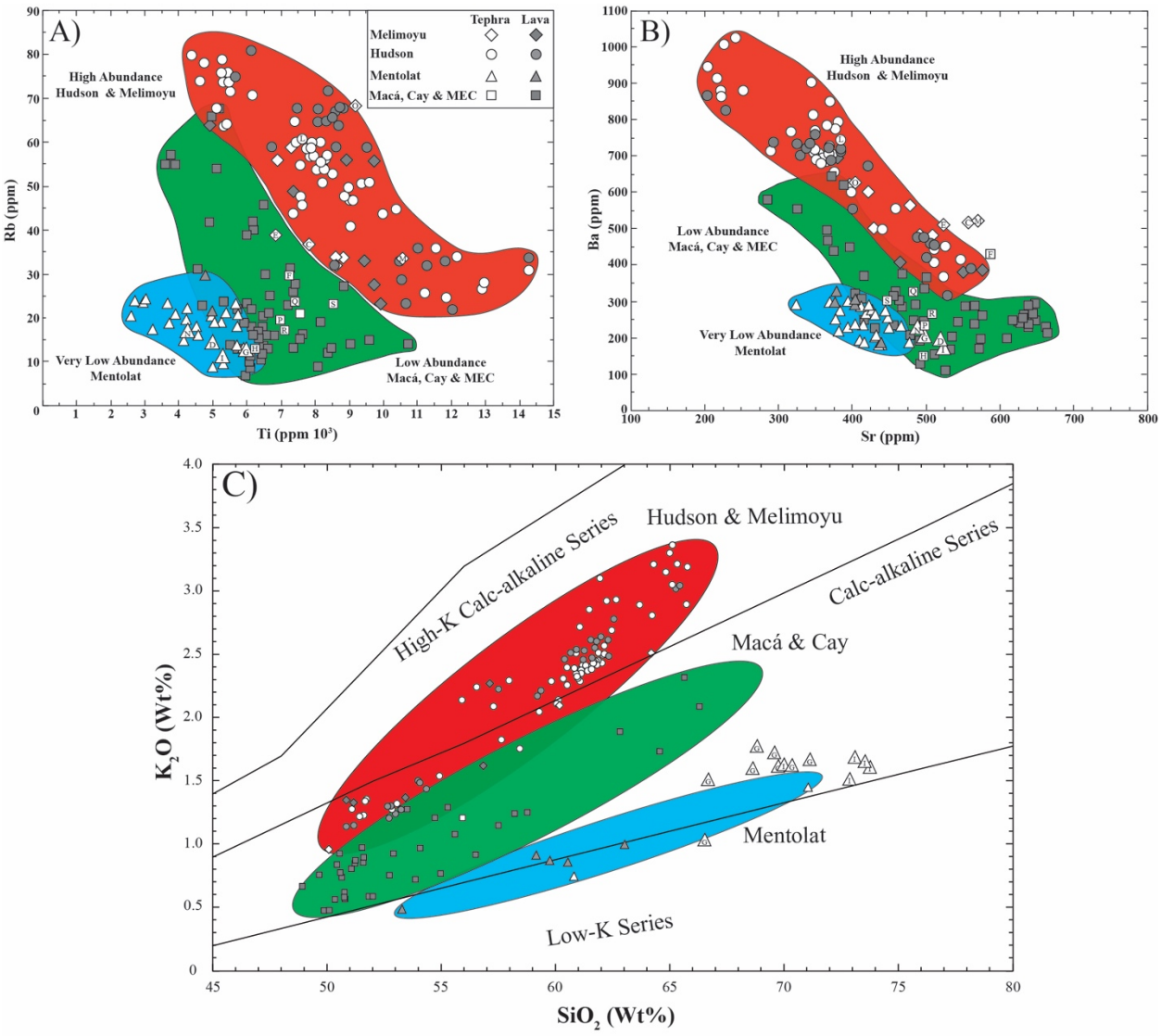

Figure 4.4. A. Ti versus Rb and B. Sr versus Ba in parts per million (ppm) for published data of bulk tephras (white) and lavas (black) from Melimoyu, Mentolat, Macá, Cay, Hudson, and MECs (Futa and Stern, 1988; López-Escobar et al. 1993; Naranjo and Stern, 1998, 2004; D'Orazio et al. 2003; Gutiérrez et al. 2005, Kratzmann et al. 2009, 2010), and the bulk tephras from this study (white symbols with corresponding tephra nomenclature) **C**. SiO_2 versus K_2O for samples of both lava and tephra glasses from Melimoyu, Mentolat, Macá, Cay, and Hudson Volcanoes and many of the minor eruptive centers in the region (Futa and Stern, 1988; López-Escobar et al. 1993; Naranjo and Stern, 1998, 2004; D'Orazio et al. 2003; Gutiérrez et al. 2005, Kratzmann et al. 2009, 2010) illustrating the distinctions of the eruptive products from these centers into the petrochemical classifications of High Abundance (HA), Low abundance (LA), and Very Low Abundance (VLA; Hickey et al. 1986, Hickey-Vargas et al. 1989; López-Escobar et al. 1993, 1995a, 1995b; Sellés et al. 2004; Stern et al. 2015; Watt et al. 2011)..

K_2O, LILE, HFSE, and REE (Fig. 4.4), but also by the abundance of hydrous phases such as amphibole (Fig. 4.5) and biotite which are uncommon or absent in the eruptive products from the other Type-1 LA centers of the SSVZ (Watt et at., 2011; Weller et al. 2015, Stern et al. 2016). Mentolat lavas (López-Escobar et al. 1993) and tephras (Naranjo and Stern, 2004) are similar to other VLA-type centers further to the north such as Huequi (Watt et al. 2011), Calbuco (López-Escobar et al. 1995b; Hickey –Vargas et al. 1995) and Nevado de Longaví (Sellés et al. 2004; Rodríguez et al. 2007), which also produce volcanic products with VLA-type chemistry and have amphibole as an abundant phenocryst phase.

Source volcano identification from previous tephrochonologic studies done in the SSVZ were based on the comparison with major and trace element analysis of published whole rock, glass and bulk tephra chemical analysis (Haberle and Lumley, 1998; Naranjo and Stern, 1998, 2004; Carel et al. 2011; Stern et al. 2015, 2016; Weller et al. 2014, 2015). These studies demonstrated that regionally widespread tephra are derived from explosive eruptions of Melimoyu, Mentolat, Macá, and Hudson, and that bulk tephra trace element analysis preserve the high- (HA), low- (LA), and very low- (VLA) abundance characteristics necessary for correlation among and source volcano identification of tephras from these centers. The same methodology is used here to chemically distinguish between the different tephra deposits, identify potential source volcanoes, and correlate the tephra from the lower Río Cisnes valley with other tephra previously identified in outcrop and in lake cores from the region (Naranjo and Stern, 1998, 2004; Stern et al. 2015, 2016; Weller et al. 2014, 2015).

4.4 Methods

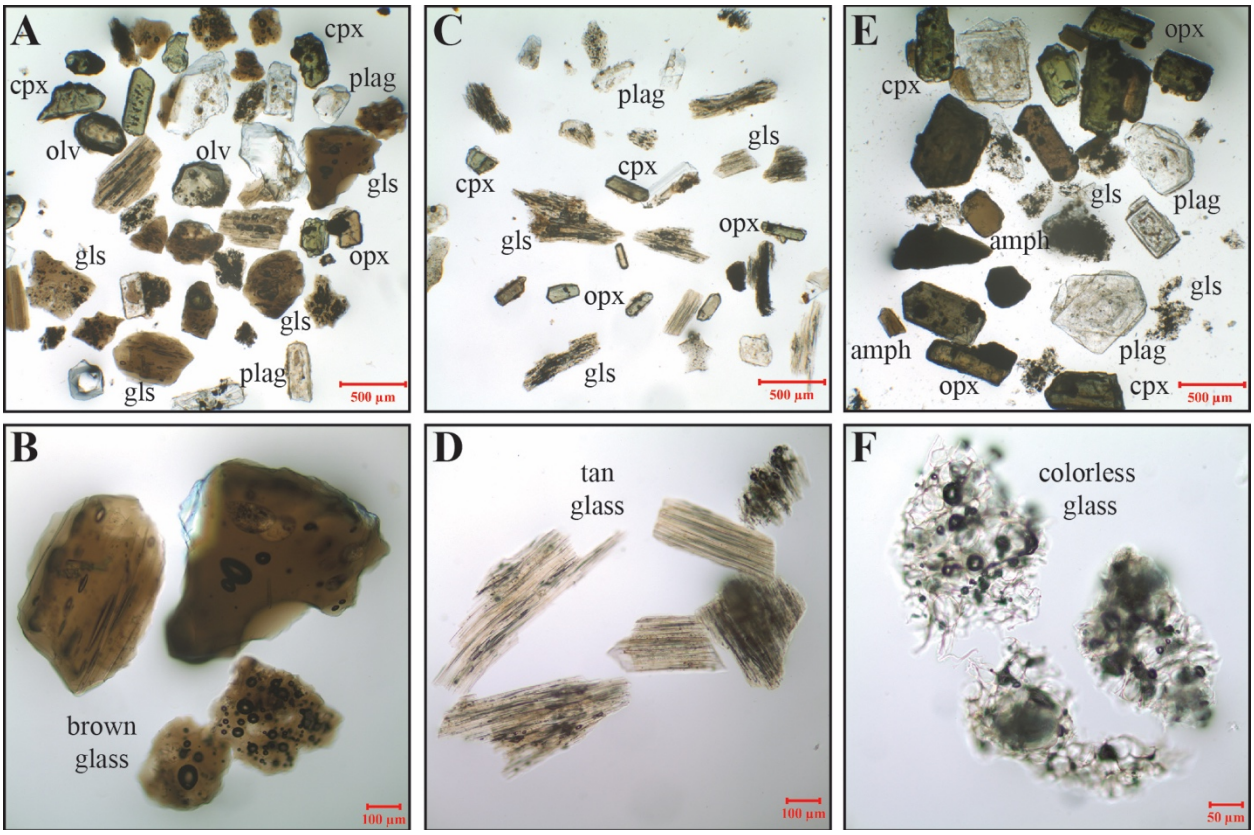

Figure 4.5. Photomicrographs, of samples from the LLM core, showing representative features of the petrochemically distinct types of tephra from the different source volcanoes. **A** and **B;** Melimoyu derived MEL2 tephra containing brown to dark brown glass with vesicles that are generally circular but also containing a smaller proportion of glass with elongated vesicles. Abundant plagioclase occurs with less abundant clino- and orthopyroxene and olivine. **C** and **D;** Hudson-derived tephra containing light brown to tan glass with elongated cylindrical vesicles and phenocrysts of orthopyroxene, clinopyroxene, plagioclase but lacking amphibole and olivine. **E** and **F;** Mentolat derive (tephra I) containing colorless glass with circular vesicles, abundant phenocryst of plagioclase, clinopyroxene, orthopyroxene, and amphibole

Cores from the lakes were taken using a modified Livingston piston corer until the sediments reflected a transition from predominately organic rich lacustrine sediments to finely laminated glacial-lacustrine clays and sands. Transmitted x-rays images were taken of the cores to help in identification of the tephra deposits (Figs. 4.2 and 4.3). The white layers, or denser lithologies, are typically tephra deposits except in the deeper portions of the cores which includes the fine-grained glacial-lacustrine clays and sands. The dark material is the less-dense organic rich lacustrine sediments the tephra are preserved within.

The tephra deposits were removed from the core with a knife, and washed in water to remove the clay fraction and organic matter. A portion of the deposit was examined using a petrographic microscope to describe features such as tephra glass color, vesicles abundance and morphology, as well as to determine the abundance and identity of mineral phases. Another bulk portion of the deposit was powdered in a moly-tungsten shatter box, dissolved in a mixture of HF and HNO_3 for trace element analysis using an ELAN D CR ICP-MS. At the concentration level within these tephra, trace-element compositions are accurate within ±10% based on repeat analyses of internal and external standards with known compositions (Saadat and Stern, 2011).

Strontium isotopic ratios were measured on a Finnigan-Mat 261 four-collector static Thermal Ionization Mass Spectrometer. Powdered samples were dissolved in HF and $HClO_3$. Based on replicate analysis of the SRM-987 standard yielded a mean $^{87}Sr/^{86}Sr$ of 0.71025±2 (2σ) and the $^{87}Sr/^{86}Sr$ were corrected to SRM-987=0.710299±8. Errors of the 2σ refer to the last two digits of the $^{87}Sr/^{86}Sr$ ratio. Further details of the analytical procedure are outlined in Farmer et al. (1991).

Major element compositions of the hand-picked white pumice separates were determined using a Jeol JXA-733 Electron Microprobe that was operating at 15 KV accelerating potential with

a 5 nA probe current. A defocused beam was used to obtain the analysis on the glasses.

New radiocarbon age determinations as well as age of previously identify explosive eruptions observed in outcrop and in lake cores from the region, control the chronology of the cores (Table 4.1; Naranjo and Stern, 2004; de Porras et al. 2012, 2014). AMS radiocarbon ages were determined on organic matter and converted to calendar years before present (cal yrs BP) by applying the ShCal113 curve (Hogg et al. 2013) to the CALIB 7.0.4 program (Stuiver et al. 1998, 2013).

4.5 Results

4.5.1 General

A summary of the stratigraphic information for each tephra layer is presented in Table 4.1, including a potential source volcano. The tephra deposits are named from A to S in chronologic order (Figs. 4.2 and 4.3), some of which were not collected but can be correlated to tephra in the other lake cores such as Lago Shaman based on the stratigraphic relations between the cores. Table 4.2 presents a description of each of the tephra sampled including the color and vesicle morphology of the most abundant glass type, abundance of phenocryst phases, maximum grain size, and a classification as either HA, LA or VLA based on the petrochemistry, petrography and trace-element contents of each tephra, which are presented in Tables 4.3 and 4.4. Table 4.5 presents tephra glass major-elements compositions for the two thickest and coarsest tephra observed in the LLM core (tephra G and I) and Table 4.6 presents the strontium isotopic ratios for the tephra I and other proximal, medial, and distal Mentolat derived tephras (Fig. 4.6).

Similar to other observations of tephra deposits found in outcrop and in cores from volcanoes of the SSVZ, three petrochemically and petrographically distinct types of deposits were observed in the cores, including High Abundance (HA), Low Abundance (LA) and Very Low

Table 4.2. Petrographic features of the tephra

Laguna Las Mellizas (LLM)

	Phenocryst						Glass				Max Grain Size
Tephra	**Oliv**	**Plag**	**Cpx**	**Opx**	**Amph**	**Bio**	**Color**	**Vesicles**	**Morph.**	**Microlites**	**(mm)**
C	XX	XXX	XX	X	-	-	Br	XX	Circular	XX	2.2
D	-	XXX	XX	XX	XX	-	C	XX	Circular	-	4.8
E	X	XXX	XX	X	X	-	DBr	XXX	Circular	X	2.9
F	X	XXX	X	X	-		PBr	XX	Circular	XX	0.36
G	X	XXX	XX	XX	XX	-	C	XX	Circular	-	7
I	X	XXX	XX	XX	XX	-	C	XX	Circular	-	7.5
L	-	XX	XX	XX	-	-	T	XXX	Elongate	-	1.2
M	-	XX	X	X	X	X	DBr	XXX	Elongate	XXX	0.45
N	X	XXX	XX	XX	XX	-	C	XX	Circular	-	1.7
O	-	XX	XX	X	-	-	DBr	-	-	XX	1
P	XX	XXX	XXX	X	X	-	DBr	-	-	X	5
Q	X	XXX	XXX	X	X	-	Blk	-	-	-	4.3
R	-	XXX	XX	X	-	X	Blk	-	-	X	0.9
S	X	XXX	XX	X	X	-	Or	XX	Circular	XX	0.4

Laguna Junco (LJU)

	Phenocryst						Glass				Max Grain Size
Tephra	**Oliv**	**Plag**	**Cpx**	**Opx**	**Amph**	**Bio**	**Color**	**Vesicles**	**Morph.**	**Microlites**	**(mm)**
C	XX	XXX	XX	X	-	-	Br	XX	Circular	XX	1.2
G	X	XXX	XX	XX	XX	-	C	XX	Circular	-	3.2
H	X	XXX	X	X	X	-	DBr	XXX	Elongate	XXX	2
I	X	XXX	XX	XX	XX	-	C	XX	Circular	-	5
M	-	XX	X	X	X	X	DBr	XXX	Elongate	XXX	0.25
N	X	XXX	XX	XX	XX	-	C	XX	Circular	-	0.7
O	-	XX	XX	X	-	-	DBr	-	-	XX	1
P	XX	XXX	XXX	X	X	-	DBr	-	-	X	3

Color: Pale (P), Light (L), Dark (D), Tan (T) Brown (Br), Orange (Or), Colorless (C), Black (Blk)
Abundance: XXX Abundant, XX Moderate, X Rare. - None

Table 4.3a. Trace element contents in part-per-million (ppm) of tephra from Laguna Las Mellizas core

Lake	LLM	LLM	LLM	LLM	LLM	LLM	LLM
Section	T2	T2	T3	T3	T3	T3	T4
Depth	46-49	94-96	0-3	49.5-50	71-77	86-92	15-15.5
Source	Melimoyu	Mentolat	Melimoyu	M/C/M	Mentolat	Mentolat	Hudson
Tephra Name	C, MEL2	D	E	F	G	I	L
Chemical Type	HA	VLA	HA	LA	VLA	VLA	HA
Lab #	**DW15-22**	**DW15-23**	**DW15-24**	**DW15-25**	**DW15-26**	**DW15-27**	**DW15-28**
Ti	7237	4962	6816	7200	5734	5057	7568
V	239	242	249	310	297	249	163
Cr	51	DL	35	94	17	DL	DL
Mn	1227	1504	1267	1141	1772	1489	1143
Co	64	34	55	53	47	33	58
Ni	60	45	53	65	46	42	36
Cu	72	43	63	104	32	19	136
Zn	136	126	135	120	121	121	146
Rb	38	13	38	29	12	9	60
Sr	560	529	531	592	487	535	392
Y	30	21	30	22	18	17	40
Zr	245	93	246	140	94	67	383
Nb	13	3	11	6	3	2	18
Cs	0.88	0.82	0.92	0.81	0.49	0.46	1.47
Ba	527	185	505	421	179	146	733
La	29.05	7.96	28.33	18.69	9.54	6.94	41.27
Ce	67.5	20	63.8	43	22.2	16.9	92
Pr	7.91	2.74	7.7	5.24	2.84	2.22	11.05
Nd	32.4	13.1	32.5	22.9	13.4	11.3	45
Sm	7.63	3.47	7.3	5.92	3.28	2.94	10.01
Eu	2.71	1.34	2.59	2.13	1.26	1.27	3.38
Gd	10.37	4.87	10.17	7.5	4.66	3.81	13.7
Tb	1.12	0.59	1.07	0.81	0.5	0.46	1.44
Dy	5.92	3.56	5.66	4.23	3.06	2.88	7.27
Ho	1.04	0.68	1.01	0.74	0.54	0.52	1.35
Er	3.5	2.26	3.47	2.63	1.95	1.84	4.79
Tm	0.38	0.2	0.37	0.18	0.15	0.14	0.51
Yb	3.18	2.05	2.9	2.01	1.72	1.58	4.13
Lu	0.38	0.22	0.36	0.22	0.18	0.15	0.54
Hf	5.2	2.3	5.2	3.2	2.2	1.6	8.4
Pb	7.7	4.6	7.9	5.2	3.8	3.2	12.8
Th	2.3	0.5	2.2	1.5	0.6	0.4	3.6
U	1.1	0.4	1.1	0.8	0.4	0.3	1.7

DL: Detection Limit, M/C/M: Macá, Cay, or one of the MEC

Table 4.3b. Trace element contents in part-per-million (ppm) of tephra from Laguna Las Mellizas core

Lake	LLM	LLM	LLM	LLM	LLM	LLM	LLM
Section	T4	T4	T4	T4	T5	T5	T5
Depth	33.5-34.5	67-68	71-72	74-76	19-21	35-37	51-52
Source	Melimoyu	Mentolat	Melimoyu	M/C/M	M/C/M	M/C/M	M/C/M
Tephra Name	M	N, MEN1	O	P	Q	R	S
Chemical Type	HA	VLA	HA	LA	LA	LA	LA
Lab #	**DW15-29**	**DW15-30**	**DW15-31**	**DW15-32**	**DW15-33**	**DW15-34**	**DW15-35**
Ti	10345	4333	9072	6991	7354	7032	8489
V	343	206	207	364	214	274	276
Cr	19	DL	DL	30	DL	19	DL
Mn	1346	1498	1288	1263	1228	1113	959
Co	55	39	37	51	26	39	29
Ni	44	36	33	46	36	38	34
Cu	181	82	113	87	55	180	326
Zn	159	123	165	139	141	149	160
Rb	33	16	68	18	23	16	23
Sr	570	497	412	514	490	513	454
Y	29	18	43	20	27	21	25
Zr	212	114	329	81	150	86	126
Nb	11	8	21	2	4	3	4
Cs	0.84	1.15	2.93	1.03	0.89	0.97	1.19
Ba	508	211	618	222	320	257	295
La	29.1	8.89	41.25	8.97	14.19	9.85	13.66
Ce	67.8	22.1	91.8	22.3	35	23.6	33.3
Pr	8.26	2.96	10.95	2.91	4.61	3.11	4.2
Nd	36.1	13.6	46.3	14	20.7	14.7	19
Sm	8.31	3.43	10.62	3.83	5.51	4	5.05
Eu	2.72	1.39	3.19	1.41	2.01	1.57	1.9
Gd	11.18	4.63	14.38	5.13	7.65	5.41	6.7
Tb	1.21	0.54	1.58	0.61	0.9	0.64	0.85
Dy	5.8	3.27	8.44	3.55	5.21	3.83	4.68
Ho	1.02	0.61	1.52	0.73	0.98	0.75	0.93
Er	3.32	2.13	5.04	2.33	3.15	2.33	2.91
Tm	0.34	0.2	0.57	0.21	0.35	0.2	0.27
Yb	2.79	1.99	4.44	1.98	2.89	2.16	2.66
Lu	0.33	0.24	0.6	0.18	0.32	0.23	0.32
Hf	4.7	5.3	7.5	2.2	3.8	2.2	3.4
Pb	8.2	10.3	14.1	5.9	7.8	7.3	11.7
Th	2.1	0.5	5.3	0.7	1.4	0.8	1.4
U	1	0.4	2.7	0.5	0.8	0.6	1

DL: Detection Limit, M/C/M: Macá, Cay, or one of the MEC

Table 4.4a. Trace element contents in part-per-million (ppm) of tephra from Laguna Junco core

Lake	LLJ	LLJ	LLJ	LLJ
Section	T3	T5	T5	T5
Depth	53-55	71-72	83.5-85	92-93
Source	Melimoyu	Mentolat	M/C/M	Mentolat
Tephra Name	C, MEL2	G	H	I
Chemical Type	HA	VLA	LA	VLA
Lab #	DW15-36	DW15-37	DW15-38	DW15-39
Ti	8378	6321	5945	5468
V	264	281	325	213
Cr	41	17	59	DL
Mn	1181	1235	1151	1426
Co	32	33	74	29
Ni	47	41	55	34
Cu	84	61	93	50
Zn	137	118	117	108
Rb	34	11	12	11
Sr	574	519	504	525
Y	29	21	18	20
Zr	230	91	63	76
Nb	10	3	3	2
Cs	0.76	0.49	0.64	0.52
Ba	495	214	144	178
La	29.88	12.88	6.65	11.68
Ce	66.5	24.2	15.4	20.9
Pr	8.39	3.73	2.3	3.5
Nd	35.5	16.4	11	15.6
Sm	7.78	4.15	3.12	3.86
Eu	2.63	1.49	1.1	1.48
Gd	10.51	5.42	4.28	5.29
Tb	1.12	0.62	0.5	0.6
Dy	5.62	3.76	3.07	3.78
Ho	1.01	0.7	0.61	0.7
Er	3.57	2.41	1.88	2.16
Tm	0.36	0.2	0.16	0.21
Yb	2.94	2.01	1.72	2.14
Lu	0.35	0.23	0.18	0.22
Hf	5.1	2.3	1.6	2.1
Pb	8	4.3	4.4	4.2
Th	2.3	0.6	0.4	0.4
U	1.1	0.5	0.9	0.7

DL: Detection Limit, M/C/M: Macá, Cay, or one of the MEC

Table 4.4b. Trace element contents in part-per-million (ppm) of tephra from Laguna Junco core

Lake	LLJ	LLJ	LLJ	LLJ
Section	T6	T7	T7	T7
Depth	38-39	10.5-11	16-16.5	19-20
Source	Melimoyu	Mentolat	Melimoyu	M/C/M
Tephra Name	M	N, MEN1	O	P
Chemical Type	HA	VLA	HA	LA
Lab #	DW15-40	DW15-41	DW15-42	DW15-43
Ti	10650	4137	9218	6999
V	342	153	219	350
Cr	20	DL	DL	29
Mn	1242	1123	1236	1197
Co	40	64	33	43
Ni	39	33	30	42
Cu	167	83	136	108
Zn	156	97	154	129
Rb	33	16	67	19
Sr	579	497	411	493
Y	32	21	43	21
Zr	221	120	315	88
Nb	16	5	20	3
Cs	0.88	1.12	2.78	1.01
Ba	515	229	619	226
La	31.67	13.45	41.83	10.99
Ce	72.1	27.9	90.2	23.9
Pr	9.05	4.42	11.18	3.4
Nd	38.6	18.7	47.3	16.1
Sm	8.71	4.44	10.96	4.35
Eu	3	1.58	3.24	1.52
Gd	11.93	5.65	14.69	5.64
Tb	1.32	0.72	1.69	0.65
Dy	6.46	4.03	8.22	3.92
Ho	1.17	0.73	1.55	0.73
Er	3.74	2.41	5.11	2.43
Tm	0.38	0.22	0.55	0.24
Yb	3.14	2.2	4.44	2.08
Lu	0.39	0.26	0.58	0.21
Hf	7.9	3.2	7.4	2.3
Pb	8.9	7	14.7	6.8
Th	2.3	0.6	5.2	0.8
U	1.3	1.1	2.6	0.9

DL: Detection Limit, M/C/M: Macá, Cay, or one of the MEC

Abundance (VLA) chemical types (Fig. 4.4; Weller et al. 2015; Stern et al. 2015, 2016; Kratzmann et al. 2009). Tephras that are HA chemical types could be derived from either Melimoyu, Hudson or the Puyuhuapi group. Previously described tephras observed near Melimoyu and Hudson attest to the active nature of these centers throughout the Holocene and during late-glacial time (Naranjo and Stern 1998, 2004; Stern et al. 2015, 2016; Weller et al. 2014, 2015). However, no tephra in this region have been previously attributed to eruptions from the Puyuhuapi group, which have abundant phenocrysts of olivine and lack orthopyroxene, amphibole, and biotite (López-Escobar et al. 1995a). Since there are no HA type tephra from the cores in the lower Río Cisnes valley with these characteristics, we believe that none of these tephra are derived from the Puyuhuapi group.

All of the eruptions with HA chemistry are therefore thought to be derived from either Melimoyu or Hudson volcanoes. Melimoyu deposits such as the MEL2 tephra, which are heterogeneous mixtures of more primitive mafic and evolved felsic components (Naranjo and Stern, 2004), are characterized by tephra glass which is brown in color, generally containing minor amounts of rounded vesicles and variable plagioclase microlites, but also with infrequent brown glass with elongated vesicles that lack mineral microlites (Fig. 4.5; Stern et al. 2015). In contrast, glass from previously described Hudson eruptions (Ho, H1, H2; Weller et al. 2015, Stern et al. 2015, 2016), which are also heterogeneous mixtures, contains abundant tan to brown glass with a high proportion of elongated vesicles and lacking plagioclase microlites (Fig. 4.5; Kratzmann et al. 2009, 2010; Weller et al. 2014, 2015). Commonly observed phenocryst phases from both of these centers include plagioclase, clinopyroxene, orthopyroxene and less common olivine, and the felsic phase of tephra MEL1 and MEL2 from Melimoyu also both contain amphibole. The lake cores from the lower Río Cisnes valley contain several amphibole- and biotite-bearing HA

petrochemical type deposits that are similar petrographically to the MEL2 tephra and contain dark brown glass with a high abundance of microlites and minor rounded vesicles. These tephras are attributed to eruptions of Melimoyu volcano since amphibole has never been reported for Hudson (López-Escobar et al. 1993; Gutiérrez et al. 2005; Kratzmann et al. 2009, 2010; Weller et al. 2014, 2015). Additionally, tephra produced from Melimoyu, which is located only ~50 km to the northwest of LLM, would be expected to be thicker and coarser than tephras from Hudson, which is ~150 km to southwest of this lake (Fig. 4.1). One thin, fine-grained tephra (tephra L in LLM) with abundant tan volcanic glass with elongated vesicles, phenocryst of plagioclase, clino- and orthopyroxene, but lacking hydrous phases, is tentatively attributed to an eruption of Hudson volcano (Figs. 4.5 and 4.7; Table 4.1).

All lavas (López-Escobar et al. 1993) and tephra (Naranjo and Stern, 2004; Stern et al. 2015, 2016; Weller et al. 2015) from Mentolat volcano have VLA-type chemistry (Fig. 4.4) and are characterized by phenocryst assemblages rich in plagioclase, clino- and orthopyroxene, amphibole, and tephra glass which is generally colorless with circular vesicles and no mineral microlites (Fig. 4.5). All of the tephra with VLA chemistry (Table 4.3 and 4.4), containing colorless volcanic glass with circular vesicles (Fig. 4.5) and abundant phenocryst phases such at plagioclase, two pyroxenes, and amphibole, which are similar in appearance and chemistry to the MEN1 eruption of Mentolat (Naranjo and Stern, 2004; Stern et al. 2016), are attributed to explosive eruptions of Mentolat volcano.

All previous published analysis of lavas and tephra from Macá, Cay, Palena group and many of the MEC located along the LOFZ are Low Abundance (LA) chemical types. The LA-type tephra are diverse in their glass color and morphology, but in general they consist of dark brown glass containing few circular vesicles and abundant mineral microlites which is similar in

color and morphology to the MAC1/D3 tephra of Macá (Weller et al. 2015). Common phenocryst include plagioclase, clinopyroxene, with minor olivine, orthopyroxene and no or only a very small amount of amphibole or biotite. These tephra deposits, with LA-character, brown glass but lacking colorless glass and abundant amphibole, are not assigned a specific source volcano, but may be derived from Macá, Cay, Palena group or one of the many other MEC within the region. In some cases, the petrochemical fields defined by eruptive products from Mentolat and the other LA-type centers overlap (Fig. 4.4). However, none of the LA-type deposits contain colorless microlite-free volcanic glass with circular vesicles nor are they rich in amphibole phenocrysts, and therefore can be distinguished from the Mentolat derived VLA-type amphibole- and colorless felsic glass-bearing deposits.

Correlation of the deposits in the lower Río Cisnes Valley with the tephra from Lago Shaman (Table 4.1; Fig. 4.7) was done by the comparison of the petrochemistry and the stratigraphic relations between the cores.

4.5.2 Tephras

Tephra A and B

Tephra A and B are the youngest samples observed in both LLM and LJU but were not collected from either core. They are thin (< 1 cm) deposits and occur in similar stratigraphic relation in both cores. These deposits, which do not occur in Lago Shaman (Fig. 4.7), are both >1,440 cal yrs BP as indicated by a new age determination from LJU.

Tephra C

Tephra C occurs as a 4 cm thick layer with a maximum grain size of 2.2 mm in the LLM core and as a 2 cm thick deposit with a maximum grain size of 1.2 mm in the LJU core. This tephra consists of brown volcanic glass with moderate to few circular vesicles and mineral

microlites (Fig. 4.5). A less abundant type of brown glass lacking mineral microlites but with abundant elongated vesicles also occurs in this deposit (Fig. 4.5). Frequently observed phenocrysts include clinopyroxene, orthopyroxene, olivine, plagioclase, but not amphibole. Tephra C is a HA petrochemical type (Fig. 4.4; Tables 3 and 4) and is similar in thickness, stratigraphic position, age, petrology, and petrochemistry to tephra 'a' from Lago Shaman (Fig. 4.7; Stern et al. 2015) which was correlated with the MEL2 eruption dated at 1,680±100 cal yrs BP in outcrop (Table 4.1 and Fig. 4.7; Naranjo and Stern, 2004) and <1,827±40 and >1,743±40 cal years BP in Lago Shaman and Mallín El Embudo respectively (Stern et al. 2015).

Tephra D

Tephra D is a 2 cm thick deposit with a maximum grain size of 4.8 mm observed only in LLM core. Tephra D is a VLA petrochemical type deposit (Fig. 4.4; Table 4.3) characterized by colorless volcanic glass with circular vesicles, and no mineral microlites. Phenocryst phases include abundant plagioclase with concentric chemical zonation, clinopyroxene, orthopyroxene, and amphibole (Table 4.2). Tephra D is similar petrochemically to tephra derived from Mentolat observed in outcrop and in lake cores near Coyhaique (Weller et al. 2015), Cochrane (Stern et al. 2016) and in Lago Shaman (Stern et al. 2015). Thus, tephra D is considered to be derived from a small to medium explosive eruption of Mentolat volcano. Based on the petrochemistry, petrology, and stratigraphic position, we correlate this deposit with tephra 'c' from Lago Shaman, which is also thought to be derived from Mentolat (Table 4.1; Fig. 4.7; de Porras et al. 2012; Stern et al. 2015).

Tephra E

Tephra E is a 3 cm thick, HA chemical type deposit with maximum grain size of 2.9 mm sitting directly below tephra D in LLM (Fig. 2; Table 4.1). Tephra E is characterized by dark

brown volcanic glass with round vesicles with minor mineral microlites and abundant phenocryst of plagioclase, frequent clinopyroxene and orthopyroxene, minor olivine and lacking amphibole. Based on these characteristics, we interpret tephra E as having been derived from Melimoyu volcano. It is not observed in Lago Shaman.

Tephra F

Tephra F is a thin <1 cm deposit with maximum grain size of 0.36 mm which was only sampled from LLM (Table 4.1) but can be correlated with a tephra in LJU based on the stratigraphy of the cores (Fig. 4.7). Tephra F is characterized by pale brown glass with minor circular vesicles and few plagioclase microlites. Phenocryst include abundant plagioclase with minor olivine, clino- and orthopyroxene, but no amphibole. Tephra F has LA-type chemistry and it could be derived from either Macá, Cay or one of the MECs (Fig. 4.4). No tephra with LA-type chemistry in the same stratigraphic position are observed in the Lago Shaman core in the upper Río Cisnes valley.

Tephra G

Tephra G is 6 cm thick deposit in LLM with a maximum grain size of 7 mm, but is only 1 cm in LJU with a maximum grain size of 3.2 mm. Tephra G is a VLA-type deposit with colorless glass and minor rounded vesicles and no mineral microlites (Fig. 4.4; Table 4.2). Phenocryst phases include abundant plagioclase, two pyroxenes, and amphibole. Thus, this tephra is likely produced by an explosive eruption of Mentolat volcano which is dated as <5,151 cal years BP in LJU. We correlate this tephra with tephra 'd' from Lago Shaman (Fig. 4.7), and possibly with the 4,336±56 cal years BP Mentolat tephra described by Mella et al. (2012) from near Puerto Cisnes, which they called MEN-1, but which is not the same tephra as the older MEN1 tephra described by Naranjo and Stern (2004) and Stern et al. (2016) further to the south. The glass in the hand-

picked pumice separates range from 65-70 weight percent SiO_2 and straddle the division between the medium- and low-K_2O fields similar to published glass analysis of other tephras from Mentolat (Fig. 4.4 and Table 4.5; Stern et al. 2016).

Tephra H

Tephra H is 1.5 cm thick deposit collected from LJU, but present also in LLM core, and is correlated based on the stratigraphic relationship of the cores. Tephra H consists of dark brown microlite-free glass with elongated vesicles, abundant plagioclase, minor olivine, clino- and orthopyroxene, and amphibole (Table 4.2). Tephra H has LA-type chemistry and is likely derived from Macá, Cay or one of the MECs (Fig. 4.4).

Tephra I

Tephra I is a 6 cm thick tephra layer in LLM and 1 cm in LJU with maximum grain size of 7.5 mm and 5 mm, respectively. Tephra I had abundant phenocryst of plagioclase, clinopyroxene, orthopyroxene, amphibole, minor olivine, and colorless glass with rounded vesicles and no mineral microlites (Fig. 4.5; Table 4.2). This tephra is a VLA chemical type and Mentolat volcano is its likely source. We correlate it with tephra 'e' of Lago Shaman (Figs. 4.4 and 4.7). The glass in the white pumice separates from this deposit are all low-K_2O glasses which range in SiO_2 content from 69-73 weight percent and are similar to published analysis of glasses from other distal Mentolat derived tephra (Fig. 4.4 and Table 4.5; Stern et al. 2016). The strontium isotopic ratios for tephra I is 0.704290±7 (Table 4.6), which is similar to both the proximal (T-36A; 0.704358±10; Naranjo and Stern, 2004) and distal MEN1 deposits (Lago Edita; 0.74375±8; Stern et al. 2016) and also overlaps the upper bound for previously reported Sr-isotopes for lavas from Mentolat volcano (Fig. 4.6; Notsu et al. 1987).

Tephra J, K and L

Tephra L underlies tephra J and K, which were not sampled in either core. Tephra L is 0.5 cm thick deposit with a maximum pumice size of 1.2 mm. Tephra L is a HA chemical type (Fig. 4.4 and Table 4.3) containing abundant tan to light brown glass with abundant vesicles that are elongated into a cylindrical shape, and lacking mineral microlites (Fig. 4.5). Common phenocryst include plagioclase, clinopyroxene, orthopyroxene, but not olivine or amphibole. The tephra glass, mineral phases, age, and petrochemistry are identical to tephra observed near Coyhaique (Weller et al. 2015) which are attributed to explosive Holocene eruptions of Hudson volcano. Some eruptions of Hudson, including the Phase 1 of the 1991 Hudson eruption (Kratzmann et al. 2009) and the H2 eruption (Naranjo and Stern, 1998) were dispersed to the north and the northeast, respectively. We tentatively attribute tephra L to a Holocene eruption of Hudson volcano that was dispersed predominately to the north. Tephra L is not observed in LJU or in Lago Shaman.

Tephra M

Tephra M is observed in LLM and LJU where it occurs as a 1 cm deposit in both cores with maximum grain size of 0.45 mm and 0.25 mm respectively (Table 4.2). Tephra M is a HA chemical type consisting of dark brown glass with few circular vesicles and abundant mineral microlites (Fig. 4.4). Phenocrysts include minor plagioclase, clinopyroxene, orthopyroxene, and a small amount of amphibole and biotite (Table 4.2). We attribute this tephra to Melimoyu volcano. No amphibole- or biotite-bearing tephra with HA chemistry occurs in the same stratigraphic position in Lago Shaman.

Tephra N

Tephra N occurs in both LLM and LJU where it occurs as a 1 cm deposit in each core with grain sizes of 1.7 and 0.7 mm respectively. From both cores, tephra N is characterized by colorless tephra glass with circular vesicles, and lacking mineral microlites, abundant phenocrysts of

Table 4.5. Major element compositions of tephra glass from teprha G and I

Lake	LLM	LLM	LLM	LLM	LLM	LLM	LLM	LLM
Depth (cm)	71-77	71-78	71-79	71-80	71-81	71-82	71-83	71-84
Tephra	G	G	G	G	G	G	G	G
Material	Glass	Glass	Glass	Glass	Glass	Glass	Glass	Glass
SiO_2	65.09	68.34	64.85	68.53	67.29	67.58	69.22	68.83
TiO_2	0.99	0.96	0.64	0.92	1.02	0.97	0.63	0.64
Al_2O_3	14.55	14.63	18.35	15.47	15.27	14.07	15.3	17.49
FeO	6.16	4.22	2.75	4.03	4.92	5.32	3.26	3.16
Fe_2O_3	-	-	-	-	-	-	-	-
MnO	0.16	0.28	0.13	0	0.15	0.12	0.41	0.2
MgO	2.05	1.14	0.73	1.34	1.48	1.79	0.99	1
CaO	4.5	3.48	5.83	4.09	4.17	4.04	2.77	3.15
Na_2O	4.74	4.53	5.38	3.72	3.59	4.07	4.57	3.74
K_2O	1.46	1.72	0.91	1.47	1.57	1.78	1.6	1.59
P_2O_5	0.24	0.34	0.24	0.24	0.28	0.16	0.29	0.16
Total	99.92	99.65	99.81	99.79	99.74	99.89	99.66	99.96

Lake	LLM	LLM	LLM	LLM	LLM	LLM	LLM	PC14 01-25
Depth (cm)	71-85	86-92	86-93	86-94	86-95	86-96	86-97	
Tephra	G	I	I	I	I	I	I	[1]MEN1
Material	Glass	Glass	Glass	Glass	Glass	Glass	Glass	Glass
SiO_2	70.31	68.98	73.04	72.45	72.38	73.46	73.01	71.05
TiO_2	0.76	0.46	0.4	0.58	0.44	0.53	0.45	0.49
Al_2O_3	14.86	19.11	14.36	14.18	15.62	14.55	14.01	14.99
FeO	3.72	2.17	2.26	2.71	2.54	2.64	2.68	-
Fe_2O_3	-	-	-	-	-	-	-	2.9
MnO	0.18	0.24	0.09	0.16	0.11	0	0.01	0.09
MgO	1.09	0.63	0.69	0.76	0.7	0.67	0.62	0.68
CaO	3.66	2.49	2.7	2.56	2.81	2.91	2.64	2.78
Na_2O	3.43	4.15	4.51	4.44	3.84	3.57	4.65	5.21
K_2O	1.65	1.59	1.63	1.66	1.45	1.58	1.62	1.44
P_2O_5	0.17	0.06	0.05	0.04	0.01	0.09	0.01	0.07
Total	99.84	99.88	99.73	99.59	99.92	99.979	99.69	99.7

Laguna Las Mellizas (LLM)

[1] Stern et al. 2016

Table 4.6. Mentolat strontium isotope ratios and strontium content

Material	Tepha	Locality	Sample #	$^{87}Sr/^{86}Sr$	Sr (ppm)	Reference
Tephra	I	Proximal	PC-2	0.70423±12	535	1
Tephra	B2	Medial	DJW-49	0.704258±9	422	2
Tephra	B2	Medial	DJW-53	0.704313±9	555	2
Tephra	MENo	Medial	DJW-51	0.70429±7	422	2
Tephra	MENo	Medial	DJW-56	0.704357±11	439	2
Tephra	MEN1; T-36A	Proximal	PC-1	0.704358±10	413	3
Tephra	MEN1	Distal	CS 1032	0.704375±8	472	4
Lava	-	Proximal	MEN-001	0.70437	380	5
Lava	-	Proximal	MEN-002	0.7044	421	5
Lava	-	Proximal	MEN-003	0.70425	451	5
Lava	-	Proximal	MEN-004	0.70437	392	5
Lava	-	Proximal	MEN-005	0.70426	419	5

References: 1. This Study; 2. Weller et al. 2015 3. Naranjo and Stern, 2004; 4. Stern et al. 2016; 5. Notsu et al. 1987

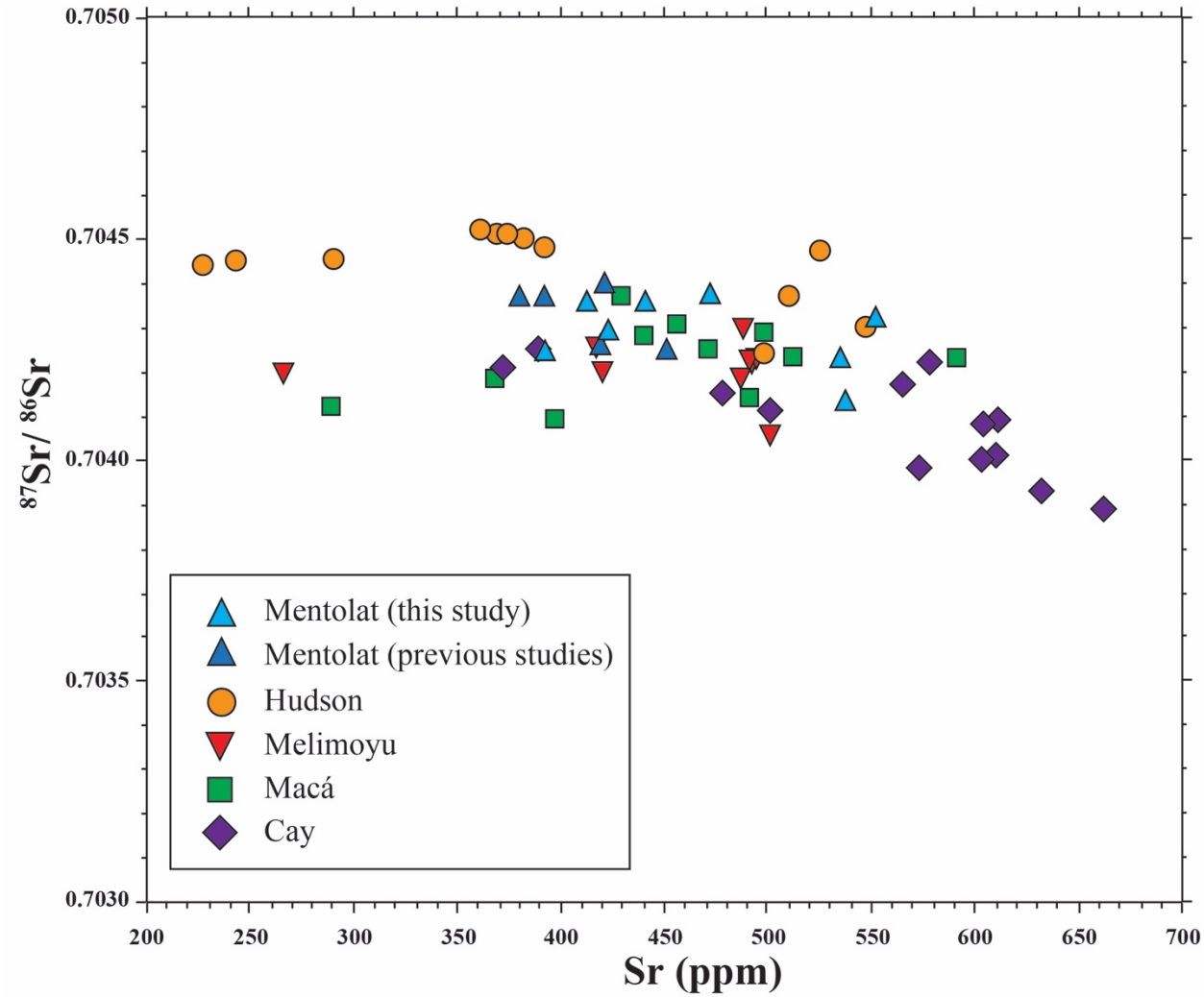

Figure 4.6. 87Sr/86Sr isotope ratios versus Sr content for lavas and tephra of Melimoyu, Mentolat, Macá, Cay, and Hudson volcanoes (Notsu et al. 1987; Futa and Stern, 1988; D'Orazio et al. 2003; Weller et al. 2014)

plagioclase, clinopyroxene, orthopyroxene, and amphibole (Table 4.2). This tephra has a VLA-type chemistry and was likely derived from Mentolat volcano (Fig. 4.4). Tephra 'i' is a VLA-type tephra in the same stratigraphic position and is tentatively correlated with tephra N of the LLM and LJU cores (Fig. 4.7). The age, petrochemistry, and petrographic features are similar to the previously observed MEN1 eruption from lake cores near Cochrane (Stern et al. 2016) and in outcrop east of Mentolat (Naranjo and Stern, 2004) which has been dated at 7690±60 cal years BP.

Tephra O

Tephra O occurs as a 1 cm and a 0.5 cm thick deposit in LLM and LJU cores and has a maximum gain size of 1 mm from both lake cores. Tephra O is a HA chemical type deposit (Fig. 4.4) with brown glass with few rounded vesicles and few mineral microlites, frequent plagioclase, and minor pyroxenes and olivine (Fig. 4.5; Table 4.2). This tephra is similar petrochemically and petrographically to tephras C and E and thus we source this eruption from Melimoyu volcano.

Tephra P

Tephra P is a LA chemical type deposit observed in both LLM and LJU as a 2 cm and 1 cm thick deposit with a maximum grain size of 5 mm and 3 mm respectively (Fig. 4.4). Tephra P consists of dark brown volcanic glass lacking vesicles or microlites (Table 4.2). Phenocrysts include abundant plagioclase, frequent clinopyroxene, olivine, minor orthopyroxene, and amphibole (Table 4.2). Tephra P may have been derived from Macá, Cay or one of the MECs.

Tephra Q

Tephra Q occurs as a 2 cm thick deposit with a maximum grain size of 4.3 mm from LLM. This tephra is characterized by LA type chemistry, black volcanic glass lacking vesicles or microlites, abundant plagioclase, clinopyroxene, minor olivine, orthopyroxene, and amphibole (Fig. 4.4; Table 4.2). Tephra Q is likely sourced from Macá, Cay or one of the MECs. Tephra Q

is tentatively correlated to an uncollected tephra in LJU based on the stratigraphy, but no tephra occurs in Lago Shaman with similar petrology or petrochemistry.

Tephra R

Tephra R is a LA chemical type deposit (Fig. 4.4) observed in LLM where it occurs as a 2 cm thick deposit with a maximum grain size of 0.9 mm. Tephra R has black glass that lacks vesicles and microlites. Observed phenocrysts include abundant plagioclase, frequent clinopyroxene, minor orthopyroxene, and biotite (Table 4.2). Tephra R is tentatively correlated to an uncollected tephra in LJU but no tephra with similar chemistry or petrology occurs in Lago Shaman core. Tephra R may have been derived from Macá, Cay or one of the MECs.

Tephra S

Tephra S is the oldest deposit sampled from the LLM core where it occurs as a 1 cm thick deposit with LA type chemistry (Fig. 4.4) and has a maximum grain size of 0.4 mm. Tephra S has orange glass with few circular vesicles and abundant mineral microlites. Tephra S consist of abundant plagioclase, minor clinopyroxene, orthopyroxene, and trace amounts of green amphibole (Table 4.2). Tephra S many have been derived from Macá, Cay or one of the MECs. Tephra S is tentatively correlated to an uncollected tephra in LJU based on the stratigraphy but no tephra occurs in Lago Shaman with similar petrology or petrochemistry.

4.6 Discussion and Conclusion

Some of the tephra in the cores from LLM and LJU correspond to other tephra observed in cores taken from Lago Shaman (Fig. 4.7; Table 4.1; Stern et al. 2015), to the south near Coyhaique (Weller et al. 2015), Cochrane (Stern et al. 2016) and to tephras observed in outcrop from the region (Naranjo and Stern, 2004). Of the 14 tephra deposits sampled, four are similar

petrographically and petrochemically to tephras previously attributed to explosive eruptions of Mentolat volcano. Four of the deposits are similar to previously described deposits from Melimoyu, one possibly from Hudson, and six may have been derived from either Macá, Cay or one of the MECs located along the LOFZ or surrounding the major volcanic centers. Mentolat derived tephra are all VLA chemical type deposits and are petrographically distinct in having colorless volcanic glass and phenocryst-rich including plagioclase, clinopyroxene, orthopyroxene, and amphibole. These deposits are thicker and coarser-grained in the LLM core consistent with their derivation from Mentolat, the geographically closest volcano to this lake. The two thickest tephra from this core (tephra G and I) have glass chemistry (Table 4.5), bulk trace-element chemistry, and tephra Sr-isotopic ratios (Table 4.6) similar to whole rock major, trace and isotopic analysis of lavas from Mentolat (López-Escobar et al. 1993).

Melimoyu derived tephra are all HA chemical types and contain brown to dark brown glass with moderate to few circular vesicles, occasionally with minor elongated vesicles, and variable amounts of plagioclase microlites. Common phenocryst include plagioclase, two pyroxenes, olivine, and sometimes amphibole and biotite. Tephras from large explosive eruptions from Hudson are also HA chemical types but consist of tan to light brown glass with abundant elongated vesicles, phenocrysts of plagioclase, clino- and orthopyroxene but lacking amphibole or biotite. Only one of the HA tephra, tephra L from LLM core, appears similar to Hudson derived tephra. Tephra from this eruption was either never sampled from the Lago Shaman, or never reached that far northeast, although tephra from the Late Glacial age Ho eruption does occur in the Lago Shamen core (Weller et al. 2014; Stern et al. 2015). Puyuhuapi group of MEC also erupted HA type basalts. However, there is no clear evidence that any of the tephra preserved in the cores

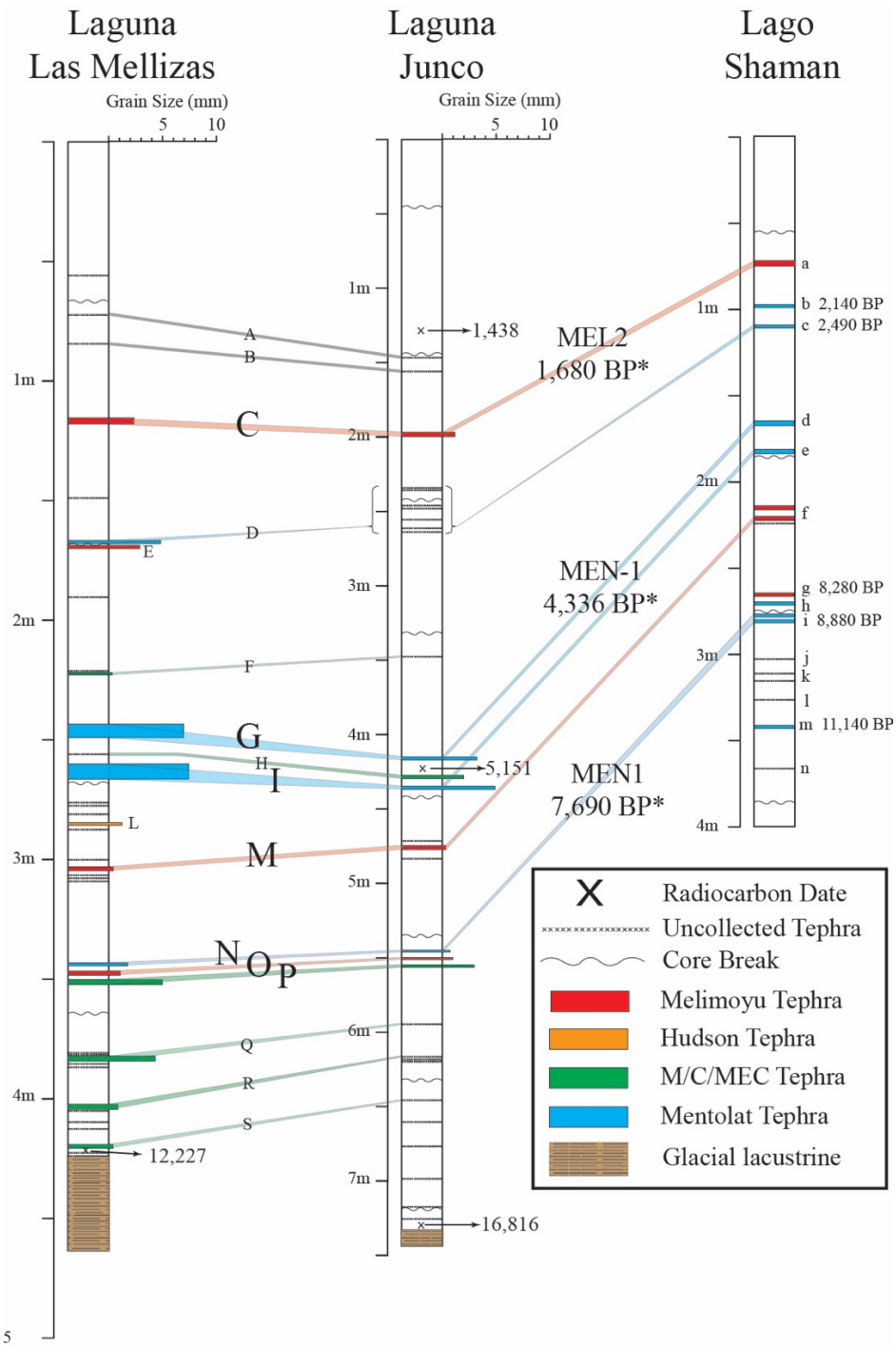

Figure 4.7. Composite stratigraphic section from Laguna Las Mellizas, Laguna Junco, and Lago Shaman (de Porras et al. 2012; Stern et al. 2015) showing the correlations for tephras A-S and the maximum grain size from each tephra sampled. Note the different length scales for each lake core. These correlations include previously identified explosive eruptions observed in outcrop, including the MEN-1 (Mella et al. 2012) and the older MEN1 (Naranjo and Stern, 2004; Stern et al. 2016) eruptions of Mentolat volcano and the MEL2 eruption of Melimoyu volcano (Naranjo and Stern, 2004).

from the Río Cisnes valley were derived from the Puyuhuapi group of MEC as these cones produce deposits with abundant olivine which lack orthopyroxene, amphibole, and biotite.

Unlike the tephra in Lago Shaman and Mallín El Embudo, LLM and LJU contain tephra that we attribute to eruptions from either Macá, Cay or MECs. These LA-type deposits are variable in petrography (glass color and morphology, mineral assemblages). Naranjo and Stern (2004) and Weller et al. (2015) attributed a basaltic-andesite tephra dated at 1,440±40 cal years BP (MAC1/D3) as being sourced from Macá volcano. However there is no evidence that the MAC1 tephra was dispersed over the Río Cisnes valley, despite the presence of some LA type tephra derived from older eruptions of Macá or Cay volcanoes in the cores from the lower Río Cisnes valley. These older LA type tephra may be preserved within the cores from Lago Shaman and Mallín El Embudo, but if so were too thin (<1 cm) to be sampled.

These results confirm the repetitive explosive activity of Mentolat, Melimoyu and Hudson throughout the Holocene. The petrochemical data and the petrographic observations suggest that the petrochemical characteristics of the products from these centers have been relatively consistent throughout the Holocene. The majority of the deposits lie within the fields created by the previously published whole rock tephra trace-element analysis from the SSVZ centers. However, several of the deposit lie outside of those fields, but are similar petrologically to the other deposits attributed to those volcanoes. We suggest that these outliers are the result of the fact that these tephras, and many tephras observed from SSVZ centers, are heterogeneous mixtures of both mafic and felsic components (Kratzmann et al. 2009; Scasso et al. 1994; Scasso and Carey, 2005; Weller et al. 2015). Density differences between these components are such that proximal deposits would likely have a higher proportion of dense mafic material and thus would have different bulk trace

element contents than the more distal felsic component rich deposits, while still preserving the HA, LA and VLA character of the tephra.

These tephra records, and those form Lago Shaman and Mallín El Embudo, indicate that local population centers such as Puerto Cisnes could be impacted by eruptions from Mentolat, Melimoyu, and potentially one of the other centers located within the region such as Macá or Cay, which have also produced regionally widespread tephra deposits during the Holocene.

4.7 References

Carel M, Siani G, Delpech G (2011) Tephrostratigrapy of a deep-sea sediment sequence off the south Chilean margin: New insight into the Hudson volcanic activity since the last glacial period. J Volcanol Geotherm Res. 208: 99-111

de Porras ME, Maldonado A, Abarzúa AM, Cárdenas ML, Francois JP, Martel-Cea A, Stern, CR (2012) Postglacial vegetation, fire and climate dynamics at Central Chilean Patagonia (Lake Shaman, 44°S). Quat Sci Revs 50: 71–85

de Porras ME, Maldonado A, Quintana FA, Martel-Cea1 JO, Reyes O, Méndez C (2014) Environmental and climatic changes in Central Chilean Patagonia since the Late Glacial (Mallín El Embudo, 44°S). Climates of the Past 10: 1063–1078

D'Orazio M, Innocenti F, Manetti P, Tamponi M, Tonarini S, González-Ferrán O, Lahsen A (2003) The Quaternary calc-alkaline volcanism of the Patagonian Andes close to the Chile triple junction: geochemistry and petrogenesis of volcanic rocks from the Cay and Maca volcanoes (~45°S, Chile). J S Amer Earth Sci 16(4): 219–242

Farmer, G.L., Broxton, D.E., Warren, R.G., Pickthorn, W., (1991) Nd, Sr, and O isotopic variations in metaluminous ash-flow tuffs and related volcanic rocks at Timber Mountain/

Oasis Valley Caldera, Complex, SW Nevada: implication for the origin and evolution of large-volume silicic magma bodies. Contrib Mineral Petrol 109, 53–68.

Fontijn K, Lachowycz SM, Rawson H, Pyle DM, Mather TA, Naranjo JA, Moreno-Roa H (2014) Late Quaternary tephrostratigraphy of southern Chile and Argentina. Quat Sci Revs 89: 70-84

Futa K, Stern CR (l988) Sr and Nd isotopic and trace element compositions of Quaternary volcanic centers of the southern Andes. Earth Planet Sci Lett 88: 253–262

Gutiérrez F, Gioncada A, González-Ferrán O, Lahsen A, Mazzuoli R (2005) The Hudson volcano and surrounding monogenetic centres (Chilean Patagonia): an example of volcanism associated with ridge-trench collision environment. J Volcanol Geotherm Res 145: 207–233

Haberle SG, Lumley SH (1998) Age and origin of tephras recorded in postglacial lake sediments to the west of the southern Andes, 44^{o}S to 47^{o}S. J Volcanol Geotherm Res. 84: 238-256

Hickey RL, Frey FA, Gerlach DC (1986) Multiple sources for basaltic arc rocks from the Southern Volcanic Zone of the Andes (34-41°S): Trace element and isotopic evidence for contributions from subducted oceanic crust, mantle, and continental crust. J Geoph Res 91: 5963-5983.

Hickey-Vargas, R.L.; Moreno-Roa, H.; López-Escobar, L.; Frey, F.A. 1989. Geochemical variations in Andean basaltic and silicic lavas from the Villarrica-Lanín volcanic chain (39.5°S): an evaluation of source heterogeneity, fractional crystallization and crustal assimilation. Contrib Mineral Petrol 103: 361-386.

Hickey-Vargas RL, Abdollahi MJ, Parada MA, López-Escobar L, Frey FF (1995) Crustal xenoliths from Calbuco Volcano, Andean Southern Volcanic Zone: implications for crustal

composition and magma-crust interaction. Contrib Mineral Petrol 119: 331-344.

Hickey-Vargas, R.L.; Sun, M.; López-Escobar, L.; Moreno-Roa, H.; Reagan, M.K.; Morris, J.D.; Ryan J.G. 2003. Multiple subduction components in the mantle wedge: evidence from eruptive centers in the Central Southern volcanic zone, Chile. Geology 30 (3): 199-202.

Hogg A, Hua Q, Blackwell P, Niu M, Buck C, Guilderson T, Heaton TJ, Palmer JG, Paula JR, Reimer RW, Turney CSM, Zimmerman SRH (2013). SHCAL13 Southern Hemisphere Calibration, 0-50,000 years CAL BP. Radiocarbon 55(4), 1889-1903.

Kratzmann DJ, Carey S, Scasso RA, Naranjo JA (2009) Compositional variations and magma mixing in the 1991 eruptions of Hudson volcano, Chile. Bull Volcanol 71(4): 419–439

Kratzmann DJ, Carey S, Scasso RA, Naranjo JA (2010) Role of cryptic amphibole crystallization in magma differentiation at Hudson volcano, Southern Volcanic Zone, Chile. Contrib Mineral Petrol 159: 237–264

López-Escobar L, Kilian R, Kempton P, Tagiri M (l993) Petrology and geochemistry of Quaternary rocks from the southern volcanic zone of the Andes between 41°30’ and 46°00’S, Chile. Rev Geol Chile 20: 33–55

López-Escobar L, Cembrano J, Moreno H, (1995a) Geochemistry and tectonics of the chilean Southern Andes basaltic Quaternary volcanism (37-46ºS). Revista Geológica de Chile 22 (2): 219-234

López-Escobar L, Parada MA, Hickey-Vargas R, Frey FA, Kempton P, Moreno H (1995b) Calbuco Volcano and minor eruptive centers distributed along thLiquifie-Ofqui Fault Zone, Chile (41°S) contrasting origin of andesitic and basaltic magmain the Southern Volcanic Zone of the Andes. Contr Mineral Petrol 119: 345-361

Lowe DJ (2011) Tephrochronology and its application: A review. Quat Geol. 6: 107-153

Mella M, Ramos A, Kraus S, Duhart P (2012) Tefroestratigrafía, magnitud y geoquímica de erupciones holocenas mayores del volcán Mentolat, Andes del Sur (44º40'S), Chile. Actas, Congreso Geológico Chileno, No. 13, Antofagasta.

Naranjo JA, Moreno HR, Banks NG, (1993) La Eruptión del Volcán Hudson en 1991 (46^{o}S), Regieón XI, Aisén, Chile. Servicio Nacional de Geologia y Mineria 44:1-50

Naranjo JA, Stern CR (1998) Holocene explosive activity of Hudson Volcano, southern Andes. Bull Volcanol 59(4): 291–306

Naranjo JA, Stern CR (2004) Holocene tephrochronology of the southernmost part (42°30'-45°S) of the Andean Southern Volcanic Zone. Rev Geol Chile 31(2): 225–240

Rodríguez C, Sellés D, Dungan M, Langmuir C, Leeman W, (2007) Adikitic dacites formed by intracrustal crystal fractionation of water-rich parent magmas at Nevado de Longaví (36.2^{o}S; Andean Southern Volcanic Zone, Central Chile). J Petrol 48(11): 2033-2061

Saadat S, CR Stern (2011) Petrochemistry and genesis of olivine basalts from small monogenetic parasitic cones of Bazman stratovolcano, Makran arc, southeastern Iran. Lithos 125: 609-617

Scasso RA, Corbella H, Tiberi P (l994) Sedimentological analysis of the tephra from the 12–15 August l991 eruption of Hudson volcano. Bull Volcanol 56: 121–132

Scasso RA, Carey S, (2005) Morphology and formation of glassy volcanic ash from the August 12-15, 1991 eruption of Hudson volcano, Chile. Latin American J Sediment and Basin Anal 12(1): 3-21

Sellés D, Rodríguez AC, Dungan MA, Naranjo JA, Gardeweg M (2004) Geochemistry of Nevado de Longaví (36.2°S): a compositionally atypical volcano in the Southerrn Volcanic Zone of the Andes. Rev Geol Chile 31(2): 293-315

Stern CR (2004) Active Andean Volcanism: its geologic and tectonic setting. Rev Geol Chile 31(2): 161-206 doi: 10.5027/andgeoV31n2-a01.

Stern CR, de Porras ME, Maldonado A (2015) Tephrochronology of the upper Río Cisnes valley (44°S), southern Chile. Andean Geol 42(2): 173-192

Stern CR, Moreno PI, Henrique WI, Villa-Martinez RP, Sagredo E, Aravena JC, De Pol-Holz R (2016) Holocene tephrochronolgy in the area around Cochrane, southern Chile. Andean Geol 43(1): 1-19

Stuiver M, Reimer PJ, Braziunas TF (1998) High-precision radiocarbon age calibration for terrestrial and marine samples. Radiocarbon 40(3): 1127–1151

Stuiver M, Reimer PJ, Reimer R (2013) CALIB 7.0.4. http://calib.qub.ac.uk/calib/

Vargas G, Rebolledo S, Sepúlveda SA, Lahsen A, Thiele R, Townley B, Padilla C, Rauld R, Herrera MJ, Lara M (2013) Submarine earthquake rupture, active faulting and volcanism along the major Liquiñe-Ofque Fault Zone and implications for seismic hazard assessment in the Patagonian Andes. Andean Geol 40: 141-171

Völker D, Kutterolf S, Wehrmann H (2011) Comparative mass balance of volcanic edifices at the southern volcanic zone of the Andes between 33^{o}S and 46^{o}S. J Volcanol Geotherm Res. 205: 114-129

Watt SFL, Pyle DM, Mather TA (2011) Geology, petrology and geochemistry of the dome complex of Huequi volcano, southern Chile. Andean Geol 38(2): 335-348

Watt SFL, Pyle DM, Mather TA (2013) The volcanic response to deglaciation: evidence from glaciated arcs and a reassessment of global eruption records. Earth Sci Rev 122: 77-102

Weller DJ, Miranda CG, Moreno PI, Villa-Martínez RP, Stern CR (2014) A large late-glacial Ho eruption fo the Hudson volcano, southern Chile. Bull Volcanol 76: 831-849

Weller D., Miranda C.G., Moreno P.I., Villa-Martínez R., Stern C.R., (2015) Tephrochronology of the southernmost Andean Southern Volcanic Zone, Chile. Bull of Volcanol 77 (107). doi: 10.1007/s00445-015-0991-2.

Wilson T M, Cole JW, Stewart C, Cronin SJ, Johnston DM (2011) Ash storms: impacts of wind-remobilised volcanic ash on rural communities and agriculture following the 1991 Hudson eruption, southern Patagonia, Chile. Bull Volcanol 73: 223–239

Wilson T, Cole J, Johnston D, Cronin S, Stewart C, Dantas A (2012) Short-and long-term evacuation of people and livestock during a volcanic crisis: lessons from the 1991 eruption of Volcan Hudson, Chile. J Applied Volcanol 1: 2

Chapter 5

Along-strike variability of primitive magmas inferred from olivine-hosted melt inclusions, southernmost Andean Southern Volcanic Zone, Chile

To be submitted to *Lithos*, 2017

Coauthors: Charles R. Stern[1]

[1]Department of Geological Sciences, University of Colorado, Boulder, CO, USA

5.1 Abstract

Glass compositions of melt inclusions in olivine phenocrysts found in tephras derived from explosive eruptions of the four volcanoes along the volcanic front of the southernmost Andean Southern Volcanic Zone (SSVZ) are used to constrain primitive magma compositions and melt generation parameters. Primitive magmas from Hudson, Macá, and Melimoyu have similar compositions and are formed by low degrees (8-18 %) of partial melting of a relatively water-poor (~0.22 to 0.40 wt. %) mantle peridotite. Compared to these other three centers, primitive magmas from Mentolat have higher Al_2O_3 and lower MgO, TiO_2, and other incompatible minor elements, and are generated by somewhat higher degrees (12-20%) of partial melting of more water-rich (~0.33 to 0.52 wt.%) mantle peridotite. The differences in the estimated primitive parental magma compositions between Mentolat and the other three volcanic centers are consistent with difference in the more evolved magmas erupted from these centers, Mentolat magmas having higher Al_2O_3 and lower MgO, TiO_2 and other incompatible minor element contents, suggesting that these differences are controlled by melting processes in the mantle source region above the subducted oceanic plate. Parental magma S =1430-594, Cl = 777-125 and F $\leq$ 1408 ppm contents of Hudson, Macá, and Melimoyu are similar to other volcanoes further north in the SVZ. However, Mentolat primitive magmas have notably higher concentrations of S =2569-1215 and Cl =1078-704 ppm. The observed along-arc changes in parental magma chemistry may be due to the close proximity below Mentolat of a subducted Nazca Plate fracture zone that can efficiently transport hydrous mineral phases, seawater, and sediment into the mantle, driving enhanced volatile fluxed melting beneath this center compared to the others.

5.2 Introduction

Along-arc variations in the composition of convergent plate boundary magmas may be related to various subduction parameters such as the age, thickness, thermal state, and composition of the subducting oceanic lithosphere, the volume and composition of the sediments entering the trench, and the age and composition of the mantle wedge. Understanding the mechanisms causing variations in the compositions of arc magmas requires constraining details of the processes of melt generation such as primitive magma compositions, volatile contents and melting parameters, details that are often lost during modification of primitive magmas during ascent, differentiation, and eruption. However, melt inclusions hosted in early formed phenocryst minerals (Fig. 5.1) are a potentially valuable source of information on the composition of primitive magmas and the conditions of melt generation. Melt inclusions are small pockets of silicate melts trapped inside of phenocrysts at magmatic temperatures and pressures. The phenocrysts act as pressure vessels during eruption, keeping the melt inclusions isolated from the ascending and evolving magma, which may change in composition and temperature. Additionally, the phenocrysts prevent or at least retard degassing of the melt inclusions. This has made melt inclusions a valuable source of information concerning the concentrations in magmas of magmatic volatiles such as H_2O, S, Cl, and F (Wallace 2005; Portnyagin et al. 2007).

To better understand the along-strike petrochemical variability observed in the eruptive products of the volcanoes of the southernmost Andean Southern Volcanic Zone (SSVZ; Fig. 5.2), melt inclusions observed in olivines (Figs. 5.1 and 5.3) occurring in tephra deposits derived from explosive eruptions of the four volcanoes along the volcanic front of the southernmost SSVZ have been examined. We present melt inclusion compositions, including volatile contents, that are fractionation-corrected back to primitive magmas in equilibrium with mantle peridotite (Fo_{90}) in order to better understand the pre-eruptive conditions and primitive magmatic compositions during

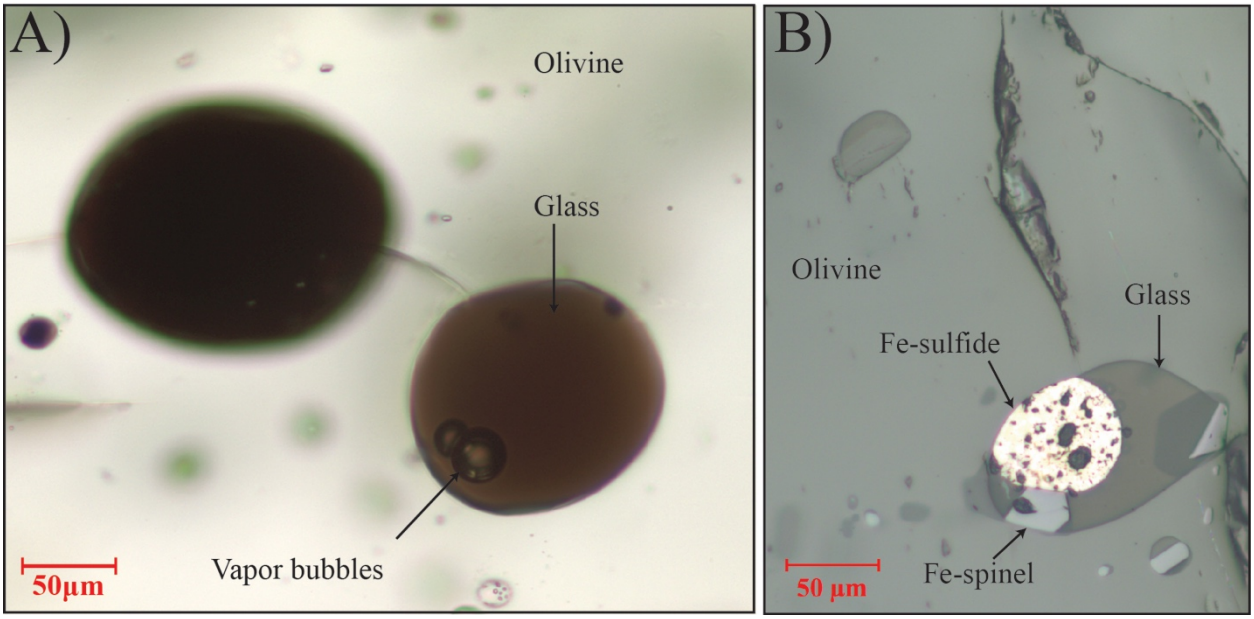

Figure 5.1. A. Plane light photomicrograph of a typical Mentolat-derived melt inclusion (MEN4) analyzed in this study. Melt inclusions are generally homogenous with small vapor bubbles indicating the high water contents of these magmas before entrapment. **B.** Reflected light photomicrograph of a Macá-derived melt inclusion (MAC8) containing a Fe-sulfide and a Fe-rich spinel. Melt inclusion containing crystals were avoided, but provide information on the primary phases during early magmatic evolution.

the early phase of magma evolution below the volcanic front of the southernmost Andean SSVZ. Watt et al. (2013) previously analyzed melt inclusions and calculated primitive parental magma compositions for volcanic centers further north in the Andean SSVZ. Kratzmann et al. (2010) also presented compositional data for melt inclusions in plagioclase and pyroxene phenocrysts occurring within tephra derived from three large explosive Holocene eruptions of Hudson volcano, the southernmost center in the SSVZ, but the compositions of these inclusions were more evolved than the compositions of the bulk magmas and they were not interpreted to reflect or provide information about primitive parental magmas.

5.3 Geologic Background

Volcanism in southern Chile occurs in two distinct zones, the Southern Volcanic Zone (SVZ; Fig. 5.2) and Austral Volcanic Zone (AVZ; Stern 2004), resulting from the subduction of the Nazca (7 cm/yr) and Antarctic (1-2 cm/yr) plates beneath the South American continent (DeMets et al. 2010). The SVZ is an ~1400 km long volcanic chain consisting of 60 Quaternary stratovolcanoes, at least 3 large caldera complexes and numerous monogenetic eruptive centers (MEC; Stern 2004). The SVZ is divided into four volcanic segments termed, from north-to-south, the northern (NSVZ), transitional (TSVZ), central (CSVZ), and southern (SSVZ) SVZ. The divisions of these segments are based on the geometry of the volcanic arc and the chemical characteristics of the erupted rocks, although the exact locations of the segment boundaries are still debated (Sellés et al. 2004; Volker et al. 2011).

This study focuses on tephras derived from the four volcanic centers that form the volcanic front of the southernmost SSVZ: Melimoyu, Mentolat, Macá, and Hudson (Fig. 5.2). Hudson, which had a large explosive eruption in 1991 (Kratzmann et al. 2009), is the southernmost volcano

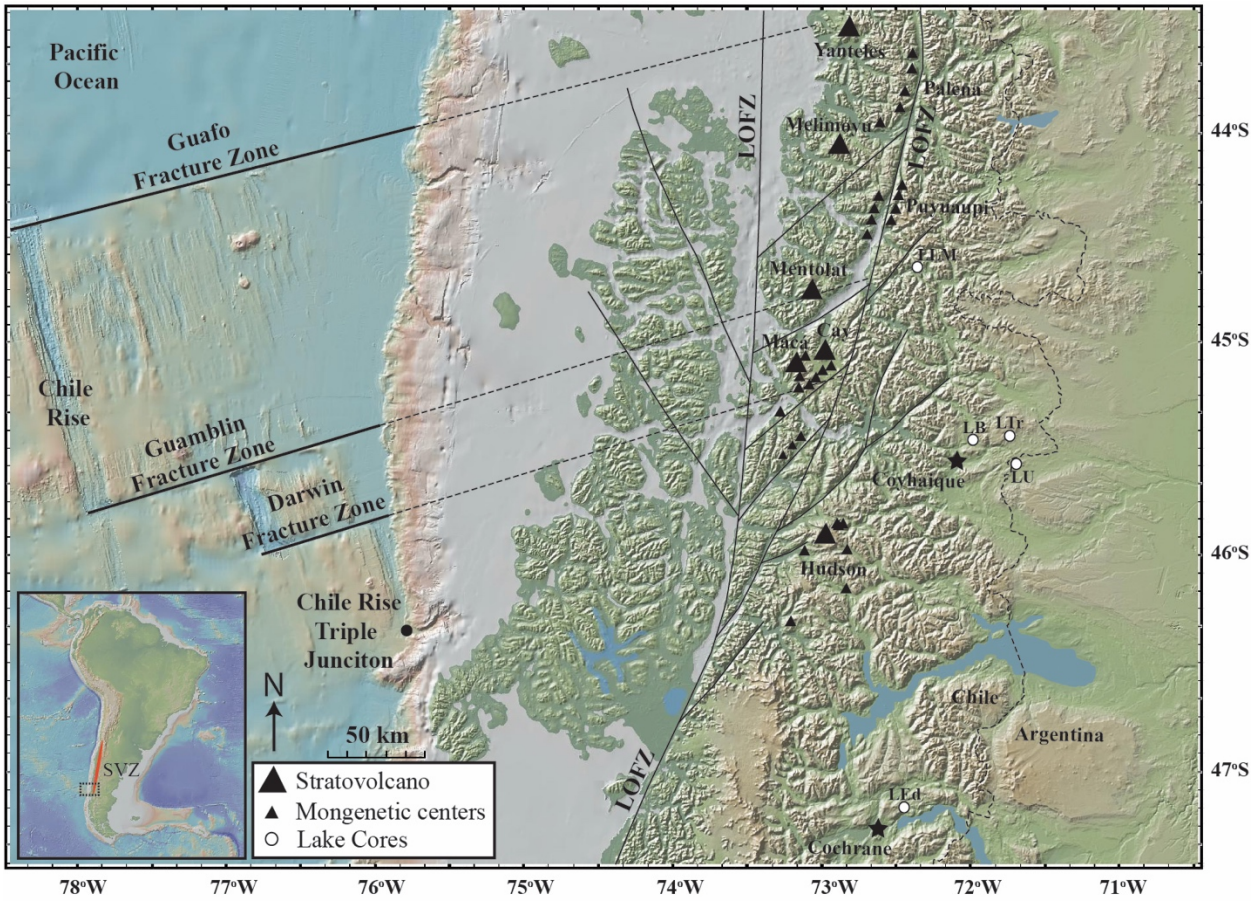

Figure 5.2. Map of the southernmost portion of the Andean Southern Volcanic Zone showing the location of Hudson, Macá, Cay, Mentolat, Melimoyu, and Yanteles volcanoes. Also shown are the location of the small monogenetic eruptive centers (MEC) located along the Liquiñe-Ofqui fault zone (LOFZ) and surrounding Hudson, Macá and Cay, the location of the Chile Rise Triple Junction where the Chile Rise enters the trench, the location of some of the lake cores from which olivines were collected, and the location of Nazca Plate fracture zones with their projected location under the South American continent.

of the SVZ and sits approximately 280 km east of the Chile Rise Triple Junction, the point where the Chile Rise, an active spreading center separating the Nazca and Antarctic Plates, enters the trench. Collision of the Chile rise with the southernmost sector of South American occurred in the Miocene and due to the slight oblique subduction of the Nazca Plate, has migrated northward along the continental margin over the last ~14 Ma (Cande and Leslie 1986). South of Hudson there is >350 km gap in recently active volcanism separating the SSVZ from the AVZ (Stern, 2004).

The volcanoes of the SSVZ ascend through relatively thin continental crust (~30 km; Hildrith and Moorebath 1988). The dominant tectonic feature in the region, the Liquiñe-Ofqui Fault Zone (LOFZ; Fig. 5.2; Cembrano et al. 1996), results from the oblique subduction of the Nazca Plate and the impingement of the Chile Rise against the continental margin (Cande and Leslie 1986). Numerous small mafic monogenetic eruptive centers (MEC) occur along segments of the LOFZ (Fig. 5.2), but the large stratovolcanoes are located on blocks bounded by these segments.

Despite limited interaction with continental crust, there is significant petrochemical diversity amongst the volcanoes of the SSVZ. López-Escobar et al. (1993, 1995) recognized these chemical differences and developed a classification based on the relative abundances in basalts of K_2O, Al_2O_3 and incompatible trace element such as high-field-strength (HFSE; Ti, Zr, Nb, Hf, U), large-ion-lithophile (LILE; Cs, Rb, Ba, Sr, K, Th), and rare-earth-elements (REE). Among the volcanoes of the SSVZ, Hudson and Melimoyu produce mafic and intermediate lavas and tephras that have relatively high concentrations of K_2O, HFSE, LILE, and REE, which corresponds to the Type-2 classification of Lopez-Escobar et al. (1993,1995) and have been termed High Abundance (HA) petrochemical centers (Stern et al. 2016, 2017; Weller et al. 2014, 2015). These are both relatively large volcanoes, with minimum volumes estimated at 147 and 142 km^3 respectively,

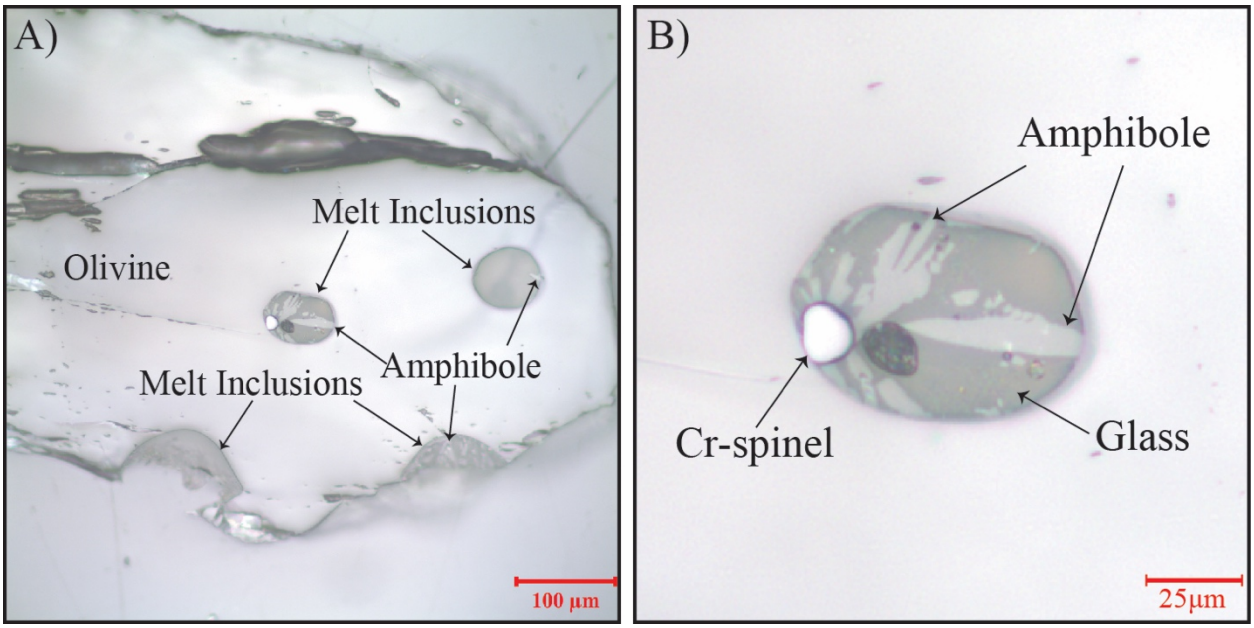

Figure 5.3. Reflected light photomicrographs of an amphibole-bearing olivine-hosted melt inclusion derived from the H1 eruption of Hudson (Naranjo and Stern 2004; Stern et al. 2016).

compared to 100 km^3 for the average SVZ volcano (Volker et al. 2011). In contrast, Macá and Mentolat, which are both relatively small volcanic centers with volumes of 39 and 36 km^3 respectively, produce mafic and intermediate lavas and tephras with relatively low concentrations of K_2O, HFSE, LILE and REE, which corresponds to the Type-1 classification of Lopez-Escobar et al. (1993, 1995) and have been termed Low Abundance (LA) petrochemical centers. However, Mentolat erupts lavas and tephras with exceptionally low concentrations of K_2O, HFSE, LILE and REE. It has therefore been further subdivided from the LA-type centers and is termed a Very Low Abundance (VLA) petrochemical center (Stern et al. 2015, 2016; Weller et al. 2015, 2017a, 2017b).

These petrochemical characteristics have been used, along with tephra isopach maps, to identify source volcanoes for tephras derived from explosive eruptions from the SSVZ centers observed in outcrops (Naranjo and Stern 1998, 2004; Stern 2008), lakes and bogs (Elbert et al. 2013; Stern et al. 2015, 2016; Weller et al. 2014, 2015, 2017a, 2017b) and Pacific Ocean sediment cores (Carel et al. 2011). Based on these characteristics, tephras produced by numerous explosive eruptions from each of these four SSVZ centers have been identified. These include: 1) for Hudson, a very large late glacial (Ho; Weller et al. 2014) and two other large Holocene eruptions (H1, H2; Naranjo and Stern 1998), as well as >25 other smaller eruptions (Weller et al. 2015, 2017a) prior to its most recent large explosive eruption in 1991 (H1991; Kratzmann et al. 2009); 2) for Macá, a late Holocene tephra in outcrop attributed to a medium sized explosive eruption (MAC1; Naranjo and Stern 2004) that is also observed, along with 13 additional tephra that also may be attributed to eruptions of Macá, in lake cores near Coyhaique (Weller et al. 2015, 2017a); 3) for Mentolat, a large mid Holocene eruption (MEN1; Naranjo and Stern 2004; Stern et al. 2016), as well as 12 other late glacial and Holocene eruptions of Mentolat preserved as tephra in lake cores near

Coyhaique (Weller et al. 2015, 2017a) and further north in the Río Cisnes valley (Stern et al. 2015; Weller et al. 2017a); and 4) for Melimoyu, two eruptions (MEL1 and MEL2; Naranjo and Stern 2004) identified by tephra in outcrop, and three other late glacial and Holocene tephra documented in lake cores in the Río Cisnes valley (Stern et al. 2015).

5.4 Samples

Olivines were selected from tephra preserved in sedimentary cores from lakes east of the SSVZ volcanoes (Fig. 5.2; Table 5.1) which have been the focus of tephrochronologic studies because of their exceptional preservation of tephras derived from large and small explosive eruptions of the volcanoes of the SSVZ (Stern et al. 2015, 2016; Weller et al. 2015, 2017a, 2017b). The cores were taken using a modified Livingstone piston corer at one meter intervals until the sediment transitioned from predominately organic matter-rich lacustrine sediments to glaciolacustrine clays and sands. Details of the lake cores, including the x-ray photographs, tephra petrochemistry, and source volcano identification are reported by Weller et al. (2014, 2015, 2017a) and Stern et al. (2015, 2016). The transmitted x-ray photograph and the bulk tephra petrochemistry for a previously undescribed core from Baguales lake (LB; Fig. 5.2) are presented in Figure A and Table A5.1 of the Appendix. The tephras in the LB core can be correlated based on both the stratigraphic relations and bulk tephra petrochemistry with tephra in the other cores taken from the region.

All of the tephra deposits from which olivines were selected are derive from Holocene to late Pleistocene explosive eruptions of the four volcanoes of the SSVZ. Each of these eruptive units contain unzoned olivine phenocrysts mixed in with other mineral phenocrysts as well as tephra and pumice fragments with a range of glass compositions. However, the deposition of these

Table 5.1. Sample location information

Eruption	Source	Lake	Latitude S	Longitude W	Core	Section	Depth (cm)	Age (cal yrs BP)	Error
H2	Hudson	Baguales	45°29'53.7"	71°55'5.6"	PC1104	AT1	66-74	3868±84	-
H1	Hudson	Edita	47°9'5.40"	72°21'12.50"	PC0902	AT7	20-38	7689±23	-
Ho	Hudson	Las Mellizas	45°32'31.9"	71°48'32.3"	PC1106	AT6	0-55	18,459	205
B2	Mentolat	Tranquilo	45°27'29.1"	71°44'43.1"	PC1203	AT3	0-4	1,426	367
D1	Mentolat	Unco	45°34'29.4"	71°43'7.6"	PC1103	ET1	94-95	1,774	216
I	Mentolat	Lake Las Mellizas	44°39'01.1"	72°19'50.41"	0115B	BT3	86-92	>5,151	-
MAC1	Macá	Baguales	45°29'53.7"	71°55'5.6"	PC1104	AT1	21-30	1,922	215
MEL2	Melimoyu	Lake Las Mellizas	44°39'01.1"	72°19'50.41"	0115B	BT2	46-49	~1680	-

tephra within lacustrine systems acts to mix and eliminate any stratigraphic preservation of sequentially variable eruptive phases produced through the duration of the eruption.

5.4.1 Hudson olivines

Olivine phenocrysts were selected from tephra produced by three of the four Holocene to late Pleistocene explosive eruptions of Hudson: H2, H1, and Ho (Table 5.1). These three eruptions of Hudson, as well as H1991, are similar in their mineral phenocrysts, although the average compositions of the eruptions have varied from more to progressively less mafic from late-glacial to historic times (Weller et al. 2014). These tephras all consist of phenocrysts of plagioclase, clinopyroxene, orthopyroxene, and olivine with variable amounts of dense black mafic glass (Weller et al. 2014) and more felsic pumice lapilli. The olivines in these Hudson-derived tephra were collected from three different lake cores (Fig. 5.2; Table 5.1). The H2 tephra (~3,868±84 cal years BP; Weller et al. 2017a) was taken from the lake Baguales core (LB; Figs. 5.2 and A5.1 of the Appendix), the H1 tephra (~7,750 cal years BP; Stern et al. 2016) from lake Edita (LEd) near Cochrane, and the Ho tephra (18,459±205 cal years BP; Weller et al. 2015, 2017b) from lake Mellizas (LM) near Coyhaique.

5.4.2 Mentolat olivines

Throughout the Holocene, Mentolat has produced tephra consisting of abundant phenocryst of plagioclase, clinopyroxene, orthopyroxene, and amphibole (Weller et al. 2015). Only some of the Mentolat-derived tephra have abundant olivine phenocrysts. Great variability in the glass color and composition is observed in Mentolat tephra. Many of the eruptive units contain fine white pumice lapilli ranging from dacite to rhyolite in composition (Weller et al. 2017a) and a smaller proportions of dark grey mafic glasses. Olivine phenocrysts were selected from three Holocene eruptions each taken from different lake cores (Table 5.1). These eruptions include the

tephra B2 (1,426±367 cal years BP; Weller et al. 2017a) from lake Tranquillo (LTr; Fig. 5.2), tephra D1 (1,774±216 cal years BP) from lake Unco (LU), and tephra I (>5,151 cal years BP) in lake Las Mellizas (LLM) from the Río Cisnes valley east of Mentolat (Weller et al. 2017a).

5.4.3 Macá olivines

Macá has only produced one regionally widespread tephra deposit (MAC1; ~1,922±215 cal years BP; Naranjo and Stern 2004; Weller et al. 2015, 2017b). This tephra is predominately black to dark brown in color and olivine, clinopyroxene, and plagioclase are the dominant phenocrysts. The olivines were selected from this tephra in the lake Baguales core (LB; Figs. 5.2 and A5.1 of the Appendix; Table 5.1).

5.4.4 Melimoyu olivines

Melimoyu tephra generally consist of phenocryst of plagioclase, orthopyroxene, clinopyroxene, and olivine. The Melimoyu derived olivine phenocrysts were picked from the MEL2 tephra (~1,680 cal years BP) of the lake Las Mellizas (LLM; Table 5.1) core taken from the lower reaches of the Río Cisnes valley (Fig. 5.2; Weller el al. 2017a). MEL2 tephra has black to light brown glass and pumice with an andesitic bulk rock composition (Naranjo and Stern 2004).

5.5 Methods

Olivine phenocrysts were hand-picked from the tephra deposits, mounted in epoxy and polished to expose melt inclusions. Melt inclusion and mineral phenocryst major element contents were determined using a Jeol JXA-733 Electron Microprobe that was operating at 15 KV accelerating potential with a 5 nA probe current for the glasses and 20 nA probe current for the mineral phenocryst. Volatile elements were analyzed early in the analysis sequence and a defocused beam was used to minimize of loss of volatile elements such as Na, Cl and F from the

melt inclusion glasses. Repeat analyses were performed on each inclusion and their host olivine phenocrysts. Some olivine phenocrysts contained multiple inclusions that were treated as independent and not averaged with other inclusions from the same olivine. Water contents of the melt inclusions were estimated by the difference method assuming all of the missing components in the analyses were H_2O.

5.5.1 Melt Inclusion Post-entrapment Modifications

After entrapment of a melt inclusion, crystallization of olivine along the wall of the inclusion can occur, which will remove olivine constituents from the glass. We corrected for this post-entrapment crystallization (PEC) by adding increasingly forsteritic olivine back into the melt inclusion at 0.01% increments until the melt inclusion is in equilibrium with the forsterite content of the core of the host olivine (Table 5.2). These corrections are carried out using the Petrolog software (Danyushevsky and Plechov 2011) with the olivine melt equilibrium model of Ford et al. (1983).

Additionally, after entrapment, the melt inclusion can be further modified by diffusive re-equilibration with the host olivine. Danyushevky et al. (2000, 2002) observed that melt inclusion compositions were modified by diffusive exchange of Fe out of the melt inclusion. The loss of Fe can be recognized by lower FeO* (FeO as total Fe) values in the melt inclusion compared to the whole rock FeO* versus MgO trend of the host magma. The degree of Fe lost by diffusion in the melt inclusion is usually greatest in the most MgO-rich olivines (Danyushevky et al. 2002). To assess for Fe-loss, we used two methods. First, we compared uncorrected melt inclusion FeO* vs. host olivine Fo content. Additionally, we compared the FeO* fractionation trend for the melt inclusion with published whole rock and bulk tephra analyses for SSVZ volcanoes following the method of Danyushevky et al. (2000). These comparisons suggest that some of the melt inclusion

Table 5.2a. Major element compositions (wt. % oxide) for Hudson melt inclusions and the host olivine

Eruption	Ho	Ho	Ho	Ho	Ho	Ho	Ho	Ho	Ho	Ho	Ho
Inclusion	a	b	a	a	b	a	a	a	b	b	a
Lab ID	HUD13	HUD13	HUD14	HUD15	HUD15	HUD19	HUD20	HUD22	HUD22	HUD24	HUD25
n	3	2	3	3	3	4	3	2	1	2	3
SiO_2	57.54	57.90	49.70	50.34	49.42	50.37	50.96	55.39	56.00	51.55	57.07
TiO_2	1.79	1.83	1.33	1.75	1.91	1.59	1.64	1.45	1.45	1.84	1.96
Al_2O_3	17.53	17.61	18.10	16.06	15.87	17.09	16.27	15.74	16.25	16.18	17.21
FeO	7.66	5.17	8.00	9.47	9.90	7.09	8.92	8.01	8.22	9.01	5.53
MnO	0.185	0.122	0.078	0.147	0.228	0.100	0.141	0.281	0.144	0.085	0.115
MgO	2.24	1.16	3.45	3.08	3.14	2.90	4.41	3.37	2.90	4.22	1.30
CaO	7.45	6.64	11.06	8.67	8.82	9.56	9.25	7.22	7.30	8.04	6.99
Na_2O	4.75	5.59	3.18	3.78	3.51	3.52	3.33	4.02	3.75	2.86	5.31
K_2O	1.59	2.62	1.10	1.36	1.32	1.39	1.05	1.38	1.32	1.14	1.93
P_2O_5	0.781	0.853	0.464	0.464	0.475	0.548	0.842	0.485	0.468	0.830	1.073
Cr_2O_3	0.012	0.042	0.022	0.000	0.028	0.035	0.015	0.077	0.082	0.005	0.021
S	809	635	825	1718	1796	1848	911	375	465	1778	785
F	2249	2668	394	194	0	301	292	1012	0	310	778
Cl	1151	1740	517	511	667	574	632	877	785	925	1611
H_2O	0.00	0.03	3.23	4.39	4.90	5.29	2.87	2.40	1.92	3.70	1.13
Host Olivine											
Olivine	a	a	a	a	a	a	a	a	a	a	a
n	2	2	2	2	2	4	3	2	2	2	3
SiO_2	37.85	37.85	39.34	38.58	38.58	39.67	39.32	38.18	38.18	38.81	37.60
Al_2O_3	0.01	0.01	0.02	0.03	0.03	0.02	0.03	0.01	0.01	0.01	0.00
FeO	26.12	26.12	14.93	22.17	22.17	16.05	17.04	22.99	22.99	19.81	27.21
MnO	0.506	0.506	0.266	0.344	0.344	0.290	0.288	0.413	0.413	0.351	0.583
MgO	35.80	35.80	45.09	38.88	38.88	42.76	41.85	37.50	37.50	40.17	34.07
CaO	0.185	0.185	0.236	0.235	0.235	0.234	0.226	0.176	0.176	0.184	0.184
TiO_2	0.024	0.024	0.005	0.019	0.019	0.008	0.000	0.033	0.033	0.015	0.022
NiO	0.028	0.028	0.129	0.054	0.054	0.109	0.128	0.141	0.141	0.113	0.038
Cr_2O_3	0.000	0.000	0.003	0.000	0.000	0.015	0.044	0.006	0.006	0.016	0.001
Total	100.52	100.52	100.02	100.30	100.30	99.15	98.94	99.46	99.46	99.48	99.71
Fo	70.9	70.9	84.3	75.8	75.8	82.6	81.4	74.4	74.4	78.3	69.1
PEC-Corrected											
SiO_2	55.05	55.08	48.27	50.13	49.28	48.76	50.15	54.15	54.74	47.94	54.61
TiO_2	1.63	1.61	1.15	1.69	1.84	1.38	1.52	1.36	1.36	1.63	1.75
Al_2O_3	16.02	15.46	15.69	15.53	15.35	14.79	15.13	14.76	15.19	14.28	15.33
Fe_2O_3	1.512	1.762	1.105	1.382	1.421	1.195	1.193	1.386	1.299	1.186	1.717
FeO	8.56	8.59	8.91	8.41	8.63	8.84	8.83	8.81	8.74	8.84	8.50
MnO	0.169	0.107	0.068	0.142	0.220	0.086	0.131	0.264	0.135	0.075	0.103
MgO	3.73	3.56	8.28	4.66	4.82	7.35	6.90	4.67	4.68	5.91	3.34
CaO	6.81	5.82	9.59	8.38	8.53	8.27	8.60	6.77	6.82	7.10	6.23
Na_2O	4.34	4.91	2.76	3.65	3.40	3.04	3.10	3.77	3.51	2.53	4.73
K_2O	1.450	2.302	0.956	1.317	1.275	1.199	0.979	1.292	1.236	1.005	1.718
P_2O_5	0.713	0.749	0.402	0.448	0.460	0.474	0.783	0.455	0.438	0.732	0.956
Cr_2O_3	0.011	0.037	0.019	0.000	0.027	0.030	0.014	0.073	0.076	0.004	0.019
S	753	554	702	1651	1726	1568	843	352	434	1685	697
F	2091	2327	335	186	0	255	270	950	0	294	691
Cl	1070	1518	440	491	641	487	585	823	733	876	1430
H_2O	0.00	0.02	2.80	4.24	4.74	4.58	2.67	2.25	1.80	8.79	1.01

Table 5.2b. Major element compositions (wt. % oxide) for Hudson melt inclusions and the host olivine

Eruption	H2	H2	H1	H1	H1	H1	H1	Ho	Ho	Ho	Ho
Inclusion	a	a	a	a	b	a	b	a	a	a	a
Lab ID	HUD7	HUD8	HUD17	HUD18	HUD18	HUD21	HUD21	HUD3	HUD4	HUD9	HUD12
n	3	3	2	4	2	3	3	5	4	3	3
SiO_2	52.07	52.33	51.33	49.56	50.27	51.25	54.59	49.24	53.35	51.61	55.45
TiO_2	1.38	1.66	1.82	1.31	1.34	1.33	1.32	1.50	1.93	1.22	1.89
Al_2O_3	16.21	17.59	17.16	16.69	17.14	18.11	20.03	16.10	16.61	19.04	19.68
FeO	8.40	7.40	9.24	7.96	8.10	6.61	4.64	10.34	8.00	5.73	3.00
MnO	0.200	0.190	0.213	0.164	0.196	0.082	0.184	0.199	0.237	0.146	0.063
MgO	3.49	2.19	3.07	4.84	4.17	2.01	0.99	3.33	2.88	2.77	0.86
CaO	8.17	11.81	8.94	10.13	10.14	11.45	7.89	8.97	6.23	10.43	9.00
Na_2O	3.68	3.54	3.91	3.32	3.58	3.31	4.12	3.41	5.09	3.52	4.87
K_2O	1.19	1.13	1.09	0.73	0.75	0.75	0.96	1.46	1.42	0.92	1.62
P_2O_5	0.488	0.477	0.559	0.343	0.263	0.423	0.334	0.447	0.707	0.242	1.004
Cr_2O_3	0.025	0.062	0.000	0.018	0.009	0.027	0.037	0.044	0.000	0.018	0.037
S	1446	1373	1141	1125	1293	1524	1645	2042	1214	959	361
F	0	598	721	732	294	493	1583	749	71	995	401
Cl	618	622	1124	778	974	857	1205	620	890	931	1145
H_2O	4.27	1.20	2.27	4.57	3.64	4.18	4.30	4.36	3.17	3.99	2.33
Host Olivine											
Olivine	a	a	a	a	a	a	a	a	a	a	a
n	2	4	2	2	2	3	3	2	2	2	3
SiO_2	38.53	39.86	39.13	39.68	39.68	39.78	39.78	38.82	38.32	39.99	38.44
Al_2O_3	0.024	0.016	0.028	0.025	0.025	0.012	0.012	0.012	0.015	0.016	0.021
FeO	19.02	17.09	19.29	15.32	15.32	14.94	14.94	22.29	22.80	15.44	19.73
MnO	0.346	0.334	0.357	0.278	0.278	0.253	0.253	0.355	0.482	0.252	0.336
MgO	40.79	41.86	41.56	44.85	44.85	43.92	43.92	37.29	37.01	44.73	38.79
CaO	0.186	0.265	0.248	0.235	0.235	0.242	0.242	0.230	0.177	0.186	0.193
TiO_2	0.009	0.019	0.004	0.010	0.010	0.001	0.001	0.023	0.017	0.024	0.011
NiO	0.065	0.049	0.039	0.069	0.069	0.104	0.104	0.036	0.041	0.090	0.110
Cr_2O_3	0.000	0.027	0.010	0.015	0.015	0.005	0.005	0.000	0.010	0.006	0.007
Total	98.95	99.52	100.66	100.48	100.48	99.26	99.26	99.05	98.87	100.73	97.64
Fo	79.3	81.4	79.3	83.9	83.9	84.0	84.0	74.9	74.3	83.8	77.8
PEC Corrected											
SiO_2	51.03	50.50	50.58	48.43	49.01	49.02	50.97	49.15	52.33	49.14	51.68
TiO_2	1.27	1.44	1.69	1.18	1.19	1.09	1.03	1.46	1.82	1.00	1.54
Al_2O_3	14.94	15.26	15.95	14.98	15.21	14.91	15.67	15.61	15.61	15.69	16.00
Fe_2O_3	1.240	1.218	1.280	1.122	1.138	1.096	1.076	1.470	1.545	1.087	1.334
FeO	8.83	8.82	8.80	8.89	8.92	8.94	8.94	9.11	8.60	9.00	8.71
MnO	0.184	0.165	0.198	0.147	0.174	0.067	0.144	0.193	0.222	0.120	0.052
MgO	6.08	6.81	5.92	8.10	8.07	8.30	8.38	4.88	4.26	8.19	5.36
CaO	7.53	10.24	8.31	9.09	8.99	9.43	6.17	8.70	5.86	8.60	7.32
Na_2O	3.39	3.07	3.63	2.98	3.18	2.72	3.22	3.31	4.78	2.90	3.96
K_2O	1.096	0.983	1.017	0.659	0.664	0.616	0.753	1.419	1.337	0.758	1.320
P_2O_5	0.450	0.414	0.520	0.307	0.234	0.349	0.261	0.433	0.664	0.200	0.816
Cr_2O_3	0.023	0.053	0.000	0.017	0.008	0.023	0.029	0.042	0.000	0.015	0.030
S	1324	1168	1052	1000	1132	1208	1210	1966	1140	767	286
F	0	509	664	651	257	391	1165	721	66	796	318
Cl	566	529	1035	692	852	679	886	597	836	744	909
H_2O	3.94	1.04	2.11	4.10	3.23	3.44	3.37	4.23	2.98	3.29	1.89

Table 5.2c. Major element compositions (wt. % oxide) for Mentolat melt inclusions and the host olivine

Eruption	B2	B2	B2	B2	D1	D1	D1	D1	I	I	I
Inclusion	a	a	b	a	a	a	b	a	b	a	a
Lab ID	MEN17	MEN 21	MEN 21	MEN22	MEN3	MEN19	MEN 19	MEN 20	MEN1 3	MEN14	MEN15
n	4	3	2	4	2	3	1	5	2	4	3
SiO_2	51.29	48.76	48.78	49.66	50.40	50.70	50.71	49.04	58.85	53.18	52.93
TiO_2	1.25	1.12	1.17	1.10	1.11	0.95	1.04	1.41	1.14	1.11	1.28
Al_2O_3	19.29	19.21	19.82	19.08	18.13	19.95	21.63	18.51	17.17	17.32	18.18
FeO	6.32	7.20	6.17	7.10	7.60	5.63	5.40	6.87	7.55	7.94	6.69
MnO	0.099	0.111	0.160	0.186	0.159	0.214	0.015	0.095	0.144	0.101	0.156
MgO	1.95	2.57	1.78	3.47	3.43	3.33	1.43	2.62	1.97	2.70	2.17
CaO	9.51	9.92	10.51	9.35	8.14	9.34	10.12	9.52	6.26	6.89	7.94
Na_2O	3.52	3.16	3.38	3.59	3.17	1.74	2.27	3.15	4.44	2.83	2.78
K_2O	0.59	0.32	0.35	0.43	0.44	0.47	0.37	0.45	1.05	0.71	0.73
P_2O_5	0.185	0.128	0.159	0.154	0.162	0.217	0.213	0.179	0.398	0.235	0.300
Cr_2O_3	0.060	0.046	0.018	0.053	0.048	0.031	0.000	0.042	0.005	0.000	0.003
S	2122	2397	2526	2608	1774	2088	3734	2611	522	1767	2140
F	371	98	1780	73	1060	0	0	1170	719	219	789
Cl	1271	1435	1183	1241	1382	1125	1024	1273	1252	1513	1338
H_2O	5.30	6.73	6.90	5.09	6.60	6.83	5.79	7.30	0.77	6.42	6.16
Host Olivine											
Olivine	b	a	a	a	a	a	a	a	a	a	b
n	3	2	2	3	2	2	2	4	2	2	3
SiO_2	39.14	38.87	38.87	39.50	38.25	38.80	38.80	39.04	38.36	38.31	38.23
Al_2O_3	0.024	0.004	0.004	0.020	0.003	0.005	0.005	0.022	0.009	0.012	0.021
FeO	17.96	19.23	19.23	17.08	22.84	17.99	17.99	18.60	22.61	23.53	22.24
MnO	0.277	0.269	0.269	0.258	0.425	0.265	0.265	0.301	0.391	0.381	0.333
MgO	41.11	40.75	40.75	42.12	38.36	42.63	42.63	40.83	37.61	37.42	38.91
CaO	0.159	0.150	0.150	0.142	0.125	0.133	0.133	0.149	0.120	0.117	0.132
TiO_2	0.018	0.003	0.003	0.019	0.010	0.016	0.016	0.004	0.014	0.019	0.007
NiO	0.024	0.010	0.010	0.054	0.006	0.052	0.052	0.047	0.000	0.024	0.019
Cr_2O_3	0.003	0.024	0.024	0.015	0.002	0.009	0.009	0.001	0.000	0.000	0.010
Total	98.72	99.30	99.30	99.22	100.0	99.88	99.88	99.00	99.11	99.83	99.92
Fo	80.3	79.1	79.1	81.5	75.0	80.9	80.9	79.6	74.8	73.9	75.7
PEC-Corrected											
SiO_2	50.49	48.59	48.24	49.44	50.53	49.82	49.64	48.79	58.23	53.16	52.43
TiO_2	1.15	1.07	1.08	1.05	1.11	0.88	0.92	1.34	1.10	1.09	1.22
Al_2O_3	17.77	18.33	18.33	18.23	18.01	18.40	19.25	17.55	16.54	17.00	17.30
Fe_2O_3	0.798	0.761	0.782	0.791	0.808	0.614	0.634	0.800	0.965	0.820	0.779
FeO	6.99	7.01	7.00	7.04	7.06	7.15	7.19	6.98	6.95	7.21	7.00
MnO	0.091	0.106	0.148	0.177	0.158	0.197	0.014	0.090	0.139	0.099	0.148
MgO	5.07	4.76	4.72	5.43	3.89	5.76	5.65	4.87	3.63	3.83	4.09
CaO	8.76	9.46	9.72	8.94	8.09	8.61	9.01	9.03	6.03	6.77	7.56
Na_2O	3.24	3.02	3.12	3.43	3.15	1.61	2.03	2.99	4.28	2.78	2.64
K_2O	0.541	0.302	0.328	0.409	0.435	0.435	0.327	0.431	1.014	0.699	0.699
P_2O_5	0.170	0.123	0.147	0.147	0.161	0.201	0.189	0.170	0.384	0.231	0.285
Cr_2O_3	0.056	0.044	0.017	0.050	0.047	0.028	0.000	0.040	0.004	0.000	0.003
S	1933	2265	2307	2470	1753	1912	3255	2451	501	1723	2020
F	338	92	1626	69	1047	0	0	1098	690	213	745
Cl	1158	1355	1080	1175	1365	1030	893	1195	1202	1475	1262
H_2O	4.89	6.42	6.38	4.86	6.56	6.30	5.15	6.93	0.74	6.31	5.86

Table 5.2d. Major element compositions (wt. % oxide) for Melimoyu and Maca melt inclusions and the host olivine

Eruption	MEL2	MEL2	MEL2	MAC1	MAC1	MAC1	MAC1	MAC1	MAC1	MAC1
Inclusion	a	b	a	a	a	b	a	a	c	a
Lab ID	MEL1	MEL1	MEL2	MAC1	MAC2	MAC3	MAC6	MAC8	MAC8	MAC12
n	3	2	2	3	3	4	4	3	2	4
SiO_2	52.44	53.58	50.50	50.90	51.08	52.00	52.18	50.26	51.68	49.97
TiO_2	1.34	1.46	1.39	1.16	1.50	1.42	1.56	1.59	1.90	1.31
Al_2O_3	17.44	18.40	18.12	18.19	17.87	15.84	15.30	15.61	15.64	16.00
FeO	7.91	6.45	8.24	8.16	6.89	9.67	8.69	9.34	9.21	9.04
MnO	0.167	0.098	0.163	0.179	0.151	0.182	0.161	0.138	0.119	0.154
MgO	3.84	2.20	3.31	4.05	4.37	3.54	3.26	3.62	4.17	4.57
CaO	8.91	9.42	9.90	9.00	9.36	8.21	7.68	8.46	8.57	8.50
Na_2O	3.30	3.90	3.33	3.35	3.50	3.75	3.65	3.37	3.37	3.34
K_2O	1.02	1.18	0.93	0.85	1.02	1.17	1.15	1.07	1.01	1.05
P_2O_5	0.506	0.479	0.457	0.425	0.629	0.560	0.601	0.636	0.608	0.561
Cr_2O_3	0.062	0.053	0.023	0.052	0.015	0.055	0.044	0.043	0.093	0.032
S	1209	1081	1524	1016	1456	917	1209	1082	1929	1265
F	902	449	295	1164	1769	650	219	579	1900	434
Cl	719	977	723	236	547	797	694	749	628	915
H_2O	2.66	2.37	3.19	3.33	3.10	3.29	5.36	5.50	3.01	5.07
Host Olivine										
Olivine	a	a	a	a	a	a	a	a	a	a
n	2	2	2	2	3	2	2	2	2	2
SiO_2	39.02	39.02	40.21	38.65	39.18	38.55	38.15	38.44	38.44	39.18
Al_2O_3	0.026	0.026	0.011	0.013	0.026	0.012	0.024	0.019	0.019	0.028
FeO	17.20	17.20	15.48	19.53	16.01	20.69	22.39	20.38	20.38	18.85
MnO	0.293	0.293	0.245	0.347	0.252	0.355	0.415	0.380	0.380	0.333
MgO	43.28	43.28	45.30	40.05	43.07	39.50	37.88	40.76	40.76	41.77
CaO	0.210	0.210	0.199	0.186	0.191	0.214	0.199	0.228	0.228	0.203
TiO_2	0.035	0.035	0.011	0.010	0.017	0.009	0.026	0.011	0.011	0.030
NiO	0.076	0.076	0.148	0.123	0.138	0.094	0.088	0.062	0.062	0.048
Cr_2O_3	0.019	0.019	0.008	0.030	0.017	0.000	0.006	0.008	0.008	0.000
Total	100.17	100.17	101.61	98.93	98.90	99.42	99.17	100.30	100.30	100.45
Fo	81.8	81.8	83.9	78.5	82.7	77.3	75.1	78.1	78.1	79.8
PEC-Corrected										
SiO_2	50.60	50.88	48.40	50.31	49.87	51.70	52.10	50.04	51.64	49.87
TiO_2	1.17	1.21	1.14	1.10	1.36	1.37	1.54	1.54	1.86	1.28
Al_2O_3	15.22	15.29	14.93	17.30	16.19	15.30	15.04	15.08	15.31	15.62
Fe_2O_3	1.193	1.228	1.241	1.042	1.060	1.270	1.176	1.195	1.208	1.102
FeO	9.55	9.37	10.13	8.39	8.38	8.53	7.64	8.27	8.24	8.13
MnO	0.146	0.082	0.134	0.171	0.137	0.176	0.158	0.134	0.116	0.151
MgO	7.77	7.49	9.33	5.51	7.03	5.22	4.18	5.32	5.31	5.73
CaO	7.78	7.83	8.15	8.56	8.49	7.92	7.55	8.17	8.39	8.30
Na_2O	2.88	3.24	2.74	3.19	3.17	3.62	3.58	3.26	3.30	3.26
K_2O	0.888	0.980	0.769	0.813	0.928	1.134	1.135	1.033	0.992	1.028
P_2O_5	0.442	0.398	0.376	0.404	0.570	0.541	0.591	0.614	0.595	0.548
Cr_2O_3	0.054	0.044	0.019	0.049	0.014	0.053	0.043	0.041	0.091	0.031
S	1040	872	1209	964	1311	881	1184	1039	1876	1230
F	776	362	234	1105	1593	624	214	556	1847	422
Cl	618	788	574	224	492	766	679	719	610	889
H_2O	2.32	1.97	2.63	3.17	2.81	3.17	5.27	5.32	2.94	4.95

Table 5.2e. Major element compositions (wt. % oxide) for Mentolat and Macá melt inclusions and the host olivine

Eruption	I	MAC1	MAC1	MAC1
Inclusion	b	b	a	a
Lab ID	MEN15	MAC12	MAC13	MAC14
n	2	2	4	3
SiO_2	54.81	48.94	50.05	52.76
TiO_2	1.13	1.95	1.77	1.70
Al_2O_3	18.35	16.37	17.90	15.79
FeO	7.20	9.84	8.04	9.43
MnO	0.109	0.205	0.164	0.075
MgO	2.88	5.35	4.13	3.66
CaO	8.49	8.54	9.65	7.23
Na_2O	4.02	3.22	3.39	4.16
K_2O	0.84	1.08	0.71	1.34
P_2O_5	0.359	0.528	0.489	0.621
Cr_2O_3	0.018	0.027	0.055	0.034
S	1903	1131	1253	1007
F	1601	0	148	2006
Cl	1697	816	165	959
H_2O	1.10	3.62	3.33	2.74
Host Olivine				
Olivine	**b**	**a**	**a**	**a**
n	**3**	**2**	**2**	**2**
SiO_2	38.23	39.18	39.63	38.25
Al_2O_3	0.021	0.028	0.037	0.019
FeO	22.24	18.85	15.51	23.98
MnO	0.333	0.333	0.240	0.419
MgO	38.91	41.77	44.25	37.60
CaO	0.132	0.203	0.185	0.195
TiO_2	0.007	0.030	0.002	0.030
NiO	0.019	0.048	0.138	0.079
Cr_2O_3	0.010	0.000	0.004	0.008
Total	99.92	100.45	100.01	100.59
Fo	75.7	79.8	83.6	73.6
PEC-Corrected				
SiO_2	54.68	48.93	49.08	52.77
TiO_2	1.11	1.93	1.61	1.68
Al_2O_3	17.96	16.15	16.26	15.66
Fe_2O_3	0.884	1.229	1.029	1.412
FeO	6.91	8.73	8.40	8.30
MnO	0.107	0.203	0.149	0.074
MgO	3.85	6.06	7.46	4.10
CaO	8.31	8.42	8.77	7.18
Na_2O	3.93	3.17	3.08	4.13
K_2O	0.820	1.065	0.646	1.332
P_2O_5	0.352	0.521	0.444	0.616
Cr_2O_3	0.018	0.027	0.050	0.034
S	1850	1112	1128	995
F	1556	0	133	1983
Cl	1650	802	149	948
H_2O	1.07	3.57	3.02	2.72

have experienced varying degrees of Fe-loss, particularly for olivine from the Hudson and Melimoyu derived inclusions, but less so for the Mentolat and Macá inclusions.

Ideally, the Fe-loss correction would be based on whole rock analysis done for each tephra deposit. However, due to the heterogeneous nature of these tephras, which represent the end processes of mixing and setting within the lakes themselves, and also segregation of material during areal transport, it is difficult to know what the bulk whole rock composition of these tephra was originally. Thus, bulk tephra analyses are not useful to assess for the degree of Fe-loss. Instead, to correct for diffusion related re-equilibration, the FeO* content of the melt inclusions are either corrected to the average of the highest FeO* in other olivines from the same volcanoes deemed to be unaffected or least affected by diffusion related Fe-loss (Table A5.2 of the Appendix). Where sufficient data is not available for this determination, the melt inclusion compositions are corrected to the FeO* content of previously published whole rock compositions of lavas from the different centers. The latter method was only utilized for the melt inclusions from Melimoyu.

Melt inclusion can also loose volatile gasses by diffusion, formation of vapor bubbles, and by rupturing of the host crystal (Wallace 2005). Two criteria were used to assess for melt inclusion degassing. If the PEC and Fe loss-corrected melt inclusion failed either of these criteria, they were excluded from further modeling (Table A5.2 of the Appendix). Melt inclusions with PEC and Fe loss-corrected S content below 500 ppm were deemed to be degassed following the criteria established by Kelley et al. (2010) and therefore are excluded from further modeling. Additionally, PEC and Fe loss-corrected melt inclusions with water contents less than 1.5 wt. % after PEC-correction were discarded because they have likely lost water and other volatiles and produced unrealistic results after modeling.

5.5.2 Parental Magma Composition

The least degassed PEC and Fe loss-corrected melt compositions were fractionation-corrected back to primary melts in equilibrium with mantle olivine by incrementally adding equilibrium olivine and/or clinopyroxene to each inclusion composition until mantle equilibrium is reached (Table 5.3). Mantle equilibrium is defined on a chemical basis for the olivine composition and the calculations are complete when the olivine reaches Fo_{90} (Stolper and Newman 1994). These calculations are performed using Petrolog in increments of 0.01% carried out at 1 kbar and a QFM+1 buffer using the olivine-melt equilibrium model of Ford et al. (1983) and a clinopyroxene-melt equilibrium model of Ariskin et al. (1993). To assess for the syn-crystallization of other phases prior to melt entrapment, we examined major element trends in CaO, Al_2O_3, and MgO for the PEC-corrected melt inclusion (Fig. 5.4). The data suite for each volcanic center show variations consistent with the fractionation of olivine at all the centers, and clinopyroxene at Mentolat, Macá, Hudson, but not Melimoyu. None of the melt inclusions preserve evidence for significant plagioclase fractionation as seen by their nearly constant Al_2O_3 contents with decreasing MgO (Fig. 5.4). Clinopyroxene saturation is indicated by the slight downward trend in CaO with decreasing MgO initiated at different MgO contents for each center and thus we apply the olivine-clinopyroxene cotextic up to these specified MgO contents after which olivine is assumed to be the only liquidus phase (Table A5.2 of the Appendix).

The amount of olivine and clinopyroxene addition varied between the different centers but as a whole, the suite of data required an average olivine addition of ~20% which ranged to as high as 24% and to as low as 12% (Table A5.2 of the Appendix). These values are similar to the average olivine addition made to estimate primitive magma compositions from the melt inclusion in olivine

Table 5.3a. Major element compositions for melt inclusions in equilibrium with mantle olivine

Volcano	Hudson	Hudson	Hudson	Hudson	Hudson	Hudson	Hudson	Hudson	Hudson
Eruption	H2	H1	H1	H1	H1	H1	Ho	Ho	Ho
Inclusion	a	a	a	b	a	b	a	a	a
Lab ID	HUD 7	HUD 17	HUD 18	HUD 18	HUD 21	HUD 21	HUD 3	HUD 4	HUD 9
SiO_2	48.49	48.05	46.98	47.14	47.22	48.71	47.31	49.24	47.23
TiO_2	0.95	1.25	0.98	0.98	0.91	0.85	0.97	1.19	0.83
Al_2O_3	11.35	12.08	12.50	12.61	12.38	12.87	11.03	10.79	12.95
Fe_2O_3	2.436	2.341	2.242	2.250	2.198	2.205	2.527	2.589	2.200
FeO	9.21	9.17	9.10	9.06	9.08	9.04	9.42	9.13	9.12
MnO	0.138	0.147	0.123	0.144	0.056	0.118	0.129	0.145	0.099
MgO	15.07	14.61	14.42	14.30	14.52	14.88	15.02	14.81	14.56
CaO	6.17	6.96	7.59	7.46	7.83	5.07	7.92	5.74	7.10
Na_2O	2.53	2.69	2.48	2.63	2.26	2.64	2.21	3.12	2.40
K_2O	0.819	0.754	0.550	0.550	0.511	0.619	0.947	0.872	0.626
P_2O_5	0.336	0.385	0.256	0.194	0.290	0.214	0.289	0.433	0.165
Cr_2O_3	0.017	0.000	0.014	0.007	0.019	0.024	0.028	0.000	0.012
S	997	790	838	949	1013	1005	1320	756	640
F	0	499	545	216	327	967	484	44	664
Cl	426	777	580	715	570	736	401	554	621
H_2O	2.48	1.56	2.76	2.68	2.75	2.76	2.20	1.94	2.71

Volcano	Hudson	Hudson	Hudson	Hudson	Hudson	Hudson	Melimoyu	Melimoyu	Melimoyu
Eruption	Ho	Ho	Ho	Ho	Ho	Ho	MEL2	MEL2	MEL2
Inclusion	a	a	b	a	a	b	a	b	a
Lab ID	HUD 14	HUD 15	HUD 15	HUD 19	HUD 20	HUD 24	MEL1	MEL1	MEL 2
SiO_2	46.60	48.31	47.73	47.21	47.64	48.28	47.92	48.17	46.45
TiO_2	0.96	1.15	1.26	1.12	1.20	1.27	0.91	0.95	0.93
Al_2O_3	13.14	11.24	11.11	12.05	11.91	11.43	11.86	11.98	12.10
Fe_2O_3	2.169	2.318	2.379	2.358	2.324	2.266	2.447	2.471	2.524
FeO	9.05	8.81	9.10	9.21	9.23	9.29	9.67	9.55	9.97
MnO	0.057	0.097	0.150	0.070	0.103	0.059	0.114	0.064	0.109
MgO	14.18	14.02	14.49	14.68	14.89	15.43	15.87	15.48	16.02
CaO	8.03	8.10	7.98	6.74	6.77	6.27	6.06	6.14	6.61
Na_2O	2.31	2.49	2.32	2.48	2.44	1.97	2.25	2.54	2.22
K_2O	0.800	0.896	0.871	0.977	0.771	0.784	0.693	0.768	0.623
P_2O_5	0.337	0.305	0.314	0.386	0.616	0.572	0.345	0.312	0.305
Cr_2O_3	0.016	0.000	0.019	0.024	0.011	0.004	0.042	0.035	0.015
S	594	1129	1180	1277	672	1231	821	693	993
F	284	128	0	208	215	215	612	287	192
Cl	372	336	438	397	466	640	488	626	471
H_2O	2.34	2.26	2.27	2.70	2.10	2.38	1.81	1.54	2.13

Table 5.3b. Major element compositions for melt inclusions in equilibrium with mantle olivine

Volcano	Macá	Macá	Macá	Macá	Macá	Macá	Macá	Macá	Macá	Macá
	MAC	MAC	MAC	MAC	MAC	MAC	MAC	MAC	MAC	MAC
Eruption	1	1	1	1	1	1	1	1	1	1
Inclusion	a	a	b	a	a	c	a	b	a	a
Lab ID	MAC1	MAC2	MAC3	MAC6	MAC8	MAC8	MAC12	MAC12	MAC13	MAC14
SiO_2	47.56	47.75	48.36	49.67	47.95	48.44	48.00	46.61	47.25	49.10
TiO_2	0.84	1.11	1.01	1.10	1.18	1.40	1.01	1.49	1.34	1.14
Al_2O_3	13.24	13.21	11.35	11.18	11.58	11.55	12.38	12.46	13.50	10.99
Fe_2O_3	2.150	2.079	2.483	2.241	2.368	2.289	2.222	2.289	1.988	2.513
FeO	9.08	8.76	9.27	8.62	9.22	9.10	8.89	9.39	8.73	9.17
MnO	0.131	0.112	0.130	0.113	0.103	0.087	0.120	0.157	0.124	0.050
MgO	14.62	13.95	15.10	14.17	14.97	14.80	14.32	14.87	13.78	14.93
CaO	6.55	6.92	6.01	6.66	6.28	6.38	6.58	6.50	7.28	6.14
Na_2O	2.44	2.59	2.67	2.57	2.50	2.48	2.58	2.45	2.55	2.79
K_2O	0.622	0.757	0.838	0.814	0.794	0.747	0.814	0.822	0.536	0.900
P_2O_5	0.309	0.465	0.400	0.424	0.472	0.448	0.434	0.402	0.369	0.416
Cr_2O_3	0.038	0.011	0.039	0.031	0.032	0.069	0.025	0.021	0.042	0.023
S	746	1081	660	843	792	1430	970	867	946	683
F	854	1314	467	153	424	1408	333	0	112	1361
Cl	173	406	573	484	548	465	701	625	125	650
H_2O	2.42	2.29	2.34	2.40	2.55	2.22	2.62	2.54	2.51	1.84

Volcano	Mentolat	Mentolat	Mentolat	Mentolat	Mentolat	Mentolat	Mentolat	Mentolat	Mentolat	Mentolat
Eruption	B2	B2	B2	B2	D1	D1	D1	D1	I	I
Inclusion	a	a	b	a	a	a	b	a	a	a
Lab ID	MEN17	MEN 21	MEN 21	MEN22	MEN 3	MEN 19	MEN 19	MEN 20	MEN14	MEN 15
SiO_2	48.94	47.94	47.64	48.24	49.20	49.06	48.45	48.33	50.71	50.31
TiO_2	0.95	0.88	0.90	0.89	0.83	0.73	0.76	1.11	0.79	0.92
Al_2O_3	14.67	15.16	15.19	15.34	13.97	15.30	15.93	14.62	12.76	13.36
Fe_2O_3	1.672	1.651	1.669	1.638	1.784	1.431	1.426	1.687	1.904	1.752
FeO	7.88	8.10	8.09	7.81	8.30	8.08	8.04	8.10	8.52	8.23
MnO	0.075	0.088	0.123	0.149	0.119	0.164	0.012	0.075	0.072	0.112
MgO	12.57	12.84	12.71	12.27	13.54	13.60	13.22	12.90	14.50	13.83
CaO	7.23	7.83	8.06	7.52	6.99	7.16	7.45	7.52	5.71	6.32
Na_2O	2.67	2.50	2.59	2.88	2.38	1.34	1.68	2.49	2.03	2.00
K_2O	0.447	0.250	0.272	0.344	0.328	0.362	0.271	0.359	0.509	0.529
P_2O_5	0.140	0.102	0.122	0.124	0.122	0.167	0.156	0.142	0.168	0.216
Cr_2O_3	0.046	0.036	0.014	0.042	0.036	0.023	0.000	0.033	0.000	0.002
S	1549	1801	1825	2040	1284	1516	2569	1951	1215	1469
F	270	73	1286	57	767	0	0	874	150	542
Cl	928	1078	855	970	1000	817	704	951	1040	918
H_2O	2.71	2.61	2.63	2.76	2.40	2.58	2.60	2.63	2.33	2.42

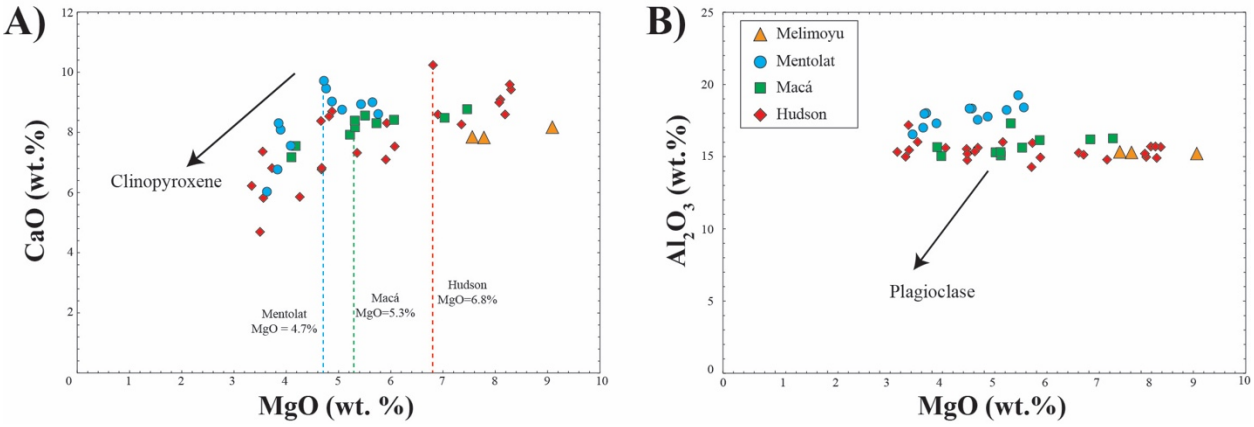

Figure 5.4. Major element variation diagrams for **A)** CaO vs MgO and **B)** Al_2O_3 vs MgO for the post-entrapment crystallization-corrected (PEC) melt inclusions compositions. Clinopyroxene saturation occurs at different MgO contents for each center while significant plagioclase fractionation didn't occur prior to melt entrapment.

from the Marianas arc (Kelley et al. 2010), lower than the average for volcanoes further north in the Andean SVZ (Wehrmann et al. 2014), and greater than was required for Hornopirén and the small monogenetic centers Apagado, South Minchinmávida, and Palena located just to the north in the Andean SSVZ (Watt et al. 2013). Where clinopyroxene addition is necessary, the average is generally low (~5%), with the exception of Hudson that required up to 19% clinopyroxene.

To calculate the S, Cl and F contents of the primitive magmas, the original volatile contents (Table 5.2) were first corrected for post-entrapment crystallization and then back calculated to primitive compositions by treating the volatile elements as perfectly incompatible and utilizing the percent olivine and clinopyroxene required for the post-entrapment crystallization correction and the fractionation correction (Table A5.2 of the Appendix).

5.5.3 Melting Parameters

To better understand the processes contributing to the petrochemical variability observed between the major centers of the SSVZ, we utilize models developed at other volcanic arcs to estimate parameters such as fraction of mantle melting (F_m), source mantle water content (C^o_{H2O}; Kelley et al. 2006), slab surface temperature (Plank et al. 2009), to generate information (Table 5.3) that can both provide a means of comparison of the physical conditions during melt generation below the different SSVZ centers and can also be used to compared to other volcanic arcs.

The concentration of incompatible minor elements are useful for evaluating mantle melting processes. At a low percent of melting, the magma will have relatively high concentrations of incompatible elements. As the melt fraction increases, their concentrations in the melt progressively decrease as they are diluted by the addition of other material into the melt. Because of this simple behavior and because Ti is likely to be retained in residual rutile and therefore

unlikely to be added to the mantle wedge during dehydration of the subducting slab, the glass TiO_2 can be used as a mantle melt fraction (F_m) proxy (Kelley et al. 2006). Solving the batch melting equation in terms of TiO_2, F_m can be estimated by making an assumption of the mantle Ti concentration (Kelley et al. 2006). Similarly, recasting the batch melting equation in terms of water and utilizing F_m from the previous formulation allows for the determination of the mantle source water content (C^o_{H2O}).

One of the major uncertainties in this formulation is therefore the original mantle TiO_2 content. A normal mid-ocean ridge basalt (NMORB) mantle source has a value of 0.133 wt% (Salters and Stracke, 2004). However, using Ti and Y systematics, the source mantle TiO_2 content has been estimated for the region just north of the SSVZ (Watt et al. 2013) with a range of values between 0.162-0.196 wt. %. To generate estimates for the mantle melt fraction (F_m) and mantle water content (C^o_{H2O}), we have used the two end member values of TiO_2 = 0.133 wt. % estimated for an NMORB source and 0.196 wt. % estimated by Watt et al. (2013) for the mantle further north below the SSVZ.

Constraints on the slab surface temperatures, which may be useful in evaluating the extent of slab dehydration or melting, are estimated using the formulations of Plank et al. (2009) that is based on the systematic change in the K_2O/H_2O in the sediment melt, as a function of temperature (Herman and Spandler 2008). These formulations assume that the primitive magma K_2O content are controlled entirely by the nature of the sediment dehydration or melting. We apply their equation to the primitive parental magmas estimated from the undegassed melt inclusions (Table A5.2 of the Appendix).

5.6 Results

Included in the results in Table 5.2 are the host-olivine compositions, the measured compositions for the individual olivine-hosted melt inclusions, and the PEC and Fe loss-corrected melt inclusion compositions (Figs. 5 and 6), in Table 5.3 are the primitive mantle melt compositions which are the fractionation corrected composition of the melt inclusion in equilibrium with mantle (Fo_{90}) olivine (Fig. 5.6) and include the primitive melt H_2O, S and Cl contents, in Table 5.4 are the compositions of the silicate mineral assemblages observed as crystals contained in the melt inclusions or in the olivines themselves, and in Table 5.5 are the slab surface temperature, thermobarometric and melting parameter estimates**.**

5.6.1 General Results

The melt inclusions are generally homogenous and contain either a single vapor bubble or no vapor bubbles (Fig. 5.1). The presence of vapor bubbles indicates high volatile contents that likely formed as a result of decompression during ascent and eruption. Some of the inclusions contained crystals that were determined to be crystallizing pre- or syn-entrapment rather than post-entrapment due to the large size with respect to the associated melt inclusion (Figs. 1 and 3).

The host olivine phenocrysts from the three Hudson eruptions (Ho, H1 and H2; Table 5.1) range in forsterite content from Fo69 to Fo84 (Table 5.2) and are typically associated with inclusions of Cr-spinel, ilmenite and in a few instances, Ca-rich plagioclase. One melt inclusion from the H1 eruption of Hudson contains elongated lath shaped amphiboles occurring with a co-entrapped Cr-spinel crystal (Fig. 5.3). Amphibole has never been previously observed in any Hudson derived lavas (Lopez-Escobar et al. 1993) or tephras (Kratzmann et al. 2009, 2010; Stern et al. 2015; Weller et al. 2014, 2015). The amphibole, which is hosted in an olivine with a forsterite content of Fo82, is a kaersutite (Table 5.4; Leake et al. 1999). Despite the absence of amphibole as a stable phase

in the eruptive products of Hudson, decreasing Dy/Yb ratio with increasing differentiation in Hudson magmas has been interpreted as a chemical indicator for amphibole crystallization at depth (Davidson et al. 2007; Kratzmann et al. 2010; Weller et al. 2014). The olivine-hosted amphibole-bearing melt inclusion is therefore of significance because it is consistent with the suggestion that amphibole may be an important cryptic fractionating phase during the early magmatic evolution of Hudson magmas, although it has not been previously observed in any Hudson samples.

Melimoyu host olivine phenocrysts from one eruption (MEL2; Table 5.1) range only between Fo82-84 (Table 5.2) and also commonly occur with Cr-spinel and ilmenite. The host olivines from three different Mentolat tephra (B2, D1 and I; Table 5.1) range in forsterite content from Fo74-82 (Table 5.2) and are typically observed with ilmenite, Ca-rich plagioclase (Table 5.4), Fe-spinel, and an unidentified Fe-sulfide. Similarly, the host olivine phenocrysts from the MAC1 eruption of Macá (Table 5.1) range in forsterite content between Fo74-84 (Table 5.2). These olivines commonly are associated with Fe-spinel, ilmenite, and an unidentified Fe-sulfide (Fig. 5.1). Adhering glass from one olivine phenocryst from Macá was analyzed for comparison with the melt inclusion composition (Table 5.4). The adhering glass is similar to the composition of the melt inclusion for most elements except for SiO_2 (53% in adhering glass and ~49% in the melt inclusions) and K_2O (1.2% in adhering glass and 1.06% in melt inclusion), which were both slightly lower in the melt inclusion consistent with the entrapment of less evolved magma compositions than the host magma.

The PEC-corrected melt inclusions for all the volcanoes range from 48-58 wt. % SiO_2 while Macá and Melimoyu inclusions range form 49-53 and 48-51 wt. % SiO_2 respectively (Fig. 5.5; Table 5.2). Those from Hudson, Macá and Melimoyu are all medium- to high-K_2O basalts and basaltic-andesites. Those from Mentolat are low- to medium-K_2O calc-alkaline compositions that

Table 5.4. Compositions (wt. % oxide) of melt inclusion hosted plagioclase and amphibole microphenocrysts and adhering glass

Mineral	Amph.	Amph.	**Mineral**	Plag.	Plag.	Plag.	**Material**	Adhering Glass
Volcano	Hudson	Hudson	**Volcano**	Mentolat	Mentolat	Mentolat	**Volcano**	Macá
Tephra	H1	H1	**Tephra**	I	I	I	**Tephra**	MAC1
Lab ID	HUD21	HUD21	**Lab ID**	MEN2	MEN2	MEN13	**Lab ID**	MAC12
n	4	1	**n**	1	1	2	**n**	1
SiO_2	41.24	42.41	**SiO_2**	47.3	54.8	47.1	**SiO_2**	53.2
TiO_2	1.72	2.10	**Al_2O_3**	33.8	26.6	33.9	**TiO_2**	1.41
Al_2O_3	13.25	11.44	**FeO**	1.10	1.98	1.3	**Al_2O_3**	16.52
FeO	12.76	12.34	**CaO**	16.1	10.5	16.7	**FeO**	8.86
MnO	0.18	0.21	**Na_2O**	1.9	4.3	1.7	**MnO**	0.23
MgO	6.96	8.46	**K_2O**	0.03	0.38	0.0	**MgO**	4.43
CaO	21.47	21.09	**MgO**	0.08	0.30	0.2	**CaO**	7.91
Na_2O	0.36	0.65	**MnO**	0.00	0.04	0.0	**Na_2O**	4.28
K_2O	0.03	0.03	**Total**	100.3	98.9	101.0	**K_2O**	1.21
Cr_2O_3	0.04	0.02	**An**	81.9	56.3	84.6	**P_2O_5**	0.4951
Cl (ppm)	4	54	**Ab**	17.9	41.3	15.1	**Cr_2O_3**	0
F (ppm)	181	0	**Or**	0.2	2.4	0.3	**S (ppm)**	1356
Total	98.0	98.7					**F (ppm)**	0
Ca	52.3	49.7					**Cl (ppm)**	848
Mg	23.6	27.8					**Total**	98.74
Fe	24.1	22.5						

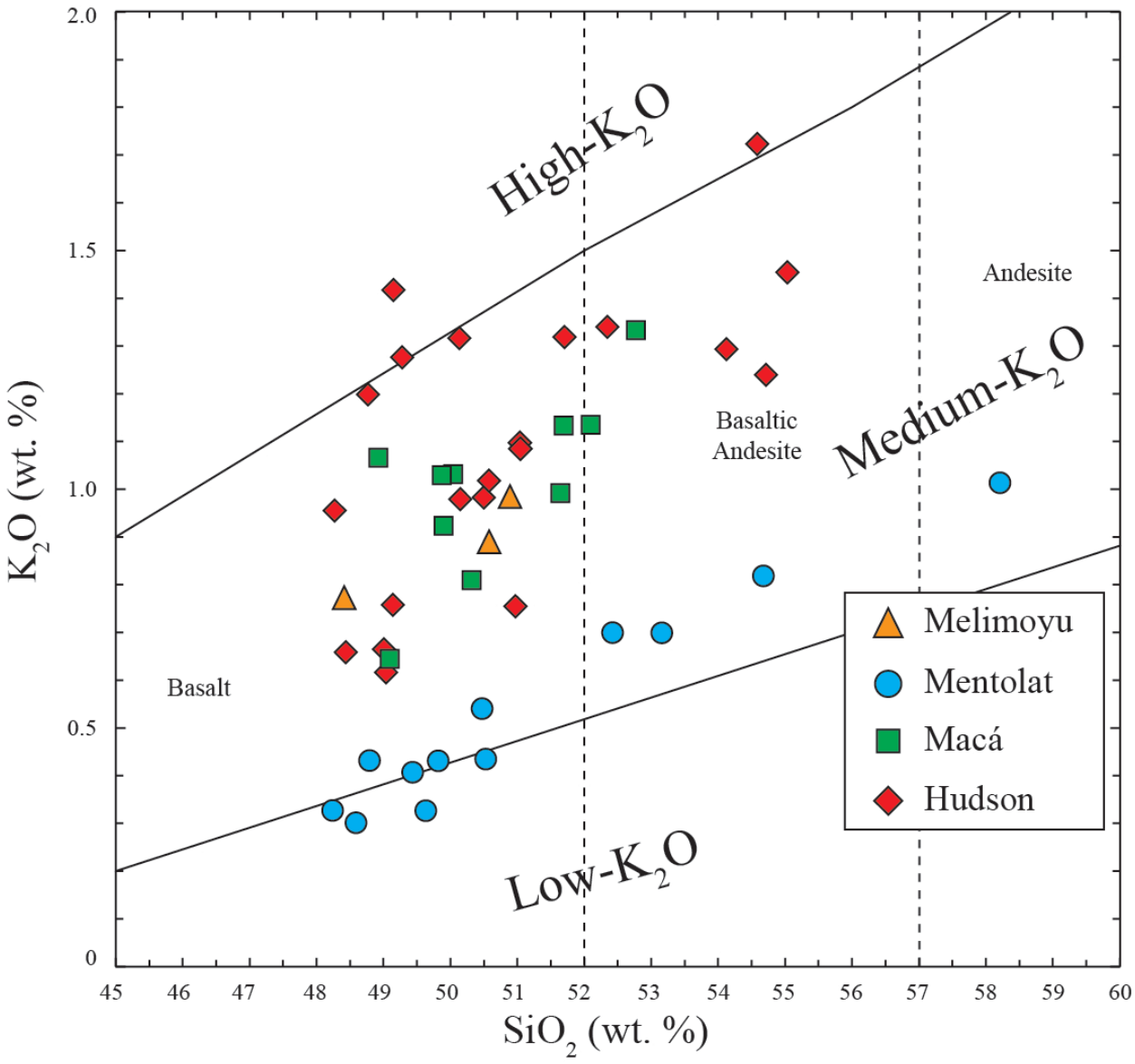

Figure 5.5. K2O versus SiO2 diagram showing the range of compositions of the post-entrapment crystallization-corrected melt inclusion compositions for each volcanic center. Melimoyu, Macá, and Hudson generally have greater K_2O content at a given SiO_2 than Mentolat, which is a Very Low Abundance-type volcanic center.

range from basalt up to andesitic in composition, consistent with the Very Low Abundance character of magmas erupted from this volcano.

5.6.2 Parental Magmas

Major element variation diagrams of the parental magma estimates from the least degassed melt inclusions Table 5.3 from each center are shown in Figure 5.6. For comparison, the PEC-corrected melt inclusion are also included, as well as fields for whole rock and glasses from those centers from previously published data (López-Escobar et al. 1993, 1995; Naranjo and Stern 1998, 2004, D'Orazio et al. 2004; Guitierrez et al. 2005, Kratzmann et al. 2009, 2010; Carel et al. 2011, Elbert et al. 2013), and primitive magmas estimated from melt inclusions for Hornopiren, Apagado, Minchinmávida and the Palena volcanic centers further north in the SSVZ (Watt et al. 2013)

The primitive magmas of Hudson, Melimoyu, and Macá are generally all similar to each other and extend to higher parental magma $MgO_{(90)}$ (the MgO of primitive magma in equilibrium with mantle olivine with Fo_{90}) compared to the primitive magma compositions determined for the volcanoes further north in the Andean SVZ (Fig. 5.6; Watt et al. 2013) However, Mentolat is distinct from the other centers in having lower $MgO_{(90)}$ contents for a given $SiO_{2(90)}$ content. Furthermore, other petrochemical characteristics identified both in the more evolved tephras and the PEC-corrected melt inclusions of Mentolat are also present in the primitive magma compositions (Fig. 5.6), so that, for example, Mentolat primitive magmas have higher Al_2O_3 and lower K_2O, and TiO_2 compared to the other SSVZ centers.

5.6.3 Melting Parameters

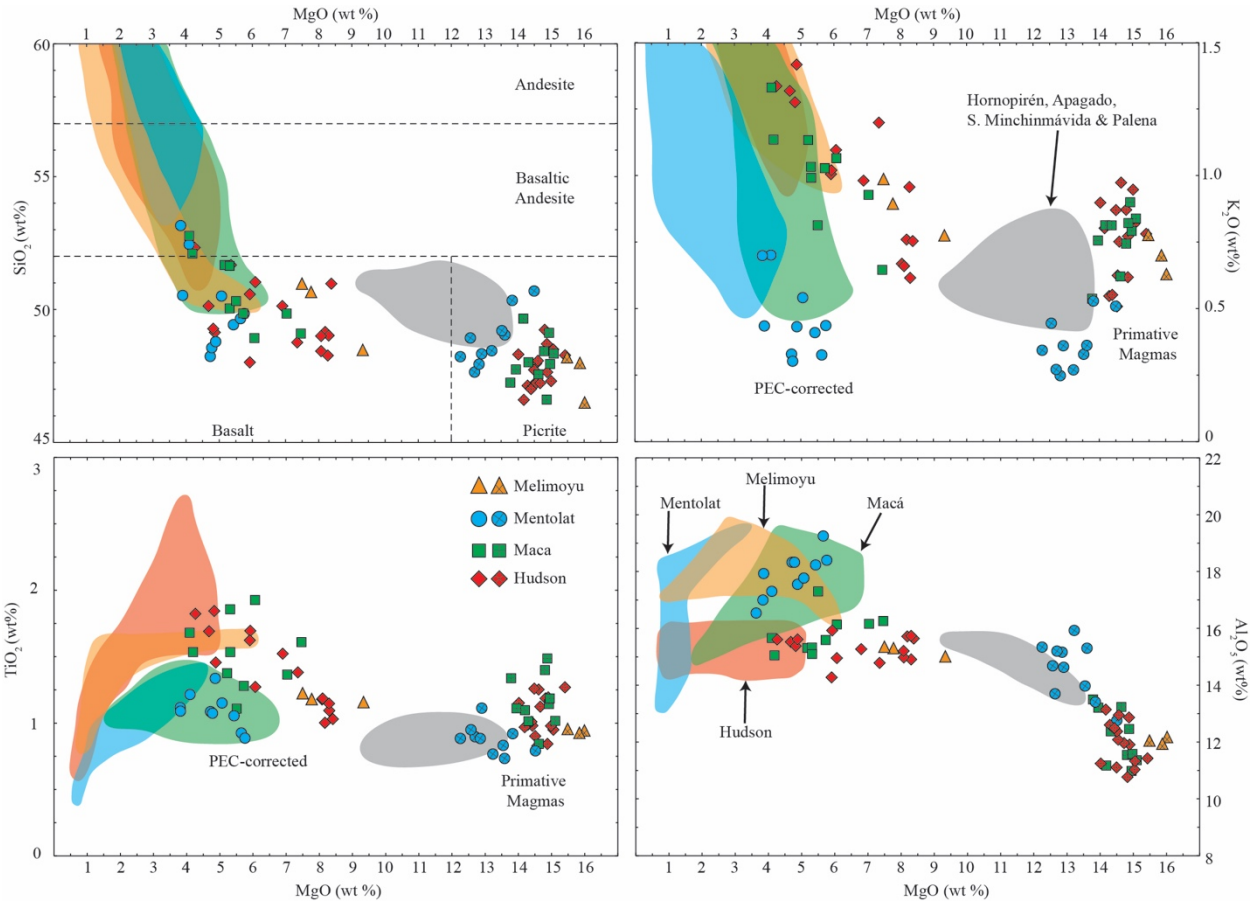

Figure 5.6. Major element variation diagrams for the primitive magmas (symbols with cross or plus sign) and the PEC-corrected melt inclusion (open symbols). Also shown are the fields for bulk rock and glass analysis for each center illustrating the petrochemical variability observed in the primitive magmas, the PEC-corrected magmas, and the more evolved eruptive products. Mentolat generally has much lower K_2O, TiO_2, MgO, and higher Al_2O_3 than the other centers that generally overlap in their magma compositions. Included for comparison are the primitive magma compositions determined for Hornopirén, and the mafic monogenetic centers north of the SSVZ centers (Watt et al. 2013).

For each assumed mantle Ti content, the fraction of melting (F_m) is generally low for Hudson, Melimoyu and Macá, with an average of 9-16%, 11-18% and 8-14% respectively, while Mentolat primitive magmas form from generally higher mantle melt fractions of 12-20%. The mantle water content C^o_{H2O} is on average uniform for Hudson, Macá, and Melimoyu at ~0.22-0.40 wt. % while beneath Mentolat, the mantle is somewhat more rich in water with an average C^o_{H2O} of 0.33-52 wt. %.

The slab surface temperatures are estimated using the K-thermometer of Plank et al. (2009). This thermometer predicts average temperatures of 874-876^{o}C for Hudson and Macá, lower 791^{o}C for Mentolat and higher 894 ^{o}C for Melimoyu (Table 5.5). The slab surface temperatures are within the range predicted for sediment melts and the stability of minerals such as phengite that can control the concentration of K_2O, Ba, and other LILE in hydrous silicate melts (Hermann and Splandler 2008).

5.6.4 Volatiles

There is great variability in the volatile contents amongst the different volcanic centers and within the individual centers themselves (Fig. 5.7). Mentolat has the greatest parental magma volatile content of all the centers, ranging from 2569-1215 ppm S_{90} and 1078-704 ppm Cl_{90}. Hudson also has large variations but with a much lower upper limit on the S_{90} and Cl_{90} content, ranging from 1320-594 ppm and 77-336 ppm respectively. Macá and Melimoyu overlap considerably, having a range of 1430-660 and 993-693 for S_{90} and 701-125 ppm and 626-471 ppm for Cl_{90} respectively. There is no systematic change in the F_{90} contents and there is significant scatter between the different centers and within the individual centers themselves. Due to the lack

Table 5.5. Melting parameters for primary magma compositions

Source Vol.	Eruption	Lab ID	Inclusion	C^o_{Ti}=0.133 F	C^o_{Ti}=0.133 C^o_{H2O}	C^o_{Ti}=0.196 F	C^o_{Ti}=0.196 C^o_{H2O}	Slab surface temp. T (ºC)
Melimoyu	MEL2	MEL1	a	11.1	0.22	18.3	0.35	894
Melimoyu	MEL2	MEL1	b	10.4	0.18	17.3	0.28	921
Melimoyu	MEL2	MEL2	a	10.8	0.25	17.9	0.40	866
			Average	**10.8**	**0.22**	**17.8**	**0.34**	**894**
Mentolat	B2	MEN17	a	10.4	0.31	17.3	0.50	808
Mentolat	B2	MEN21	a	11.5	0.33	18.9	0.52	752
Mentolat	B2	MEN21	b	11.3	0.32	18.6	0.51	761
Mentolat	B2	MEN22	a	11.5	0.35	18.9	0.55	779
Mentolat	D1	MEN3	a	12.4	0.32	20.3	0.51	789
Mentolat	D1	MEN19	a	14.8	0.41	23.8	0.64	791
Mentolat	D1	MEN19	b	14.0	0.39	22.5	0.61	761
Mentolat	D1	MEN20	a	8.3	0.25	14.2	0.40	789
Mentolat	I	MEN14	a	13.3	0.33	21.6	0.53	837
Mentolat	I	MEN15	a	10.9	0.29	18.0	0.46	837
			Average	**11.8**	**0.33**	**19.4**	**0.52**	**790**
Macá	MAC1	MAC1	a	12.3	0.32	20.0	0.51	853
Macá	MAC1	MAC2	a	8.3	0.22	14.2	0.35	879
Macá	MAC1	MAC3	b	9.5	0.25	16.0	0.40	887
Macá	MAC1	MAC6	a	8.4	0.23	14.4	0.37	882
Macá	MAC1	MAC8	a	7.6	0.22	13.1	0.36	873
Macá	MAC1	MAC8	c	5.7	0.15	10.4	0.25	881
Macá	MAC1	MAC12	a	9.5	0.28	16.0	0.44	873
Macá	MAC1	MAC12	b	5.2	0.16	9.6	0.27	877
Macá	MAC1	MAC13	a	6.2	0.18	11.1	0.31	834
Macá	MAC1	MAC14	a	8.0	0.17	13.8	0.27	919
			Average	**8.1**	**0.22**	**13.9**	**0.35**	**876**
Hudson	H2	HUD7	a	10.4	0.28	17.3	0.45	879
Hudson	H1	HUD17	a	6.9	0.13	12.1	0.21	917
Hudson	H1	HUD18	a	9.9	0.30	16.6	0.49	827
Hudson	H1	HUD18	b	9.9	0.29	16.6	0.47	831
Hudson	H1	HUD21	a	11.1	0.33	18.4	0.53	820
Hudson	H1	HUD21	b	12.2	0.37	20.0	0.58	839
Hudson	Ho	HUD3	a	10.1	0.25	16.8	0.39	906
Hudson	Ho	HUD4	a	7.5	0.17	13.0	0.27	910
Hudson	Ho	HUD9	a	12.6	0.37	20.5	0.58	842
Hudson	Ho	HUD14	a	10.2	0.26	17.0	0.42	882
Hudson	Ho	HUD15	a	7.9	0.20	13.6	0.33	897
Hudson	Ho	HUD15	b	6.8	0.18	12.0	0.30	894
Hudson	Ho	HUD19	a	8.2	0.25	14.0	0.41	888
Hudson	Ho	HUD20	a	7.4	0.18	12.9	0.29	890
Hudson	Ho	HUD24	b	6.7	0.19	11.9	0.31	879
			Average	**9.2**	**0.25**	**15.5**	**0.40**	**874**

of a clear relationships with melting parameters and primitive magma chemistry, F_{90} will not be included in the subsequent discussion.

5.7 Discussion

To assess for the parameters influencing the along arc petrochemical diversity observed between the major volcanic centers of the SSVZ, we evaluate their back-calculated primitive magma compositions within the context of their mantle melting parameters and with the thermobarometric results. This information allows for the interpretation of the potential mechanisms controlling the variability in magma chemistry.

5.7.1 Parental Magma Compositions

Our estimates for the parental magma compositions are similar to other primitive magma compositions estimated from the region (Fig. 5.6; Watt et al. 2013). Melt inclusion compositions from all of the centers are picrites with Mentolat having lower $MgO_{(90)}$ contents than the other centers. Lower $MgO_{(90)}$ contents are consistent with the suggestion that mantle melting in the presence of high water contents will lead to lower MgO but higher SiO_2 contents (Wood and Turner 2009).

One notable feature of the primitive magmas from the SSVZ centers are some of the distinctive petrochemical characteristics present in the more evolved tephras, such as low K_2O and high Al_2O_3, are still preserved in the primitive magmas for Mentolat, while the liquid lines of descent for the other centers tend to converge on a common primitive composition (Fig. 5.6). This observation has two important implications for these volcanoes: 1) primitive magmas from Mentolat are compositionally distinct at generation and thus sub-arc processes acting at the time

of formation are likely responsible for this variability; and 2) the similarity in the parental melts from Hudson, Macá, and Melimoyu suggest that different diversification pathways after initial melt generation may be the cause for the petrochemical diversity observed in their eruptive products, Macá erupting Type-1 low abundance (LA) magmas, while Hudson and Melimoyu erupt Type-2 high abundance (HA) magmas.

5.7.2 Mantle melting and water content

The four SSVZ centers along the volcanic front have significant variability in their mantle melting parameters and mantle source H_2O contents. While the F_m and and C^o_{H2O} at Hudson, Macá, and Melimoyu are generally similar, Mentolat has higher F_m and C^o_{H2O}. This conclusion is consistent with the low incompatible K_2O and TiO_2 content of Mentolat magmas. Our melting parameters indicate higher degrees of partial melting at Mentolat and thus the concentration of these elements are diluted with higher percent melting. The results of the modeling suggests a positive relationship between the source mantle water enrichment and degree of mantle melting, an observation made at many subduction related volcanic arcs (Portnyagin et al. 2007; Kelley et al. 2010; Watt et al. 2013). One possible explanation for this abrupt change is the result of a heightened flux of slab derived fluids caused by dehydration of altered oceanic crust with the Guamblin Fraction Zone which when projected onto land, traces below Mentolat (Fig. 5.1). The distinctive Very Low Abundance type petrochemistry of Mentolat is similar to other amphibole-bearing centers further north in the SVZ such as Huequi (Watt et al. 2011), Nevado de Longaví (Sellés et al. 2004, Rodríguez et al. 2007), and Calbuco (Lopez-Escobar et al. 1995, Hickey-Vargas et al. 1995). The influence of fracture zones has been invoked at both Nevado de Longaví and

Calbuco (Sellés et al. 2004; Rodríguez et al. 2007) and at other Andean and Aleutian volcanoes (Singer et al. 2007; Manella et al. 2014).

5.7.3 Slab Surface Temperatures

Slab surface temperatures estimates using the K-thermometer of (Plank et al. 2009) yield temperature estimates of ~790^{o}C at Mentolat, 874-876^{o}C from Macá and Hudson, and ~894^{o}C for Melimoyu. These slab surface temperature estimates suggest that Melimoyu, Macá, and Hudson, which have hotter lab surface temperatures, could incorporate greater amounts of hydrous sediment melts that could lead to greater enrichments in their mantle source of K_2O, Ba, and LILE from the breakdown of minerals like phengite (Hermann and Spandler 2008). For Mentolat, below which lower slab surface temperatures estimated, less sediment melt might form thus transfering less K_2O, Ba and other LILE into the mantle source of this volcano.

Mentolat primitive magmas have lower K_2O, TiO_2, and MgO than Melimoyu, Macá, and Hudson (Fig. 5.6), and are generated by higher degrees of partial melting of a mantle with higher H_2O content. Higher slab surface temperatures suggest that hydrous melts from the subducting sediments and the breakdown of phengite may be contributing to the chemistry of the latter three centers (Hermann and Splandler 2008). A similar range of petrochemical variability and melting parameters are observed west-to-east across the Andean arc, from the volcanic front into the back arc, further north in the SSVZ (Watt et al. 2013). Watt et al. (2013) propose an increasing down-slab temperature gradient below the arc, with slab dehydration supplying H_2O with some dissolved solids into the mantle source below the volcanic front, and the subsequent melting of sediment associated with the breakdown of phengite producing melts with lower H_2O content but greater K_2O, Ba, and LREE content above the deeper parts of the subducted plate below the back arc.

However, in the southernmost SSVZ, the compositional variability is observed between the four volcanoes along the volcanic front, implying that factors other than position with respect to the depth of the subducting slab are affecting the chemical differences between Melimoyu, Mentolat, Macá, and Hudson. We suggest that the subduction of the Guamblin Fracture Zone may be influencing the mantle chemistry and melting parameters below Mentolat (Fig. 5.2). Fracture zones potentially host serpentinitic bodies in the altered oceanic crust (Contreras-Reyes et al. 2008; Manella et al. 2014) and would provide an efficient means to transport a high abundance of hydrous minerals, seawater, and sediments into the mantle, which could play a more important role in magma generation below Mentolat compared to the other three SSVZ centers. An enhanced water flux into the mantle source is also consistent with the abundant presence of amphibole in the eruptive products of Mentolat, while amphibole is rare or absent in lavas or tephras derived from the other centers in the SSVZ (Lopez-Escobar et al. 1993, 1995; Stern et al. 2016, 2017; Weller et al. 2015).

5.7.4 Volatiles

Sulfur

Understanding the behavior of sulfur in magmatic systems has been a longstanding challenge due to the multiple valance states of sulfur and the sensitivity of sulfur speciation to changing oxygen fugacity (fO_2), magma temperature, and melt composition (Wallace, 2005). In general, the S contents in arc magmas decease with increasing differentiation that may be caused by the fractionation of S-bearing phases or potentially the magma temperature and compositional which effects of the solubility of S (Wallace and Edmond, 2011).

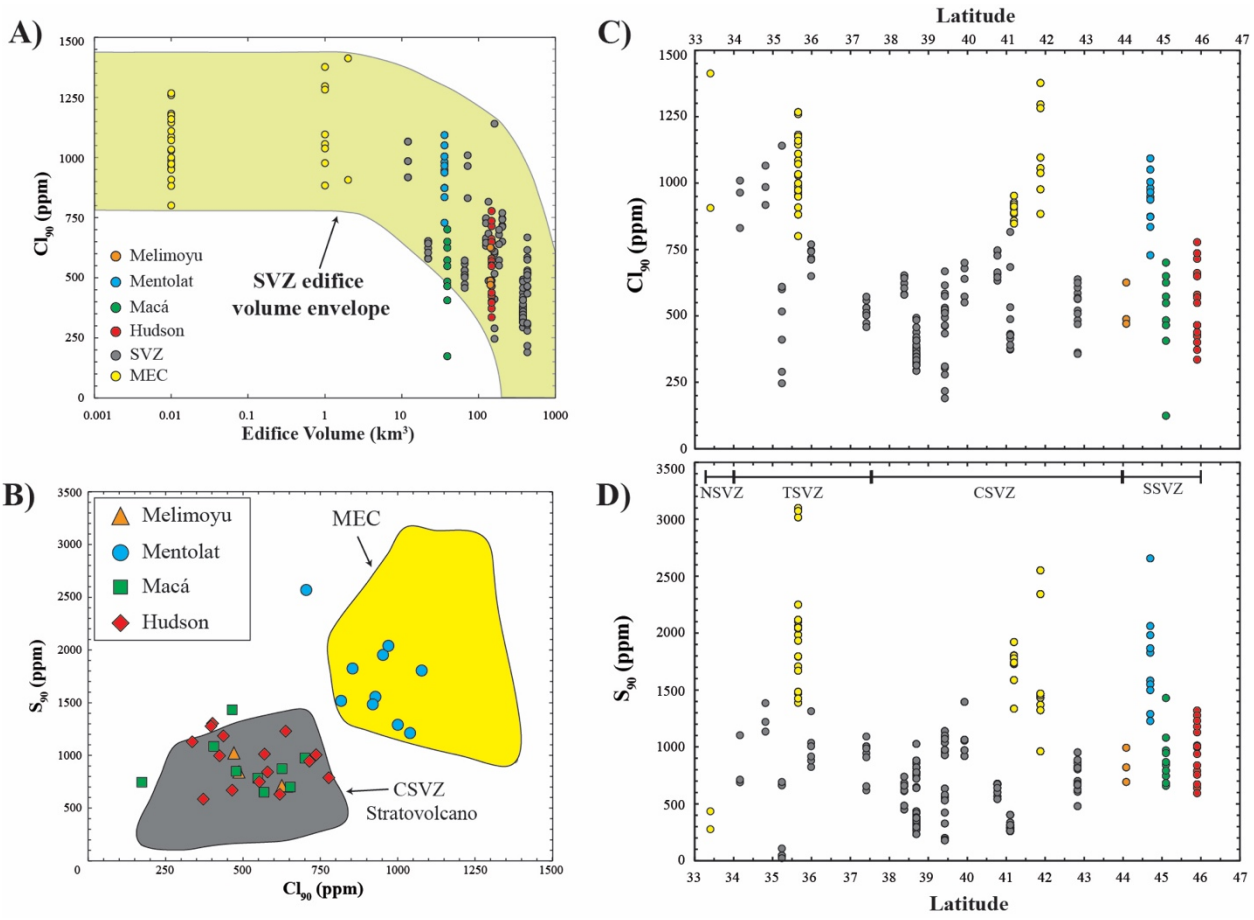

Figure 5.8. A) Melt inclusions Cl90 content versus volcano edifice size (km^3; Volker et al. 2011) for the least degassed melt inclusions from the SSVZ centers. The small MEC (yellow) have the greatest Cl_{90} contents while the Cl_{90} contents are strongly diluted at the larger centers such at Hudson and Melimoyu (~100km^3). Mentolat (~36km^3) has the highest Cl_{90} contents of the SSVZ centers and fits within the Cl_{90} and edifice volume field of Wehrmann et al. (2014). B) S_{90} and Cl_{90} contents for the SSVZ centers and the MEC of Wehrmann et al. (2014) and other larger SVZ centers for comparison. C) & D) Cl_{90} and S_{90} for the least degassed parental melt inclusions with latitude showing the wide variability in volatile contents along the SVZ.

In melt inclusions, the sulfur content can be modified by post entrapment effects caused by the diffusive re-equilibration of FeO* with the host olivine. Danyushevsky et al. (2002) demonstrated that melt inclusions that experienced significant diffusion related Fe-loss can precipitate sulfides due to the decreased solubility of S. Indeed, melt inclusion from Mentolat and Macá both contain Fe-sulfides within the glass and embedded within the host olivine phenocryst (Fig. 5.1). However, these centers were determined to be the least impacted by diffusive re-equilibration and thus we believe that these represent primary phases during early magmatic evolution and not the result of re-equilibration processes.

There is a dramatic spike in the S_{90} content at Mentolat (Fig. 5.7) that are comparable to S_{90} contents observed at other centers further north in the SVZ such as Apagado, Cabeza de Vaca, and Los Hornitos (Wehmann et al. 2014). Wehrmann et al. (2014) observed the highest S contents in primitive magmas derived from small monogenetic cones (MEC) whereas the lowest S contents generally occur in the volcanoes thought to be derived from high-degree melting and in the more evolved larger stratovolcanoes. This disparity in the S content was though to reflect either the fractionation of S-bearing phases, or to be related to the size of these centers compared to the larger stratovolcanoes that are likely to experienced stronger degassing during ascent though more complex sub-arc plumbing systems.

Mentolat, which is the smallest center in the SSVZ with an edifice volume of ~36 km^3 (Volker et al. 2011), is still much larger (~15-30X) than any of the MEC where the highest S contents are observed. Furthermore, based on our melting models, Mentolat is generated by higher degrees of partial melting than the other centers of the SSVZ and thus the S_{90} contents should be diluted similar to the behavior of other incompatible elements such as K_2O. Thus, features such as volcanic size and degree of melting are unable to explain the elevated S_{90} content of the

primitive magmas at Mentolat. Alt et al. (2013) demonstrated that dehydration reactions of serpentinites in subduction zone setting release an average of 260 ppm S into the mantle wedge. This may be an explanation for the elevated S content at Mentolat.

The S_{90} content for the primitive melts from Melimoyu and Hudson are typical for other larger centers (≥100 km^3; Volker et al. 2011) in the SVZ. However, Macá, which has an estimated volume of ~39 km^3, has S_{90} contents at the lower range that is observed for volcanoes of this size. This reduction in S_{90} may result from fractionation of S-bearing phases or degassing.

Chlorine

The lowest parental Cl_{90} concentrations are found at Melimoyu, Macá and Hudson, while Mentolat has the highest Cl_{90} content (Fig. 5.7). Wehrmann et al. (2014) observed two relationships between the Cl_{90} content of primitive magmas from the SVZ. Contrasting the behavior of S, a positive correlation exists between the Cl_{90} content and incompatible trace element ratios that indicate degree of melting and/or source region enrichment (La/Sm; Wehrmann et al. 2014). The lowest Cl_{90} abundances are observed in the volcanoes interpreted to have formed from high-degree melts (low La/Sm) or from the most depleted mantle sources. Enhanced subduction input into the sub-arc mantle causes higher degrees of partial melting and dilution of the incompatible elements such as Cl_{90}. Additionally, there exists an inverse relationship between the size of the volcanic edifice and the Cl_{90} abundances (Fig. 5.7). Volcanoes with the largest edifice have the lowest Cl_{90} abundances while the smaller centers generally have the highest Cl_{90} contents (Fig. 5.7). The low Cl_{90} contents at Hudson and Melimoyu, which are the largest centers in the SSVZ, are similar to volcanoes of a comparable size further north in SVZ while Macá and Mentolat, that are both relatively small centers, generally fit within the Cl_{90} and edifice volume

field created for other centers of the SVZ. Thus, the volcanoes of the SSVZ fit the proposed Cl content and edifice volume model proposed by Wehrmann et al. (2014).

Based on the melt inclusion data and the estimated melting parameters, the lowest Cl_{90} abundances are observed in magmas that are generated by relatively low degree of partial melting. Mentolat, which has an average F_m between 20%-12% has the highest Cl_{90} abundances similar to the primitive melts from the small mafic cinder cones (MEC) of Apagado, Cabeza de Vaca, and Los Hornitos in the Andean CSVZ (Wehrmann et al. 2014). The elevated Cl_{90} at Mentolat could be the result of enhanced seawater transport into the sub-arc mantle in the highly altered oceanic crust beneath Mentolat. An important point is that S or Cl has never been measured in melt inclusion from Nevado de Longaví, Huequi, or Calbuco. These volcanoes also have an unusual magma chemistry similar to Mentolat and have amphibole as a stable phase (Hickey-Vargas et al. 1995; Sellés et al. 2004; Rodriquez et al. 2007; Watt et al. 2011; Weller et al. 2015) and in the case of Nevado de Longaví and Calbuco, fracture zones have been invoked as potential mechanisms to explain the abnormal magma chemistry.

5.8 Conclusion

In summary, some of the along-strike chemical diversity in the arc volcanoes of the SSVZ is also observed in the primitive magmas from these centers, with Mentolat having MgO-poor primitive melts with lower incompatible elements such as K_2O, TiO_2, and higher Al_2O_3, and C^o_{H2O} and are generated by higher degrees of melting. Primitive melts from Mentolat indicate lower slab surface temperatures than the other centers. The melting parameters and chemical characteristics support an enhanced water transport into the mantle above the subducted Guamblin Fracture Zone causing hydrous flux melting in the sub arc mantle beneath Mentolat. Melts with high water

contents are further supported by the abundance of amphibole in the eruptive products from this center. In contrast, Hudson, Macá, and Melimoyu all have relatively similar parental magma compositions that are MgO-rich, have higher K_2O, TiO_2, and lower Al_2O_3, with lower C^o_{H2O} and are generated by low degrees of partial melting at high and high slab surface temperatures. The magma chemistry and slab surface temperatures indicate that hydrous melts of subducting sediments could play a role in magma genesis below these centers.

The relatively high concentration of S_{90} and Cl_{90} at Mentolat may be the result of the close proximity beneath Mentolat of the Guamblin Fracture Zone which could efficiently transport hydrous mineral assemblages and potentially sediments and seawater to the subduction zone. Fracture zones composed of altered oceanic crust could generate an anomalously high water content in the sub-arc mantle beneath this center and explain the dramatic change in magma chemistry and melting parameters at Mentolat. The S_{90} contents at the other centers are likely controlled by the fractionation of S-bearing phases or strong degassing while the Cl_{90} content is likely controlled by degree of melting and degassing during passage though more complex sub-arc plumbing systems.

5.9 References

Alt JC, Schwarzenbach EM, Früh-Green GL, Shanks III, WC, Bernasconi SM, Garrido CJ, Crispini L, Gaggero L, Padrón-Navarta, Marchesi C (2013) The role of serpentinites in cycling of carbon and sulfur: Seafloor serpentinization and subduction metamorphism. Lith 178:40-54, http://dx.doi.org/10.1016/j.lithos.2012.12.006

Ariskin AA, Frenkel MY, Barmina GS, Nielsen R (1993) COMAGMAT: A FORTRAN program to model magma differentiation processes. Comput Geosci 19:1155–1170, doi:10.1016/0098-3004(93)90020-6.

Cande SC, Leslie RB (1986) Late Cenozoic Tectonics of the Southern Chile Trench. J Geophys Res 91(B1): 471–496

Carel M, Siani G, Delpech G (2011) Tephrostratigrapy of a deep-sea sediment sequence off the south Chilean margin: New insight into the Hudson volcanic activity since the last glacial period. J Volcanol Geotherm Res. 208: 99-111

Cembrano J, Hervé F, Lavenu A (l996) The Liquiñe-Ofqui fault zone: long-lived intra-arc fault system in southern Chile. Tectonophys 259: 55–66

Contreras-Reyes E, Grevemeyer I, Flueh ER, Scherwath M, Heesemann M (2007) Alteration of the subducting oceanic lithosphere at the southern central Chile trenchouter rise. Geochem Geophys Geosyst 8

Contreras-Reyes E, Grevemeyer I, Flueh ER, Reichert C (2008) Upper lithospheric structure of the subduction zone offshore of southern Arauco peninsula, Chile, at 38°S. J Geophys Res 113

Danyushevsky L V, Plechov P (2011), Petrolog3: Integrated software for modeling crystallization processes, Geochem Geophys Geosyst 12, Q07021, doi:10.1029/2011GC003516.

Danyushevsky, LV, Della-Pasqua FN, Sokolov S (2000) Re-equilibration of melt inclusions trapped by magnesian olivine phenocrysts from subduction-related magmas: petrological implications. Cont Mineral Petrol 138: 68-83

Danyushevsky LV, McNeill AW, Sobolev AV (2002) Experimental and petrological studies of melt inclusions in phenocrysts from mantle-derived magmas: an overview of techniques, advantages and complications. Chem Geol 183: 5-24

DeMets C, Gordon RG, Argus, DF (2010) Geologicaly current plate motions. Geophys J Int 181: 1-80

D'Orazio M, Innocenti F, Manetti P, Tamponi M, Tonarini S, González-Ferrán O, Lahsen A (2003) The Quaternary calc-alkaline volcanism of the Patagonian Andes close to the Chile triple junction: geochemistry and petrogenesis of volcanic rocks from the Cay and Maca volcanoes (~45°S, Chile). J S Amer Earth Sci 16(4): 219–242

Elbert J, Wartenburg R, von Gunten L, Urrutia R, Fisher D, Fujak M, Hamann Y, Greber ND, Grosjean M (2013) Late Holocene air temperature variability reconstructed from the sediments of Laguna Escondida, Patagonia Chile. Palaeogeog Palaeoclimat Palaeoecol 396: 482-492

Ford CE, DG Russell, JA Groven, Fisk MR (1983) Distribution coefficients of Mg2+, Fe2+, Ca2+ and Mn2+ between olivine and melt. J Petrol 24:256–265

Futa K, Stern CR (l988) Sr and Nd isotopic and trace element compositions of Quaternary volcanic centers of the southern Andes. Earth Planet Sci Lett 88: 253–262

Gutiérrez F, Gioncada A, González-Ferrán O, Lahsen A, Mazzuoli R (2005) The Hudson volcano and surrounding monogenetic centres (Chilean Patagonia): an example of volcanism associated with ridge-trench collision environment. J Volcanol Geotherm Res 145: 207–233

Hermann J, Spandler CJ (2008) Sediment melts at sub-arc depths: an experimental study. J Petrol 49:717–740

Hickey-Vargas R, Holbik S, Tormey D, Frey FA, Moreno Roa H (2016) Basaltic rocks from the

Andean Southern Volcanic Zone: Insight from the comparison of along-strike and small-scale geochemical variations and their sources. Lithos 258-259: 115-132

Hildreth W, Moorbath S (1988) Crustal contributions to arc magmatism in the Andes of Central Chile. Contrib Mineral Petrol 98:455-489

Jacques G, Hoernle, KL, Gill, J, Hauff, F, Wehrmann, H, Garbe-Schönberg, D, van den Bogaard, P, Bindeman I, Lara LE (2013) Across-arc geochemical variations in the Andean Southern Volcanic Zone, Chile (34.5-38.0°S): Constraints on mantle wedge and slab input compositions. Geochem et Cosmoch Acta 123: 218–243

Kelley KA, Plank T, Grove TL, Stolper EM, Newman S, Hauri E (2006) Mantle melting as a function of water content beneath back-arc basins. J Geophys Res 111 B09208 doi:10.1029/2005JB003732.

Kelley KA, Plank T, Newman S, Stolper EM, Grove TL, Parman S, Hauri E (2010) Mantle melting as a function of water content beneath the Mariana arc. J Petrol 51: 1711–1738 doi:10.1093/petrology/egq036.

Kratzmann DJ, Carey S, Scasso RA, Naranjo JA (2009) Compositional variations and magma mixing in the 1991 eruptions of Hudson volcano, Chile. Bull Volcanol 71(4): 419–439

Kratzmann DJ, Carey S, Scasso RA, Naranjo JA (2010) Role of cryptic amphibole crystallization in magma differentiation at Hudson volcano, Southern Volcanic Zone, Chile. Contrib Mineral Petrol 159: 237–264

Leake B, Woolley A, Arps C, Birch W, Gilbert M, Grice J, Hawthorne F, Kato A, Kisch H, Krivovichev V, Linthout K, Laird J, Mandarino J, Maresch W, Nickel E, Rock N, Schumacher J, Smith D, Stephenson, N., Ungaretti L,Whittaker E, Youzhi G (1997). Nomenclature of amphiboles: report of the subcommittee on amphiboles of the International

Mineralogical Association, Commission on New Minerals and Minerals Names. Amer Mineral 82:1019-1037

López-Escobar L, Kilian R, Kempton P, Tagiri M (l993) Petrology and geochemistry of Quaternary rocks from the southern volcanic zone of the Andes between 41°30' and 46°00'S, Chile. Rev Geol Chile 20: 33–55

López-Escobar L, Parada MA, Hickey-Vargas R, Frey FA, Kempton P, Moreno H (1995) Calbuco Volcano and minor eruptive centers distributed along thLiquifie-Ofqui Fault Zone, Chile (41°S) contrasting origin of andesitic and basaltic magmain the Southern Volcanic Zone of the Andes. Contr Mineral Petrol 119: 345-361

Manea VC, Leeman WP, Gerya T, Manea M, Zhu, G (2014) Subduction of fracture zones controls mantle melting and geochemical signature above slabs. Nat Commun 5:5095 doi: 10.1038/ncomms6095

Naranjo JA, Stern CR (1998) Holocene explosive activity of Hudson Volcano, southern Andes. Bull Volcanol 59(4): 291–306

Naranjo JA, Stern CR (2004) Holocene tephrochronology of the southernmost part (42°30'-45°S) of the Andean Southern Volcanic Zone. Rev Geol Chile 31(2): 225–240

Plank T, LB Cooper, Manning C. E. (2009) Emerging geothermometers for estimating slab surface temperatures. Nat Geosci 2: 611–615 doi:10.1038/ngeo614

Portnyagin, M., K. Hoernle, P. Plechov, N. Mironov, and S. Khubunaya (2007), Constraints on mantle melting and composition and nature of slab components in volcanic arcs from volatiles (H2O, S, Cl, F) and trace elements in melt inclusions from the Kamchatka Arc. Earth Planet Sci Lett 255: 53–69 doi:10.1016/j.epsl.2006.12.005

Rodríguez C, Sellés D, Dungan M, Langmuir C, Leeman W, (2007) Adikitic dacites formed by intracrustal crystal fractionation of water-rich parent magmas at Nevado de Longaví (36.2^{o}S; Andean Southern Volcanic Zone, Central Chile). J Petrol 48(11): 2033-2061

Salters VJM, Stracke A (2004) Composition of the depleted mantle. Geochem Geophys Geosyst 5 Q05B07 doi:10.1029/2003GC000597

Sellés D, Rodríguez AC, Dungan MA, Naranjo JA, Gardeweg M (2004) Geochemistry of Nevado de Longaví (36.2°S): a compositionally atypical volcano in the Southerrn Volcanic Zone of the Andes. Rev Geol Chile 31(2): 293-315

Singer BS, Jicha BR, Leeman WP, Rogers NW, Thirlwall MF, Ryan J, Nicolaysen KE (2007) Along-strike trace element and isotopic variaiton in Aleutian Island arc basalt: Subduction melts sediments and dehydrates serpentine. J of Geophys Res 112 doi:10.1029/2006JB004897

Stern CR (2004) Active Andean Volcanism: its geologic and tectonic setting. Rev Geol Chile 31(2): 161-206

Stern CR (2008) Holocene tephrochronology record of large explosive eruptions in the southernmost Patagonian Andes. Bull Volcanol 70(4): 435–454

Stern CR, de Porras ME, Maldonado A (2015) Tephrochronology of the upper Río Cisnes valley (44°S), southern Chile. Andean Geol 42(2): 173-192

Stern CR, Moreno PI, Henrique WI, Villa-Martinez RP, Sagredo E, Aravena JC, De Pol-Holz R (2016) Holocene tephrochronolgy in the area around Cochrane, southern Chile. Andean Geol 43(1): 1-19

Stolper E, Newman S (1994) The role of water in the petrogenesis of Mariana trough magmas. Earth Planet Sci Lett 121: 293–325

Vargas G, Rebolledo S, Sepúlveda SA, Lahsen A, Thiele R, Townley B, Padilla C, Rauld R, Herrera MJ, Lara M (2013) Submarine earthquake rupture, active faulting and volcanism along the major Liquiñe-Ofque Fault Zone and implications for seismic hazard assessment in the Patagonian Andes. Andean Geol 40: 141-171

Völker D, Kutterolf S, Wehrmann H (2011) Comparative mass balance of volcanic edifices at the southern volcanic zone of the Andes between 33^{o}S and 46^{o}S. J Volcanol Geotherm Res. 205: 114-129

Wallace PJ (2005) Volatiles in subduction zone magmas: concentrations and fluxes based on melt inclusions and volcanic gas data. J Volcanol Geotherm Res 140:217–240. doi:10.1016/j.volgeores.2004.07.23

Wallace PJ, Edmonds M (2011) The sulfur budget in magmas:evidence from melt inclusions, submarine glasses, and volcanic gas emissions. Rev Mineral Geochem 73:215–246. doi:10.2138/ rmg.2011.73.8Watt SFL, Pyle DM, Mather TA (2011) Geology, petrology and geochemistry of the dome complex of Huequi volcano, southern Chile. Andean Geol 38(2): 335-348

Watt SFL, Pyle DM, Mather TA, Naranjo JA (2013) Arc magma compositions controlled by linked thermal and chemical gradients above the subducting slab. Geophs Res Lett 40(11): 2550-2556

Wehrmann H, Hoernle K, Jacques G, Garbe-Schönberg D, Schumann K, Mahlke J, Lara L, 2014 Sulphur and chlorine geochemistry of mafic to intermediate tephras from the Chilean Southern Volcanic Zone (33–43°S) compared with those from the Central American Volcanic Arc. Int J Earth Sci 103:1945-1962

Weller DJ, Miranda CG, Moreno PI, Villa-Martínez RP, Stern CR (2014) A large late-glacial Ho eruption fo the Hudson volcano, southern Chile. Bull Volcanol 76: 831-849

Weller DJ, Miranda CG, Moreno PI, Villa-Martínez RP, Stern CR (2015) Tephrochronology of the Andean Southern Volanic Zone, Chile. Bull Volcanol 76: 831-849

Weller DJ, de Porras E, Maldonado A, Stern CR (2017a) Holocene tephrochronology of the lower Río Cisnes Valley, southern Chile. Andean Geol (in prep)

Weller DJ, dePorras E, Maldonado A, Stern CR (2017b) New age controls on the tephrochronology of the southernmost Andean Southern Volcanic Zone, Chile. Bull Volcanol (in prep)

Wood BJ, Turner SP (2009) Origin of primitive high-Mg andesite: Constraints from natural examples and experiments, Earth Planet Sci Lett 283: 59–66 doi:10.1016/j.epsl.2009.03.032.

Chapter 6

A method for the preparation and measurement of trace elements using solution based ICP-MS techniques

6.1 Introduction

The measurement of trace elements by ICP-MS techniques is widely used for geologic samples and can provide accurate results for elements at relatively low concentrations. A challenge of using ICP-MS techniques is the complete decomposition of sample while stabilizing all analytes in solution. Here, I outline the development, methodology, and results for an open container hydrofluoric (HF) and perchloric acid ($HClO_4$) digestion technique of mafic to felsic geologic samples for the simultaneous measurement of 36 trace elements using solution based ICP-MS.

6.2 Methods

6.2.1 Reagents

Water

Deionized water (DI) was used to clean the labware during acid leaching. 18.1 MΩ cm^{-1} Milli-Q (from a Millipore purification system) water was used to dilute acids to the appropriate concentration, and as the medium for the standards solutions and acid mixtures.

Hydrochloric, Nitric, and Hydrofluoric Acid

The hydrochloric (HCl) and nitic (HNO_3) acids used during the digestion process were distilled using a sub boiling quartz still and diluted to the appropriate concentration using Milli-Q water. Hydrofluoric acid (48%; hereafter % refers to a v/v basis) was distilled using a two-bottle Teflon still. Nitric acid used in the mixed standard solution and the acid mixtures was 70% Optima Grade diluted to 2% using Milli-Q water.

Perchloiric Acid

During the sample digestion, highly purified 70% ARISTAR ULTRA trace metal grade perchloric ($HClO_4$) acid was used without further purification.

Boric Acid

99.5% purity electrophoresis grade boric acid (H_3BO_3) was used both in the samples and standards without further purification.

6.2.2 Labware

All of the sample and solutions were stored in LDPE Nalgene bottles. Prior to use, bottles were treated by allowing a 12 hour soak in Alconox detergent and deionized (DI) water. In a three stage acid leaching process, the bottles were soaked in three different acid mixtures for 12 hours at each step and then brought to a boil before proceeding to the next step. The three acid mixtures include: 1) 1:1 HCl and DI water, 2) 1:1:1 HCl, HNO_3, DI water, 3) 1:1 HNO_3 and DI water. Bottles were then washed in Milli-Q water and allowed to dry.

Prior to use, Teflon PTFE beakers were allowed to sit for 12 hours in Alconox detergent and DI water followed by a 12 hour soak in 1:1 HCl and DI water. The Teflon containers were then brought to a boil in the acid mixture and allowed to cool before washing in Milli-Q water and dried.

6.2.3 ICP-MS Instrumentation and data acquisition

The analysis were performed on a Thermo Finnigan Element2 sector field inductively-coupled plasma mass spectrometer operating at standard conditions and tuned to reduce the interference of oxides and maximize the signal intensity and stability.

Spectroscopic interferences were minimized by analyzing isotopes lacking monoatomic or polyatomic compounds with the same mass-to-charge as the analyte. In some cases, interferences could be avoided by analyzing elements at different resolutions. Where this was not possible, isotopes were selected based on the overall abundance of the analyte isotope, and the abundance of isotope potentially contributing to the interference. For example, analyte isotopes were selected

if the isotope had a high natural abundance and the potential isobaric interference contained an isotope with a low natural abundance thus reducing the impact of interferences.

For the analyses, the external standard solutions were diluted 10:1 and the samples were diluted 20:1 with 2% HNO_3 to achieve the appropriate concentrations. Samples were analyzed in sets of 6, with 4 standards and an acid blank being analyzed before and after each set of 6 samples. Sample concentrations were determined from blank-corrected counts compared to the linear combination of the preceding and following linear standard curves.

6.2.4 Standards

Three standard solutions were prepared from 32 single element standards and one multi-element standard (the 4^{th} standard consisted of pure acids). The mixed standard solutions were prepared by spiking the appropriate volumes (determined gravimetrically) of the standards into intermediate solutions for trace and minor elements. The appropriate volumes of the intermediate solutions were then added to the three standard solutions. A few high-abundance elements were spiked directly into the standard solutions (Ti, P, and K). Initial testing of these three standard solutions indicated that some elements were removed by the formation of insoluble phases, so they were treated with an acid mixture (2% HNO_3, 1.5% H_3BO_3, and 0.7% HF) to keep all of the elements in solution (see sample preparation).

6.2.5 Sample Preparation

Samples were first powdered using a pestle and mortar and homogenized before transferring to beakers for digestion. Sample digestion was done on 50-100 mg of sample in open Teflon PTFE containers by first adding ~2-4 ml of 4N HCl followed by 1-2 ml HF and allowed to sit overnight. Samples were then evaporated to dryness and allowed to sit overnight in ~1 ml $HClO_4$. The samples were evaporated to dryness a second time and allowed to cool.

After digestion, samples were treated using two different methods: 1) one group of samples were brought into solution using ~15-20 ml of 7N HNO_3 and transferred to sample bottles and allowed to sit overnight. Samples were then checked to ensure complete dissolution. If any sample remained, 7N HNO_3 was added in 1 ml increments until no visible sample remained. Testing of these samples (and the standard solutions) indicated the loss of elements as insoluble precipitates (See below), and thus treatment with a second method was necessary. These samples were evaporated to dryness and brought into solution using a mixture of 2% HNO_3, 1.5% H_3BO_3, and 0.7% HF (hereafter referred to as the acid mixture). 15 ml of this acid mixture was added and allowed to sit overnight. If the sample failed to go into solution, additional acid was added in 1ml steps until no visible sample remained. 2) Based on the observations from the first set of samples, after digestion, the second group of samples were brought into solution using only the 2% HNO_3 1.5% H_3BO_3, and 0.7% HF acid mixture by adding 15 ml and allowing to sit overnight. If any sample remained, more of the mixture was added in 1 ml increments until the samples appeared to have dissolved. However, several of these samples, specifically samples with mafic chemistry (higher Ca, Mg, Fe, and Al) commonly had a microcrystalline, cloudy white precipitate. The precipitate was highly stable and unaffected by the addition of more acid (HNO_3 (up to 4%), HCl (up to 4%), or H_3BO_3 (up to 5%)) or heating in oven at 70^{o}C for ~12 hours.

Two different sample preparation methods were necessary due to the insoluble behavior of high-field-strength elements (HFSE; Hf, Nb, Zr, Ta) when F^- ions were not in the solution. Fluoride is known to stabilize these elements as fluoro-complexes and inhibit the formation of insoluble compounds (Raczek et al. 2001; Hu et al. 2008; Makishima et al. 2009). However, in the presence of F^-, rare earth elements (REE) readily complex and form insoluble REE-bearing fluorides and are efficiently removed from the solution (Farrell et al. 1980; Boer et al. 1993; Hu et

al. 2010). To stop the formation of REE-fluorides, H_3BO_3 was added to bring the solutions up to 1.5%. Excess F^- is combined with H_3BO_3 to produce a fluorboirc acid matrix (Boer et al. 1993) which stabilizes the solution (Ferrell et al. 1980).

To summarize, in order to stabilize all of the elements in solution, it was necessary to keep the samples and standard solutions in a mixture of HNO_3, HF, and H_3BO_3. The samples previously brought into solution using only HNO_3, were evaporated and brought back into solution using the acid mixture. The second group of samples was brought into solution using only the HNO_3, H_3BO_3, and HF mixture.

6.3 Results

Accuracy of the analytical results was assessed with international rock reference material BHVO-1 (Table 6.1 and Fig. 6.1) and a internal lab standard (Valmont Dike (VMD); Table 6.2 and Fig. 6.2). Analysis of the 36 trace and minor elements developed in this method are in generally good agreement with recommended values for the reference materials, across more than five orders of magnitude in concentration (Fig. 6.1). Accuracy of the results was generally better than 10% (in % deviation of recommended values for BHVO-1) for most elements. However, P, K, Rb, Cs, Hf, and Th (Table 6.1 and Fig. 6.1) are notably higher/lower than the recommended values . Amongst these elements, most of these are above the reported values with the exception of P and Cs (Fig. 6.1).

Comparison of the VMD sample is based on an independently determined analysis from ACME Laboratory and LEGS at the University of Colorado (Table 6.2 and Fig. 6.2). ACME laboratory uses an alternative digestion technique than was developed in this study or is used in

Table 6.1. Comparison of the recommended values for the reference material BHVO-1 with measured values

	Recommended BHVO-1	Measured BHVO-1	% deviation	Isotope
P (wt %)	0.273	0.238	-14.7	31
K (wt %)	0.52	0.65	19.7	39
Ti (wt %)	2.71	2.87	5.7	49
Mn (wt %)	0.17	0.17	1.5	55
Sc	31.8	31.9	0.3	45
V	317	351	10.6	51
Cr	289	301	4.2	52
Co	45	47	5.5	59
Ni	121	122	1.0	60
Cu	136	143	5.3	63
Zn	105	107	2.3	66
Rb	9.05	10.65	17.6	85
Sr	395	427	8.0	88
Y	27.6	24.9	-9.8	89
Zr	179	174	-2.6	91
Nb	17.11	18.31	7.0	93
Cs	0.13	0.09	-33.5	133
Ba	139	150	8.2	137
La	15.8	16.9	7.0	139
Ce	39	43	9.7	140
Pr	5.7	5.6	-2.3	141
Nd	25.2	25.5	1.4	143
Sm	6.2	6.4	4.0	147
Eu	2.06	2.12	3.0	151
Gd	6.4	6.8	6.1	157
Tb	0.96	0.94	-2.6	159
Dy	5.2	5.8	11.4	163
Ho	0.99	0.98	-1.1	165
Er	2.4	2.7	12.1	167
Tm	0.33	0.34	4.3	169
Yb	2.02	2.17	7.3	172
Lu	0.291	0.324	11.4	175
Hf	4.38	5.74	31.1	178
Pb	2.08	2.09	0.5	208
Th	1.08	1.64	52.2	232
U	0.42	0.44	5.3	238

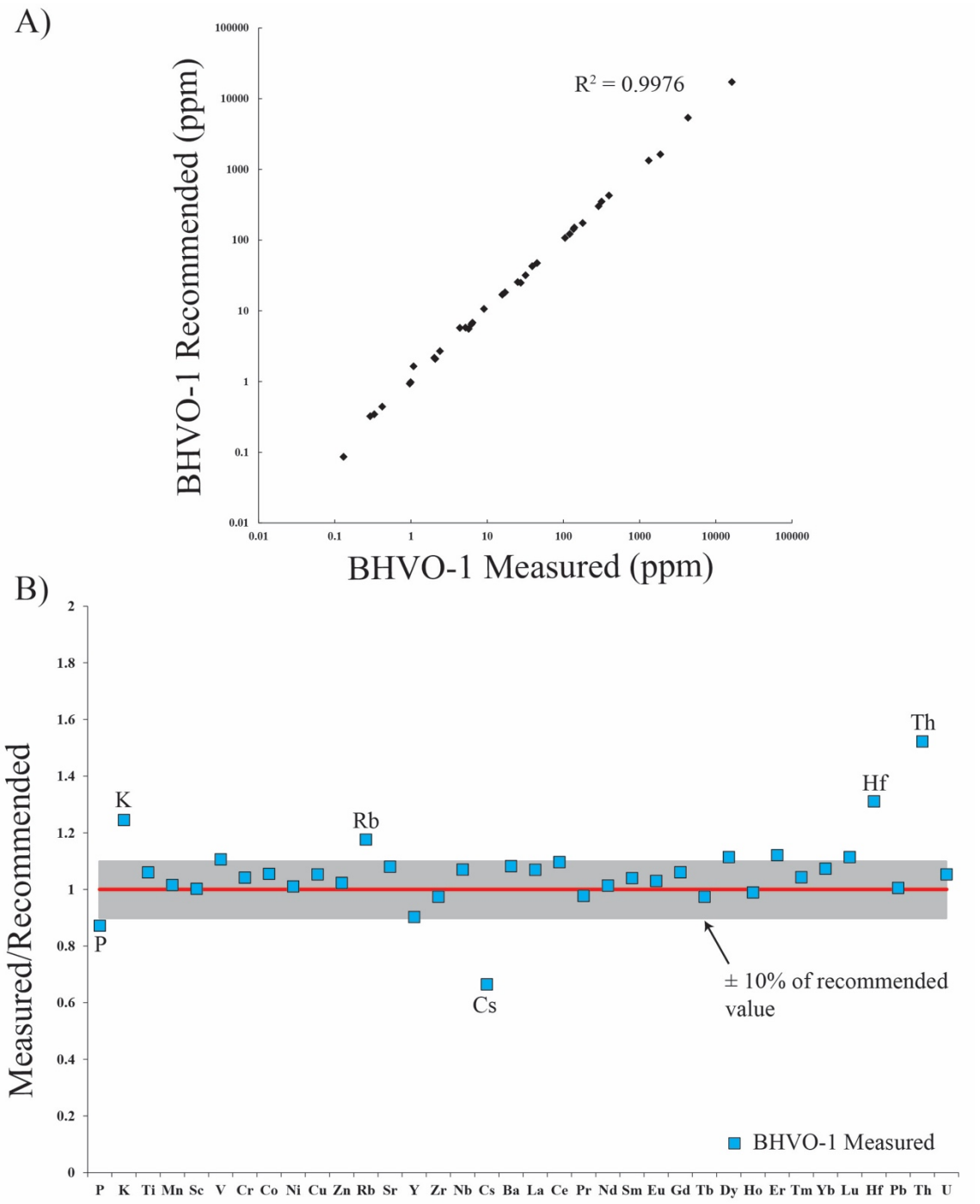

Figure 6.1. A) Measured versus recommended values for the BHVO-1 reference material in parts per million (ppm) in log-log space. The measured values are in good agreement with the recommended values **B)** The recovery yield for the 36 elements normalized to the BHVO-1 showing the ±10% field (grey). Most elements are within ±10% of the reported values. The majority of the elements outside the ±10% field are above the reported values and therefore not the result of low recovery yield due to incomplete digestion or the incorporation into insoluble phases

LEGS (LEGS uses a modified method as presented in Ferrel et al. 1980). To decompose the samples, the ACME labs uses an alkali fusion method. The alkali fusion of rock samples results in the formation of glasses that are then easily dissolved in dilute nitric acid (Totland et al. 1992). The fusion technique has many advantages compared to the open container HF and $HClO_4$ method. Fusion into glasses is effective at dissolving all refractory minerals and it allows for the determination of all major elements (Totland et al. 1992) which is not possible in the open container HF and $HClO_4$ method. Furthermore, the fusion method is not known to produce insoluble phases that have been documented using the open container HF and $HClO_4$ method (Ferrel et al. 1980; Boer et al. 1993, Yokoyama et al.1999, Hu et al. 2010).

The VMD data from ACME, LEGS, and those obtained from this study are included in Table 6.2. Comparison of the data from this study and from LEGS is based on the % deviation in comparison to the VMD determined from ACME labs. The VMD analysis from this study is in overall good agreement with the values reported from ACME laboratories (Fig. 6.2) with nearly all elements within the ±10% field. Several elements, and particularly the heavy REE (HREE) have concentrations slightly elevated with respect to the ACME reported values. Similar to the observations of the BHVO-1 analysis, the elements outside the ±10% field are determined to have concentrations greater than the reported VMD values (Fig. 6.2). Higher concentrations in the BHVO-1 and VMD indicate that low recovery yield resulting from incomplete digestion is not the cause for these differences.

Pyrolite normalized REE plots for VMD from this study are generally smooth and are in good agreement with the ACME value (Fig. 6.2). However, analysis from the LEGS laboratory are generally less smooth, and show large deviations notably for the elements Eu, Gd, and Er (Fig. 6.2). These deviations for Eu and Gd can distort and mask features of REE patterns such as

Table 6.2. Laboratory comparison of the trace element contents (ppm) of Valmont Dike (VMD) as compared to the ACME Labs

	ACME	LEGS		This Study	
	VMD	VMD	% deviation of LEGS	VMD	% deviation of measured
P	3448	-	-	3839	11.4
K	34287	-	-	34404	0.3
Sc	24	-	-	25	2.3
Ti	5755	6179	7.4	6248	8.6
V	258	328	27.1	269	4.5
Cr	82	78	-4.6	80	-3.1
Mn	1626	1610	-1.0	1625	-0.1
Co	32	38	21.8	34	7.8
Ni	30	51	71.2	30	-1.6
Cu	-	190	-	188	-
Zn	-	135	-	105	-
Rb	94.4	96.1	1.8	94.8	0.4
Sr	988.2	997.2	0.9	1017.7	3.0
Y	24.3	25.7	5.8	22.7	-6.6
Zr	137.6	141.5	2.9	141.2	2.6
Nb	18.6	21.2	14.0	17.8	-4.4
Cs	3.1	2.9	-7.6	2.8	-8.7
Ba	897	864	-3.7	918	2.3
La	40.60	38.45	-5.3	38.13	-6.1
Ce	74.20	78.85	6.3	78.34	5.6
Pr	9.59	9.57	-0.2	9.75	1.7
Nd	37.90	38.83	2.4	39.36	3.9
Sm	7.30	7.98	9.3	7.42	1.7
Eu	1.89	2.32	22.8	1.98	4.7
Gd	5.85	8.82	50.8	6.42	9.8
Tb	0.87	0.95	9.1	0.84	-3.3
Dy	4.57	4.98	9.0	5.16	12.8
Ho	0.85	0.93	9.6	0.94	10.5
Er	2.40	2.92	21.7	2.77	15.4
Tm	0.38	0.35	-8.2	0.41	9.2
Yb	2.41	2.52	4.8	2.76	14.4
Lu	0.38	0.34	-10.0	0.39	3.2
Hf	3.80	4.03	5.9	4.35	14.5
Pb	-	14.84	-	16.00	-
Th	8.20	8.36	2.0	9.97	21.6
U	2.50	2.48	-0.7	2.37	-5.3

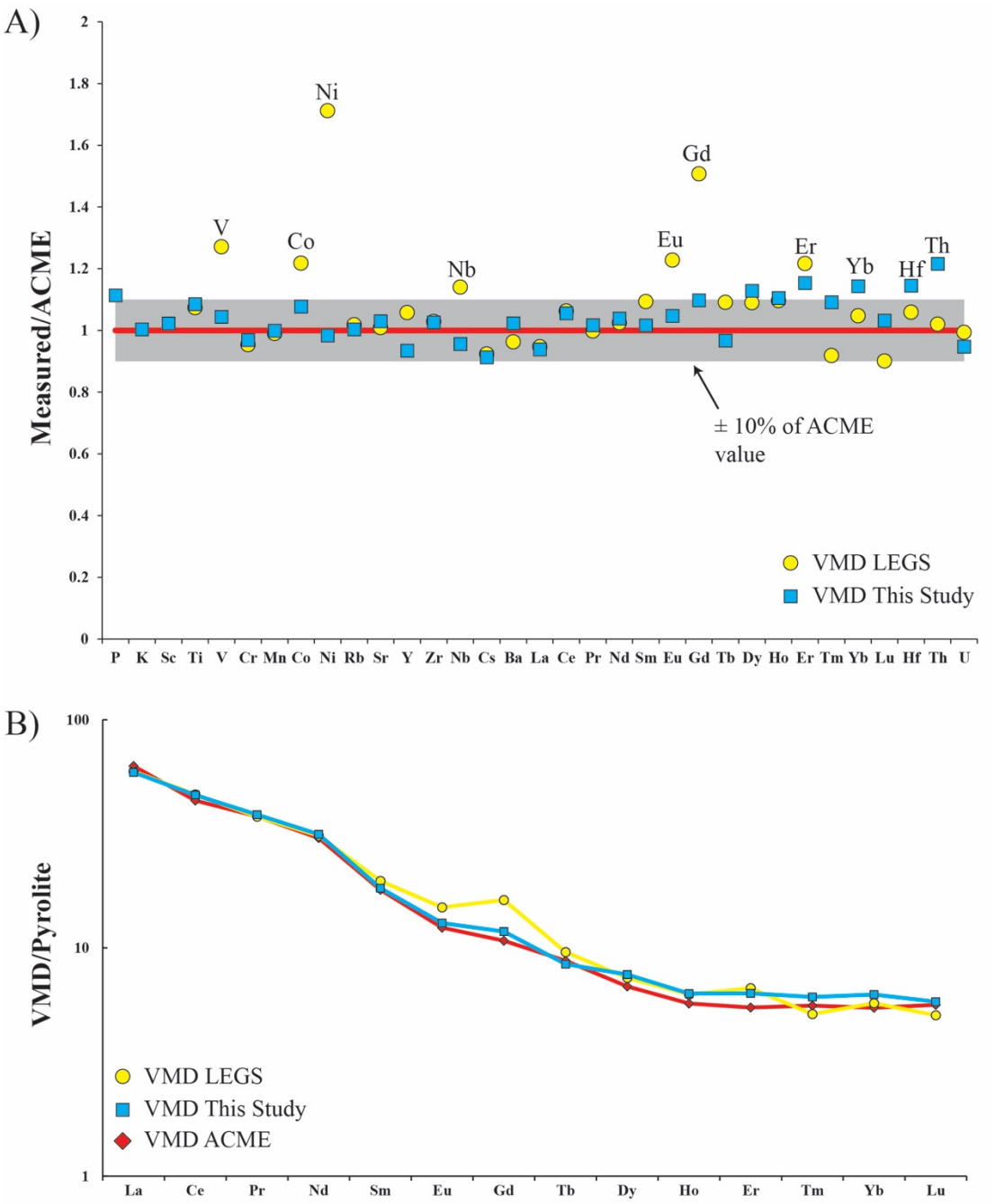

Figure 6.2. A) The recovery yield for 36 elements normalized to the VMD values reported from the AMCE lab showing the ±10% field (grey) for the AMCE values. Most elements are generally better than ±10% of the reported values. The LEGS analysis are generally within the ±10% field except V, Co, Ni, Nb, Eu, Gd and Er. **B)** Pyrolite normalized REE diagram for the Valmont Dike from three laboratories, ACME (red), LEGS (yellow), and this study (blue). The values from this study show good agreement with ACME analysis and produce generally smooth REE trends. Some heavy REE from this study are slightly elevated compared to the ACME data.

europium anomalies that have important petrologic implications.

It must be emphasized that these conclusions are based on a single analysis of each rock standard. Deviations from recommended values might be attributable to analytical noise or random contamination rather than some methodological bias. Numerous uncertainties can also enter the process of converting analyte concentrations in solution back to their abundance in the solid phase: these include pipetting errors, weighing errors, and incomplete recovery during digestion. The slight overall tendency for elevated values could arise from the first two errors, or from instrumental drift during analysis. A more thorough examination of these issues would require repeated analysis of the rock standards.

6.4 Discussion and Conclusion

The incorporation of the major elements (Na, Mg, Ca, Fe and Al; Croudace 1980) and trace elements (Yokoyama et al.1999) into insoluble fluorides during HF and $HClO_4$ decomposition is well understood. Yokoyama et al. (1999) observed precipitates during HF and $HClO_4$ decomposition and used x-ray diffraction (XRD) analysis to study the chemical make up of these complex compounds. It was revealed that these compounds were highly variable in their chemistry and dependent on the composition of the rock sample (Yokoyama et al. 1999). For example, samples with high concentrations of Mg, Ca, Fe, and Al tended to favor the formation of highly stable and insoluble fluoride compounds containing these cations (i.e. $CaAlF_5$, $CaMg_2Al_2F_2$, MgF_2, AlF_3, etc.). Depending on the identity of the fluorides, trace elements with a similar ionic charge and radius as the major elements could be selectively removed from the solution by filling atomic sites normally occupied by major elements.

An interesting result from the study of Yokoyama et al. (1999) was the 100% recovery of the 22 trace elements measured despite the formation of the white precipitates. XRD experiments revealed that these precipitates were TiO_2, $KClO_4$, and other HFSE bearing-oxides but contained no evidence for the incorporation of REE or other trace elements. This study also demonstrated the importance of using both HF and no less than 1ml of $HClO_4$ during digestion. During the HF evaporation step, Yokoyama et al. (1999) observed the formation of insoluble trace- and REE-bearing fluorides. However, when 1 ml of HClO4 was used (for a 50 mg sample) the insoluble fluorides converted to TiO2 and KClO4. Yokoyama et al. (1999) found that insoluble trace and REE-bearing fluorides remained when using less than 1 ml of $HClO_4$ during decomposition.

Similar to the observations of Yokoyama et al. (1999), insoluble precipitates formed in my samples after digestion using HF and $HClO_4$. The precipitates tended to form in samples more mafic in chemistry (higher Mg, Ca, Ti, and Al). Since these elements are not measured in this method, it is difficult to constrain the composition of the insoluble precipitates. This insoluble material never formed in the BHVO-1 or VMD samples during decomposition. Therefore, the measured BHVO-1 or VMD cannot be used to assess if the white material observed in other samples are the same TiO_2 and $KClO_4$ observed by Yokoyama et al. (1999).

Nonetheless, this method for simultaneously analyzing 36 trace and minor elements developed in this study produce values in good agreement with recommended values for reference materials BHVO-1 (Fig. 6.1) and also reproduce values generated using the alkali glass fusion digestion method (Fig S2). There is no clear evidence for the systematic loss of elements due to incomplete digestion or due to the incorporation of elements into insoluble phases.

6.5 Recommendations

Numerous studies have shown that the addition of HNO_3 or HCl to the solution post HF attack but prior to HF evaporation can reduce the formation of insoluble fluoride precipitates (Dulski et al. 2001; Hu et al. 2010). This finding is consistent with the observations made during preparation for my samples. Insoluble precipitates were not observed in the samples redissolved in 7N HNO_3. Additionally, it has been suggested that reducing the HF evaporation step could also inhibit the formation of the fluorides (Croudace 1980, Boer et al. 1993; Dulski et al. 2001; Navarro et al. 2008). Hu et al. (2010) found that excess fluoride ions during the evaporation step promoted the formation of the insoluble fluorides and the addition of nitric acid acted to inhibit their formation by diluting the fluoride ion concentration. Thus, careful monitoring of the samples during HF evaporation to ensure the sample does not "bake", combined with the addition of HNO_3 prior to, and during evaporation may be an additional step to inhibit fluoride formation and enhance recovery of elements potentially incorporated into these phases.

Thus, I recommend adding three minor steps during the sample digestion: 1) Add 1-2 ml of HNO_3 post HF attack but prior to evaporation and potentially during evaporation. Additionally, I recommend monitoring the solution carefully to ensure that the sample remains damp during HF evaporation. After evaporation of $HClO_4$, 2) Add ~5 ml of HCl and allow to sit for 12 hours before evaporating to insipient dryness, 3) Add ~5 ml HNO_3 and allow to sit for 12 hours before drying to insipient dryness. These additional steps could inhibit the formation of insoluble phases and potentially enhancing recovery.

6.6 Reference

Boer RH, Beukes GJ, Meyer FM, Smith CB (1993) Fluoride precipitates in silicate wet chemistry: implications on REE fractionation. Chem Geol 104:93-98

Croudace IW (1980) A possible error source in silicate wet-chemistry caused by insoluble fluorides. Chem Geol 31:1584-1590

Dulski P (2001) Reference Materials for Geochemical Studies: New Analytical Data by ICP-MS and Critical Discussion of Reference Values. J Geostand Geoanal 25 (1):87-125

Farrell RF, Matthes SA, Mackie AJ (1980) A simple, low-cost method for the dissolution of metal and mineral samples in plastic pressure vessels, Report of investigations - Bureau of Mines 8480:1-19

Hu Z, Gao S, Liu Y, Hu S, Zhao L, Li Y, Wang Q (2010) NH_4F assisted high pressure digestion of geological samples for multi-element analysis by ICP-MS. J Anal Atom Spectom 25:408-413

Hu Z, Gao S, Liu Y, Xu J, Hu S, Chen H (2009) Niobium and Tantalum Concentrations in MIST SRM 610 Revisited. J Geostand Geoanal Res 32:347-360

Makishima A, Tanaka R, Nakamura E (2009) Precise elemental and isotopic analyses in silicate samples employing ICP-MS: application of hydrofluoric acid solution and analytical techniques. Anal Sci 25:1181-1187

Navaro M, Andrade S, Ulbrich H, Gomes CB, Girardi VAV (2008) The direct determination of rare earth elements in basaltic and related rocks using ICP-MS: testing the efficiency of microwave oven sample decomposition procedures. J Geostand Geoanal Res 32:167-180

Raczek I, Stoll B, Hofmann AW, Jochum KP (2001) High-precision trace element data for the USGS Reference Materials BCR-1, BCR-2, BHVO-1, BHVO-2, AGV-1, AGV-2, DTS-1, DTS-2, GSP-1, GSP-2 by ID-TIMS and MIC-SSMS. J Geostand Geoanal

Totland M, Jarvis I, Jarvis KE (1992) An assessment of dissolution techniques for the analysis of geological samples by plasma spectrometry. Chem Geo 95:35-62

Yokoyama T, Makishima A, Nakamura E (1999) Evaluation of the coprecipitation of incompatible trace elements with fluoride during silicate rock dissolution by acid digestion. Chem Geo 157:175-187

Chapter 7

Cumulative Bibliography

Alt JC, Schwarzenbach EM, Früh-Green GL, Shanks III, WC, Bernasconi SM, Garrido CJ, Crispini L, Gaggero L, Padrón-Navarta, Marchesi C (2013) The role of serpentinites in cycling of carbon and sulfur: Seafloor serpentinization and subduction metamorphism. Lith 178:40-54, http://dx.doi.org/10.1016/j.lithos.2012.12.006

Ariskin AA, Frenkel MY, Barmina GS, Nielsen R (1993) COMAGMAT: A FORTRAN program to model magma differentiation processes. Comput Geosci 19:1155–1170, doi:10.1016/0098-3004(93)90020-6.

Bertrand S, Araneda A, Vargas P, Jana P, Fagel N, Urrutia R (2012). Using the N/C ratio to correct bulk radiocarbon ages from lake sediments: Insights from Chilean Patagonia. Quat Geochron 12: 23-29

Bertrand S, Daga R, Bedert, R, Fontijn K (2014) Deposition of the 2011-2012 Cordon Caulle tephra (Chile, 40°S) in lake sediments: implications for tephrochronology and volcanology. J Geophys Res 119: 2555-2573

Best JL (1992) Sedimentology and event timing of a catastrophic volcaniclastic mass flow, Volcán Hudson, southern Chile. Bull Volcanol 54: 299–318

Björck S, Rundgren M, Ljung K, Unkel I, Wallin A (2012) Multi-proxy analyses of a peat bog on Isla de los Estados, easternmost Tierra del Fuego: a unique record of the variable Southern Hemisphere Westerlies since the last deglaciation. Quat Sci Rev 42: 1-14

Bronk Ramsey, C (2008) Deposition models for chronological records. Quat Sci Rev 27: 42-60

Cande SC, Leslie RB (1986) Late Cenozoic Tectonics of the Southern Chile Trench. J Geophys Res 91(B1): 471–496

Carel M, Siani G, Delpech G (2011) Tephrostratigrapy of a deep-sea sediment sequence off the south Chilean margin: New insight into the Hudson volcanic activity since the last glacial period. J Volcanol Geotherm Res. 208: 99-111

Cembrano J, Hervé F, Lavenu A (l996) The Liquiñe-Ofqui fault zone: long-lived intra-arc fault system in southern Chile. Tectonophys 259: 55–66

Contreras-Reyes E, Grevemeyer I, Flueh ER, Scherwath M, Heesemann M (2007) Alteration of the subducting oceanic lithosphere at the southern central Chile trenchouter rise. Geochem Geophys Geosyst 8

Contreras-Reyes E, Grevemeyer I, Flueh ER, Reichert C (2008) Upper lithospheric structure of the subduction zone offshore of southern Arauco peninsula, Chile, at 38°S. J Geophys Res 113

Danyushevsky L V, Plechov P (2011), Petrolog3: Integrated software for modeling crystallization processes, Geochem Geophys Geosyst 12, Q07021, doi:10.1029/2011GC003516.

Danyushevsky, LV, Della-Pasqua FN, Sokolov S (2000) Re-equilibration of melt inclusions trapped by magnesian olivine phenocrysts from subduction-related magmas: petrological implications. Cont Mineral Petrol 138: 68-83

Danyushevsky LV, McNeill AW, Sobolev AV (2002) Experimental and petrological studies of melt inclusions in phenocrysts from mantle-derived magmas: an overview of techniques, advantages and complications. Chem Geol 183: 5-24

DeMets C, Gordon RG, Argus, DF (2010) Geologicaly current plate motions. Geophys J Int 181: 1-80

de Porras ME, Maldonado A, Abarzúa AM, Cárdenas ML, Francois JP, Martel-Cea A, Stern, CR (2012) Postglacial vegetation, fire and climate dynamics at Central Chilean Patagonia (Lake Shaman, 44°S). Quat Sci Revs 50: 71–85

de Porras ME, Maldonado A, Quintana FA, Martel-Cea1 JO, Reyes O, Méndez C (2014) Environmental and climatic changes in Central Chilean Patagonia since the Late Glacial (Mallín El Embudo, 44°S). Climates of the Past 10: 1063–1078

D'Orazio M, Innocenti F, Manetti P, Tamponi M, Tonarini S, González-Ferrán O, Lahsen A (2003) The Quaternary calc-alkaline volcanism of the Patagonian Andes close to the Chile triple junction: geochemistry and petrogenesis of volcanic rocks from the Cay and Maca volcanoes (~45°S, Chile). J S Amer Earth Sci 16(4): 219–242

Elbert J, Wartenburg R, von Gunten L, Urrutia R, Fisher D, Fujak M, Hamann Y, Greber ND, Grosjean M (2013) Late Holocene air temperature variability reconstructed from the sediments of Laguna Escondida, Patagonia Chile. Palaeogeog Palaeoclimat Palaeoecol 396: 482-492

Farmer, G.L., Broxton, D.E., Warren, R.G., Pickthorn, W., (1991) Nd, Sr, and O isotopic variations in metaluminous ash-flow tuffs and related volcanic rocks at Timber Mountain/ Oasis Valley Caldera, Complex, SW Nevada: implication for the origin and evolution of large-volume silicic magma bodies. Contrib Mineral Petrol 109, 53–68.

Fontijn K, Lachowycz SM, Rawson H, Pyle DM, Mather TA, Naranjo JA, Moreno-Roa H (2014) Late Quaternary tephrostratigraphy of southern Chile and Argentina. Quat Sci Revs 89: 70-84

Ford CE, DG Russell, JA Groven, Fisk MR (1983) Distribution coefficients of Mg2+, Fe2+, Ca2+ and Mn2+ between olivine and melt. J Petrol 24:256–265

Futa K, Stern CR (l988) Sr and Nd isotopic and trace element compositions of Quaternary volcanic centers of the southern Andes. Earth Planet Sci Lett 88: 253–262

Gutiérrez F, Gioncada A, González-Ferrán O, Lahsen A, Mazzuoli R (2005) The Hudson volcano and surrounding monogenetic centres (Chilean Patagonia): an example of volcanism associated with ridge-trench collision environment. J Volcanol Geotherm Res 145: 207–233

Gonzáles-Ferrán O (1994) Volcanes de Chile. Instituto Geografico Militar, Santiago, 640 p

Haberle SG, Lumley SH (1998) Age and origin of tephras recorded in postglacial lake sediments to the west of the southern Andes, 44^{o}S to 47^{o}S. J Volcanol Geotherm Res. 84: 238-256

Hermann J, Spandler CJ (2008) Sediment melts at sub-arc depths: an experimental study. J Petrol 49:717–740

Hickey RL, Frey FA, Gerlach DC (1986) Multiple sources for basaltic arc rocks from the Southern Volcanic Zone of the Andes (34-41°S): Trace element and isotopic evidence for contributions from subducted oceanic crust, mantle, and continental crust. J Geoph Res 91: 5963-5983.

Hickey-Vargas, R.L.; Moreno-Roa, H.; López-Escobar, L.; Frey, F.A. 1989. Geochemical variations in Andean basaltic and silicic lavas from the Villarrica-Lanín volcanic chain (39.5°S): an evaluation of source heterogeneity, fractional crystallization and crustal

assimilation. Contrib Mineral Petrol 103: 361-386.

Hickey-Vargas RL, Abdollahi MJ, Parada MA, López-Escobar L, Frey FF (1995) Crustal xenoliths from Calbuco Volcano, Andean Southern Volcanic Zone: implications for crustal composition and magma-crust interaction. Contrib Mineral Petrol 119: 331-344.

Hickey-Vargas, R.L.; Sun, M.; López-Escobar, L.; Moreno-Roa, H.; Reagan, M.K.; Morris, J.D.; Ryan J.G. 2003. Multiple subduction components in the mantle wedge: evidence from eruptive centers in the Central Southern volcanic zone, Chile. Geology 30 (3): 199-202.

Hickey-Vargas R, Holbik S, Tormey D, Frey FA, Moreno Roa H (2016) Basaltic rocks from the Andean Southern Volcanic Zone: Insight from the comparison of along-strike and small-scale geochemical variations and their sources. Lithos 258-259: 115-132

Hildreth W, Moorbath S (1988) Crustal contributions to arc magmatism in the Andes of Central Chile. Contrib Mineral Petrol 98:455-489

Hogg A, Hua Q, Blackwell P, Niu M, Buck C, Guilderson T, Heaton TJ, Palmer JG, Paula JR, Reimer RW, Turney CSM, Zimmerman SRH (2013). SHCAL13 Southern Hemisphere Calibration, 0-50,000 years CAL BP. Radiocarbon 55(4), 1889-1903.

Jacques G, Hoernle, KL, Gill, J, Hauff, F, Wehrmann, H, Garbe-Schönberg, D, van den Bogaard, P, Bindeman I, Lara LE (2013) Across-arc geochemical variations in the Andean Southern Volcanic Zone, Chile (34.5-38.0°S): Constraints on mantle wedge and slab input compositions. Geochem et Cosmoch Acta 123: 218–243

Kelley KA, Plank T, Grove TL, Stolper EM, Newman S, Hauri E (2006) Mantle melting as a function of water content beneath back-arc basins. J Geophys Res 111 B09208 doi:10.1029/2005JB003732.

Kelley KA, Plank T, Newman S, Stolper EM, Grove TL, Parman S, Hauri E (2010) Mantle

melting as a function of water content beneath the Mariana arc. J Petrol 51: 1711–1738 doi:10.1093/petrology/egq036.

Kratzmann DJ, Carey S, Scasso RA, Naranjo JA (2009) Compositional variations and magma mixing in the 1991 eruptions of Hudson volcano, Chile. Bull Volcanol 71(4): 419–439

Kratzmann DJ, Carey S, Scasso RA, Naranjo JA (2010) Role of cryptic amphibole crystallization in magma differentiation at Hudson volcano, Southern Volcanic Zone, Chile. Contrib Mineral Petrol 159: 237–264

Leake B, Woolley A, Arps C, Birch W, Gilbert M, Grice J, Hawthorne F, Kato A, Kisch H, Krivovichev V, Linthout K, Laird J, Mandarino J, Maresch W, Nickel E, Rock N, Schumacher J, Smith D, Stephenson, N., Ungaretti L,Whittaker E, Youzhi G (1997). Nomenclature of amphiboles: report of the subcommittee on amphiboles of the International Mineralogical Association, Commission on New Minerals and Minerals Names. Amer Mineral 82:1019-1037

López-Escobar L, Kilian R, Kempton P, Tagiri M (l993) Petrology and geochemistry of Quaternary rocks from the southern volcanic zone of the Andes between 41°30’ and 46°00’S, Chile. Rev Geol Chile 20: 33–55

López-Escobar L, Parada MA, Hickey-Vargas R, Frey FA, Kempton P, Moreno H (1995) Calbuco Volcano and minor eruptive centers distributed along thLiquifie-Ofqui Fault Zone, Chile (41°S) contrasting origin of andesitic and basaltic magmain the Southern Volcanic Zone of the Andes. Contr Mineral Petrol 119: 345-361

Lowe DJ (2011) Tephrochronology and its application: A review. Quat Geol. 6: 107-153

Manea VC, Leeman WP, Gerya T, Manea M, Zhu, G (2014) Subduction of fracture zones controls mantle melting and geochemical signature above slabs. Nat Commun 5:5095 doi: 10.1038/ncomms6095

Markgraf V, Whitlock C, Haberle S (2007) Vegetation and fire history during the last 18,000 cal yr B.P. in Southern Patagonia: Mallín Pollux, Coyhaique, Province Aisén (45°41'30", 71°50'30"W, 640 m elevation). Palaeogeogr Palaeoclimatol Palaeoecol 254: 492-507

McCulloch RD, Figuerero MJ, Mengoni GL, Barclay R, Mansilla C (2016) A Holocene record of environmental change from Río Zeballos, central Patagonia. The Holocene DOI: 10.1177/0959683616678460

Mella M, Ramos A, Kraus S, Duhart P (2012) Tefroestratigrafía, magnitud y geoquímica de erupciones holocenas mayores del volcán Mentolat, Andes del Sur (44º40'S), Chile. Actas, Congreso Geológico Chileno, No. 13, Antofagasta.

Moreno P, Alloway BV, Villarosa G, Outes V, Henríquez WI, De Pol-Holz R, Pearce NJG (2015) A past-millennium maximum in postglacial activity from Volcán Chaitén, southern Chile. Geology 43: 47-50

Miranda CG, Moreno PI, Vilanova I, Villa-Martínez RP (2013) Glacial fluctuations in the Coyhaique-Balmaceda sector of central Patagonia (45°S-46°S) during the last glacial termination. Bollettino di Geofisica 54: 268-271

Naranjo JA (l991) Nueva erupción del volcán Hudson. Rev Geol Chile 18: 183–184

Naranjo JA, Moreno HR, Banks NG, (1993) La Eruptión del Volcán Hudson en 1991 (46°S), Regieón XI, Aisén, Chile. Servicio Nacional de Geologia y Mineria 44:1-50

Naranjo JA, Stern CR (1998) Holocene explosive activity of Hudson Volcano, southern Andes. Bull Volcanol 59(4): 291–306

Naranjo JA, Stern CR (2004) Holocene tephrochronology of the southernmost part (42°30'-45°S) of the Andean Southern Volcanic Zone. Rev Geol Chile 31(2): 225–240

Nelson E, Forsythe R, Arit I (1994) Ridge collision tectonics in terrane development. J S Amer Earth Sci 7(3-4): 271–278

Orihashi Y, Naranjo JA, Motoki A, Sumino H, Hirata D, Anma R, Nago K (2004) Quaternary volcanic activity of Hudson and Lautaro volcanoes, Chilean Patagonia: New constraints from K-Ar ages. Rev Geol Chile 31: 207–224

Plank T, LB Cooper, Manning C. E. (2009) Emerging geothermometers for estimating slab surface temperatures. Nat Geosci 2: 611–615 doi:10.1038/ngeo614

Portnyagin, M., K. Hoernle, P. Plechov, N. Mironov, and S. Khubunaya (2007), Constraints on mantle melting and composition and nature of slab components in volcanic arcs from volatiles (H2O, S, Cl, F) and trace elements in melt inclusions from the Kamchatka Arc. Earth Planet Sci Lett 255: 53–69 doi:10.1016/j.epsl.2006.12.005

Prieto A, Stern CR, Esterves J (2013) The peopling of the Fuego-Patagonian fjords by littoral hunter-gatherers after the mid-Holocene H1 eruption of Hudson volcano. Quat Internat 317: 3-13

Rawson H, Naranjo JA, Smith, V, Fontijn K, Pyle DM, Mather TA, Moreno H (2015) The frequency and magnitude of post-glacial explosive eruptions at Volcán Mocho Choshuenco, southern Chile. J Volcanol Geotherm Res 299: 103-129

Rodríguez C, Sellés D, Dungan M, Langmuir C, Leeman W, (2007) Adikitic dacites formed by intracrustal crystal fractionation of water-rich parent magmas at Nevado de Longaví (36.2^{o}S; Andean Southern Volcanic Zone, Central Chile). J Petrol 48(11): 2033-2061

Saadat S, CR Stern (2011) Petrochemistry and genesis of olivine basalts from small monogenetic parasitic cones of Bazman stratovolcano, Makran arc, southeastern Iran. Lithos 125: 609-617

Salters VJM, Stracke A (2004) Composition of the depleted mantle. Geochem Geophys Geosyst 5 Q05B07 doi:10.1029/2003GC000597

Scasso RA, Corbella H, Tiberi P (l994) Sedimentological analysis of the tephra from the 12–15 August l991 eruption of Hudson volcano. Bull Volcanol 56: 121–132

Scasso RA, Carey S, (2005) Morphology and formation of glassy volcanic ash from the August 12-15, 1991 eruption of Hudson volcano, Chile. Latin American J Sediment and Basin Anal 12(1): 3-21

Sellés D, Rodríguez AC, Dungan MA, Naranjo JA, Gardeweg M (2004) Geochemistry of Nevado de Longaví (36.2°S): a compositionally atypical volcano in the Southerrn Volcanic Zone of the Andes. Rev Geol Chile 31(2): 293-315

Siani G, Colin C, Mechel E, Carel M, Richter T, Kissel C, Dewilde F (2010) Late Glacial to Holocene terrigenous sediment record in the Northern Patagonian margin: paleoclimate implications. Palaeogeogr Palaeoclimatol Palaeoecol 297: 26-36

Siani G, Michel E, De Pol-Holz R, DeVries T, Lamy F, Carel M, Isguder G, Dewilde F, Lourantou A (2013) Carbon isotope records reveal precise timing of enhanced Southern Ocean upwelling during the last deglaciation. Nature Communications 4: 2758 DOI: 10.1038/ncomms3758

Singer BS, Jicha BR, Leeman WP, Rogers NW, Thirlwall MF, Ryan J, Nicolaysen KE (2007) Along-strike trace element and isotopic variaiton in Aleutian Island arc basalt: Subduction

melts sediments and dehydrates serpentine. J of Geophys Res 112 doi:10.1029/2006JB004897

Stern CR (l991) Mid-Holocene tephra on Tierra del Fuego (54°S) derived from the Hudson volcano (46°S): evidence for a large explosive eruption. Rev Geol Chile 18: 139–146

Stern CR (2004) Active Andean Volcanism: its geologic and tectonic setting. Rev Geol Chile 31(2): 161-206

Stern CR (2008) Holocene tephrochronology record of large explosive eruptions in the southernmost Patagonian Andes. Bull Volcanol 70(4): 435–454

Stern CR, de Porras ME, Maldonado A (2015) Tephrochronology of the upper Río Cisnes valley (44°S), southern Chile. Andean Geol 42(2): 173-192

Stern CR, Moreno PI, Henrique WI, Villa-Martinez RP, Sagredo E, Aravena JC, De Pol-Holz R (2016) Holocene tephrochronolgy in the area around Cochrane, southern Chile. Andean Geol 43(1): 1-19

Stolper E, Newman S (1994) The role of water in the petrogenesis of Mariana trough magmas. Earth Planet Sci Lett 121: 293–325

Stuiver M, Reimer PJ, Braziunas TF (1998) High-precision radiocarbon age calibration for terrestrial and marine samples. Radiocarbon 40(3): 1127–1151

Stuiver M, Reimer PJ, Reimer R (2013) CALIB 7.0.4. http://calib.qub.ac.uk/calib/

Tormey DR, Hickey-Vargas R, Frey FA, López-Escobar L (1991) Recent lavas from the Andean volcanic front (33 to 42°S): Interpretations of along-arc compositional variations. Geol Soc Spec Pap 265

Unkel I, Fernandez M, Björck S, Ljung K, Wohlfarth B (2010) Records of environmental changes during the Holocene from Isla de los Estados (54.4^{o}S), southern Tierra del Fuego. Global Planet Change 74: 99-113

Van Daele M, Bertrand S, Meyer I, Moernaut J, Vandoorne W, Siani G, Tanghe N, Ghazoui Z, Pino M, Urrutia R, De Batist M (2016) Late Quaternary evolution of Lago Castor (Chile, 45.6°S): Timing of the deglaciation in northern Patagonia and evolution of the southern westerlies during the last 17 kyr. Quat Sci Rev 133: 130-146

Vargas G, Rebolledo S, Sepúlveda SA, Lahsen A, Thiele R, Townley B, Padilla C, Rauld R, Herrera MJ, Lara M (2013) Submarine earthquake rupture, active faulting and volcanism along the major Liquiñe-Ofque Fault Zone and implications for seismic hazard assessment in the Patagonian Andes. Andean Geol 40: 141-171

Villa-Martínez R, Moreno PI, Valenzuela MA (2012) Deglacial and postglacial vegetation changes on the eastern slopes of the central Patagonian Andes (47^{o}S). Quat Sci Rev 32: 86-99

Völker D, Kutterolf S, Wehrmann H (2011) Comparative mass balance of volcanic edifices at the southern volcanic zone of the Andes between 33^{o}S and 46^{o}S. J Volcanol Geotherm Res. 205: 114-129

Wallace PJ (2005) Volatiles in subduction zone magmas: concentrations and fluxes based on melt inclusions and volcanic gas data. J Volcanol Geotherm Res 140:217–240. doi:10.1016/j.volgeores.2004.07.23

Wallace PJ, Edmonds M (2011) The sulfur budget in magmas:evidence from melt inclusions, submarine glasses, and volcanic gas emissions. Rev Mineral Geochem 73:215–246. doi:10.2138/ rmg.2011.73.8Watt SFL, Pyle DM, Mather TA (2011) Geology, petrology and

geochemistry of the dome complex of Huequi volcano, southern Chile. Andean Geol 38(2): 335-348

Watt SFL, Pyle DM, Mather TA (2011) Geology, petrology and geochemistry of the dome complex of Huequi volcano, southern Chile. Andean Geol 38(2): 335-348

Watt SFL, Pyle DM, Mather TA, Naranjo JA (2013) Arc magma compositions controlled by linked thermal and chemical gradients above the subducting slab. Geophs Res Lett 40(11): 2550-2556

Watt SFL, Pyle DM, Mather TA (2013) The volcanic response to deglaciation: evidence from glaciated arcs and a reassessment of global eruption records. Earth Sci Rev 122: 77-102

Wehrmann H, Hoernle K, Jacques G, Garbe-Schönberg D, Schumann K, Mahlke J, Lara L, 2014 Sulphur and chlorine geochemistry of mafic to intermediate tephras from the Chilean Southern Volcanic Zone (33–43°S) compared with those from the Central American Volcanic Arc. Int J Earth Sci 103:1945-1962

Weller DJ, Miranda CG, Moreno PI, Villa-Martínez RP, Stern CR (2014) A large late-glacial Ho eruption fo the Hudson volcano, southern Chile. Bull Volcanol 76: 831-849

Weller DJ, Miranda CG, Moreno PI, Villa-Martínez RP, Stern CR (2015) Tephrochronology of the Andean Southern Volanic Zone, Chile. Bull Volcanol 76: 831-849

Weller DJ, de Porras E, Maldonado A, Stern CR (2017a) Holocene tephrochronology of the lower Río Cisnes Valley, southern Chile. Andean Geol (in prep)

Weller DJ, dePorras E, Maldonado A, Stern CR (2017b) New age controls on the tephrochronology of the southernmost Andean Southern Volcanic Zone, Chile. Bull Volcanol (in prep)

Wilson T M, Cole JW, Stewart C, Cronin SJ, Johnston DM (2011) Ash storms: impacts of wind-remobilised volcanic ash on rural communities and agriculture following the 1991 Hudson eruption, southern Patagonia, Chile. Bull Volcanol 73: 223–239

Wilson T, Cole J, Johnston D, Cronin S, Stewart C, Dantas A (2012) Short-and long-term evacuation of people and livestock during a volcanic crisis: lessons from the 1991 eruption of Volcan Hudson, Chile. J Applied Volcanol 1: 2

Wood BJ, Turner SP (2009) Origin of primitive high-Mg andesite: Constraints from natural examples and experiments, Earth Planet Sci Lett 283: 59–66 doi:10.1016/j.epsl.2009.03.032.

Wright HE Jr, (1967) A square-rod piston sampler for lake sediments. J Sed Petrol 37: 975–976

Appendix

A2 Chapter 2 Appendix

The appendix includes all of the supplementary files for which consists of X-ray images for the all of the lake cores with the tephra correlations and the bulk tephra petrochemistry for all the sampled tephra collected from each sediment core.

Figures

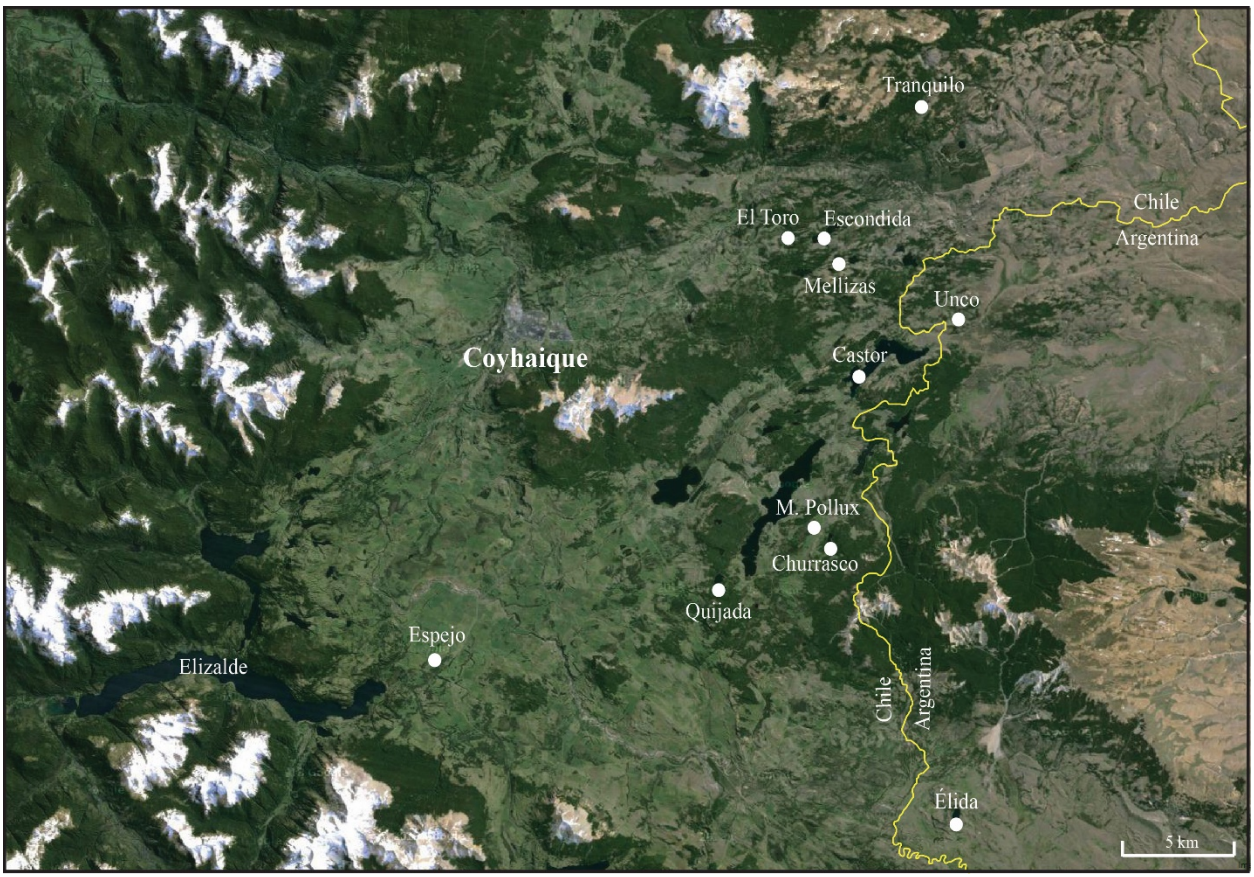

Figure A2.1. Google map image of the location of the lakes cored for this study and other nearby lakes (Pollux, Escondida, Castor) for which tephra from cores have been previously described by Markgraf et al. (2007) and Elbert et al. (2013). The precise location of the new cores are: Lago Espejo (45°45'27.31"S; 72° 8'4.04"W), Lago Quijada (45°42'53.54"S; 71°54'32.22"W, Lago Churrasco (45°41'30.76"S, 71°49'14.21"W), Lago Élida (45°50'25.46"S; 71°43'14.03"W), Lago Unco (45°34'29.30"S; 71°43'9.36"W), Las Mellizas (45°32'34.83"S; 71°48'47.51"W), El Toro (45°31'48.01"S; 71°51'14.44"W), Lago Tranquilo (45°27'25.98"S; 71°49'29.11"W).

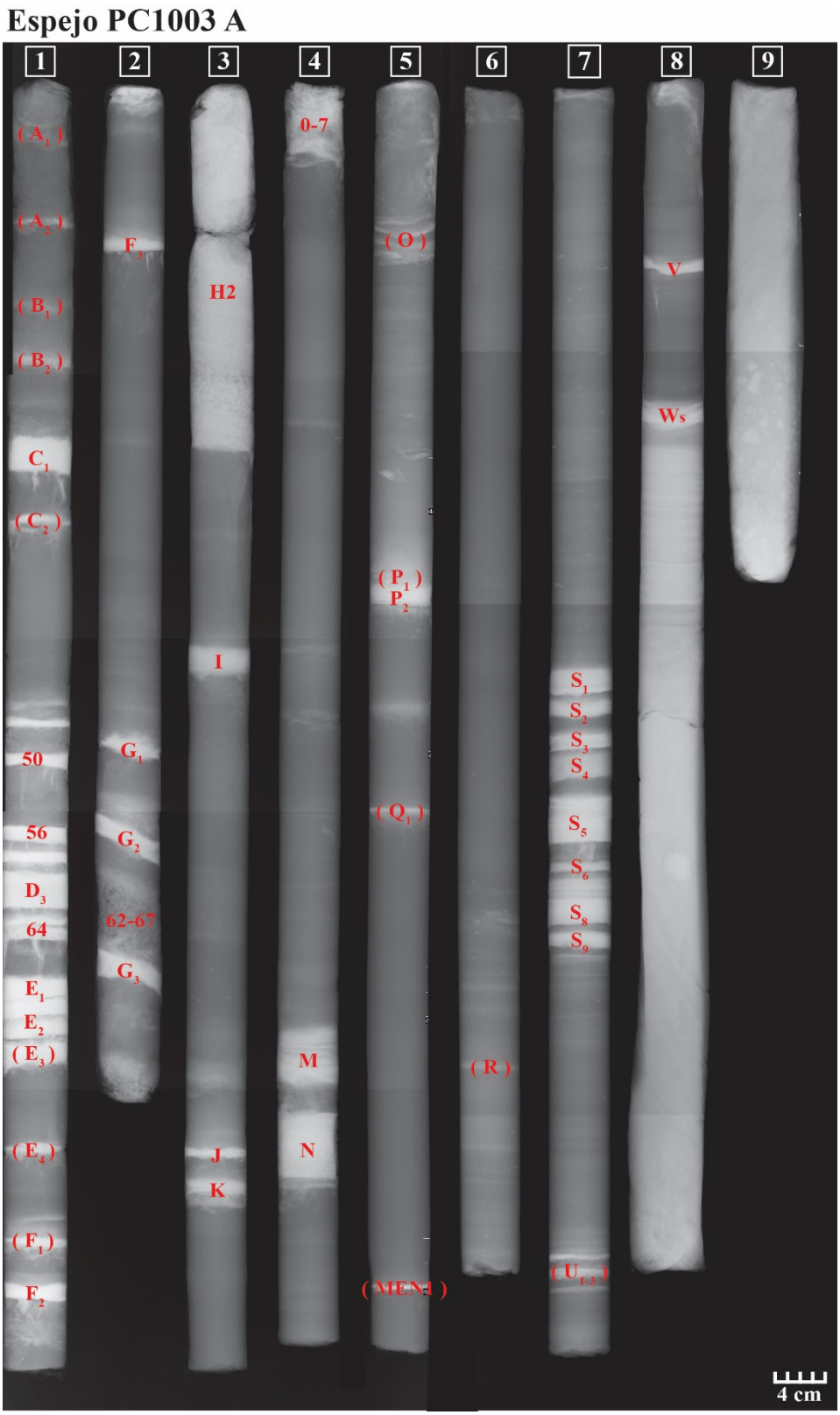

Figure A2.2. X-ray image and tephra identification for the core from Espejo lake.

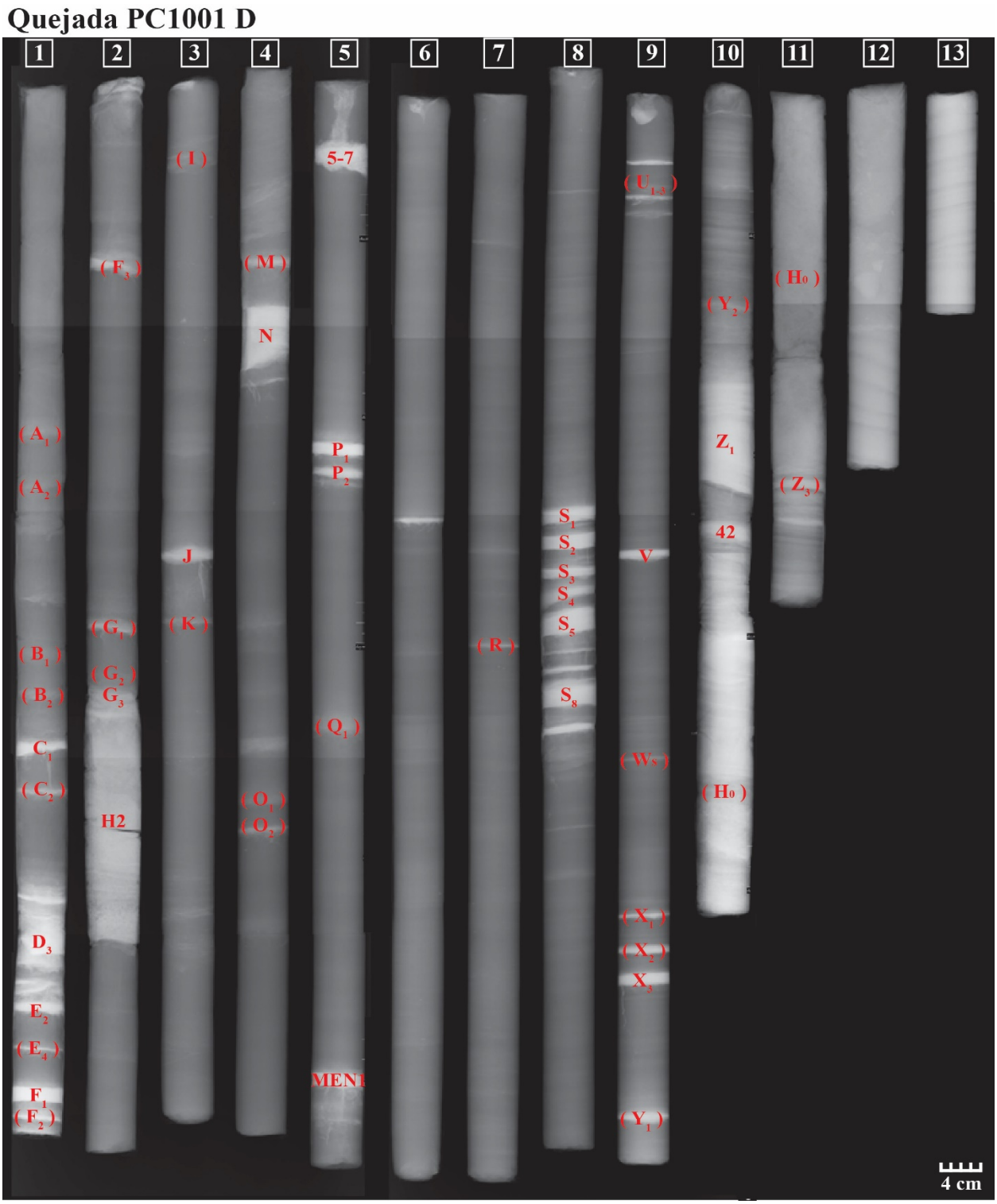

Figure A2.3. X-ray image and tephra identification for the core from Quijada lake.

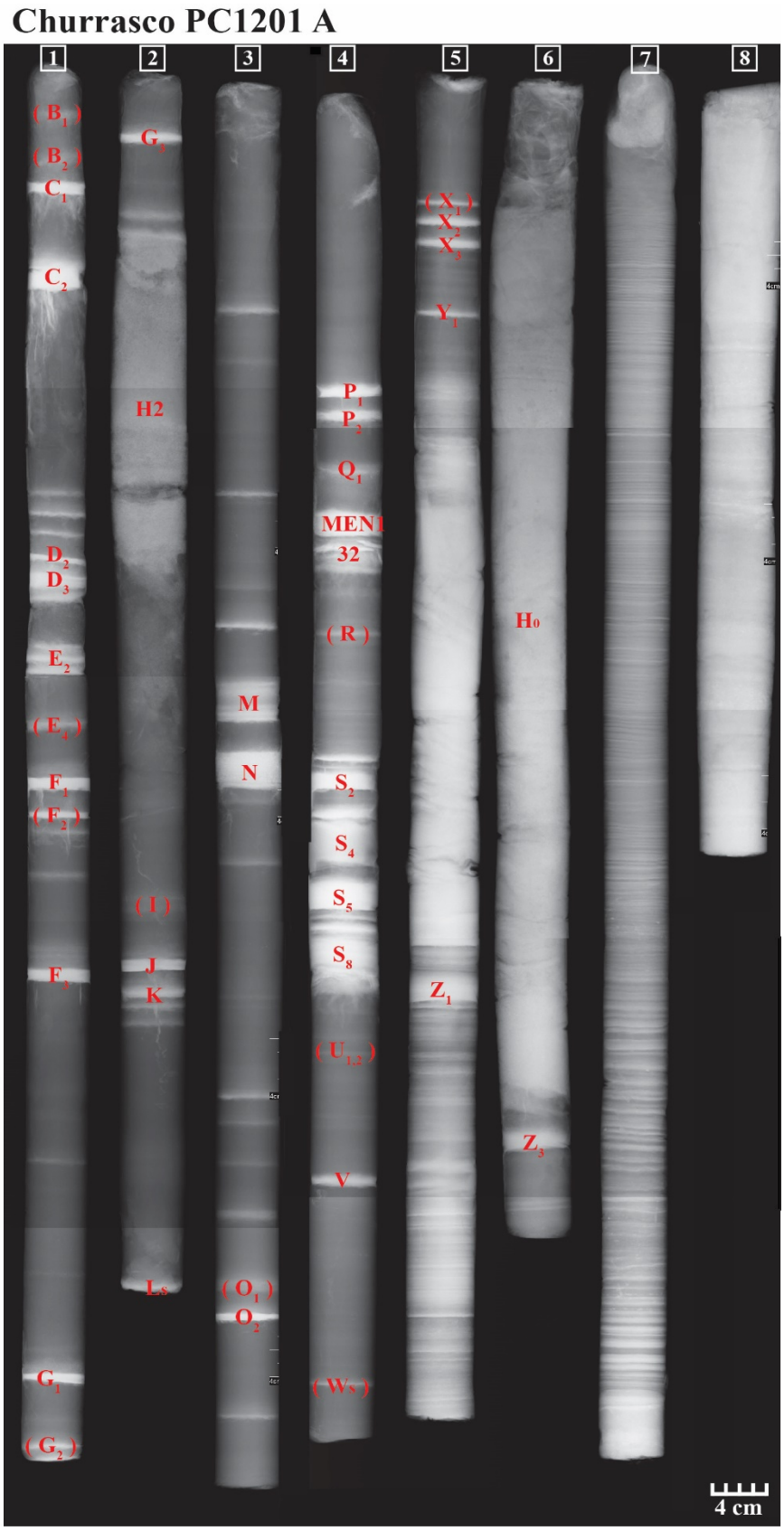

Figure A2.4. X-ray image and tephra identification for the core from Churrasco lake.

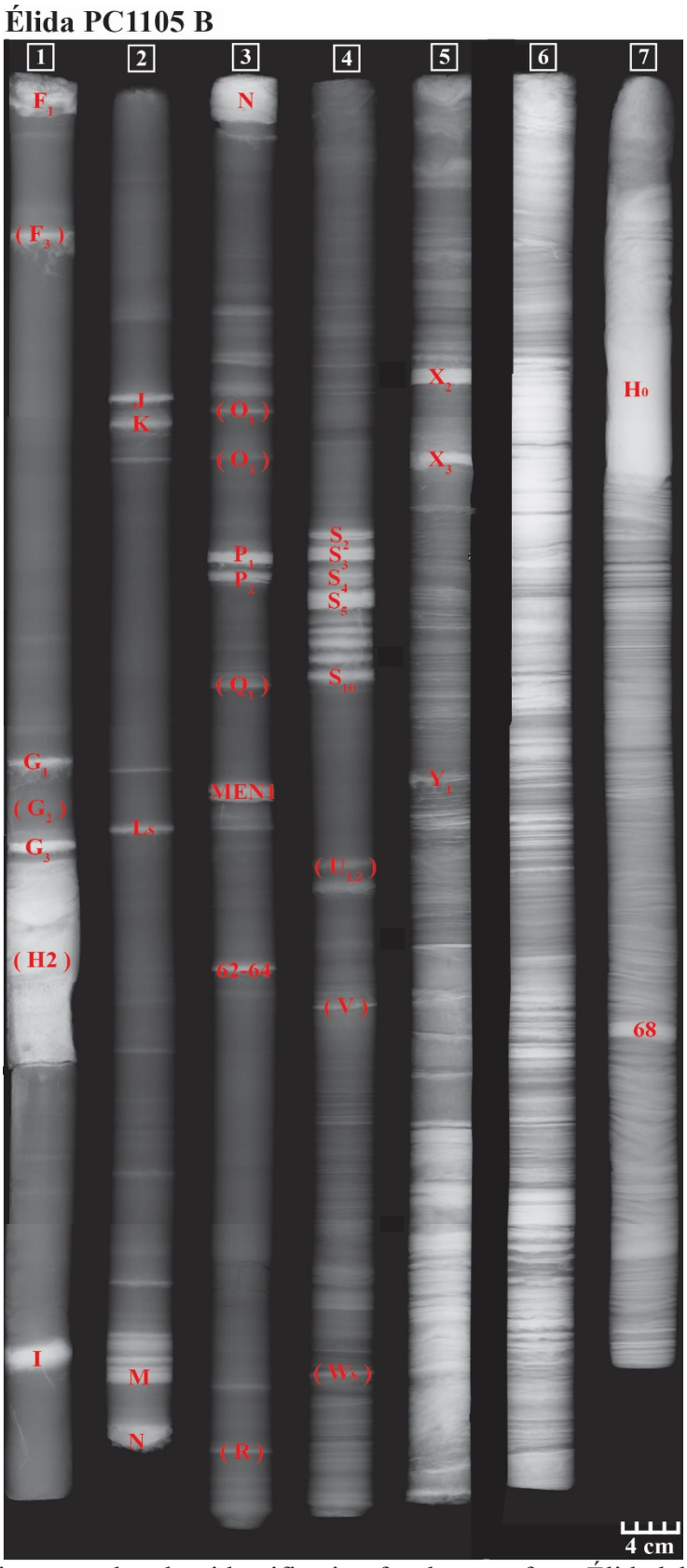

Figure A2.5. X-ray image and tephra identification for the core from Élida lake.

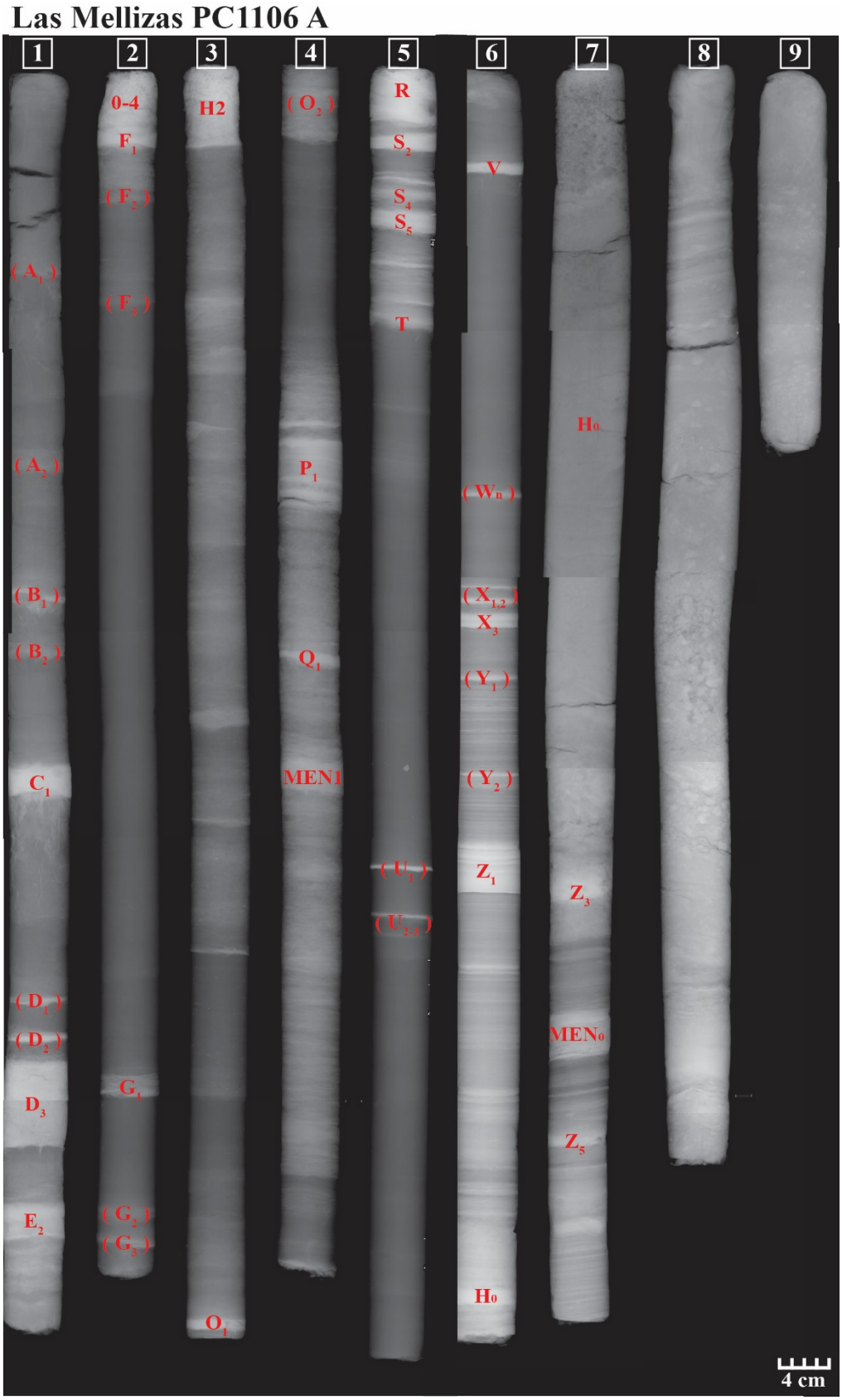

Figure A2.6. X-ray image and tephra identification for the core from Las Mellizas lake.

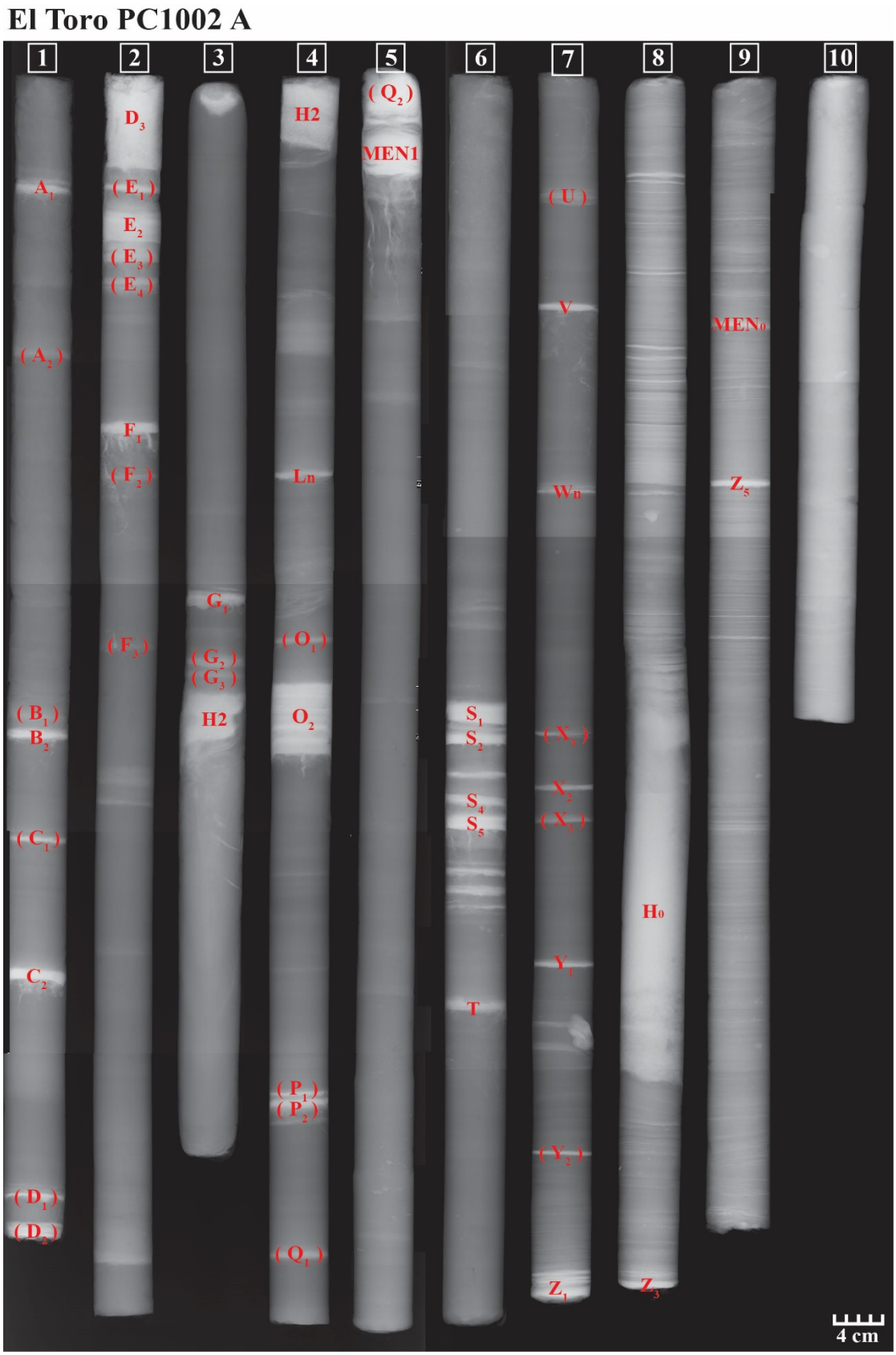

Figure A2.7. X-ray image and tephra identification for the core from El Toro lake.

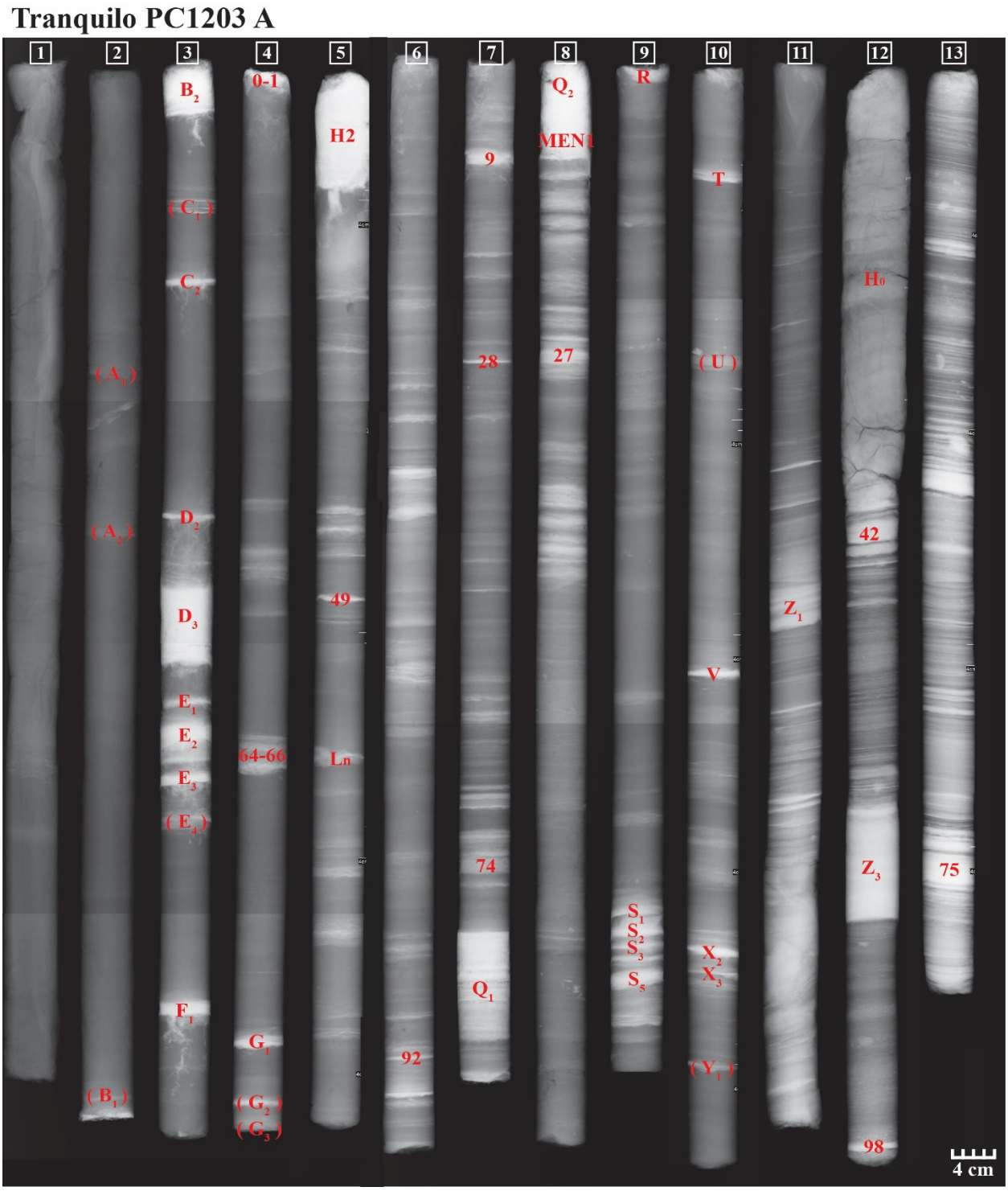

Figure A2.8. X-ray image and tephra identification for the core from Tranquilo lake.

Tables

Table A2.1. Ages for the S1 to S10 tephra sequence, Ho and the earliest (deepest) organic material in the cores from Miranda et al. (2013) and Weller et al. (2014).

Lake	Laboratory code	Core	Material	Core depth (cm)	^{14}C yrs BP	cal yr BP (range 2σ)	median cal yr BP
< S1							
Espejo	CAMS-159612	PC1003AT7	Bulk	1,125-1,126	12,235±40	13,898-14,508	14,088
> S10							
El Toro	UCIAMS-122968	PC1002AT7	Bulk	1,174-1,175	12,530±30	14,239-15,114	14,735
Élida	CAIMS-154874	PC1105BT4	Bulk	1,143-1,144	12,575±30	14,266-15,174	14,838
Espejo	CAMS-154864	PC1003AT7	Bulk	1,137-1,138	12,605±30	14,582-15,180	14,910
Quijada	CAMS-159608	PC1001DT8	Bulk	1,507-1,508	12,625±40	14-585-15,200	14,940
< Ho							
Unco	UCIAMS-122978	PC1103ET8	Bulk	1,419-1,420	13,430±50	16,204 - 16,875	16,612
Unco	CAMS-159614	PC1103ET8	Bulk	1,423-1,424	13,720±45	16,692 - 17,018	16,850
Las Mellizas	CAMS-159606	PC1106AT6	Bulk	1,348-1,349	13,810±110	16,691 - 17,178	16,914
Quijada	CAMS-159607	PC1001DT10	Bulk	1,664-1,665	14,220±45	16,992 - 17,595	17,299
> Ho							
Unco	CAMS-159613	PC1103ET9	Bulk	1,517-1,518	14,345±45	17,132 - 17,788	17,443
Las Mellizas	UCIAMS-122999	PC1106BT7	Bulk	1,452-1,453	14,670±45	17,573 - 18,368	17,847
Quijada	CAMS-154860	PC1001ET9	Macro	1,685-1,686	14,735±30	17,648 - 18,432	17,920
Las Mellizas	UCIAMS-123030	PC1106BT7	Bulk	1,457-1,458	14,800±90	17,661 - 18,509	18,014
Basal ages (deepest organic material)							
Unco	CAMS-159613	PC1103ET9	Bulk	1,517-1518	14,345±45	17,132-17,778	17,443
Las Mellizas	UCIAMS-122999	PC1106BT7	Bulk	1,452-1,453	14,670±45	17,573-18,368	17,847
Quijada	CAMS-154860	PC1001ET9	Macro	1,685-1,686	14,735±30	17,648-18,432	17,920
El Toro	CAMS-159611	PC1002BT6	Bulk	1,245-1,246	14,660±45	17,562-18,052	17,836

Table A2.2a. Description of tephra deposits

Teprha	Chem. type	Source	n	Other tephra	Glass							
					Color	Vesicles Abun.			Vesicle	Microlites		
						High	Low	None	Morph	High	Low	None
A1	**LAM**	**-**	**1**		Blk	-	-	X	-	X	-	-
A2	**-**	**-**	**0**		-	-	-	-	-	-	-	-
B1	**-**	**-**	**0**		-	-	-	-	-	-	-	-
B2	**LAF**	**MEN**	**3**		C, Blk	X (C)	X (Blk)	-	Circ	X (Blk)	X	X (C)
C1	**HAM**	**HUD**	**4**		DBr, Blk	-	X	-	Circ	X	-	-
C2	**HAM**	**HUD**	**3**		DBr, Blk	-	X	-	Circ	X	-	-
D1	**LAF**	**MEN**	**1**		Blk, C	X (C)	X (Blk)	-	Circ	X (Blk)	-	X (C)
D2	**HAM**	**HUD**	**3**		DOr, Blk	-	X	-	Circ	-	X	-
D3	**LAM**	**MACA**	**6**	MAC1[2]	DBr, Blk	-	X	-	Circ	-	-	X
E1	**HAM**	**HUD**	**2**		DOr, LBr, Blk	X	-	-	Elong,Circ	-	X	-
E2	**HAM**	**HUD**	**7**		Blk, LBrn	-	X	-	Circ	X	-	-
E3	**LAM**	**-**	**1**		Blk	-	-	X	-	-	X	-
E4	**-**	**-**	**0**		-	-	-	-	-	-	-	-
F1	**HAM**	**HUD**	**7**		DOr, Br, Blk	-	X	-	Circ	X	-	-
F2	**HAM**	**HUD**	**1**		DOr, Br, Blk	-	X	-	Circ	X	-	-
F3	**HAM**	**HUD**	**1**		DOr, Br, Blk	-	X	-	Circ	X	-	-
G1	**LAM**	**-**	**7**		Br, Blk	-	X	-	Circ	-	X	-
G2	**LAM**	**-**	**2**		DBr, Blk	-	X	-	Circ	-	X	-
G3	**LAM**	**-**	**3**		Blk, DBr	-	X	-	Circ	X	-	-
H2	**HA**	**HUD**	**7**	T8[3]; HW5[4]	LBr, C	X	-	-	Elong	-	-	X
I	**HAM**	**HUD**	**3**		PBr, DBr, C	X	X	-	Circ, Elong	-	X	-
J	**HAM**	**HUD**	**3**		DBr, Blk	-	X	-	Circ	X	-	-
K	**HAM**	**HUD**	**4**		Blk, DBr	-	X	-	Circ	X	-	-
Ls	**LAM**	**-**	**3**		Blk, DBr	-	X	-	Circ	X		-
Ln	**LAF**	**MEN**	**2**		C, Br, Blk	X	-	-	Circ	-	-	X
M	**HAM**	**HUD**	**3**		LBr, C	X	-	-	Elong	-	-	X
N	**HAM**	**HUD**	**6**		LBr, C	X	-	-	Elong	-	-	X
O1	**LAF**	**MEN**	**1**		C, Blk	X (C)	X (Blk)	-	Circ	X (B)	X (C)	-
O2	**LAM**	**-**	**4**		C, Blk	-	X	-	Circ	X	-	-
P1	**LAM**	**-**	**6**		Blk, C	-	-	X	-	X	-	-
P2	**HAM**	**HUD**	**4**		DBr, Blk	X	-	-	Elong	-	X	-
Q1	**LAF**	**MEN**	**3**		C, Blk	-	X	-	Circ		X	-
Q2	**LAF**	**MEN**	**2**		Blk, C	-	X	-	Circ	-	X	-
MEN1	**LAF**	**MEN**	**4**		C, Blk	X	-	-	Circ	-	-	X
R	**LAF**	**MEN**	**2**		C, Blk	X	-	-	Circ	-	-	X

S1	**HAM**	**HUD**	**4**	DBr, Or, Blk	-	X	-	Circ	-	X	-
S2	**HAM**	**HUD**	**8**	DBr, Blk	X	-	-	Circ	X	-	-
S3	**HAM**	**HUD**	**4**	DBr, Blk		X	-	Circ	X	-	-
S4	**HA**	**HUD**	**6**	C, LBr	X	-	-	Elong	-	-	X
S5	**HAM**	**HUD**	**7**	Blk, DBr, O	-	X	-	Circ	X	-	-
S6	**HAM**	**HUD**	**1**	Blk, DBr	-	X	-	Circ	X	-	-
S7	**HAM**	**HUD**	**1**	DBr, Blk	-	X	-	Circ	X	-	-
S8	**HAM**	**HUD**	**4**	DBr, Blk		X	-	Circ	X	-	-
S9	**HAM**	**HUD**	**1**	DBr, Blk	-	X	-	Circ	X	-	-
S10	**HAM**	**HUD**	**1**	DBr, Blk	-	X	-	Circ	X	-	-
T	**LAF**	**MEN**	**3**	C, Blk	X	-	-	Circ		X	-
U1	**-**	**-**	**0**	**-**	**-**	**-**	**-**	**-**	**-**	**-**	**-**
U2	**-**	**-**	**0**	**-**	**-**	**-**	**-**	**-**	**-**	**-**	**-**
U3	**-**	**-**	**0**	**-**	**-**	**-**	**-**	**-**	**-**	**-**	**-**
V	**HAM**	**HUD**	**9**	DBr, Blk	-	X	-	Circ	X	-	-
Ws	**HAM**	**HUD**	**2**	DOr, Br	X		-	Circ	X	-	-
Wn	**LAM**	**-**	**2**	DBr	-	X	-	Circ	X	-	-
X1	**HAM**	**HUD**	**1**	DOr, Br	X	-	-	Elong	-	X	-
X2	**HAM**	**HUD**	**4**	DOr, Br	X	-	-	Elong	-	X	-
X3	**HAM**	**HUD**	**6**	LOr, Blk	-	X	-	Circ	-	X	-
Y1	**LAM**	**-**	**4**	Blk, DBr	-	X	-	Circ	X	-	-
Y2	**-**	**-**	**0**	-	-	-	-	-	-	-	-
Z1	**HAM**	**HUD**	**14**	LBr, Blk	-	X	-	Circ	-	X	-
Z2, H0	**HAM**	**HUD**	**5**	LBr	X	-	-	Elong	-	X	-
Z3	**LAM**	**-**	**6**	Blk, Or, Br	-	X	-	Circ	X	-	-
Z4, MEN0	**LAF**	**MEN**	**5**	C, Blk	X	-	-	Circ	-	-	X
Z5	**LAM**	**-**	**4**	Blk, C	-	-	X	-	X	-	-

Color	Pale (P), Light (L), Dark (D), Brown (Br), Orange (Or), Colorless (C), Black (Blk)
Phenocryst Morphology	Euhedral (E) , Subhedral (S), Anhedral (A)
Abundance	>30% (High), <30% (Low), Trace (Tr)
Vesicle Morphology	Circular (Circ), Elongate (Elong)

[1] Naranjo and Stern 1998; [2] Naranjo and Stern 2004; [3]Elbert et al. 2013; [4]Haberle and Lumley 1998

Table A2.2b. Description of tephra deposits

Teprha	Plagioclase							Clinopyroxene				Orthopyroxene			
	Morph.	Abundance			Inclusions			Morph.	Abundance			Morph.	Abundance		
		High	Low	None	Morph.	Low	None		High	Low	None		High	Low	None
A1	S, A	-	X	-	-	X	-	-	-	-	X	-	-	-	X
A2	-	-	-	-	-	-	-	-	-	-	-	-	-	-	-
B1	-	-	-	-	-	-	-	-	-	-	-	-	-	-	-
B2	S, A	X	-	-	-	X	-	S, A	-	X	-	E, S	-	X	-
C1	E, S	-	X	-	-	X	-	A	-	X	-	-	-	-	X
C2	S, A	-	X	-	-	X	-	S	-	X	-	-	-	-	X
D1	E, S	X	-	-	-	X	-	S, A	-	X	-	E, S	-	X	-
D2	S, A	X	-	-	-	X	-	S, A	-	X	-	E	-	Tr	-
D3	E, S	X	-	-	-	X	-	A	-	X	-	-	-	-	-
E1	S, A	X	-	-	-	X	-	A	-	X	-	S	-	X	-
E2	E, S	-	X	-	-	X	-	E, S	-	X	-	-	-	-	X
E3	E, S	-	X	-	-	X	-	A	-	X	-	-	-	-	X
E4	-	-	-	-	-	-	-	-	-	-	-	-	-	-	-
F1	S, A	-	X	-	-	X	-	A	-	Tr	-	A	-	Tr	-
F2	S	X	-	-	-	X	-	A	-	X	-	A	-	Tr	-
F3	A	-	X	-	-	X	-	A	-	X	-	-	-	-	X
G1	S, A	X	-	-	-	X	-	A	-	X	-	S	-	Tr	-
G2	E, S	X	-	-	-	X	-	S, A	-	X	-	S	-	X	-
G3	E, S	X	-	-	-	X	-	A	-	Tr	-	S	-	Tr	-
H2	E, S	X	-	-	-	X	-	S, A	X	-	-	E, S	X	-	-
I	S, A	-	X	-	-	X	-	A	-	X	-	E	-	Tr	-
J	A	-	X	-	-	X	-	-	-	-	X	E	-	Tr	-
K	S, A	-	X	-	-	X	-	S, A	-	Tr	-	-	-	-	X
Ls	S,A	X	-	-	X	-	-	A	-	X	-	-	-	-	-
Ln	E, S	X	-	-	-	X	-	S	-	X	-	S	-	X	-
M	S, A	X	-	-	-	X	-	A	-	X	-	A	-	X	-
N	E, S	X	-	-	-	X	-	A	-	X	-	E, S	-	X	-
O1	E, S	X	-	-	X	-	-	-	-	-	X	A	-	X	-
O2	S,A	X	-	-	-	X	-	A	-	X	-	E, S	-	X	-
P1	E, S	X	-	-	-	X	-	A	-	X	-	-	-	-	-
P2	S	-	X	-	-	-	X	A	-	X	-	-	-	-	X
Q1	E, S	X	-	-	-	X	-	S, A	-	X	-	E, S	X	-	-
Q2	E, S	X	-	-	-	X	-	E, S	X	-	-	E, S	X	-	-
MEN1	E, S	X	-	-	-	X	-	E, S	X	-	-	E, S	X	-	-
R	E, S	X	-	-	-	X	-	S, A	X	-	-	E, S	X	-	-
S1	S, A	X	-	-	-	X	-	-	-	-	X	-	-	-	X
S2	S, A	-	X	-	-	X	-	A	-	X	-	-	-	-	X
S3	S, A	-	X	-	-	X	-	A	-	X	-	-	-	-	X

S4	E, S	X	-	-	-	X	-	E, S	-	X	-	E, S	-	X	-
S5	S, A	-	X	-	-	X	-	A	-	X	-	-	-	-	X
S6	A	-	X	-	-	-	X	-	-	-	X	-	-	-	X
S7	S	-	X	-	-	X	-	A	-	Tr	-	-	-	-	X
S8	A	-	X	-	-	X	-	-	-	-	X	-	-	-	X
S9	A	-	X	-	-	X	-	-	-	-	X	-	-	-	X
S10	S, A	-	X	-	-	X	-	-	-	-	X	-	-	-	X
T	E, S	X	-	-	-	-	X	E, S	-	X	-	E, S	X	-	-
U1	-	-	-	-	-	-	-	-	-	-	-	-	-	-	-
U2	-	-	-	-	-	-	-	-	-	-	-	-	-	-	-
U3	-	-	-	-	-	-	-	-	-	-	-	-	-	-	-
V	S, A	-	X	-	-	-	X	A, S	-	X	-	S	-	Tr	-
Ws	S	X	-	-	-	-	X	S	-	X	-	-	-	-	X
Wn	S	X	-	-	-	X	-	A	-	X	-	-	-	-	X
X1	S, A	-	X	-	-	X	-	A	-	Tr	-	-	-	-	X
X2	S, A	-	X	-	-	X	-	A	-	X	-	-	-	-	X
X3	S, A	-	X	-	-	-	X	A, S	-	X	-	-	-	-	X
Y1	S	X	-	-	-	X	-	A	-	X	-	A	-	X	-
Y2	-	-	-	-	-	-	-	-	-	-	-	-	-	-	-
Z1	E, S	X	-	-	-	X	-	A	-	X	-	-	-	-	X
Z2, H0	S, A	X	-	-	-	X	-	E, S	-	X	-	E	-	X	-
Z3	S, E	X	-	-	-	X	-	A	-	X	-	A	-	X	-
Z4, MEN0	E, S	X	-	-	X	-	-	A, S	X	-	-	E, S	X	-	-
Z5	A, S	X	-	-	X	-	-	A	-	X	-	-	-	-	X

Table A2.2c. Description of tephra deposits

Teprha	Amphibole				Olivine				Biotite			
	Morph.	Abundance			Morph.	Abundance			Morph.	Abundance		
		High	Low	None		High	Low	None		High	Low	None
A1	-	-	-	X	-	-	-	X	-	-	-	X
A2	-	-	-	-	-	-	-	-	-	-	-	X
B1	-	-	-	-	-	-	-	-	-	-	-	X
B2	S	-	X	-	A	-	Tr	-	-	-	-	X
C1	-	-	-	X	A	-	X	-	-	-	-	X
C2	-	-	-	X	-	-	-	X	-	-	-	X
D1	S	-	Tr	-	A	-	Tr	-	-	-	-	X
D2	-	-	-	X	A	-	X	-	-	-	-	X
D3	-	-	-	-	A	-	X	-	-	-	-	X
E1	-	-	-	X	-	-	-	X	-	-	-	X
E2	-	-	-	X	A	-	Tr	-	-	-	-	X
E3	-	-	-	X	-	-	-	X	-	-	-	X
E4	-	-	-	-	-	-	-	-	-	-	-	X
F1	-	-	-	X	-	-	-	X	-	-	-	X
F2	S	-	Tr	-	-	-	-	X	-	-	-	X
F3	-	-	-	-	-	-	-	X	-	-	-	X
G1	-	-	-	X	-	-	-	X	-	-	-	X
G2	-	-	-	X	-	-	-	X	-	-	-	X
G3	-	-	-	X	A	-	Tr	-	-	-	-	X
H2	-	-	-	X	-	-	-	X	-	-	-	X
I	-	-	-	X	-	-	-	X	-	-	-	X
J	A	-	Tr	-	-	-	-	X	-	-	-	X
K	-	-	-	X	-	-	-	X	-	-	-	X
Ls	-	-	-	-	A	-	Tr	-	-	-	-	X
Ln	E, S	X	-	-	-	-	-	-	-	-	-	X
M	-	-	-	X	-	-	-	X	-	-	-	X
N	-	-	-	X	-	-	-	X	-	-	-	X
O1	E,S	X	-	-	-	-	-	X	E,S	X	-	-
O2	-	-	-	X	A	-	Tr	-	-	-	-	X
P1	S, A	-	X	-	-	-	-	X	-	-	-	X
P2	-	-	-	X	-	-	-	X	-	-	-	X
Q1	S	-	X	-	-	-	-	-	-	-	-	X
Q2	S	-	X	-	-	-	-	X	-	-	-	X
MEN1	S, A	X	-	-	-	-	-	X	-	-	-	X
R	S	-	X	-	-	-	-	X	E,S	-	X	-
S1	-	-	-	X	-	-	-	X	-	-	-	X
S2	-	-	-	X	-	-	-	X	-	-	-	X
S3	-	-	-	X	-	-	-	X	-	-	-	X
S4	-	-	-	X	-	-	-	X	-	-	-	X

S5	-	-	-	X	-	-	-	X	-	-	-	X
S6	-	-	-	X	-	-	-	X	-	-	-	X
S7	-	-	-	X	-	-	-	X	-	-	-	X
S8	-	-	-	X	-	-	-	X	-	-	-	X
S9	-	-	-	X	-	-	-	X	-	-	-	X
S10	-	-	-	X	-	-	-	X	-	-	-	X
T	S	-	Tr	-	A	-	Tr	-	-	-	-	X
U1	-	-	-	-	-	-	-	-	-	-	-	X
U2	-	-	-	-	-	-	-	-	-	-	-	X
U3	-	-	-	-	-	-	-	-	-	-	-	X
V	-	-	-	X	-	-	-	X	-	-	-	X
Ws	-	-	-	X	-	-	-	X	-	-	-	X
Wn	-	-	-	X	-	-	-	X	-	-	-	X
X1	-	-	-	X	-	-	-	X	-	-	-	X
X2	-	-	-	X	-	-	-	X	-	-	-	X
X3	-	-	-	X	-	-	-	X	-	-	-	X
Y1	-	-	-	X	-	-	-	X	-	-	-	X
Y2	-	-	-	-	-	-	-	-	-	-	-	X
Z1	-	-	-	X	A	-	Tr	-	-	-	-	X
Z2, H0	-	-	-	X	A	-	Tr	-	-	-	-	X
Z3	S, A	-	X	-	A	-	Tr	-	-	-	-	X
Z4, MEN0	S	-	X	-	-	-	-	X	-	-	-	X
Z5	A	-	X	-	A	-	X	-	-	-	-	X

Table A2.3a. Trace element compositions of tephra in Lago Espejo core PC1003 A

	Core Top to H2											
Tephra	**C1**	**-**	**-**	**D3**	**-**	**E1**	**E2**	**F1**	**F2**	**G1**	**G2**	**-**
Section	**AT1**	**AT1**	**AT1**	**AT1**	**AT1**	**AT1**	**AT1**	**AT1**	**AT2**	**AT2**	**AT2**	**AT2**
Depth (cm)	**25-28**	**50**	**56**	**60-62**	**64**	**68**	**71-74**	**92**	**12**	**51**	**58-60**	**62-67**
Source	**HUD**			**MACA**		**HUD**	**HUD**	**HUD**	**HUD**	**-**	**-**	**HUD**
Lab #	**1303**	**1304**	**1305**	**1306**	**1307**	**1308**	**1309**	**1310**	**1311**	**1312**	**1313**	**1314**
Ti	9847	6875	7008	6746	8577	7590	7975	8931	9157	6623	5651	5685
V	286	239	234	229	258	268	268	267	274	231	221	146
Cr	15	94	63	76	16	67	38	52	14	100	107	29
Mn	1364	1176	1055	1055	1267	1219	1214	1232	1311	1069	960	956
Co	42	47	41	37	36	44	42	37	38	39	40	65
Ni	29	72	55	73	38	68	43	51	34	65	58	37
Cu	105	44	64	52	39	86	56	93	46	143	50	36
Zn	118	100	102	95	113	115	106	108	112	91	76	94
Rb	30	20	24	26	42	27	32	24	51	18	22	61
Sr	506	602	606	580	516	602	552	523	492	581	646	326
Y	32	23	23	23	33	26	27	26	31	21	18	36
Zr	207	161	175	178	263	196	192	193	199	134	103	362
Nb	10	7	8	8	12	9	9	7	11	6	5	15
Cs	0.9	0.6	0.7	0.6	1.1	0.8	0.9	0.6	1.2	0.4	0.6	1.5
Ba	503	335	354	363	565	422	438	380	532	307	320	667
La	27.7	21.1	22.6	23.4	35.3	28.2	27.4	23.7	28.0	18.0	15.2	37.5
Ce	63.2	47.8	50.7	52.5	78.7	63.0	59.7	54.6	64.0	40.8	34.3	83.5
Pr	8.10	6.11	6.30	6.51	9.63	7.77	7.37	6.96	8.33	5.25	4.43	9.94
Nd	34.8	25.5	26.9	28.5	39.5	32.2	31.1	29.5	34.4	22.7	19.4	39.7
Sm	7.17	5.25	5.67	5.58	7.99	6.59	6.09	6.52	7.35	4.69	4.00	8.38
Eu	2.25	1.74	1.78	1.70	2.26	1.95	1.96	2.12	2.26	1.68	1.45	2.10
Gd	8.30	5.89	6.30	6.28	8.88	7.08	7.41	7.51	8.54	5.50	4.91	8.95
Tb	1.10	0.78	0.81	0.75	1.18	0.93	0.93	0.95	1.17	0.70	0.62	1.21
Dy	6.05	4.58	4.46	4.59	6.26	5.05	5.32	5.44	6.20	3.88	3.58	6.65
Ho	1.26	0.82	0.91	0.92	1.26	0.98	1.00	0.98	1.22	0.78	0.67	1.36
Er	3.66	2.63	2.88	2.74	3.76	2.94	3.09	2.95	3.46	2.56	2.00	4.18
Tm	0.44	0.38	0.36	0.38	0.48	0.38	0.40	0.44	0.43	0.27	0.24	0.57
Yb	2.83	2.24	2.21	2.35	3.33	2.58	2.81	2.63	3.05	2.13	1.72	3.85
Lu	0.46	0.33	0.33	0.33	0.49	0.41	0.41	0.40	0.45	0.32	0.24	0.61
Hf	5.1	4.0	4.0	3.9	6.1	4.7	4.8	4.6	6.1	3.2	2.8	9.2
Pb	6.1	4.8	5.1	5.2	8.6	8.1	7.1	5.0	7.2	4.2	3.8	12.4
Th	4.1	2.8	3.3	3.5	5.7	4.6	4.8	2.9	7.0	2.4	2.4	7.0
U	0.7	0.5	0.5	0.7	1.1	0.7	0.9	0.5	1.0	0.3	0.4	1.5

Table A2.3b. Trace element compositions of tephra in Lago Espejo core PC1003 A

	Core Top to H2				H2 to S10						
Tephra	**-**	**G3**	**H2**	**H2**	**I**	**J**	**K**	**-**	**-**	**M**	**N**
Section	**AT2**	**AT2**	**AT3**	**AT3**	**AT3**	**AT3**	**AT3**	**AT4**	**AT4**	**AT4**	**AT4**
Depth (cm)	**62-67**	**69**	**0-30**	**0-30**	**44-46**	**82**	**84**	**0-7**	**0-7**	**76-78**	**80-85**
Source	**HUD**	**-**	**HUD**	**HUD**	**HUD**	**HUD**	**HUD**	**HUD**	**HUD**	**HUD**	**HUD**
Lab #	**1315**	**1316**	**1317**	**1318**	**1319**	**1320**	**1321**	**1322**	**1323**	**1324**	**1325**
Ti	4709	5740	6199	7225	11528	10464	10786	8200	7395	8237	9731
V	100	228	137	145	216	332	285	144	159	187	211
Cr	4	107	9	7	16	16	20	30	18	31	36
Mn	820	938	967	1026	1813	1316	1309	1157	998	1214	1480
Co	43	44	18	20	36	33	34	30	28	26	28
Ni	25	56	28	25	37	36	38	46	41	45	49
Cu	24	32	52	32	78	53	52	41	38	43	18
Zn	91	76	93	107	148	124	123	131	101	115	133
Rb	73	22	57	67	31	32	40	38	38	49	45
Sr	159	641	351	343	548	559	511	607	595	424	430
Y	39	18	42	41	34	31	33	34	29	38	39
Zr	443	107	396	403	202	231	211	241	237	345	315
Nb	18	5	17	18	14	11	13	13	13	15	15
Cs	1.8	0.6	1.7	1.6	0.7	0.8	1.1	0.9	0.9	1.2	1.2
Ba	742	312	705	762	547	479	495	608	622	601	590
La	42.2	15.4	39.5	43.1	33.1	30.8	31.8	31.8	31.5	37.7	38.1
Ce	90.4	34.3	87.6	94.7	74.7	70.6	70.5	70.3	68.5	81.8	86.0
Pr	10.9	4.30	10.3	11.2	9.07	8.98	8.99	8.82	8.44	10.4	10.7
Nd	43.3	18.7	41.4	45.1	38.9	36.6	38.8	38.8	34.4	42.6	43.5
Sm	8.35	3.96	8.63	9.17	8.40	7.75	7.87	8.28	6.94	9.01	9.02
Eu	1.91	1.43	2.78	2.49	2.76	2.36	2.42	2.74	2.53	2.48	2.56
Gd	8.97	4.79	9.26	10.06	9.21	8.75	8.76	9.32	7.54	9.13	10.14
Tb	1.23	0.61	1.17	1.39	1.17	1.10	1.15	1.16	0.99	1.27	1.38
Dy	7.01	3.38	7.01	8.07	6.76	6.24	6.21	6.32	5.70	7.12	7.59
Ho	1.50	0.66	1.38	1.55	1.28	1.14	1.16	1.22	1.04	1.40	1.45
Er	4.51	2.01	4.27	4.76	3.93	3.43	3.81	3.85	3.22	4.48	4.54
Tm	0.60	0.26	0.58	0.65	0.50	0.47	0.47	0.47	0.44	0.57	0.62
Yb	4.49	1.70	4.04	4.40	3.17	3.02	3.18	3.13	2.87	3.87	4.04
Lu	0.64	0.21	0.59	0.68	0.48	0.42	0.44	0.51	0.46	0.64	0.60
Hf	10.2	2.6	8.6	9.5	4.4	5.2	5.9	5.2	5.6	7.6	7.0
Pb	13.8	3.8	11.5	13.3	7.6	7.6	8.1	9.9	10.3	10.6	10.1
Th	8.2	2.3	6.5	7.4	3.5	3.8	6.1	4.3	4.5	5.8	5.2
U	1.8	0.4	1.5	1.6	0.6	0.7	1.0	0.9	0.9	1.2	1.0

Table A2.3c. Trace element compositions of tephra in Lago Espejo core PC1003 A

	H2 to S10		S10							
Tephra	**N**	**P2**	**S1**	**S2**	**S3**	**S4**	**S5**	**S6**	**S8**	**S9**
Section	**AT4**	**AT5**	**AT7**	**AT7**	**AT7**	**AT7**	**AT7**	**AT7**	**AT7**	**AT7**
Depth (cm)	**80-85**	**39-41**	**45**	**47**	**50**	**51-53**	**55-58**	**60**	**63-65**	**66**
Source	**HUD**	**HUD**	**HUD**	**HUD**	**HUD**	**HUD**	**HUD**	**HUD**	**HUD**	**HUD**
Lab #	**1326**	**1327**	**1328**	**1329**	**1330**	**1331**	**1332**	**1333**	**1334**	**1335**
Ti	7603	17067	10576	11126	10730	7964	12159	11097	12712	12702
V	174	383	292	297	292	115	309	288	300	301
Cr	32	14	24	21	21	6	19	25	19	27
Mn	1211	1777	1425	1424	1409	1470	1514	1395	1504	1461
Co	23	41	35	33	30	29	37	36	54	49
Ni	53	48	44	42	45	28	45	46	44	49
Cu	21	58	87	41	53	43	60	49	51	56
Zn	122	151	121	131	124	131	129	122	129	135
Rb	45	27	31	30	25	57	26	26	22	25
Sr	483	513	558	597	570	352	607	575	604	625
Y	37	42	33	37	36	48	39	36	39	38
Zr	325	219	237	270	257	465	283	263	274	255
Nb	14	9	12	13	12	23	13	12	11	11
Cs	1.1	0.6	0.7	1.1	0.9	1.5	0.8	0.8	0.5	0.8
Ba	613	385	566	632	587	734	565	457	455	548
La	36.1	29.1	34.2	36.2	35.5	46.7	37.1	32.7	36.3	36.7
Ce	80.1	68.9	77.2	81.8	80.4	104.9	85.7	76.1	86.6	84.5
Pr	9.87	9.66	9.77	10.4	10.2	12.5	11.0	9.84	11.1	10.9
Nd	41.8	45.5	43.6	44.2	44.3	50.9	47.4	41.3	49.4	49.2
Sm	8.30	9.44	8.66	9.30	8.93	10.61	9.72	8.92	10.26	9.78
Eu	2.70	3.01	2.68	2.72	2.73	2.90	2.87	2.69	3.06	3.04
Gd	9.29	11.38	9.16	10.15	10.22	11.75	11.26	10.12	14.35	11.02
Tb	1.22	1.52	1.21	1.26	1.29	1.58	1.42	1.29	1.41	1.35
Dy	7.30	8.20	6.66	7.45	6.93	9.00	7.80	7.26	7.82	7.50
Ho	1.35	1.57	1.26	1.38	1.28	1.75	1.39	1.27	1.46	1.40
Er	4.38	4.75	3.71	4.17	4.17	5.70	4.61	3.86	4.22	4.39
Tm	0.54	0.60	0.44	0.56	0.54	0.75	0.63	0.48	0.61	0.55
Yb	3.85	3.93	3.19	3.44	3.29	5.20	3.80	3.32	3.87	3.65
Lu	0.58	0.53	0.46	0.51	0.46	0.77	0.54	0.53	0.53	0.52
Hf	6.8	5.0	4.8	5.7	5.3	10.5	5.7	5.5	5.7	5.5
Pb	10.4	6.9	11.1	7.8	7.2	13.7	7.4	7.4	7.3	7.2
Th	5.2	3.0	3.3	3.6	3.2	10.2	3.6	3.5	3.4	3.8
U	1.0	0.6	0.6	0.7	0.5	1.7	0.6	0.7	0.6	0.7

Table A2.3d. Trace element compositions of tephra in Lago Espejo core PC1003 A

	S10 to Core Bottom	
Tephra	**V**	**Ws**
Section	**AT8**	**AT8**
Depth (cm)	**14**	**24-26**
Source	**HUD**	**HUD**
Lab #	**1336**	**1337**
Ti	11499	12586
V	292	256
Cr	18	9
Mn	1287	1487
Co	63	81
Ni	42	39
Cu	61	43
Zn	120	131
Rb	36	40
Sr	490	486
Y	36	44
Zr	239	298
Nb	11	12
Cs	1.2	1.3
Ba	499	515
La	30.0	32.6
Ce	70.6	77.1
Pr	9.20	10.3
Nd	39.6	45.1
Sm	8.04	9.88
Eu	2.57	2.97
Gd	9.34	11.15
Tb	1.27	1.46
Dy	6.69	8.32
Ho	1.30	1.64
Er	3.91	4.91
Tm	0.52	0.62
Yb	3.43	3.96
Lu	0.48	0.66
Hf	5.4	6.5
Pb	8.8	8.8
Th	4.1	4.4
U	0.8	0.9

Table A2.4a. Trace element compositions of tephra in Lago Quijada PC1001 D

	Core Top to H2						H2 to S10	
Tephra	**C1**	**D3**	**E2**	**F1**	**G2**	**H2**	**J**	**N**
Section	**DT1**	**DT1**	**DT1**	**DT1**	**DT2**	**DT2**	**DT3**	**DT4**
Depth (cm)	**60**	**78-80**	**85**	**93**	**57**	**58-82**	**43**	**21-27**
Source	**HUD**	**MACA**	**HUD**	**HUD**	**-**	**HUD**	**HUD**	**HUD**
Lab #	**CS-2201**	**CS-2202**	**CS-2203**	**CS-2204**	**CS-2205**	**CS-2206**	**CS-2207**	**CS-2208**
Ti	10287	9678	8716	9803	5662	7930	10011	7715
V	307	222	265	281	220	137	304	176
Cr	17	70	55	25	45	12	15	20
Mn	1337	1201	1327	1237	1054	1266	1272	1164
Co	49	40	51	38	45	22	35	70
Ni	27	52	31	36	48	24	34	39
Cu	54	98	78	96	82	39	66	28
Zn	119	110	121	123	95	115	121	109
Rb	22	20	20	28	-	39	24	37
Sr	446	467	435	454	397	391	508	439
Y	28	21	20	29	15	31	29	37
Zr	200	180	169	215	82	299	211	312
Nb	8	8	10	9	3	15	10	14
Cs	-	-	-	-	-	-	-	-
Ba	472	347	318	458	170	634	449	618
La	25.3	20.5	19.5	27.2	8.4	34.0	29.4	35.5
Ce	58.8	47.4	43.8	62.8	20.0	74.8	66.5	81.6
Pr	7.68	6.00	5.64	7.89	2.51	8.99	8.37	9.89
Nd	34.4	25.2	24.1	33.0	12.1	37.8	35.9	39.8
Sm	7.25	5.45	5.11	7.42	3.01	7.74	7.55	8.84
Eu	2.13	1.57	1.61	1.97	0.82	2.30	2.09	2.55
Gd	8.38	5.85	5.42	8.47	3.38	8.84	8.70	9.77
Tb	0.98	0.72	0.72	0.89	-	1.01	0.91	1.11
Dy	5.65	4.07	4.06	5.77	2.80	6.05	5.50	7.15
Ho	1.01	0.78	0.77	0.97	-	1.07	0.92	1.25
Er	3.37	2.42	2.25	3.45	1.54	3.67	3.06	3.93
Tm	0.30	0.27	0.29	0.25	DL	0.35	0.23	0.40
Yb	2.87	2.09	2.00	2.80	1.45	3.31	2.78	3.85
Lu	-	-	0.29	-	-	0.35	-	0.42
Hf	4.8	4.4	4.4	5.2	2.3	7.0	4.8	7.2
Pb	6.6	6.5	7.1	8.0	4.5	10.6	7.7	10.3
Th	2.7	3.0	3.7	3.6	-	4.7	2.9	4.6
U	0.7	0.7	0.9	0.8	0.2	1.1	0.7	1.1

Table A2.4b. Trace element compositions of tephra in Lago Quijada PC1001 D

	H2 to S10						
Tephra	**N**	**N**	**-**	**-**	**P1**	**P2**	**MEN1**
Section	**DT4**	**DT4**	**DT5**	**DT5**	**DT5**	**DT5**	**DT5**
Depth (cm)	**21-27**	**21-27**	**5-7**	**5-7**	**33**	**36**	**92**
Source	**HUD**	**HUD**	**-**	**-**	**-**	**HUD**	**MEN**
Lab #	**CS-2208-D**	**CS-2209**	**CS-2210**	**CS-2211**	**CS-2212**	**CS-2213**	**CS-2214**
Ti	7872	9022	7210	10401	7360	17400	5016
V	161	116	129	167	207	289	205
Cr	20	23	23	37	29	11	10
Mn	1188	1347	1103	1505	1069	1716	1626
Co	71	32	63	30	59	38	46
Ni	33	29	33	46	34	37	27
Cu	28	97	38	151	84	75	22
Zn	113	123	106	150	110	147	110
Rb	41	40	28	37	10	19	-
Sr	440	317	380	387	397	417	454
Y	37	37	30	36	16	35	11
Zr	326	337	294	287	60	190	51
Nb	18	16	13	14	2	8	1
Cs	-	-	-	-	-	-	-
Ba	625	583	528	547	189	323	110
La	36.5	35.5	30.0	33.5	7.9	24.1	4.9
Ce	81.6	82.4	69.1	76.0	19.4	59.2	12.5
Pr	10.00	10.41	8.56	9.68	2.61	8.17	1.71
Nd	41.3	40.9	36.1	40.5	11.8	37.7	8.7
Sm	8.90	9.16	7.60	8.56	3.27	8.71	2.17
Eu	2.61	2.44	2.27	2.45	1.01	2.66	0.86
Gd	9.85	10.07	8.34	9.64	3.69	9.96	2.54
Tb	1.25	1.25	1.02	1.14	0.47	1.22	DL
Dy	7.09	7.18	5.99	7.36	3.07	7.20	2.03
Ho	1.26	1.33	1.07	1.23	0.55	1.33	-
Er	4.13	4.34	3.73	4.02	1.83	3.96	1.16
Tm	0.49	0.51	0.36	0.42	0.17	0.43	-
Yb	3.86	4.11	3.34	3.75	1.78	3.30	1.05
Lu	0.44	0.49	0.36	0.40	-	0.40	-
Hf	9.0	7.9	6.7	6.8	1.9	4.5	1.4
Pb	10.5	10.5	9.8	9.7	5.8	5.3	3.8
Th	6.4	4.8	4.1	4.3	1.4	2.4	-
U	1.2	1.2	1.0	1.0	0.3	0.5	0.1

Table A2.4c. Trace element compositions of tephra in Lago Quijada PC1001 D

	S10					
Tephra	**S1**	**S2**	**S3**	**S4**	**S5**	**S8**
Section	**DT8**	**DT8**	**DT8**	**DT8**	**DT8**	**DT8**
Depth (cm)	**41**	**43**	**46**	**48**	**50-52**	**57-59**
Source	**HUD**	**HUD**	**HUD**	**HUD**	**HUD**	**HUD**
Lab #	**CS-2215**	**CS-2216**	**CS-2217**	**CS-2218**	**CS-2219**	**CS-2220**
Ti	9885	11648	11389	6714	12337	12663
V	259	226	294	85	200	291
Cr	26	19	22	5	18	18
Mn	1306	1418	1439	1265	1621	1498
Co	43	35	35	11	36	30
Ni	37	33	38	14	26	39
Cu	86	112	88	134	64	72
Zn	124	139	128	124	142	130
Rb	26	21	17	51	19	16
Sr	520	518	511	267	498	549
Y	29	32	34	40	31	36
Zr	218	239	249	400	243	263
Nb	12	12	12	20	12	11
Cs	-	-	-	-	-	-
Ba	529	511	495	647	423	427
La	31.9	31.2	33.0	37.1	29.5	34.0
Ce	74.3	72.2	78.0	86.4	69.3	83.0
Pr	9.20	9.35	9.96	10.40	9.21	10.92
Nd	38.3	39.9	40.9	42.7	37.9	46.4
Sm	8.19	8.43	8.88	9.34	8.28	9.89
Eu	2.34	2.44	2.41	2.52	2.52	2.86
Gd	8.96	9.39	9.88	10.42	9.29	11.13
Tb	1.01	1.13	1.14	1.28	1.17	1.35
Dy	6.15	6.17	6.42	7.72	6.67	7.41
Ho	1.04	1.11	1.14	1.50	1.21	1.26
Er	3.40	3.76	3.75	4.65	3.77	3.96
Tm	0.27	0.39	0.33	0.60	0.47	0.38
Yb	2.85	3.27	3.26	4.63	3.09	3.41
Lu	-	0.42	-	0.66	0.43	0.40
Hf	4.8	5.3	5.4	10.3	5.8	5.8
Pb	12.1	7.0	7.2	12.9	6.9	6.9
Th	2.8	2.7	2.6	7.9	2.9	2.8
U	0.6	0.7	0.6	1.5	0.7	0.6

Table A2.4d. Trace element compositions of tephra in Lago Quijada PC1001 D

	S10 to Core Bottom				
Tephra	**V**	**X3**	**Z1**	**Z1**	**-**
Section	**DT9**	**DT9**	**DT10**	**DT10**	**DT10**
Depth (cm)	**42**	**82**	**27-38**	**27-38**	**42**
Source	**HUD**	**HAM**	**HAM**	**HAM**	
Lab #	**CS-2221**	**CS-2222**	**CS-2223**	**CS-2224**	**CS-2225**
Ti	12278	11899	10227	11884	11348
V	301	210	301	233	291
Cr	18	6	35	26	39
Mn	1328	1405	1282	1428	1379
Co	30	18	30	37	35
Ni	36	26	36	32	32
Cu	85	85	86	47	106
Zn	120	127	112	120	117
Rb	25	25	25	19	24
Sr	445	424	451	372	437
Y	34	36	28	22	29
Zr	243	282	190	173	210
Nb	11	11	9	8	9
Cs	-	-	-	-	-
Ba	460	451	404	320	404
La	28.9	29.5	23.3	17.2	24.5
Ce	70.0	71.5	54.6	41.8	57.3
Pr	9.14	9.01	6.81	5.52	7.25
Nd	39.1	40.2	29.2	23.0	32.8
Sm	8.84	9.36	6.66	5.22	7.07
Eu	2.44	2.61	1.98	1.65	1.99
Gd	9.89	10.35	7.76	5.74	8.04
Tb	1.17	1.20	0.91	0.79	0.96
Dy	7.04	7.30	5.68	4.47	5.71
Ho	1.19	1.26	0.96	0.84	1.00
Er	3.93	4.44	3.07	2.72	3.43
Tm	0.39	0.41	0.32	0.31	0.30
Yb	3.27	3.83	2.65	2.34	2.93
Lu	0.35	0.39	0.32	0.30	-
Hf	5.6	6.3	4.4	4.4	4.9
Pb	7.4	7.9	7.2	5.8	6.8
Th	2.9	3.1	3.4	2.6	3.2
U	0.8	0.7	0.8	0.7	0.8

Table A2.5a. Trace element compositions of tephra in Lago Churrasco PC1201 A

	Core Top to H2									
Tephra	**C1**	**C2**	**D2**	**D3**	**E2**	**F1**	**F3**	**G1**	**G3**	**H2**
Section	**AT1**	**AT1**	**AT1**	**AT1**	**AT1**	**AT1**	**AT1**	**AT1**	**AT2**	**AT2**
Depth (cm)	**8**	**14**	**35**	**36**	**41-43**	**51**	**65**	**94**	**4**	**12-36**
Source	**HUD**	**HUD**	**HUD**	**MACA**	**HUD**	**HUD**	**HUD**	**-**	**-**	**HUD**
Lab #	**CS-4139**	**CS-4140**	**CS-4141**	**CS-4142**	**CS-4143**	**CS-4144**	**CS-4145**	**CS-4146**	**CS-4147**	**CS-4148**
Ti	10853	10308	7851	8618	8319	10010	9993	6598	6461	5131
V	356	315	274	302	290	309	348	240	247	115
Cr	17	12	48	51	41	25	14	92	89	6
Mn	1343	1273	1032	1149	1111	1196	1280	978	926	855
Co	35	28	32	32	31	31	33	40	35	21
Ni	35	33	51	55	43	37	35	63	70	26
Cu	70	105	76	131	64	150	133	78	73	25
Zn	131	122	101	109	105	116	113	88	82	91
Rb	36	49	29	35	32	38	55	20	18	87
Sr	548	506	616	584	558	476	509	592	573	181
Y	34	34	25	28	25	31	33	31	21	45
Zr	224	228	200	233	191	232	209	137	133	528
Nb	9	10	8	10	8	9	8	15	6	22
Cs	1.0	1.1	0.6	0.7	0.7	0.7	1.0	0.3	0.3	1.9
Ba	522	513	406	464	427	469	539	297	284	868
La	30.6	32.8	26.0	31.3	28.7	30.8	31.6	18.9	18.3	51.6
Ce	69.5	74.1	57.7	69.8	62.1	69.6	69.7	42.5	40.3	112.5
Pr	9.1	9.6	7.3	8.7	7.9	9.0	9.3	5.5	5.4	13.4
Nd	38.6	39.0	29.5	34.8	31.9	36.3	38.9	23.2	21.9	49.6
Sm	7.88	8.46	6.16	7.26	6.67	7.85	7.94	4.99	4.76	10.08
Eu	2.23	2.32	1.81	2.08	1.87	2.08	2.27	2.23	1.45	2.34
Gd	9.7	9.7	7.3	8.6	7.6	8.9	9.2	5.9	5.6	11.6
Tb	1.11	1.15	0.79	0.91	0.88	1.05	1.10	0.67	0.67	1.50
Dy	6.64	6.55	5.00	5.82	5.17	6.03	6.46	4.10	4.18	8.20
Ho	1.19	1.24	0.96	1.02	1.00	1.17	1.23	0.77	0.80	1.78
Er	3.78	4.02	2.89	3.19	3.13	3.77	3.79	2.51	2.50	5.59
Tm	0.41	0.46	0.32	0.39	0.32	0.42	0.44	0.26	0.26	0.75
Yb	3.35	3.47	2.55	2.96	2.56	3.29	3.52	2.18	2.12	5.42
Lu	0.40	0.45	0.34	0.38	0.35	0.43	0.48	0.26	0.24	0.78
Hf	4.9	4.9	4.4	5.0	4.1	5.0	5.0	6.8	3.0	11.8
Pb	6.9	8.8	6.9	8.7	7.7	8.5	9.0	4.9	5.0	17.7
Th	3.1	4.2	2.8	3.9	3.6	3.3	4.3	5.6	2.2	9.6
U	0.8	1.0	0.6	0.9	0.8	0.9	1.0	0.5	0.4	2.1

Table A2.5b. Trace element compositions of tephra in Lago Churrasco PC1201 A

	H2 to S10										
Tephra	**J**	**K**	**Ls**	**M**	**N**	**O2**	**P1**	**P2**	**Q1**	**MEN1**	**-**
Section	**AT2**	**AT2**	**AT2**	**AT3**	**AT3**	**AT3**	**AT4**	**AT4**	**AT4**	**AT4**	**AT4**
Depth (cm)	**65**	**66**	**88**	**44-46**	**48-51**	**89**	**21**	**23**	**27-29**	**30**	**32**
Source	**HUD**	**HUD**	**-**	**HUD**	**HUD**	**-**	**-**	**HUD**		**MEN**	**-**
Lab #	**CS-4149**	**CS-4150**	**CS-4151**	**CS-4152**	**CS-4153**	**CS-4154**	**CS-4155**	**CS-4156**	**CS-4157**	**CS-4158**	**CS-4159**
Ti	10279	10764	7639	8080	9566	5280	5370	14039	4093	4425	6364
V	321	306	376	173	201	184	220	290	148	189	210
Cr	16	15	20	16	20	20	22	11	7	8	12
Mn	1201	1134	1227	1095	1306	920	923	1472	1093	1515	891
Co	31	27	35	20	18	25	23	31	20	29	28
Ni	32	35	36	34	40	29	34	36	29	32	31
Cu	149	81	121	108	45	101	94	102	85	26	115
Zn	118	116	110	109	118	107	102	145	128	118	119
Rb	33	37	18	58	47	15	13	22	20	8	38
Sr	522	481	465	349	436	412	444	421	349	537	396
Y	32	34	23	44	40	18	16	37	24	11	25
Zr	232	216	88	410	335	73	57	192	131	48	144
Nb	11	9	2	18	16	8	4	10	5	2	7
Cs	0.6	0.8	0.8	1.3	1.0	1.0	0.7	0.6	1.6	0.4	2.5
Ba	487	491	214	702	627	189	183	316	244	109	399
La	34.3	34.6	10.2	45.9	40.9	8.4	8.1	25.8	11.7	5.4	19.1
Ce	75.7	73.4	23.3	102.6	91.4	18.9	18.5	60.9	26.5	13.6	41.7
Pr	9.9	10.1	3.4	12.7	11.6	2.6	2.7	8.4	3.8	1.8	5.4
Nd	37.1	38.9	14.5	50.1	45.4	12.2	11.4	37.2	16.1	8.3	20.7
Sm	8.43	8.74	4.01	10.14	9.60	2.92	2.71	8.03	3.59	1.97	4.63
Eu	2.38	2.33	1.33	2.61	2.79	1.04	1.00	2.49	1.21	0.81	1.47
Gd	9.7	10.2	4.9	11.6	11.2	3.5	3.5	9.6	4.4	2.6	5.6
Tb	1.16	1.24	0.68	1.56	1.45	0.49	0.46	1.21	0.58	0.32	0.70
Dy	6.38	6.73	4.26	8.29	8.14	2.80	2.63	6.49	3.46	2.06	3.73
Ho	1.28	1.43	0.88	1.77	1.64	0.59	0.52	1.30	0.72	0.38	0.77
Er	3.89	4.14	2.60	5.39	4.92	1.85	1.70	3.82	2.34	1.15	2.56
Tm	0.46	0.52	0.31	0.71	0.64	0.25	0.22	0.48	0.28	0.14	0.33
Yb	3.36	3.58	2.26	5.05	4.60	1.54	1.44	3.24	2.23	1.20	2.43
Lu	0.41	0.47	0.31	0.74	0.59	0.24	0.21	0.45	0.32	0.14	0.32
Hf	5.3	5.1	2.3	9.8	7.6	2.7	1.8	4.2	3.4	1.2	3.3
Pb	10.1	8.8	7.1	15.5	11.9	4.8	4.2	4.7	6.2	2.5	6.0
Th	3.9	4.2	1.1	7.2	5.6	2.4	1.6	2.3	1.7	0.6	3.2
U	0.9	0.9	0.5	1.6	1.2	0.4	0.4	0.6	0.6	0.2	1.0

Table A2.5c. Trace element compositions of tephra in Lago Churrasco PC1201 A

	S10				
Tephra	**S2**	**S2**	**S4**	**S5**	**S8**
Section	**AT4**	**AT4**	**AT4**	**AT4**	**AT4**
Depth (cm)	**50**	**50**	**52-55**	**57**	**61-63**
Source	**HUD**	**HUD**	**HUD**	**HUD**	**HUD**
Lab #	**CS-2650**	**CS-2650-D**	**CS-2651**	**CS-2652**	**CS-2653**
Ti	11122	10908	8057	12449	12628
V	284	275	124	311	283
Cr	18	18	4	16	15
Mn	1356	1313	1379	1444	1618
Co	34	32	51	29	31
Ni	27	25	15	26	26
Cu	104	99	34	73	108
Zn	116	111	120	125	116
Rb	27	26	56	25	20
Sr	557	546	328	576	560
Y	37	36	49	40	39
Zr	256	250	443	272	260
Nb	13	13	21	12	11
Cs	0.9	0.8	1.2	0.5	0.3
Ba	605	577	698	509	421
La	34.1	33.4	45.8	36.1	35.4
Ce	80.3	77.5	100.0	84.2	84.4
Pr	10.2	10.0	12.4	11.1	10.9
Nd	41.5	42.0	50.5	47.4	45.5
Sm	8.71	8.62	9.88	9.44	9.36
Eu	2.62	2.63	2.90	2.78	2.85
Gd	9.7	9.5	11.2	10.4	10.8
Tb	1.28	1.23	1.47	1.34	1.39
Dy	6.72	6.58	8.70	7.31	7.33
Ho	1.35	1.30	1.75	1.43	1.37
Er	3.67	3.90	5.31	4.25	4.23
Tm	0.53	0.53	0.76	0.57	0.55
Yb	3.33	3.37	5.24	3.60	3.45
Lu	0.53	0.50	0.78	0.55	0.52
Hf	5.7	5.3	9.4	5.8	5.4
Pb	4.3	4.0	9.8	3.9	3.9
Th	3.6	3.0	7.6	3.3	3.2
U	0.8	0.7	1.7	0.7	0.7

Table A2.5d. Trace element compositions of tephra in Lago Churrasco PC1201 A

	S10 to Core Bottom									
Tephra	**V**	**X1**	**X2**	**Y1**	**Z1**	**Z1**	**H0**	**H0**	**H0**	**Z3**
Section	**AT4**	**AT5**	**AT5**	**AT5**	**AT5**	**AT5**	**AT6**	**AT6**	**AT6**	**AT6**
Depth (cm)	**78**	**10**	**12**	**17**	**61-63**	**66**	**11-14**	**17-22**	**67-74**	**77**
Source	**HUD**	**HUD**	**HUD**	**-**	**HUD**	**HUD**	**HUD**	**HUD**	**HUD**	**-**
Lab #	**CS-2654**	**CS-2655**	**CS-2656**	**CS-2657**	**CS-2658**	**CS-2659**	**CS-2703**	**CS-2704**	**CS-2705**	**CS-2660**
Ti	12367	12557	11706	7115	11780	11583	7176	7843	10076	6577
V	291	246	183	236	332	310	256	198	266	240
Cr	14	9	7	15	37	37	14	13	17	7
Mn	1251	1369	1337	1182	1388	1252	1174	1097	1276	1136
Co	40	21	24	33	32	32	29	32	25	27
Ni	25	19	16	22	39	28	16	17	21	19
Cu	92	143	108	149	66	157	95	56	56	86
Zn	111	122	111	105	108	106	105	110	122	98
Rb	32	33	33	22	30	31	27	50	41	20
Sr	478	462	433	486	511	482	451	415	509	464
Y	37	42	42	25	34	34	24	34	34	22
Zr	233	270	280	104	200	214	124	255	232	84
Nb	11	10	18	4	9	10	7	14	12	2
Cs	0.7	0.8	1.1	1.3	0.6	0.9	1.6	1.8	1.1	1.2
Ba	431	438	442	262	391	400	332	558	546	239
La	30.6	31.1	31.0	13.7	25.8	26.1	16.1	31.7	31.5	10.2
Ce	70.0	73.3	71.3	31.5	58.2	61.3	36.0	70.0	68.4	23.3
Pr	9.1	9.7	9.5	4.1	7.6	7.9	4.7	8.9	8.8	3.2
Nd	40.0	42.4	40.2	18.2	32.4	32.7	20.6	36.7	38.5	15.2
Sm	8.40	9.25	9.04	4.40	7.03	7.22	5.23	8.14	8.26	3.89
Eu	2.55	2.79	2.85	1.43	2.11	2.27	1.69	2.32	2.46	1.26
Gd	9.3	10.0	9.6	5.1	8.0	8.2	6.2	9.4	9.2	4.6
Tb	1.25	1.37	1.37	0.76	1.13	1.16	0.87	1.14	1.25	0.67
Dy	6.74	7.86	7.54	4.16	6.34	6.23	4.77	6.30	6.32	3.87
Ho	1.30	1.57	1.58	0.93	1.21	1.22	0.90	1.22	1.30	0.76
Er	4.01	4.63	4.52	2.63	3.58	3.62	2.95	3.62	3.77	2.39
Tm	0.54	0.57	0.61	0.34	0.53	0.52	0.35	0.51	0.45	0.37
Yb	3.41	4.19	4.09	2.47	3.36	3.31	2.42	3.43	3.24	2.24
Lu	0.47	0.58	0.58	0.36	0.47	0.47	0.37	0.50	0.53	0.36
Hf	5.0	5.8	8.7	3.0	4.4	4.7	3.5	6.3	5.7	2.3
Pb	4.8	5.5	5.5	6.1	3.4	4.1	7.7	10.2	8.2	4.3
Th	3.3	3.7	7.1	3.7	4.2	3.8	3.4	5.9	5.3	1.8
U	0.8	1.0	1.1	1.0	0.9	0.9	0.7	1.3	1.3	0.7

Table A2.6a. Trace element compositions of tephra in Lago Élida PC1105 B

	Core Top to H2			H2 to S10						
Tephra	**F1**	**G1**	**G3**	**I**	**J**	**K**	**Ls**	**M**	**N**	**N**
Section	**BT1**	**BT1**	**BT1**	**BT1**	**BT2**	**BT2**	**BT2**	**BT2**	**BT2**	**BT3**
Depth (cm)	**1**	**47**	**53**	**89**	**22**	**24**	**52**	**90**	**94**	**0-3**
Source	**HUD**	**-**	**-**	**HUD**	**HUD**	**HUD**	**-**	**HUD**	**HUD**	**HUD**
Lab #	**CS 4160**	**CS 4161**	**CS 4162**	**CS 4163**	**CS 4164**	**CS 4165**	**CS 4166**	**CS 4167**	**CS 4168**	**CS 4169**
Ti	7266	5964	6237	6016	9288	9475	6022	7121	7413	8347
V	247	215	221	118	268	254	302	135	139	158
Cr	30	84	79	5	17	12	30	7	13	26
Mn	1029	932	926	1001	1156	1071	1093	1070	1136	1266
Co	32	29	32	14	33	26	39	15	14	16
Ni	40	58	49	25	34	34	36	28	30	40
Cu	56	85	186	63	165	122	134	139	178	74
Zn	108	91	94	110	126	130	111	119	118	127
Rb	28	17	28	67	31	37	18	58	53	45
Sr	517	544	524	301	494	460	429	307	320	407
Y	25	19	21	41	29	30	18	45	42	39
Zr	167	124	142	409	215	193	78	408	402	333
Nb	8	5	6	18	19	10	2	19	17	16
Cs	0.7	0.3	0.6	1.5	0.7	0.9	1.0	1.3	1.3	1.0
Ba	369	258	334	718	420	434	180	645	627	576
La	23.7	16.3	18.8	42.1	28.9	29.8	8.7	42.3	40.8	37.3
Ce	53.1	37.7	42.1	91.0	64.4	66.0	20.0	94.6	89.4	84.1
Pr	6.7	4.7	5.2	11.1	8.2	8.3	2.8	11.2	11.1	10.4
Nd	26.3	19.6	22.2	44.7	35.0	33.4	13.0	44.0	41.1	40.6
Sm	5.60	4.26	4.84	8.45	6.89	7.14	3.17	9.15	8.60	8.83
Eu	1.70	1.40	1.37	2.20	1.98	2.07	0.95	2.43	2.38	2.48
Gd	6.6	4.9	5.5	9.8	8.4	8.4	4.1	10.8	10.2	10.1
Tb	0.77	0.57	0.67	1.19	0.94	0.95	0.46	1.23	1.23	1.21
Dy	4.36	3.56	3.91	6.84	5.19	5.43	3.28	7.27	7.24	6.83
Ho	0.80	0.68	0.72	1.35	0.96	0.98	0.62	1.39	1.39	1.29
Er	2.47	1.98	2.28	4.45	3.09	3.30	1.93	4.44	4.28	4.26
Tm	0.30	0.21	0.26	0.57	0.37	0.40	0.21	0.60	0.61	0.56
Yb	2.30	1.85	1.91	4.18	2.64	2.71	1.78	4.29	4.50	4.03
Lu	0.32	0.25	0.25	0.59	0.36	0.38	0.25	0.63	0.57	0.53
Hf	3.4	2.8	3.0	8.5	7.0	4.2	1.8	8.2	8.2	6.9
Pb	5.6	3.5	5.2	11.6	6.5	6.5	4.6	11.5	10.7	8.7
Th	3.2	2.0	2.3	6.0	5.0	3.6	1.1	5.6	5.3	4.5
U	0.9	0.5	0.7	2.0	1.0	1.0	0.5	1.7	1.7	1.3

Table A2.6b. Trace element compositions of tephra in Lago Élida PC1105 B

	H2 to S10					S10				
Tephra	**P1**	**P2**	**P2**	**MEN1**	**-**	**S2**	**S3**	**S4**	**S5**	**S10**
Section	**BT3**	**BT3**	**BT3**	**BT3**	**BT3**	**BT4**	**BT4**	**BT4**	**BT4**	**BT4**
Depth (cm)	**33**	**34**	**34**	**50**	**62-64**	**32**	**33**	**35**	**36**	**41**
Source	**-**	**HUD**	**HUD**	**MEN**	**-**	**HUD**	**HUD**	**HUD**	**HUD**	**HUD**
Lab #	**CS 4170**	**CS 4171**	**CS 4171-D**	**CS 4172**	**CS 4173**	**CS-2551**	**CS-2552**	**CS-2553**	**CS-2554**	**CS-2555**
Ti	6173	14403	15394	4504	7985	10055	10422	7787	11146	13528
V	251	311	331	217	380	268	265	160	254	280
Cr	27	13	15	8	14	21	17	11	15	19
Mn	1008	1479	1538	1502	1187	1286	1302	1285	1350	1431
Co	27	34	36	30	33	30	44	31	27	51
Ni	35	37	38	34	41	23	22	16	22	25
Cu	153	141	141	21	204	63	101	160	97	77
Zn	111	142	140	106	129	111	119	117	114	117
Rb	17	25	26	11	23	29	25	49	23	24
Sr	460	436	464	572	454	550	555	372	541	586
Y	17	39	36	12	23	33	37	45	38	41
Zr	70	198	207	50	104	238	260	410	262	229
Nb	2	8	9	1	3	13	14	19	19	12
Cs	0.7	0.6	0.6	0.3	1.5	0.4	0.4	1.1	0.6	0.5
Ba	205	332	327	111	243	501	487	633	440	421
La	9.3	26.5	25.7	5.3	12.3	34.0	33.4	43.2	33.3	35.0
Ce	21.7	64.1	65.0	13.6	28.1	77.5	78.2	96.9	77.7	80.5
Pr	2.8	8.6	8.6	1.9	3.8	9.9	10.0	11.8	10.2	10.8
Nd	12.6	39.0	37.9	9.0	17.9	41.0	42.0	48.5	44.1	46.5
Sm	3.15	8.67	8.74	2.03	4.32	8.56	8.42	10.04	8.72	9.81
Eu	1.03	2.62	2.66	0.99	1.38	2.48	2.54	2.69	2.69	2.97
Gd	3.9	10.0	10.2	2.6	5.3	8.7	9.4	10.3	9.8	10.6
Tb	0.45	1.26	1.23	0.26	0.67	1.10	1.30	1.39	1.27	1.37
Dy	3.26	7.13	7.14	2.11	4.28	6.09	6.69	8.15	6.65	7.38
Ho	0.61	1.35	1.33	0.43	0.86	1.16	1.33	1.60	1.32	1.46
Er	1.91	4.23	4.15	1.32	2.78	3.56	3.97	4.78	3.74	4.12
Tm	0.21	0.50	0.48	0.14	0.33	0.48	0.51	0.70	0.55	0.54
Yb	1.70	3.51	3.64	1.29	2.46	3.00	3.35	4.77	3.49	3.54
Lu	0.23	0.48	0.46	0.13	0.29	0.47	0.49	0.66	0.56	0.56
Hf	1.7	4.1	4.6	1.2	2.7	5.2	5.3	8.5	7.7	5.0
Pb	5.5	5.4	5.5	2.5	7.4	6.5	4.7	10.1	4.3	4.5
Th	1.4	2.3	2.8	0.4	1.7	3.5	3.5	6.8	6.3	4.5
U	0.6	0.7	0.8	0.2	0.6	0.6	0.7	1.4	0.6	0.7

Table A2.6c. Trace element compositions of tephra in Lago Élida PC1105 B

	S10 to Core Bottom						
Tephra	**X2**	**X3**	**Y1**	**H0**	**H0**	**H0**	**-**
Section	**BT5**	**BT5**	**BT5**	**BT7**	**BT7**	**BT7**	**BT7**
Depth (cm)	**20**	**26**	**48.5**	**21-28**	**21-28**	**10-29**	**68**
Source	**HUD**	**HUD**	**-**	**HUD**	**HUD**	**HUD**	**-**
Lab #	**CS-2556**	**CS-2557**	**CS-2558**	**CS-2559**	**CS-2701**	**CS-2702**	**CS-2560**
Ti	12522	11933	7147	11211	10342	9972	11478
V	244	221	221	329	309	288	316
Cr	4	6	24	37	39	27	38
Mn	1454	1414	1210	1314	1243	1223	1304
Co	26	19	51	38	65	38	32
Ni	15	14	23	34	30	22	26
Cu	92	52	82	62	70	73	129
Zn	118	122	106	106	109	107	108
Rb	32	36	32	26	26	30	28
Sr	477	457	496	493	498	466	480
Y	43	42	26	31	30	32	33
Zr	279	292	119	181	177	194	213
Nb	12	12	5	8	12	11	9
Cs	0.7	1.1	1.9	0.5	0.7	1.0	0.7
Ba	444	452	320	355	355	409	393
La	30.2	30.7	15.1	23.0	21.9	24.9	24.8
Ce	72.4	73.7	34.2	53.4	51.3	56.5	57.3
Pr	9.7	9.6	4.5	6.9	6.7	7.4	7.4
Nd	41.1	40.9	20.4	28.6	29.3	31.7	31.7
Sm	9.18	8.86	4.65	6.62	6.43	7.07	6.72
Eu	2.71	2.58	1.51	2.00	2.13	2.16	2.14
Gd	9.9	10.0	5.4	7.2	7.9	8.3	7.8
Tb	1.37	1.34	0.81	1.03	1.03	1.01	0.98
Dy	7.62	7.57	4.34	5.38	5.73	6.40	5.73
Ho	1.55	1.48	0.94	1.15	1.07	1.10	1.13
Er	4.25	4.50	2.79	3.43	3.50	3.46	3.31
Tm	0.58	0.61	0.35	0.44	0.42	0.43	0.45
Yb	4.04	3.92	2.50	2.93	2.79	3.05	3.17
Lu	0.57	0.59	0.38	0.41	0.43	0.52	0.40
Hf	5.9	6.1	3.1	4.0	4.4	4.7	4.5
Pb	5.4	5.4	6.4	2.7	6.1	6.5	3.8
Th	4.1	4.2	3.7	3.5	5.3	5.0	3.1
U	0.8	0.9	0.9	0.7	0.8	1.0	0.7

Table A2.7a. Trace element compositions of tephra in Las Mellizas PC1106 A & B

	Core Top to H2								H2 to S10	
Tephra	**C1**	**D3**	**E2**	**-**	**-**	**F1**	**G1**	**H2**	**O1**	**P1**
Section	**AT1**	**AT1**	**AT1**	**AT2**	**AT2**	**AT2**	**AT2**	**BT2**	**AT3**	**AT4**
Depth (cm)	**53-56**	**78-84**	**90-93**	**0-4**	**0-4**	**5**	**78-80**	**56-60.5**	**98**	**31**
Source	**HUD**	**MACA**	**HUD**	**MEN**	**MEN**	**HUD**	**-**	**HUD**	**MEN**	**-**
Lab #	**CS2011**	**CS2012**	**CS2013**	**CS2014**	**CS2015**	**CS2016**	**CS2017**	**CS-2401**	**CS2018**	**CS2019**
Ti	8868	4844	7511	4453	5013	11545	6813	8030	6627	7184
V	200	153	208	148	187	169	204	172	157	218
Cr	11	107	62	164	83	4	91	11	56	24
Mn	1231	961	1089	1058	871	1303	1038	1276	1162	1270
Co	40	50	44	63	46	28	46	19	71	41
Ni	37	88	65	122	67	35	62	14	46	40
Cu	52	215	56	34	42	29	60	94	78	106
Zn	112	79	106	86	84	118	100	113	116	130
Rb	41	14	27	12	16	33	16	56	22	18
Sr	471	593	587	573	615	470	553	441	378	498
Y	33	18	26	15	19	43	22	38	28	24
Zr	205	117	199	94	129	291	138	314	108	92
Nb	10	5	9	4	7	12	7	16	5	4
Cs	0.2	-	-	-	-	-	-	1.1	0.4	0.4
Ba	484	245	407	201	255	482	296	699	289	250
La	30.2	15.3	26.8	12.4	16.3	31.9	18.2	40.0	14.1	11.0
Ce	69.5	35.1	59.6	28.3	36.9	74.9	43.7	85.3	32.5	26.1
Pr	9.0	4.6	7.3	3.7	5.1	10.1	5.6	10.7	4.3	3.6
Nd	39.9	19.2	31.6	15.5	20.9	46.1	22.6	43.5	20.3	16.5
Sm	8.16	4.10	6.51	3.47	4.49	9.82	5.29	9.09	4.82	4.35
Eu	2.41	1.47	1.86	1.26	1.56	2.97	1.58	3.24	1.54	1.49
Gd	9.4	4.9	7.2	4.1	4.8	10.9	5.9	11.4	6.0	5.4
Tb	1.13	0.65	0.80	0.51	0.79	1.45	0.67	1.42	0.69	0.75
Dy	6.61	3.36	4.73	2.94	3.76	8.35	4.13	7.12	4.74	4.32
Ho	1.28	0.73	0.89	0.56	0.86	1.66	0.77	1.45	0.92	0.92
Er	3.77	2.08	3.01	1.72	2.23	5.01	2.46	4.44	2.93	2.64
Tm	0.48	0.31	0.31	0.21	0.37	0.60	0.26	0.58	0.31	0.40
Yb	3.25	1.81	2.55	1.36	1.93	4.28	2.25	4.06	2.79	2.60
Lu	0.43	0.29	0.27	0.19	0.36	0.58	0.24	0.59	0.31	0.37
Hf	5.2	2.9	4.6	2.3	3.2	6.9	3.3	7.8	2.8	2.6
Pb	8.2	3.9	7.3	3.3	4.2	8.1	5.2	10.4	9.1	8.5
Th	4.4	1.9	3.8	1.5	2.2	4.0	2.3	5.8	2.3	1.7
U	1.0	0.4	0.7	0.3	0.5	0.9	0.4	1.3	0.6	0.5

Table A2.7b. Trace element compositions of tephra in Las Mellizas PC1106 A & B

	H2 to S10						S10		
Tephra	**P1**	**P1**	**P1**	**Q1**	**MEN1**	**R**	**S2**	**S4**	**S5**
Section	**AT4**	**AT4**	**AT4**	**AT4**	**AT4**	**AT5**	**AT5**	**AT5**	**AT5**
Depth (cm)	**31**	**33-38**	**33-38**	**47**	**54-56**	**0-4**	**6**	**9**	**11-13**
Source	**-**	**-**	**-**	**MEN**	**MEN**	**MEN**	**HUD**	**HUD**	**HUD**
Lab #	**CS2019-D**	**CS2020**	**CS2020-D**	**CS2021**	**CS2022**	**CS2023**	**CS2024**	**CS2025**	**CS2026**
Ti	6612	6621	6527	6435	5633	6326	10334	7868	11043
V	192	175	163	186	186	197	228	88	222
Cr	21	14	14	24	12	18	19	5	17
Mn	1211	1239	1231	967	1788	1451	1300	1382	1326
Co	38	29	29	36	45	37	72	76	45
Ni	42	27	30	41	32	41	42	25	40
Cu	108	38	38	215	21	29	59	70	60
Zn	123	112	120	99	117	117	122	135	121
Rb	15	18	17	15	6	14	23	50	21
Sr	468	430	429	418	598	493	553	368	561
Y	23	24	23	20	15	20	35	43	36
Zr	85	92	92	89	46	92	243	393	257
Nb	3	3	3	4	2	5	13	20	13
Cs	0.2	0.5	0.4	0.2	-	-	-	0.8	-
Ba	237	258	258	227	115	253	575	690	488
La	9.9	10.6	10.7	12.0	6.0	13.3	34.6	41.2	35.2
Ce	24.2	25.8	25.7	28.1	15.0	30.4	80.0	94.8	84.0
Pr	3.4	3.7	3.6	3.6	2.2	3.9	10.2	11.6	10.7
Nd	15.3	16.1	16.0	17.6	10.0	17.8	44.2	47.0	45.2
Sm	3.96	4.44	4.34	4.08	2.36	4.16	9.03	9.84	10.01
Eu	1.34	1.48	1.51	1.30	1.09	1.41	2.68	3.03	2.80
Gd	4.9	5.2	5.1	4.9	3.1	4.9	9.9	11.1	10.7
Tb	0.61	0.74	0.64	0.46	0.39	0.51	1.23	1.50	1.28
Dy	4.17	4.56	4.56	3.79	2.67	3.84	6.87	8.44	7.25
Ho	0.82	1.00	0.92	0.65	0.47	0.69	1.29	1.76	1.41
Er	2.43	2.73	2.69	2.23	1.58	2.20	3.86	5.18	4.19
Tm	0.29	0.41	0.31	0.22	0.21	0.22	0.47	0.81	0.54
Yb	2.43	2.57	2.55	2.01	1.45	2.09	3.65	4.91	3.68
Lu	0.24	0.39	0.31	0.23	0.15	0.22	0.47	0.81	0.48
Hf	2.4	2.8	2.7	2.3	1.2	2.4	5.7	9.4	5.9
Pb	8.0	8.4	8.3	7.2	3.6	6.4	7.6	12.2	6.9
Th	1.6	1.8	1.7	2.1	0.6	1.6	3.3	7.9	3.2
U	0.4	0.5	0.4	0.5	0.1	0.3	0.6	1.6	0.7

Table A2.7c. Trace element compositions of tephra in Las Mellizas PC1106 A & B

	S9 to Core Bottom									
Tephra	**T**	**T**	**V**	**V**	**V**	**Wn**	**X3**	**X3**	**X3**	**Z1**
Section	**AT5**	**AT5**	**AT6**	**AT6**	**BT5**	**BT5**	**AT6**	**AT6**	**BT6**	**AT6**
Depth (cm)	**19**	**19**	**7**	**7**	**70**	**96.5**	**42**	**42**	**9**	**64-68**
Source	**MEN**	**MEN**	**HUD**	**HUD**	**HUD**	**-**	**HUD**	**HUD**	**HUD**	**HUD**
Lab #	**CS2027**	**CS-2027-D**	**CS2028**	**CS-2028-D**	**CS-2402**	**CS-2403**	**CS2029**	**CS-2029-D**	**CS-2404**	**CS2030**
Ti	5197	4785	13397	11360	12948	6165	9909	8510	12094	10819
V	75	85	302	304	383	363	254	272	256	283
Cr	13	15	18	15	17	27	26	21	6	33
Mn	1008	979	1368	1259	1268	902	1222	1138	1260	1309
Co	99	96	41	39	43	43	42	39	36	41
Ni	30	9	46	14	18	19	41	14	11	47
Cu	113	114	120	113	224	507	90	85	109	51
Zn	110	110	129	123	128	109	117	110	129	119
Rb	34	37	28	30	30	17	35	33	38	26
Sr	320	298	479	438	478	456	471	414	466	495
Y	28	28	35	34	37	18	31	28	43	31
Zr	152	146	233	215	231	68	219	197	293	195
Nb	5	8	11	10	10	2	9	8	12	9
Cs	1.3	2.2	-	0.7	0.5	0.9	-	0.8	0.7	-
Ba	360	370	423	429	420	199	465	457	474	403
La	15.4	16.5	29.3	32.4	30.8	9.8	28.8	30.6	32.1	24.6
Ce	37.0	38.7	68.8	75.1	70.3	22.1	65.7	67.1	74.4	57.2
Pr	4.9	5.1	9.1	9.7	9.3	3.0	8.2	8.4	9.8	7.2
Nd	20.8	22.1	40.4	41.4	42.2	13.0	34.9	36.9	43.5	31.8
Sm	5.18	5.73	8.75	9.97	9.01	3.37	7.39	7.95	9.41	6.91
Eu	1.50	1.85	2.53	3.08	2.94	1.21	2.18	2.49	3.14	2.10
Gd	6.1	7.3	9.7	12.1	11.5	4.4	8.4	9.6	12.5	7.6
Tb	0.75	0.96	1.15	1.44	1.37	0.58	0.97	1.14	1.49	0.96
Dy	5.36	5.33	6.82	7.16	7.06	3.31	5.71	5.82	8.14	5.95
Ho	0.99	1.08	1.22	1.47	1.39	0.67	1.09	1.12	1.52	1.10
Er	3.31	3.39	3.95	4.39	4.35	1.92	3.36	3.68	4.82	3.39
Tm	0.36	0.44	0.45	0.54	0.53	0.25	0.37	0.42	0.62	0.39
Yb	3.12	3.12	3.38	3.54	3.51	1.92	3.02	3.06	4.08	3.19
Lu	0.38	0.51	0.41	0.55	0.53	0.27	0.38	0.45	0.65	0.36
Hf	4.3	4.9	5.3	5.5	5.5	1.9	5.0	4.9	6.7	4.2
Pb	11.7	10.0	7.5	5.5	7.3	8.4	8.3	5.9	7.8	7.4
Th	3.8	4.6	3.2	3.3	2.9	1.8	5.4	5.1	3.9	3.9
U	1.1	1.1	0.7	0.7	0.7	0.5	1.0	1.0	0.8	0.7

Table A2.7d. Trace element compositions of tephra in Las Mellizas PC1106 A & B

Tephra	Z1	Z1	Z1	H0	Z3	Z3	Z3	MEN0	MEN0	Z5
Section	AT6	BT6	BT6	AT6	AT7	AT7	AT7	A7	AT7	AT7
Depth (cm)	64-68	28-30	30-32	97	62-64	62-64	62-64	73-76	73-76	82
Source	-	HUD	HUD	HUD	-	-	-	MEN	MEN	-
Lab #	CS-2030-D	CS-2405	CS-2406	CS2031	CS2032	CS2032-D	CS-2032-D	CS2033	CS-2033-D	CS2034
Ti	9206	7528	10438	7611	6121	5950	5304	4975	4267	5697
V	307	338	437	155	192	180	221	189	237	200
Cr	26	58	30	19	9	9	8	23	20	21
Mn	1191	913	1208	1103	1064	1028	963	1157	1061	1116
Co	37	40	55	24	24	24	27	32	31	27
Ni	19	29	23	35	31	30	11	38	16	34
Cu	48	153	131	3783	180	171	161	50	47	71
Zn	107	95	116	104	101	96	98	89	76	94
Rb	28	27	32	42	18	17	21	11	13	25
Sr	435	581	491	442	501	489	428	479	423	457
Y	28	23	31	29	20	20	18	15	13	19
Zr	171	132	196	208	81	76	70	61	53	72
Nb	8	5	8	11	3	3	3	2	1	3
Cs	0.7	0.9	0.5	0.6	0.4	0.4	1.0	-	0.7	0.6
Ba	400	304	396	525	261	251	241	153	147	280
La	25.2	18.4	24.6	28.2	9.6	9.6	9.5	5.6	5.5	10.6
Ce	56.8	42.1	55.4	64.5	22.8	22.4	21.9	13.4	13.1	24.1
Pr	7.4	5.4	7.3	7.9	3.1	3.0	2.9	1.8	1.8	3.2
Nd	31.1	23.3	30.4	31.9	14.3	13.8	14.1	9.0	8.8	14.7
Sm	7.14	4.93	6.92	7.07	3.76	3.66	3.66	2.29	2.24	3.68
Eu	2.38	1.80	2.36	2.09	1.19	1.26	1.38	0.92	0.99	1.15
Gd	9.1	6.3	8.6	8.1	4.4	4.2	4.8	2.8	2.9	4.3
Tb	1.16	0.77	1.05	0.95	0.50	0.52	0.58	0.29	0.41	0.52
Dy	5.95	4.28	5.86	5.70	3.72	3.88	3.71	2.55	2.27	3.51
Ho	1.18	0.83	1.16	1.09	0.68	0.69	0.72	0.44	0.52	0.69
Er	3.42	2.59	3.67	3.24	2.34	2.18	2.27	1.64	1.58	2.23
Tm	0.41	0.33	0.43	0.39	0.25	0.25	0.28	0.16	0.20	0.25
Yb	3.05	2.23	3.10	3.01	2.09	2.04	1.93	1.57	1.53	1.96
Lu	0.42	0.33	0.43	0.37	0.25	0.23	0.31	0.15	0.22	0.23
Hf	4.6	3.1	4.4	5.2	2.2	2.3	2.5	1.9	1.6	2.1
Pb	4.9	5.9	6.3	9.7	7.8	7.5	5.6	4.7	2.9	6.8
Th	3.5	3.4	3.4	5.0	1.6	1.6	1.8	0.9	0.7	2.5
U	0.7	0.7	0.8	1.1	0.5	0.5	0.4	0.2	0.2	0.7

Table A2.8a. Trace element compositions of tephra in El Toro PC1002 A & B

	Core Top to H2									
Tephra	**A1**	**B1**	**C2**	**D3**	**D3**	**E2**	**F1**	**G1**	**H2**	**H2**
Section	**AT1**	**AT1**	**AT1**	**AT2**	**AT2**	**AT2**	**AT2**	**AT3**	**AT3**	**AT4**
Depth (cm)	**8**	**50**	**70**	**0-7**	**0-7**	**12-15**	**28**	**41**	**49-52**	**0-5**
Source	**-**	**-**	**HUD**	**MACA**	**MACA**	**HUD**	**HUD**	**-**	**HUD**	**HUD**
Lab #	**CS2101**	**CS2102**	**CS2103**	**CS2104**	**CS2105**	**CS2106**	**CS2107**	**CS2108**	**CS2109**	**CS2110**
Ti	5905	7434	8768	5093	6059	7774	9467	6526	7810	7909
V	97	283	161	144	191	232	206	195	157	97
Cr	11	16	13	190	85	61	23	97	25	12
Mn	1086	1288	1128	1147	937	1126	1171	976	1100	1259
Co	22	31	24	56	49	47	33	38	17	24
Ni	31	38	37	140	76	52	38	60	41	27
Cu	73	102	118	45	42	93	108	70	133	47
Zn	109	125	112	87	86	104	111	91	113	115
Rb	13	12	34	10	11	23	33	11	39	37
Sr	367	419	448	538	587	542	471	535	377	388
Y	20	23	31	16	20	24	30	19	33	34
Zr	91	100	203	104	137	204	216	136	294	317
Nb	3	3	9	4	5	9	9	6	14	15
Cs	-	-	-	-	-	-	-	-	-	-
Ba	199	224	450	216	274	413	440	266	582	662
La	9.1	10.0	29.1	12.9	17.1	25.4	28.5	17.0	32.4	33.6
Ce	22.2	24.2	67.3	30.5	39.9	60.0	64.8	37.9	73.4	75.3
Pr	2.8	3.3	8.2	3.8	5.1	7.3	8.1	4.8	9.1	8.9
Nd	14.0	15.8	36.1	16.5	22.2	30.2	35.8	22.4	36.5	36.6
Sm	3.96	4.18	7.63	3.66	4.64	6.45	7.46	4.84	7.74	8.11
Eu	1.08	1.25	2.00	1.10	1.30	1.67	1.96	1.36	1.96	2.34
Gd	4.4	4.8	8.4	4.2	5.5	7.3	8.2	5.2	8.6	8.9
Tb	0.52	0.59	0.92	0.44	0.57	0.78	0.94	0.65	1.01	1.08
Dy	3.66	3.86	6.02	2.92	3.60	4.96	5.83	3.87	6.26	6.47
Ho	0.59	0.67	0.95	0.43	0.52	0.81	0.95	0.56	1.01	1.18
Er	2.20	2.45	3.40	1.49	1.96	2.66	3.39	2.20	3.50	3.98
Tm	0.13	0.16	0.32	-	-	0.24	0.30	0.13	0.27	0.37
Yb	1.83	2.28	2.95	1.39	1.74	2.47	2.92	1.74	3.31	3.70
Lu	-	-	-	-	-	-	-	-	-	0.45
Hf	2.5	2.9	4.8	2.6	3.2	4.8	4.9	3.1	6.8	7.6
Pb	7.0	7.4	8.9	3.8	5.0	7.6	7.8	4.8	10.5	11.1
Th	1.2	1.1	3.9	1.3	1.5	3.5	3.8	1.6	4.6	5.0
U	0.4	0.4	0.9	0.3	0.3	0.8	0.8	0.4	1.1	1.3

Table A2.8b. Trace element compositions of tephra in El Toro PC1002 A & B

	Core Top to H2		H2 to S10					S10		
Tephra	**H2**	**H2**	**Ln**	**O2**	**O2**	**Q2**	**MEN1**	**S1**	**S2**	**S4**
Section	**AT4**	**BT3**	**AT4**	**AT4**	**AT4**	**AT5**	**AT5**	**AT6**	**AT6**	**AT6**
Depth (cm)	**0-5**	**0-8**	**31**	**48-53**	**48-53**	**0-3**	**5-8**	**50-52**	**52.5**	**57.5**
Source	**HUD**	**HUD**	**MEN**	**-**	**-**	**MEN**	**MEN**	**HUD**	**HUD**	**HUD**
Lab #	CS-2110-D	CS-2451	CS2111	CS2112	CS2113	CS2114	CS2115	CS2116	CS2117	CS2118
Ti	7439	6808	5642	5925	6473	5663	3371	9683	10076	6690
V	147	235	133	135	111	106	-	181	178	-
Cr	12	32	34	21	8	18	5	22	18	6
Mn	1240	1117	903	1005	1185	991	1188	1218	1264	1125
Co	25	24	23	42	23	30	18	31	26	16
Ni	11	26	46	32	34	33	19	41	39	30
Cu	46	42	93	56	36	52	21	51	92	76
Zn	109	105	91	92	112	100	78	120	117	114
Rb	52	26	23	11	16	13	-	25	22	41
Sr	392	487	412	447	399	449	568	532	534	305
Y	36	24	22	19	24	20	11	31	34	40
Zr	294	126	120	76	102	81	46	224	249	373
Nb	16	5	3	2	3	3	4	12	12	17
Cs	1.0	0.7	-	-	-	-	-	-	-	-
Ba	693	331	292	205	262	222	110	534	608	625
La	40.4	17.2	13.0	8.6	10.8	9.4	5.1	33.6	34.3	36.0
Ce	88.6	38.0	30.5	20.8	26.5	22.6	12.4	75.5	78.5	83.4
Pr	10.7	5.1	4.0	2.8	3.5	3.0	1.7	9.4	10.0	10.2
Nd	40.6	21.7	18.5	13.6	16.4	14.2	7.8	42.0	41.5	41.6
Sm	9.37	4.92	4.30	3.63	4.46	3.82	2.01	8.32	8.62	8.90
Eu	3.09	1.87	1.20	1.16	1.37	1.16	0.92	2.46	2.58	2.40
Gd	11.8	5.9	4.8	4.3	5.3	4.5	2.5	9.4	9.7	10.0
Tb	1.35	0.80	0.56	0.52	0.64	0.53	0.35	1.00	1.16	1.20
Dy	7.20	4.24	3.85	3.52	4.59	3.66	1.97	6.22	6.51	7.36
Ho	1.42	0.88	0.62	0.58	0.72	0.60	0.36	1.02	1.14	1.29
Er	4.55	2.62	2.31	2.18	2.61	2.61	1.16	3.55	3.94	4.35
Tm	0.57	0.32	-	0.14	0.17	0.17	0.10	0.26	0.31	0.43
Yb	3.98	2.33	2.12	2.01	2.30	2.01	1.13	2.97	3.42	4.18
Lu	0.60	0.37	-	-	-	-	-	-	-	0.46
Hf	8.1	3.2	3.1	2.1	2.8	2.3	2.8	4.8	5.4	8.6
Pb	9.4	5.8	7.3	6.7	9.0	7.3	3.6	12.2	7.7	12.1
Th	5.8	2.0	2.5	1.1	1.3	1.2	1.7	3.0	3.0	6.6
U	1.3	0.5	0.7	0.4	0.5	0.4	0.1	0.6	0.7	1.5

Table A2.8c. Trace element compositions of tephra in El Toro PC1002 A & B

	S10	S10 to Core Bottom								
Tephra	**S5**	**T**	**T**	**T**	**T**	**V**	**V**	**V**	**Wn**	**X2**
Section	**AT6**	**AT6**	**AT6**	**AT6**	**BT5**	**AT7**	**AT7**	**BT5**	**AT7**	**BT6**
Depth (cm)	**59**	**74**	**74**	**74**	**20.5**	**19**	**19**	**67**	**33**	**8**
Source	**HUD**	**MEN**	**MEN**	**MEN**	**MEN**	**HUD**	**HUD**	**HUD**	**-**	**HUD**
Lab #	**CS2119**	**CS2120**	**CS2120-D**	**CS-2120-D**	**CS-2452**	**CS2121**	**CS-2121-D**	**CS-2453**	**CS2122**	**CS-2454**
Ti	10959	7407	7260	6745	6236	13056	11485	12216	5449	11461
V	237	188	189	246	173	275	296	396	157	360
Cr	19	18	17	16	10	16	14	18	21	13
Mn	1374	1235	1197	1187	1056	1328	1211	1195	844	1295
Co	27	29	29	30	22	28	28	47	26	25
Ni	34	32	31	14	12	41	16	20	33	15
Cu	176	122	122	115	177	140	129	174	142	110
Zn	132	128	123	122	118	129	119	127	87	130
Rb	21	18	17	23	39	32	31	31	15	33
Sr	538	425	416	407	379	495	439	489	429	487
Y	34	22	22	22	28	37	34	35	17	40
Zr	258	108	104	96	141	253	213	226	70	250
Nb	15	4	4	3	4	15	9	10	2	9
Cs	-	-	-	1.4	1.8	-	0.6	0.5	-	0.6
Ba	463	260	257	264	330	449	420	416	199	432
La	33.8	11.1	10.9	12.2	14.2	30.5	30.5	29.0	9.8	29.4
Ce	78.5	27.3	27.3	28.7	33.7	72.2	70.3	67.7	22.3	67.1
Pr	10.2	3.6	3.6	3.8	4.5	9.2	9.1	9.0	2.9	9.2
Nd	43.2	17.1	16.7	17.7	20.2	40.5	39.3	36.6	12.7	39.8
Sm	9.27	4.32	4.45	4.64	5.19	8.94	9.05	8.39	3.22	8.45
Eu	2.54	1.38	1.29	1.65	1.68	2.73	2.94	2.62	0.99	2.91
Gd	10.1	5.1	4.9	6.0	6.1	10.4	11.4	10.4	3.8	10.7
Tb	1.16	0.63	0.65	0.80	0.85	1.30	1.41	1.28	0.45	1.38
Dy	6.80	4.36	4.03	4.55	4.89	7.21	7.31	6.77	3.05	7.19
Ho	1.20	0.73	0.73	0.89	1.06	1.30	1.37	1.27	0.48	1.44
Er	3.75	2.41	2.36	2.87	3.14	4.05	4.39	3.82	1.89	4.30
Tm	0.34	0.18	0.21	0.37	0.39	0.48	0.51	0.51	-	0.52
Yb	3.13	2.24	2.17	2.52	2.91	3.66	3.57	3.47	1.67	3.75
Lu	-	-	-	0.37	0.46	0.45	0.50	0.47	-	0.55
Hf	7.0	2.8	2.9	2.8	3.9	7.5	5.5	4.8	2.0	5.7
Pb	9.2	9.1	8.9	7.1	11.7	8.1	6.0	9.8	7.8	7.5
Th	3.9	2.0	2.2	2.1	3.2	5.0	3.2	2.8	2.2	3.2
U	0.7	0.7	0.7	0.6	0.9	0.8	0.7	0.7	0.6	0.7

Table A2.8d. Trace element compositions of tephra in El Toro PC1002 A & B

	S10 to Core Bottom								
Tephra	**Y1**	**Y1**	**Y1**	**Z1**	**Z1**	**Z1**	**Z1**	**H0**	**H0**
Section	**AT7**	**AT7**	**BT6**	**AT7**	**AT7**	**BT6**	**BT6**	**AT8**	**AT8**
Depth (cm)	**70**	**70**	**23**	**98-101**	**98-101**	**48-50**	**50**	**70-80**	**70-80**
Source	**-**	**-**	**-**	**HUD**	**HUD**	**HUD**	**HUD**	**HUD**	**HUD**
Lab #	**CS2123**	**CS-2123-D**	**CS-2455**	**CS2124**	**CS-2124-D**	**CS-2456**	**CS-2457**	**CS2125**	**CS2125-D**
Ti	6454	6347	6638	9343	8965	8434	9938	7382	7421
V	232	293	322	203	231	376	406	-	74
Cr	17	16	18	27	27	50	28	16	17
Mn	1128	1128	1115	1123	1113	1016	1173	1022	1053
Co	24	26	42	25	28	33	38	15	16
Ni	28	15	18	44	18	32	26	36	37
Cu	113	109	170	155	149	172	111	97	98
Zn	107	110	119	109	112	107	120	104	109
Rb	14	20	18	33	38	32	31	36	37
Sr	427	447	494	439	415	523	466	444	441
Y	19	21	22	31	30	26	30	28	29
Zr	89	88	94	198	183	152	195	226	234
Nb	3	2	6	9	11	6	8	12	12
Cs	-	1.1	0.8	-	1.3	0.9	0.6	-	-
Ba	229	250	235	460	445	364	394	540	549
La	11.0	12.7	11.3	24.8	25.7	21.3	24.2	27.7	28.8
Ce	26.3	28.4	26.7	58.5	58.5	47.9	54.2	61.6	63.4
Pr	3.3	3.8	3.6	7.4	7.4	6.2	7.1	7.4	7.7
Nd	15.2	17.3	15.8	30.3	31.7	26.1	30.7	31.4	32.1
Sm	3.90	4.43	4.05	6.75	7.29	5.73	6.57	6.72	6.82
Eu	1.20	1.43	1.39	2.01	2.35	1.91	2.28	1.96	2.03
Gd	4.5	5.5	5.1	8.0	9.5	6.9	8.1	7.6	7.4
Tb	0.52	0.71	0.68	0.94	1.08	0.82	1.02	0.85	0.88
Dy	3.63	4.22	4.22	5.75	6.10	4.63	5.64	5.57	5.38
Ho	0.61	0.84	0.82	0.96	1.19	0.91	1.11	0.91	0.92
Er	2.20	2.62	2.38	3.26	3.69	3.29	3.55	2.96	3.15
Tm	0.15	0.36	0.31	0.28	0.46	0.37	0.42	0.29	0.23
Yb	1.96	2.18	2.18	3.00	3.21	2.47	2.83	2.75	2.90
Lu	-	0.37	0.33	-	0.47	0.39	0.45	-	-
Hf	2.4	2.5	3.1	4.6	5.1	3.8	4.3	5.4	5.3
Pb	8.3	7.3	8.7	9.0	7.4	7.8	6.1	9.3	9.5
Th	2.1	2.3	2.6	4.4	4.7	3.6	3.4	4.1	4.3
U	0.6	0.6	0.5	1.0	1.0	0.7	0.7	1.1	1.1

Table A2.8e. Trace element compositions of tephra in El Toro PC1002 A & B

	S10 to Core Bottom										
Tephra	**H0**	**H0**	**H0**	**H0**	**Z3**	**MEN0**	**MEN0**	**MEN0**	**Z5**	**Z5**	**Z5**
Section	**AT8**	**BT7**	**BT7**	**BT7**	**BT7**	**AT9**	**AT9**	**BT7**	**AT9**	**AT9**	**BT7**
Depth (cm)	**70-80**	**34-37**	**34-37**	**34-37**	**48**	**20**	**20**	**71**	**32**	**32**	**84**
Source	**HUD**	**HUD**	**HUD**	**HUD**	**-**	**MEN**	**MEN**	**MEN**	**-**	**-**	**-**
Lab #	**CS2126**	**3650**	**3651**	**3651-D**	**CS-2458**	**CS2127**	**CS-2127-D**	**CS-2459**	**CS2128**	**CS-2128-D**	**CS-2460**
Ti	7260	8802	7861	7789	5860	4041	3942	4762	5796	5733	6232
V	103	198	181	182	355	94	185	289	166	271	345
Cr	12	20	9	9	13	16	18	25	21	22	23
Mn	1037	1247	1120	1116	1014	899	929	1048	1158	1165	1146
Co	52	27	59	60	42	18	18	36	29	29	32
Ni	36	25	20	61	19	37	14	21	43	18	21
Cu	50	32	29	28	107	76	73	55	140	136	153
Zn	102	124	114	118	111	89	94	94	114	109	121
Rb	47	38	52	52	20	40	48	12	36	39	18
Sr	410	499	393	397	481	342	344	393	434	413	480
Y	33	29	35	34	20	19	20	10	22	22	20
Zr	282	216	285	282	76	95	89	65	85	78	79
Nb	14	22	14	13	2	4	3	2	3	3	2
Cs	-	1.1	1.4	1.3	0.9	2.7	3.9	0.3	2.1	2.9	0.8
Ba	635	523	620	616	231	302	303	127	304	299	225
La	32.5	28.4	34.4	34.7	8.9	12.4	13.4	4.6	12.8	12.9	8.4
Ce	73.3	62.4	74.5	75.1	21.3	27.8	28.1	11.6	28.9	28.3	20.5
Pr	8.9	7.5	9.1	9.0	2.8	3.3	3.4	1.6	3.6	3.8	2.9
Nd	38.1	32.2	36.6	37.3	13.4	15.0	15.1	6.9	16.2	16.4	12.5
Sm	7.83	6.75	7.48	7.83	3.55	3.67	3.70	1.88	4.00	3.89	3.55
Eu	2.17	2.29	2.43	2.31	1.25	0.84	1.23	0.75	1.06	1.48	1.32
Gd	8.7	8.3	9.6	9.2	4.5	4.0	4.4	2.3	4.9	5.2	4.5
Tb	1.04	0.89	1.12	1.14	0.59	-	0.64	0.28	0.55	0.68	0.57
Dy	6.20	5.62	6.28	6.42	3.55	3.14	3.33	1.91	3.70	3.88	3.48
Ho	1.08	0.97	1.24	1.27	0.73	0.48	0.68	0.37	0.63	0.77	0.72
Er	3.69	3.10	3.47	3.97	2.13	1.98	2.25	1.09	2.26	2.47	2.15
Tm	0.33	0.36	0.46	0.47	0.26	-	0.27	0.14	0.15	0.32	0.26
Yb	3.34	2.91	3.72	3.52	2.04	1.94	2.17	1.02	2.06	2.26	1.96
Lu	-	0.37	0.48	0.44	0.27	-	0.34	0.15	-	0.36	0.29
Hf	6.8	6.2	6.8	6.5	1.9	2.9	2.6	1.6	2.6	2.3	2.0
Pb	11.2	8.2	10.9	10.8	7.1	12.9	11.2	4.5	12.0	9.9	7.5
Th	5.0	7.0	5.5	5.8	1.3	4.2	4.2	0.7	3.6	3.5	1.2
U	1.3	1.2	1.7	1.7	0.5	1.5	1.4	0.5	1.8	1.7	0.7

Table A2.9a. Trace element compositions of tephra in Lago Unco PC1103 E

	Core Top to H2						H2 to S10			
Tephra	**B1**	**D1**	**D2**	**E2**	**G1**	**H2**	**I**	**Ln**	**-**	**N**
Section	**ET1**	**ET1**	**ET1**	**ET2**	**ET3**	**ET3**	**ET4**	**ET4**	**ET6**	**ET6**
Depth (cm)	**57**	**94**	**97**	**21**	**45**	**57-69**	**14**	**63**	**29**	**38**
Source	**-**	**MEN**	**HUD**	**HUD**	**-**	**HUD**	**HUD**	**MEN**	**-**	**HUD**
Lab #	**CS 4123**	**CS 4124**	**CS 4125**	**CS 4126**	**CS 4127**	**CS 4128**	**CS 4129**	**CS 4130**	**CS 4131**	**CS 4132**
Ti	7073	6901	10131	8105	6847	7898	6710	7467	7034	7470
V	287	334	372	269	284	190	184	268	250	196
Cr	17	17	19	56	98	15	7	15	14	14
Mn	1427	1418	1382	1243	1110	1260	1062	1166	1246	1112
Co	33	44	47	39	46	21	15	32	26	29
Ni	34	38	41	55	65	33	27	33	31	30
Cu	66	86	90	88	68	28	82	73	100	104
Zn	135	130	137	127	104	123	116	128	123	123
Rb	22	17	32	33	20	53	71	30	28	63
Sr	457	455	532	560	616	445	305	504	388	299
Y	23	21	36	27	21	34	41	25	29	45
Zr	99	93	211	223	144	310	419	136	109	430
Nb	2	2	8	19	6	16	18	4	4	19
Cs	0.9	0.7	0.6	0.6	0.2	0.9	1.3	0.7	1.1	1.3
Ba	225	190	459	399	280	624	717	363	287	651
La	9.8	8.5	27.1	26.7	17.6	36.3	41.9	17.1	13.9	42.9
Ce	23.6	20.8	61.3	59.2	40.2	78.2	90.5	40.1	32.6	94.6
Pr	3.18	2.86	7.71	7.31	5.23	9.39	10.70	5.18	4.26	11.63
Nd	15.3	14.2	33.5	30.4	23.0	39.8	43.2	23.3	20.1	46.9
Sm	4.10	3.41	7.08	6.26	4.75	7.80	8.61	5.33	4.72	9.24
Eu	1.07	0.93	2.15	1.75	1.37	2.16	2.09	1.47	1.36	2.25
Gd	4.79	4.25	8.06	7.11	5.53	8.89	9.87	5.95	6.03	10.37
Tb	0.56	0.47	0.88	0.80	0.57	1.01	1.14	0.72	0.68	1.24
Dy	3.98	3.68	5.61	4.87	3.92	6.38	7.02	4.58	4.94	7.67
Ho	0.74	0.66	1.01	0.87	0.67	1.13	1.37	0.82	0.95	1.53
Er	2.59	2.29	3.25	2.89	2.15	3.87	4.25	2.81	3.02	4.74
Tm	0.28	0.20	0.32	0.29	0.23	0.39	0.53	0.28	0.32	0.60
Yb	2.35	1.96	2.88	2.57	1.86	3.38	4.12	2.42	2.73	4.50
Lu	0.25	0.21	0.31	0.30	0.19	0.44	0.52	0.28	0.33	0.57
Hf	2.2	1.9	4.2	7.7	2.8	6.0	8.5	3.0	2.4	8.4
Pb	5.5	4.8	5.5	6.0	3.4	8.3	11.1	7.0	8.1	11.8
Th	0.8	0.6	2.3	6.0	1.8	4.4	6.0	2.0	1.6	5.6
U	0.4	0.3	0.7	0.7	0.4	1.0	1.4	0.7	0.6	1.4

Table A2.9b. Trace element compositions of tephra in Lago Unco PC1103 E

	H2 to S10						S10			
Tephra	**-**	**O2**	**O2**	**P1**	**MEN1**	**R**	**S2**	**S2**	**S4**	**S5**
Section	**ET6**	**ET6**	**ET7**	**ET7**	**ET7**	**ET8**	**ET8**	**ET8**	**ET8**	**ET8**
Depth (cm)	**53**	**100**	**0-5**	**30**	**47-50**	**0-3**	**22**	**22**	**23.5**	**25-27**
Source	**-**	**-**	**-**	**-**	**MEN**	**MEN**	**HUD**	**HUD**	**HUD**	**HUD**
Lab #	**CS 4133**	**CS 4134**	**CS 4135**	**CS 4136**	**CS 4137**	**CS 4138**	**CS-2601**	**CS-2601-D**	**CS-2602**	**CS-2603**
Ti	6617	6498	6973	6347	5342	6719	10745	10811	7714	11940
V	292	301	286	282	252	285	278	282	138	276
Cr	38	27	17	26	102	22	18	18	5	16
Mn	1065	1068	1213	1026	1622	1168	1335	1338	1338	1445
Co	30	31	24	27	31	28	31	32	38	29
Ni	40	35	32	36	34	36	22	24	14	24
Cu	140	97	53	107	23	47	177	178	121	80
Zn	103	107	120	108	142	116	121	119	122	119
Rb	37	20	21	16	9	18	28	29	56	24
Sr	477	527	476	494	570	524	543	551	334	584
Y	23	20	22	17	12	20	36	37	47	39
Zr	142	81	97	71	50	85	257	259	441	271
Nb	3	2	2	12	2	3	13	13	20	20
Cs	1.0	0.7	1.0	0.7	0.3	0.8	0.8	0.8	1.1	0.8
Ba	351	230	257	208	120	224	589	589	691	509
La	15.5	9.7	10.7	8.6	6.0	9.8	34.6	34.8	44.7	35.7
Ce	35.3	23.0	25.4	20.6	15.0	23.2	79.6	80.7	98.6	84.4
Pr	4.61	3.06	3.48	2.67	1.95	3.04	10.1	10.1	12.1	10.8
Nd	20.0	14.4	16.0	12.1	9.6	13.8	42.1	40.5	47.3	44.5
Sm	4.62	3.47	4.15	3.29	2.28	3.60	8.72	9.02	9.86	9.42
Eu	1.15	1.15	1.14	1.01	0.75	1.29	2.50	2.53	2.68	2.75
Gd	5.45	4.27	4.99	3.79	2.85	4.44	9.20	9.89	10.47	10.10
Tb	0.62	0.48	0.64	0.42	0.30	0.55	1.28	1.17	1.46	1.38
Dy	4.10	3.38	4.25	3.09	2.34	3.84	6.80	6.83	8.17	6.98
Ho	0.76	0.65	0.79	0.54	0.40	0.68	1.30	1.33	1.67	1.45
Er	2.56	2.17	2.60	1.79	1.43	2.27	3.87	3.88	4.91	4.11
Tm	0.27	0.20	0.28	0.21	0.11	0.23	0.48	0.51	0.75	0.56
Yb	2.38	1.92	2.14	1.77	1.33	2.07	3.35	3.53	4.73	3.56
Lu	0.31	0.19	0.29	0.17	0.12	0.22	0.51	0.50	0.73	0.56
Hf	3.3	1.9	2.4	5.0	1.3	2.2	5.5	5.4	8.9	7.8
Pb	7.6	6.1	7.2	5.9	3.5	6.6	5.2	5.3	10.0	4.2
Th	2.7	1.1	1.1	4.4	0.6	1.0	3.4	3.5	7.6	6.5
U	0.8	0.4	0.5	0.4	0.2	0.4	0.7	0.8	1.6	0.7

Table A2.9c. Trace element compositions of tephra in Lago Unco PC1103 E

	S10	S10 to Core Bottom						
Tephra	**S8**	**T**	**V**	**X3**	**Z1**	**Z1**	**-**	**-**
Section	**ET8**	**ET8**	**ET8**	**ET8**	**ET8**	**ET8**	**ET8**	**ET8**
Depth (cm)	**29-30.5**	**37**	**52**	**59**	**67**	**69-72**	**74**	**82**
Source	**HUD**	**MEN**	**HUD**	**HUD**	**HUD**	**HUD**	**-**	**-**
Lab #	**CS-2604**	**CS-2605**	**CS-2606**	**CS-2607**	**CS-2608**	**CS-2609**	**CS-2610**	**CS-2611**
Ti	12689	5963	13104	12146	10698	10864	8121	7038
V	285	131	319	225	312	305	259	295
Cr	18	10	14	7	32	36	73	13
Mn	1487	1081	1303	1527	1241	1172	982	1215
Co	30	29	31	27	58	30	42	51
Ni	27	16	22	15	30	27	35	22
Cu	86	143	166	88	100	153	196	103
Zn	126	114	116	123	103	107	87	104
Rb	23	42	32	36	31	36	40	17
Sr	580	347	476	452	465	474	401	452
Y	40	33	38	43	31	33	26	22
Zr	268	172	235	294	192	207	134	85
Nb	13	6	10	12	9	9	7	3
Cs	0.5	2.4	0.6	0.7	0.7	1.2	1.6	0.9
Ba	449	371	437	455	393	419	332	222
La	36.5	16.9	29.5	31.8	24.8	25.8	20.0	9.7
Ce	86.3	39.7	68.7	74.2	54.8	60.1	43.8	23.5
Pr	10.9	5.1	9.2	9.8	7.1	7.6	5.7	3.3
Nd	48.0	22.9	38.4	41.2	31.1	31.9	24.1	14.9
Sm	10.01	5.75	8.47	9.05	6.64	7.16	5.07	3.59
Eu	2.93	1.57	2.47	2.71	2.00	2.10	1.57	1.30
Gd	10.45	6.65	8.73	9.99	7.22	7.74	5.71	4.49
Tb	1.38	0.97	1.26	1.40	1.01	1.06	0.82	0.65
Dy	7.71	5.40	6.73	7.64	5.48	5.91	4.56	3.84
Ho	1.51	1.13	1.36	1.49	1.14	1.16	0.91	0.74
Er	4.33	3.51	4.07	4.43	3.42	3.58	2.71	2.37
Tm	0.57	0.50	0.50	0.60	0.45	0.46	0.40	0.31
Yb	3.42	3.18	3.24	3.79	3.06	3.12	2.53	2.31
Lu	0.55	0.48	0.53	0.57	0.40	0.44	0.35	0.31
Hf	5.7	4.2	4.8	6.2	4.2	4.4	3.3	2.3
Pb	4.3	9.5	4.6	5.3	3.8	5.1	5.2	4.0
Th	4.1	4.2	3.5	4.0	3.7	4.0	4.1	1.5
U	0.8	1.2	0.8	0.9	0.9	1.3	1.2	0.5

Table A2.9d. Trace element compositions of tephra in Lago Unco PC1103 E

Tephra	H0	H0	Z3	MEN0	MEN0
Section	ET8	ET9	ET9	ET9	ET9
Depth (cm)	90	0-3	37	42	43-45
Source	HUD	HUD	-	MEN	MEN
Lab #	CS-2612	CS-2700	CS-2613	CS-2614	CS-2615
Ti	7977	7810	6589	4501	6611
V	207	175	240	197	264
Cr	11	17	11	20	21
Mn	1042	1097	1139	1012	1102
Co	19	26	29	49	25
Ni	19	13	19	22	23
Cu	72	67	82	31	148
Zn	96	114	97	73	97
Rb	46	47	23	13	26
Sr	403	448	470	450	448
Y	32	34	22	15	21
Zr	238	275	86	68	80
Nb	11	22	10	3	3
Cs	1.3	1.4	1.5	0.9	1.6
Ba	517	584	246	151	263
La	30.7	32.7	10.2	6.2	10.9
Ce	67.0	71.0	23.9	14.8	25.0
Pr	8.3	8.9	3.3	2.0	3.4
Nd	34.5	36.3	15.0	9.2	14.8
Sm	7.26	7.76	3.78	2.41	3.63
Eu	2.12	2.31	1.34	0.94	1.19
Gd	7.79	8.89	4.33	2.84	4.20
Tb	1.07	1.21	0.64	0.43	0.61
Dy	5.98	6.03	3.63	2.62	3.58
Ho	1.20	1.20	0.73	0.54	0.77
Er	3.57	3.61	2.40	1.69	2.29
Tm	0.45	0.47	0.31	0.23	0.31
Yb	3.19	3.34	2.16	1.45	1.91
Lu	0.42	0.50	0.33	0.26	0.30
Hf	5.4	6.9	4.8	2.2	2.4
Pb	6.2	10.3	4.6	2.1	4.8
Th	4.7	8.1	5.0	1.8	2.6
U	1.2	1.3	1.0	0.6	0.8

Table A2.10a. Trace element compositions of tephra in Lago Traquillo PC1203 A

	Core Top to H2									
Tephra	**B2**	**C2**	**D2**	**D3**	**E1**	**E2**	**E3**	**F1**	**-**	**-**
Section	**AT3**	**AT3**	**AT3**	**AT3**	**AT3**	**AT3**	**AT3**	**AT3**	**AT4**	**AT4**
Depth (cm)	**0-4**	**20**	**42**	**49-57**	**60**	**62-64**	**67**	**89**	**0**	**64-66**
Source	**MEN**	**HUD**	**HUD**	**MACA**	**HUD**	**HUD**	**HUD**	**HUD**	**-**	**-**
Lab #	**CS 4100**	**CS 4101**	**CS 4102**	**CS 4103**	**CS 4104**	**CS 4105**	**CS 4106**	**CS 4107**	**CS 4108**	**CS 4109**
Ti	6701	8004	7525	6702	6974	6667	6888	9251	6033	6804
V	327	249	275	315	247	258	386	351	304	292
Cr	21	15	20	132	42	42	38	29	119	43
Mn	1641	1141	1247	1319	1097	1099	1395	1359	1157	1007
Co	38	41	50	51	29	33	45	36	50	21
Ni	23	26	30	107	42	43	39	37	100	41
Cu	45	154	241	62	109	111	127	156	48	76
Zn	140	129	140	123	117	115	135	138	111	125
Rb	10	38	31	20	26	27	16	38	18	62
Sr	450	415	443	713	450	462	419	469	620	367
Y	16	27	25	17	20	20	16	26	14	23
Zr	61	186	151	150	185	185	83	211	134	167
Nb	8	10	8	7	9	9	3	9	5	8
Cs	0.4	0.9	1.0	0.3	0.4	0.5	0.8	0.6	0.2	2.5
Ba	108	380	308	250	342	329	156	399	216	426
La	5.0	24.2	17.6	16.1	20.2	21.1	6.4	25.4	14.0	20.1
Ce	11.9	54.7	40.6	38.4	45.8	46.7	17.3	58.7	33.1	43.3
Pr	1.6	7.0	5.3	4.5	5.6	5.7	2.2	6.9	3.8	5.1
Nd	8.8	32.6	25.7	20.9	24.6	25.7	11.7	31.2	18.2	23.2
Sm	2.13	6.61	5.86	4.33	5.22	5.27	2.76	6.57	3.69	5.09
Eu	0.95	2.00	1.61	1.31	1.49	1.50	0.87	1.92	1.02	1.38
Gd	2.9	8.4	7.2	5.6	6.3	6.4	3.7	8.6	4.7	6.0
Tb	0.46	0.89	0.77	0.54	0.61	0.68	0.39	0.81	0.44	0.68
Dy	2.39	5.67	4.94	3.45	4.10	3.99	3.03	5.45	3.15	4.14
Ho	0.44	0.98	0.88	0.64	0.74	0.67	0.54	0.92	0.52	0.74
Er	1.57	3.18	2.94	2.06	2.42	2.40	1.78	3.09	1.78	2.50
Tm	0.16	0.35	0.32	0.18	0.26	0.26	0.18	0.31	0.16	0.26
Yb	1.33	2.68	2.49	1.85	1.96	2.26	1.61	2.66	1.44	2.48
Lu	0.17	0.33	0.31	0.21	0.23	0.23	0.17	0.30	0.14	0.27
Hf	3.0	4.7	3.6	3.6	4.4	4.1	2.2	4.5	2.6	4.1
Pb	3.0	6.9	7.2	4.3	5.5	5.7	5.0	6.4	3.6	8.1
Th	3.9	4.8	3.5	2.5	3.1	3.2	1.1	3.5	1.5	5.6
U	0.2	0.7	0.6	0.5	0.7	0.8	0.4	0.9	0.4	1.5

Table A2.10b. Trace element compositions of tephra in Lago Traquillo PC1203 A

	Core Top to H2		H2 to S10							
Tephra	**G1**	**H2**	**-**	**Ln**	**-**	**-**	**-**	**-**	**Q1**	**Q2**
Section	**AT4**	**AT5**	**AT5**	**AT5**	**AT6**	**AT7**	**AT7**	**AT7**	**AT7**	**AT8**
Depth (cm)	**91**	**0-11**	**49**	**64**	**92**	**9**	**28**	**74**	**81-90**	**0-6**
Source	**-**	**HUD**	**-**	**MEN**	**-**	**-**	**-**	**-**	**MEN**	**MEN**
Lab #	**CS 4110**	**CS 4111**	**CS 4112**	**CS 4113**	**CS 4114**	**CS 4115**	**CS 4116**	**CS 4117**	**CS 4118**	**CS 4119**
Ti	6945	6638	6560	6808	5846	5806	6576	6671	5907	6087
V	268	161	360	272	268	267	351	371	237	246
Cr	83	17	16	19	26	30	43	15	18	18
Mn	1155	1220	1581	1161	1044	936	1120	1336	1214	1360
Co	38	16	45	29	39	24	38	24	25	27
Ni	55	32	37	36	37	39	45	27	33	36
Cu	86	54	73	70	171	47	144	99	61	45
Zn	115	120	129	134	129	113	115	133	125	128
Rb	18	57	14	30	26	60	33	21	20	19
Sr	503	373	442	506	427	376	441	418	460	496
Y	14	35	18	23	22	20	21	23	22	20
Zr	140	334	107	129	110	114	129	106	91	87
Nb	12	16	3	3	4	4	3	3	3	3
Cs	0.2	1.2	0.5	0.7	1.1	2.4	1.0	1.0	0.9	0.8
Ba	213	647	173	347	260	366	302	237	221	214
La	13.3	35.8	8.5	16.0	13.5	14.9	14.3	11.4	9.5	9.1
Ce	32.4	76.7	20.7	37.7	29.2	32.3	32.3	25.8	22.1	22.0
Pr	3.8	9.3	2.7	4.8	3.9	4.1	4.1	3.5	3.0	2.8
Nd	18.3	40.3	13.7	22.6	17.9	18.6	18.8	16.9	14.3	13.8
Sm	3.70	8.14	3.17	5.02	4.31	4.28	4.50	4.15	3.65	3.54
Eu	0.90	2.20	0.84	1.38	1.19	0.99	1.02	1.03	1.13	1.00
Gd	4.5	10.3	4.3	6.5	5.6	5.1	5.4	5.1	4.4	4.4
Tb	0.37	1.09	0.46	0.66	0.57	0.49	0.56	0.58	0.51	0.46
Dy	2.92	6.57	3.38	4.65	4.02	3.58	3.92	4.31	3.62	3.45
Ho	0.49	1.19	0.56	0.81	0.73	0.72	0.70	0.77	0.64	0.63
Er	1.81	4.03	2.04	2.72	2.42	2.22	2.37	2.51	2.19	2.24
Tm	0.14	0.45	0.20	0.28	0.24	0.22	0.23	0.25	0.23	0.22
Yb	1.47	3.87	2.01	2.50	2.19	2.18	2.15	2.39	1.95	2.03
Lu	0.12	0.45	0.20	0.26	0.22	0.21	0.20	0.28	0.20	0.20
Hf	5.1	7.1	2.5	3.0	2.5	2.9	2.9	2.4	2.4	1.9
Pb	3.7	9.5	4.0	6.7	6.9	6.9	6.2	6.5	10.7	5.0
Th	4.2	5.8	0.8	2.1	2.1	4.8	2.4	1.4	1.6	1.0
U	0.5	1.4	0.3	0.7	0.7	1.3	0.7	0.6	0.5	0.4

Table A2.10c. Trace element compositions of tephra in Lago Traquillo PC1203 A

	H2 to S10			S10				S10 to Core Bottom		
Tephra	**MEN1**	**-**	**R**	**S1**	**S2**	**S3**	**S5**	**T**	**V**	**X2**
Section	**AT8**	**AT8**	**AT9**	**AT9**	**AT9**	**AT9**	**AT9**	**AT10**	**AT10**	**AT10**
Depth (cm)	**6-10**	**27**	**0**	**79**	**80**	**81**	**84**	**9**	**55**	**81**
Source	**MEN**	**-**	**MEN**	**HUD**	**HUD**	**HUD**	**HUD**	**MEN**	**HUD**	**HUD**
Lab #	**CS 4120**	**CS 4121**	**CS 4122**	**CS-2501**	**CS-2502**	**CS-2503**	**CS-2504**	**CS-2505**	**CS-2506**	**CS-2507**
Ti	5033	5267	5550	9761	10095	9084	10082	6231	11219	10582
V	245	208	266	218	213	192	213	202	255	193
Cr	9	22	15	21	18	14	13	11	10	4
Mn	2008	691	1473	1261	1227	1156	1229	1089	1192	1237
Co	36	19	33	36	57	31	29	40	27	28
Ni	34	34	35	16	17	17	20	16	16	13
Cu	20	73	43	134	190	131	113	194	156	98
Zn	145	94	124	123	118	113	117	121	116	124
Rb	9	53	18	27	25	25	23	23	28	30
Sr	596	434	567	550	569	523	559	425	468	450
Y	12	18	18	31	35	34	35	25	36	40
Zr	50	109	80	254	261	259	259	107	223	262
Nb	1	5	2	18	16	14	13	5	11	11
Cs	0.3	1.9	0.7	0.7	0.9	0.8	0.6	1.6	0.7	0.8
Ba	114	352	192	462	596	477	488	266	425	431
La	5.8	15.1	8.6	31.9	35.1	34.1	35.8	12.3	29.7	30.0
Ce	14.0	31.2	20.6	73.8	81.0	78.3	82.1	28.5	69.8	72.2
Pr	1.9	3.9	2.6	9.5	10.7	10.2	10.9	3.8	9.2	9.6
Nd	9.5	17.6	13.1	39.4	44.3	41.7	45.1	17.8	40.3	40.5
Sm	2.30	3.87	3.32	8.09	9.10	8.87	9.14	4.49	8.97	9.20
Eu	0.74	1.01	0.92	2.40	2.72	2.56	2.72	1.51	2.59	2.72
Gd	2.7	4.1	3.6	8.7	9.9	9.2	9.9	5.2	9.2	10.0
Tb	0.25	0.42	0.43	1.11	1.30	1.25	1.36	0.81	1.30	1.37
Dy	2.27	3.00	3.15	6.21	7.06	6.53	6.97	4.56	6.91	7.76
Ho	0.40	0.57	0.59	1.21	1.37	1.33	1.35	0.94	1.40	1.44
Er	1.46	1.85	1.90	3.48	3.85	3.67	4.11	2.66	3.87	4.47
Tm	0.12	0.18	0.17	0.48	0.53	0.51	0.57	0.38	0.54	0.58
Yb	1.31	1.83	1.71	3.02	3.52	3.52	3.51	2.68	3.54	4.08
Lu	0.11	0.16	0.19	0.47	0.55	0.52	0.51	0.42	0.51	0.63
Hf	1.0	2.3	1.7	7.1	7.0	6.9	6.3	3.6	5.4	6.3
Pb	2.6	7.7	4.7	7.8	7.2	6.5	5.6	9.1	6.1	6.6
Th	DL	4.0	0.8	9.5	6.9	5.9	5.1	3.7	4.5	4.7
U	0.1	1.1	0.4	0.7	0.8	0.8	0.7	0.7	0.7	0.8

Table A2.10d. Trace element compositions of tephra in Lago Traquillo PC1203 A

	S10 to Core Bottom							
Tephra	**X3**	**Z1**	**Z1**	**Z1**	**H0**	**H0**	**H0**	**H0**
Section	**AT10**	**AT11**	**AT11**	**AT11**	**AT11**	**AT11**	**AT12**	**AT12**
Depth (cm)	**83**	**49**	**50**	**51-55**	**79-89**	**89-100**	**0-10**	**10-20**
Source	**HUD**	**HUD**	**HUD**	**HUD**	**HUD**	**HUD**	**HUD**	**HUD**
Lab #	**CS-2508**	**CS-2509**	**CS-2510**	**CS-2511**	**CS-2512**	**CS-2709**	**CS-2710**	**CS-2711**
Ti	9069	7514	8056	9599	6874	7250	8091	8303
V	164	247	237	235	161	221	205	200
Cr	6	55	31	20	9	25	16	17
Mn	1094	970	1004	1197	940	1027	1146	1154
Co	84	30	30	64	16	22	41	32
Ni	12	30	22	21	13	22	18	20
Cu	59	119	87	102	97	74	55	45
Zn	107	95	91	106	97	107	108	108
Rb	36	29	31	31	47	45	43	44
Sr	426	557	478	457	396	422	457	478
Y	35	25	28	32	30	29	31	32
Zr	244	151	165	208	227	204	225	241
Nb	12	6	8	17	12	10	21	12
Cs	1.2	1.5	1.3	1.1	1.7	2.7	1.6	1.3
Ba	427	363	383	405	502	498	529	574
La	28.7	21.6	22.9	25.5	28.3	27.6	29.3	31.4
Ce	66.3	47.9	51.7	59.0	63.9	62.6	64.1	69.0
Pr	8.5	6.2	6.5	7.6	7.8	7.8	8.0	8.9
Nd	35.7	26.1	27.3	31.2	31.9	32.4	33.6	36.3
Sm	7.96	5.62	5.99	7.10	6.56	7.31	7.50	8.17
Eu	2.34	1.77	1.88	2.13	1.89	2.05	2.35	2.41
Gd	8.9	6.2	6.5	7.6	7.1	8.3	8.4	9.3
Tb	1.17	0.85	0.89	1.02	0.99	1.09	1.11	1.16
Dy	6.65	4.53	4.96	5.86	5.30	5.52	5.79	6.26
Ho	1.31	0.90	1.03	1.25	1.08	1.05	1.16	1.26
Er	3.93	2.74	2.85	3.38	3.19	3.32	3.61	3.64
Tm	0.56	0.37	0.40	0.45	0.46	0.39	0.44	0.46
Yb	3.44	2.33	2.76	3.01	2.92	3.03	3.12	3.30
Lu	0.53	0.36	0.40	0.46	0.42	0.46	0.50	0.50
Hf	5.8	3.8	3.9	6.8	5.4	4.9	7.8	6.1
Pb	7.5	5.0	4.5	4.8	7.5	10.5	9.3	9.3
Th	4.8	4.9	4.6	7.4	6.0	5.2	8.4	5.4
U	0.9	0.8	0.8	0.8	1.1	1.4	1.2	1.2

Table A2.10e. Trace element compositions of tephra in Lago Traquillo PC1203 A

	S10 to Core Bottom						
Tephra	**H0**	**H0**	**H0**	**-**	**Z3**	**-**	**-**
Section	**AT12**	**AT12**	**AT12**	**AT12**	**AT12**	**AT12**	**AT13**
Depth (cm)	**20-30**	**30-40**	**40**	**42**	**68-78**	**98**	**75**
Source	**HUD**	**HUD**	**HUD**	**-**	**-**	**-**	**-**
Lab #	**CS-2712**	**CS-2713**	**CS-2513**	**CS-2514**	**CS-2515**	**CS-2516**	**CS-2517**
Ti	8479	9607	8575	8825	6238	5891	10881
V	201	230	216	239	227	253	289
Cr	18	28	9	13	5	15	DL
Mn	1162	1295	1065	1065	1122	1040	1246
Co	22	35	24	66	21	31	55
Ni	19	25	14	18	13	15	17
Cu	41	43	71	93	48	211	108
Zn	106	114	99	100	102	102	111
Rb	45	39	38	36	17	20	33
Sr	481	497	478	475	492	535	523
Y	31	29	31	30	21	19	33
Zr	237	202	218	218	78	69	196
Nb	12	11	11	12	2	2	10
Cs	1.2	1.0	0.8	0.8	0.9	1.1	0.8
Ba	574	510	446	434	228	225	461
La	31.5	27.4	26.1	26.1	8.7	8.8	27.7
Ce	67.6	61.3	57.0	58.1	20.5	20.1	63.1
Pr	8.7	7.8	7.4	7.5	2.9	2.7	8.1
Nd	36.6	31.8	30.8	31.0	13.8	12.7	34.8
Sm	7.73	7.16	6.52	6.31	3.52	3.14	7.48
Eu	2.37	2.26	1.92	1.98	1.27	1.15	2.18
Gd	9.1	7.9	7.4	7.1	4.0	3.6	8.2
Tb	1.11	1.03	0.99	0.91	0.62	0.55	1.06
Dy	6.33	5.43	5.26	5.01	3.82	3.12	6.15
Ho	1.23	1.16	1.08	1.04	0.76	0.65	1.16
Er	3.64	3.29	3.23	3.12	2.16	2.12	3.27
Tm	0.45	0.45	0.41	0.41	0.30	0.27	0.48
Yb	3.38	2.89	2.88	2.79	1.89	1.63	3.03
Lu	0.47	0.45	0.42	0.43	0.33	0.27	0.47
Hf	5.8	5.2	5.1	4.9	2.3	2.3	4.3
Pb	9.3	8.1	5.5	5.4	3.6	5.1	4.7
Th	5.2	4.4	4.5	4.0	1.8	2.5	3.8
U	1.2	1.1	1.0	1.0	0.5	0.7	1.1

Table A2.11. Repeat analysis of internal CU lab standards and analysis of international standards.

	Internal lab standards run repetitively						International standards			
Rock type	**Basalt**		**andesite**		**rhyolite**		**basalt**		**basalt**	
Sample	**VDM***		**AN***		**PC1***		**BHVO-1**		**NIST2711**	
Lab	**CU***		**CU***		**CU***		**CU***	**USGS***	**CU***	**NIST***
No. samples	**25**		**33**		**23**		**1**		**1**	
	avg	**st dev**	**avg**	**st dev**	**avg**	**st dev**				
Ti	6179	396	3657	296	880	87	17842	16000	2975	3060
V	328	40	109	15	-	-	381	314	-	-
Cr	78	7	16	2	-	-	297	300	-	-
Mn	1610	88	981	48	443	33	1328	1270	642	638
Co	38	3	32	5	-	-	58	45	12	10
Ni	51	11	28	3	-	-	158	117	25	21
Cu	190	12	14	2	-	-	150	137	-	-
Zn	135	25	70	6	-	-	126	102	-	-
Cs	2.9	0.3	2.8	0.3	7.3	0.7	0.1	0.1	6.4	6.1
Rb	96	7	130	7	167	6.1	11	10	112	110
Sr	997	58	523	28	47	1.0	408	440	282	245
Ba	864	47	693	36	263	9.0	136	142	729	726
Y	25.7	1.9	16	0.9	17	0.8	26	28	27	25
Zr	141.5	11.2	174	8	152	3	175	180	221	230
Nb	21.2	5.5	26.0	1.8	28	1.1	20	19	18	-
Th	8.4	1.7	5.8	0.4	25.5	1.1	1.6	1.4	13.3	-
Hf	4.0	0.8	4.7	0.5	5.1	0.2	5.2	4.6	2.3	-
Pb	14.8	1.3	10.4	0.8	21.3	0.7	3.7	4	1210	1162
U	2.5	0.4	2.1	0.1	7.3	0.4	0.3	0.4	3.1	2.6
La	38.4	2.8	25.9	1.3	32.1	2.0	15.2	15.1	37.9	40.0
Ce	78.8	5.3	48.1	2.4	57.6	3.7	38.7	38.2	74.8	-
Pr	9.57	0.7	5.38	0.29	5.49	0.26	5.60	5.25	7.31	-
Nd	38.8	2.5	19.7	1.0	18.6	0.11	27.1	24.8	29.4	31.0
Sm	7.98	0.8	3.91	0.21	3.18	0.15	6.33	6.15	7.50	-
Eu	2.32	0.3	1.30	0.08	0.39	0.02	2.08	2.20	1.05	-
Gd	8.82	1.6	4.13	0.23	2.85	0.28	6.88	6.24	5.39	-
Tb	0.95	0.1	0.51	0.04	0.44	0.07	0.99	0.96	0.75	-
Dy	4.98	0.4	2.84	0.16	2.73	0.14	5.12	5.35	4.28	-
Ho	0.93	0.1	0.57	0.04	0.54	0.04	0.97	1.05	0.92	-
Er	2.92	0.3	1.83	0.11	1.80	0.06	2.72	2.56	2.52	-
Tm	0.35	0.1	0.25	0.02	0.37	0.05	0.34	0.32	0.43	-
Yb	2.52	0.2	1.87	0.10	2.28	0.10	2.02	2.01	2.25	-
Lu	0.34	0.0	0.27	0.02	0.34	0.03	0.27	0.28	0.40	-

A3 Chapter 3 Appendix

The appendix for Chapter 3 includes all of the supplementary files for which consists of X-ray images for the all of the lake cores with the tephra correlations and the bulk tephra petrochemistry for all the sampled tephra collected from each sediment core.

Figures

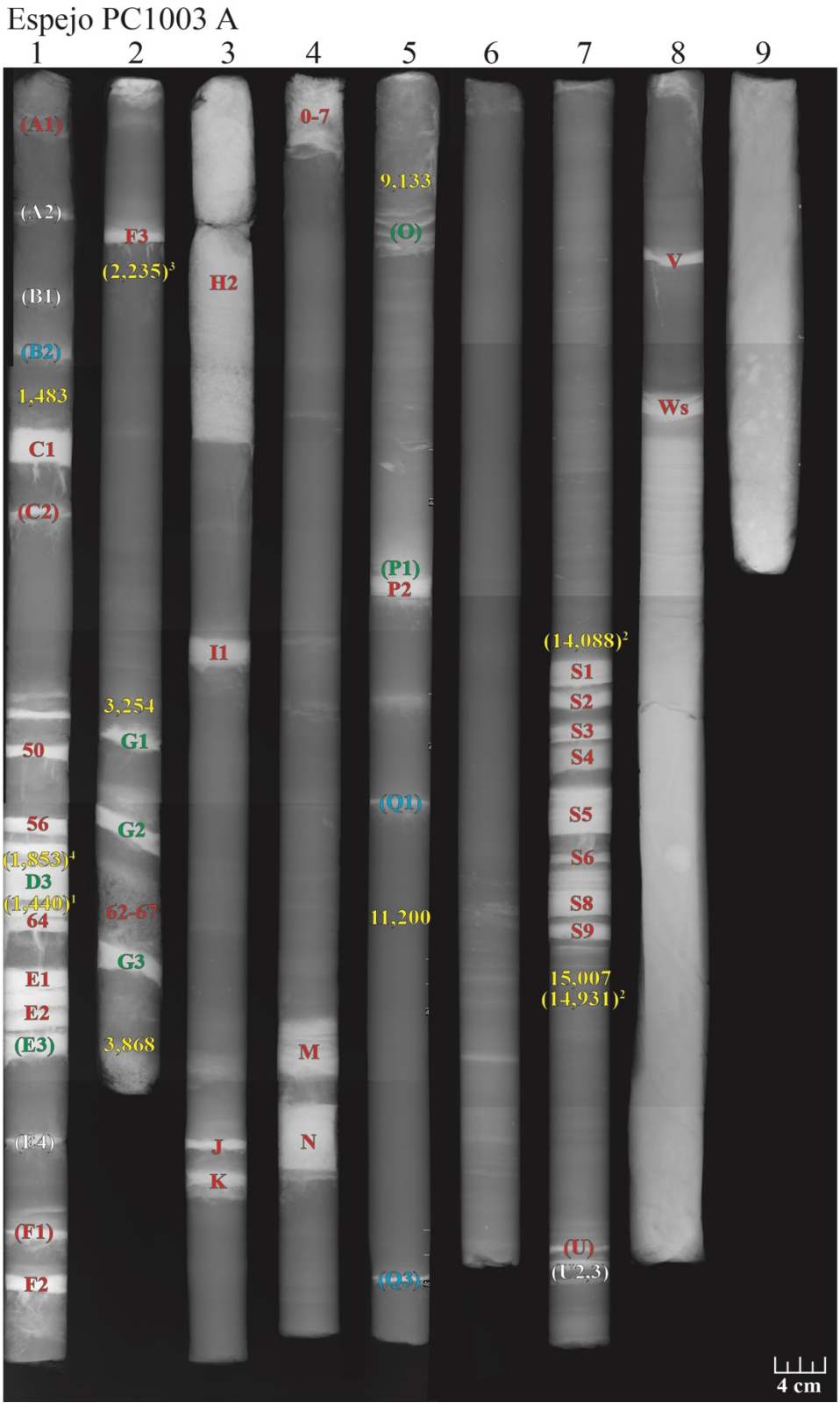

Figure A3.1. X-ray image and tephra identification for the core from Espejo lake.

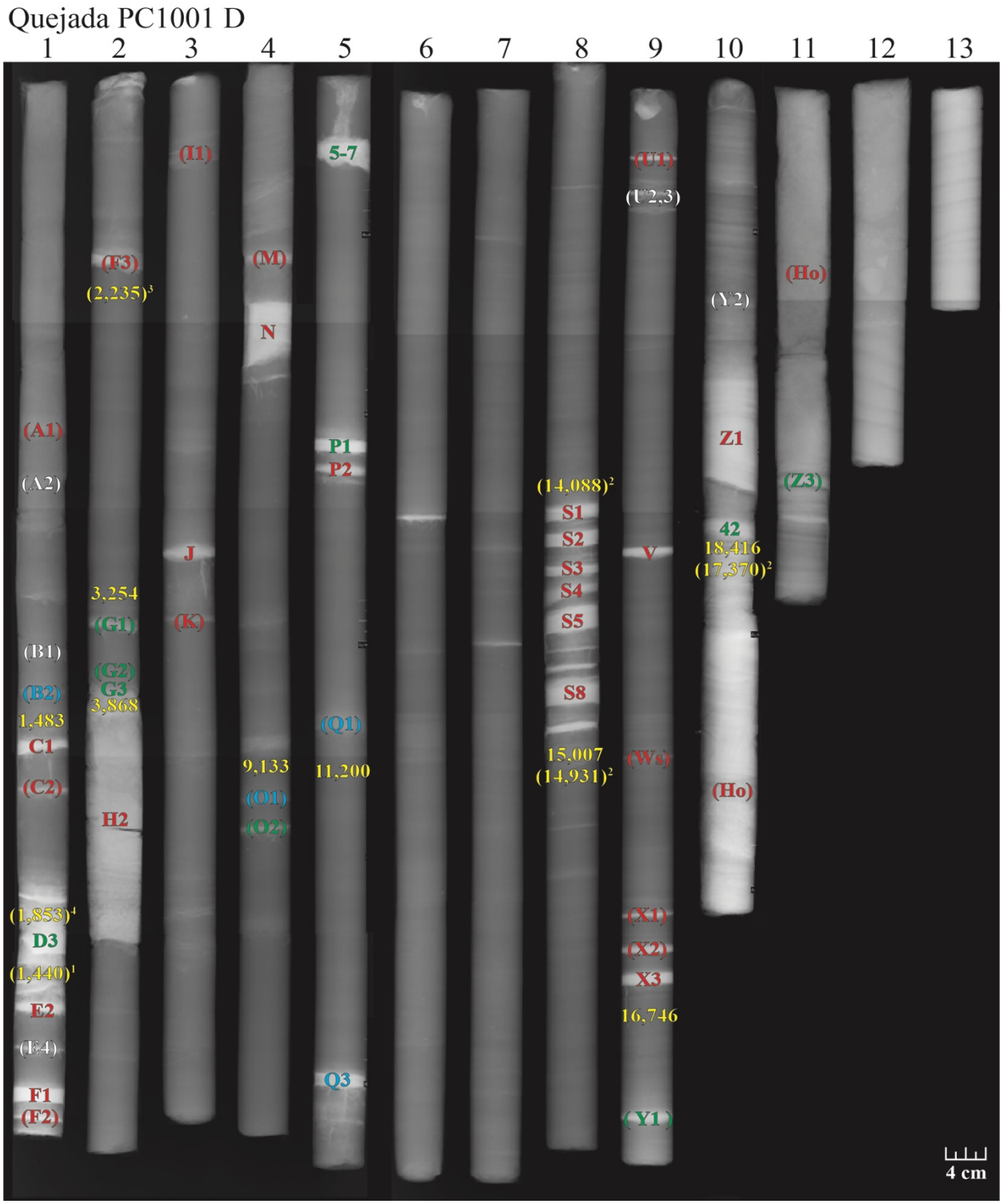

Figure A3.2. X-ray image and tephra identification for the core from Quijada lake.

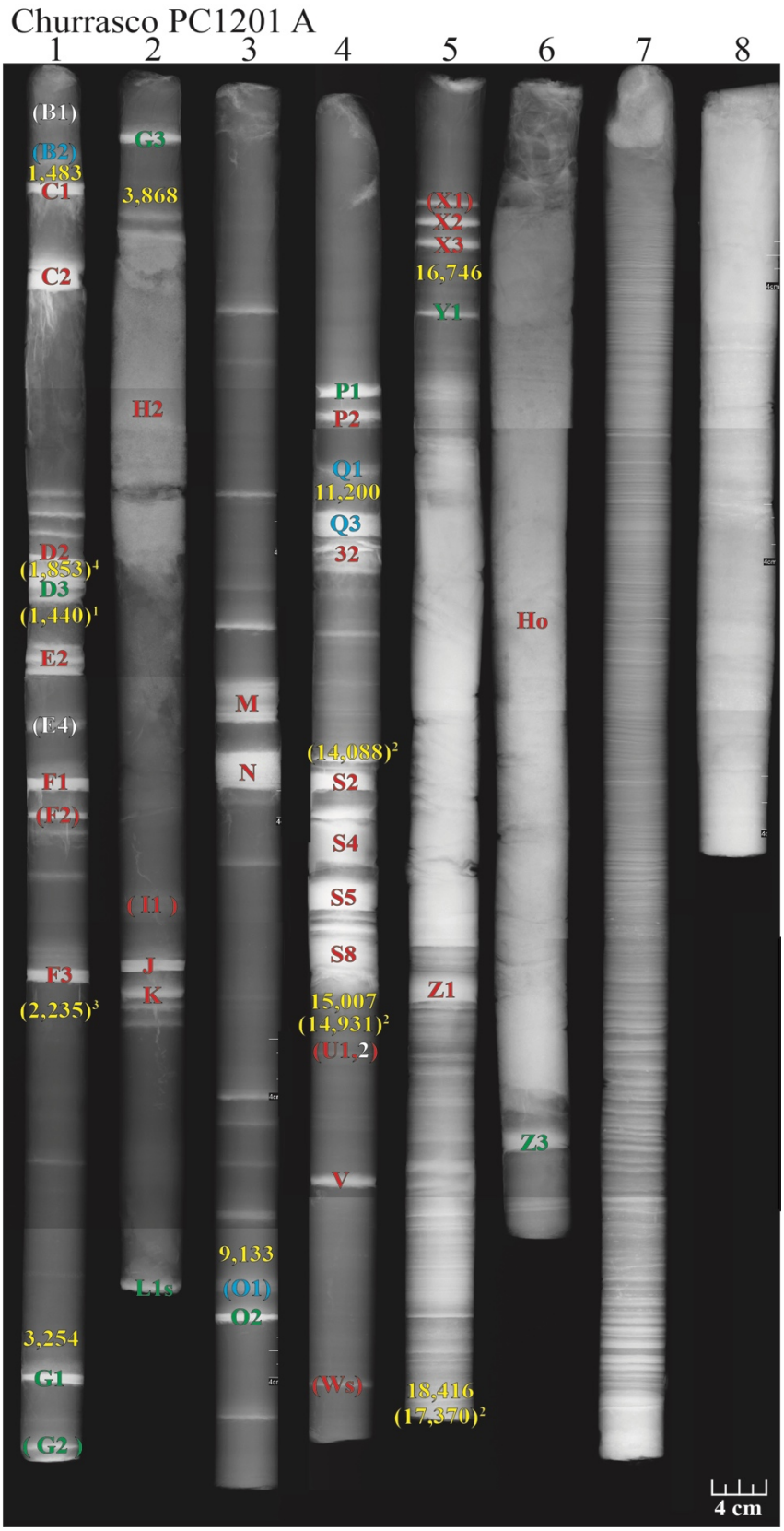

Figure A3.3. X-ray image and tephra identification for the core from Churrasco lake.

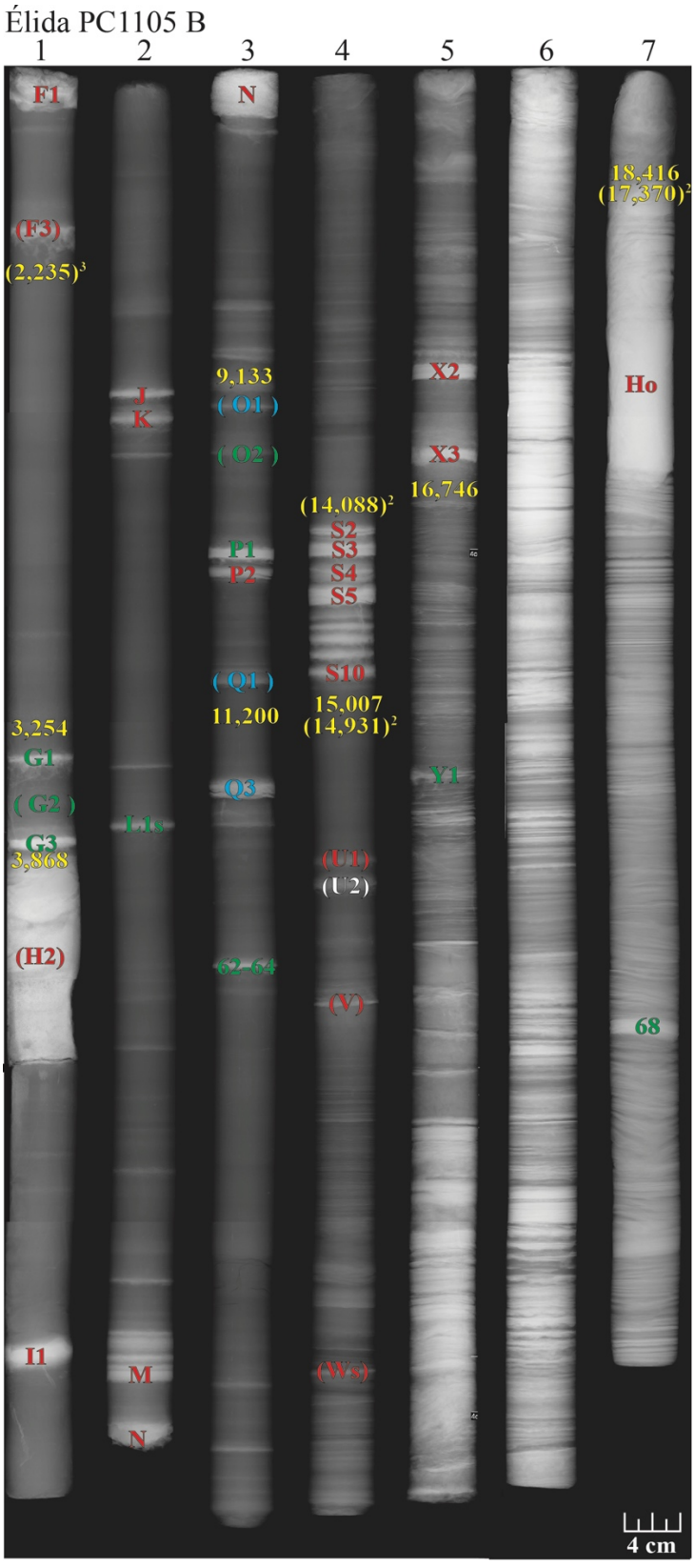

Figure A3.4. X-ray image and tephra identification for the core from Élida lake.

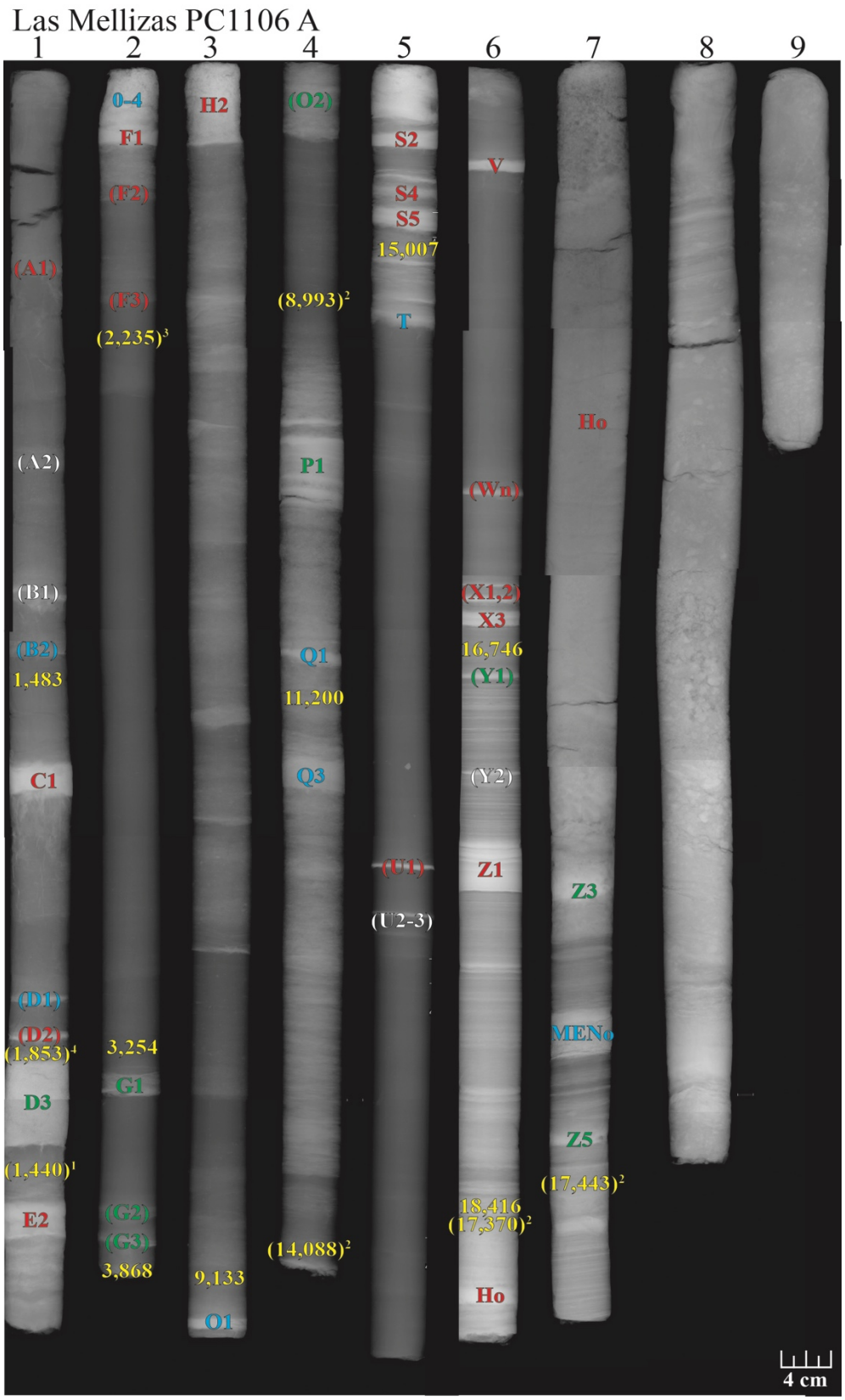

Figure A3.5. X-ray image and tephra identification for the core from Las Mellizas lake.

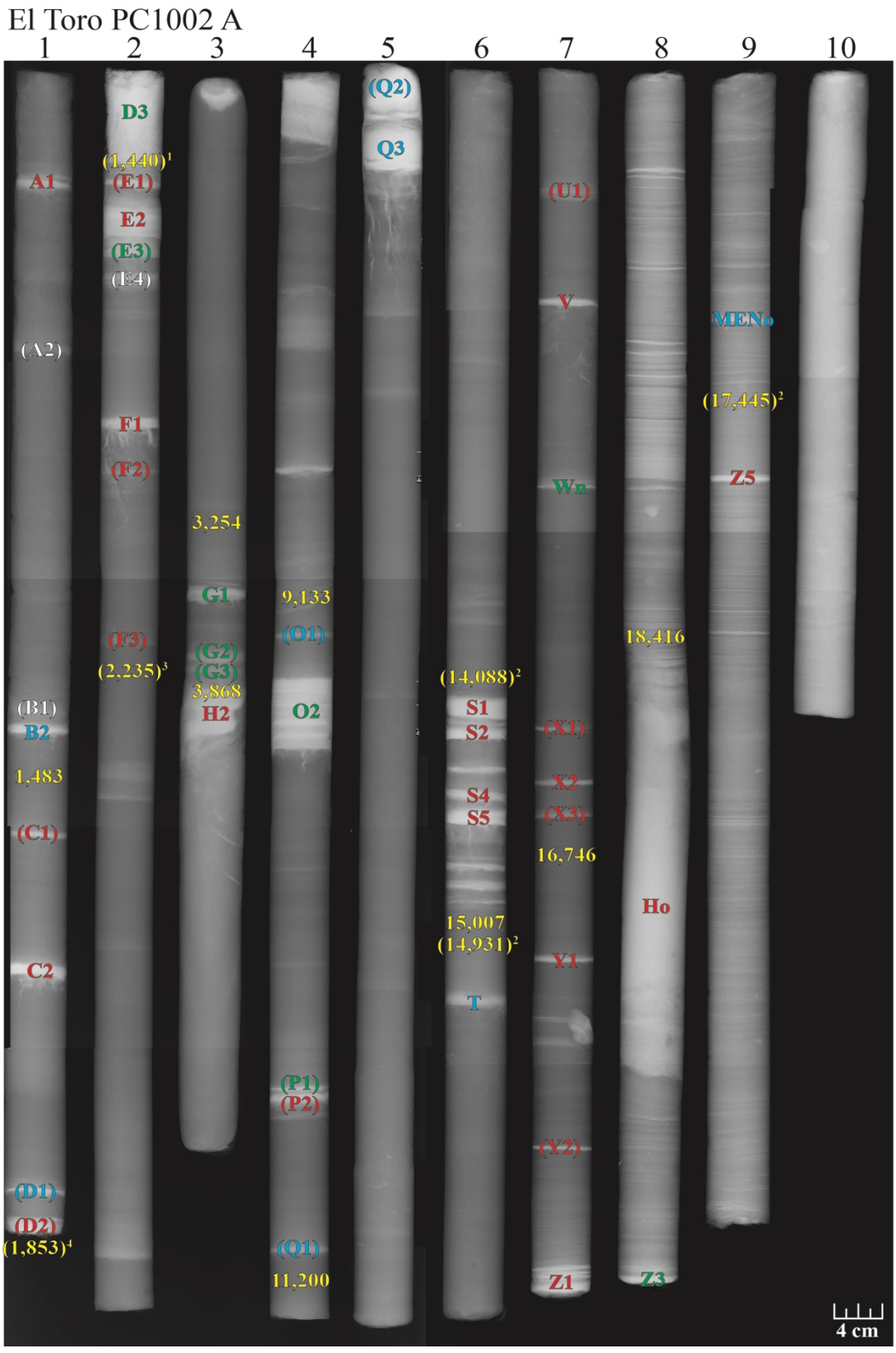

Figure A3.6. X-ray image and tephra identification for the core from El Toro lake.

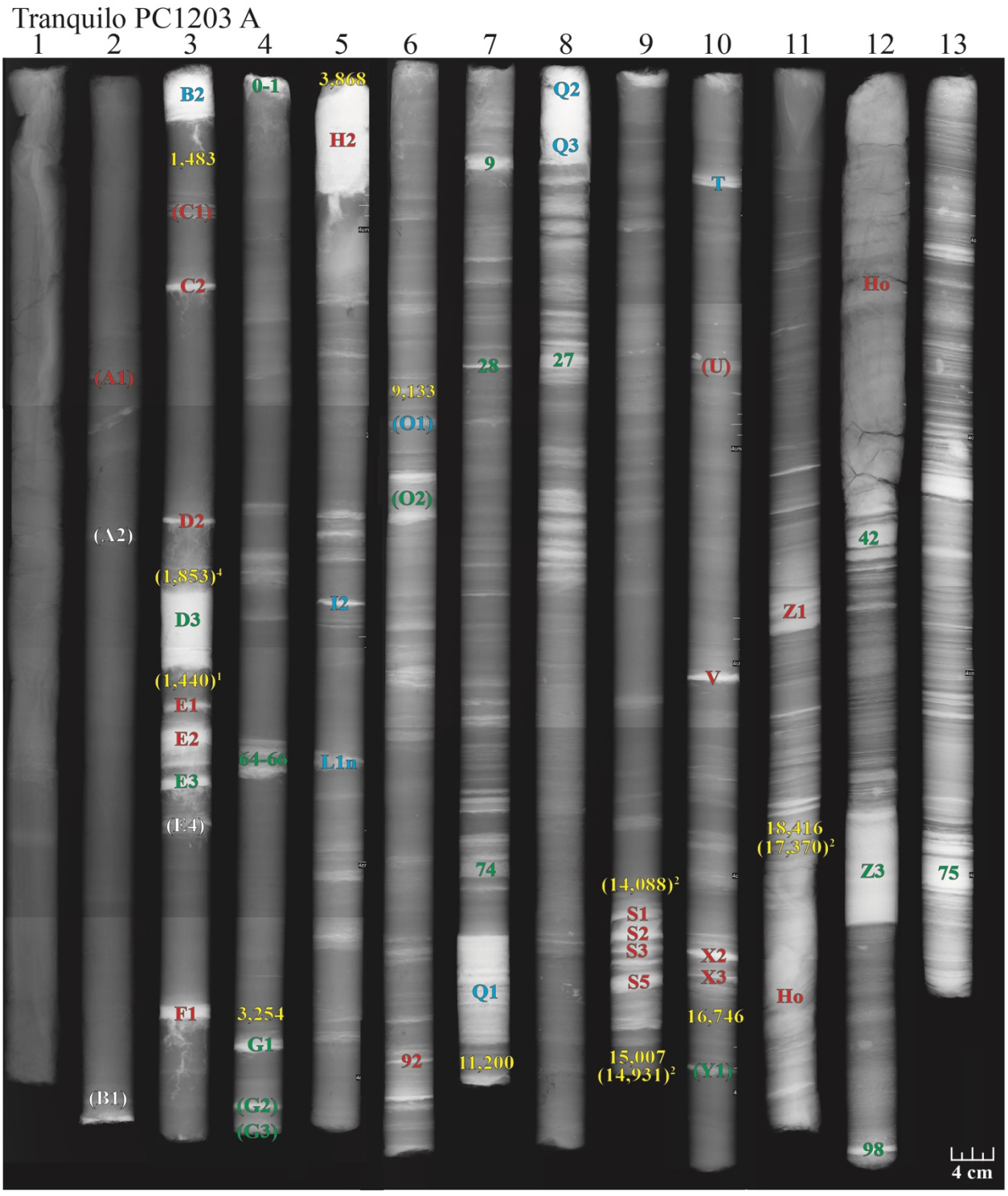

Figure A3.7. X-ray image and tephra identification for the core from Tranquilo lake.

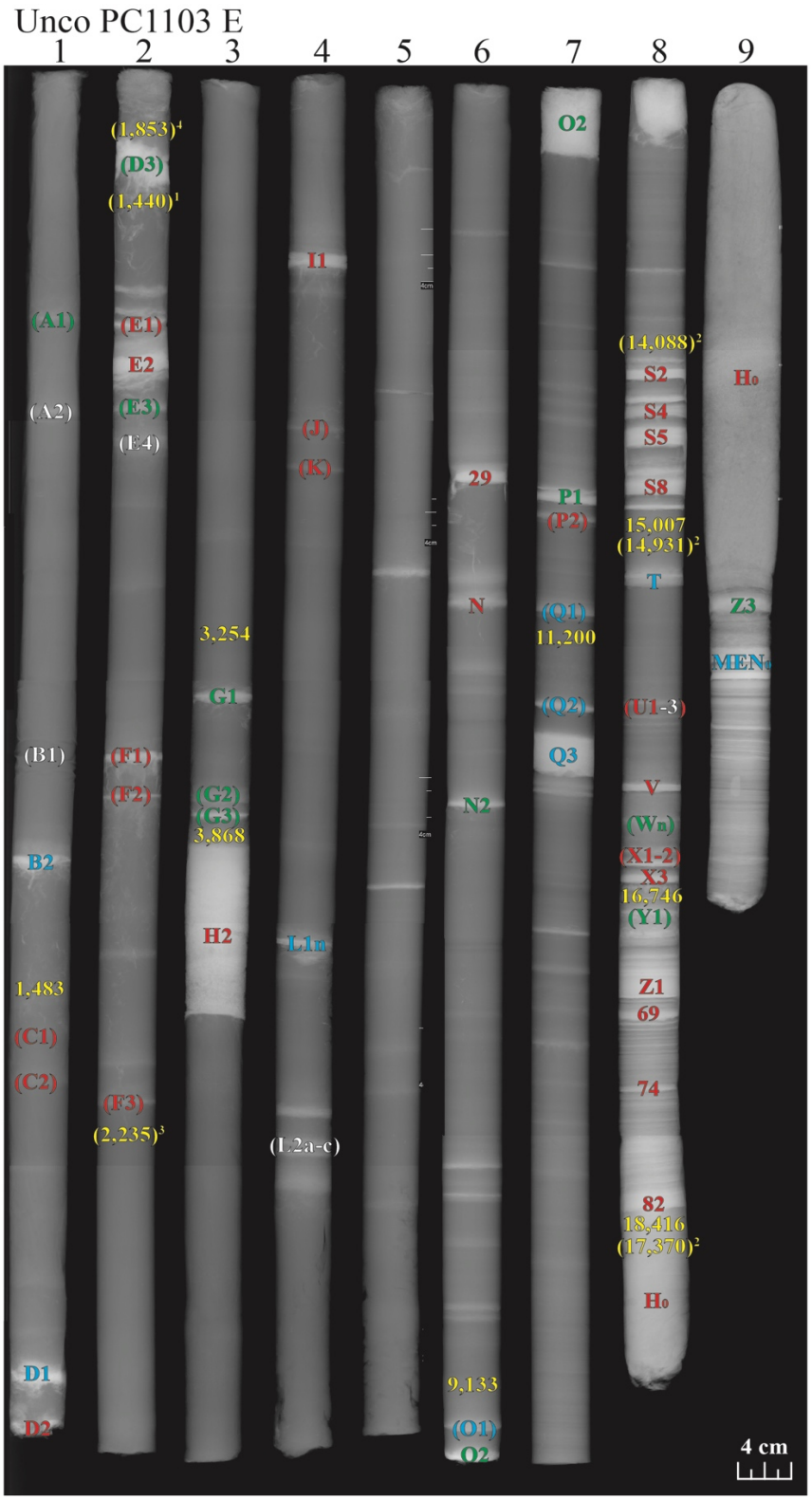

Figure A3.8. X-ray image and tephra identification for the core from Unco lake.

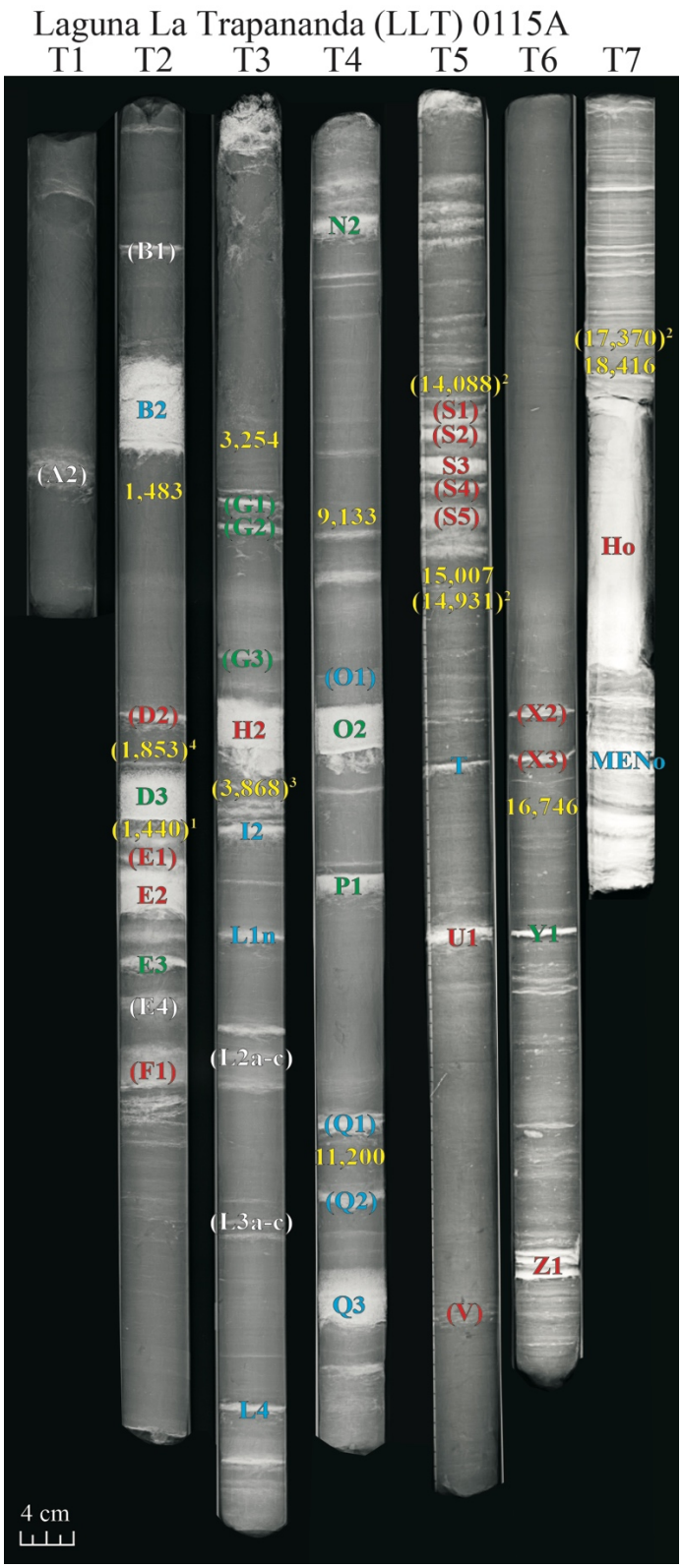

Figure A3.9. X-ray image and tephra identification for the core from Laguna La Trapananda.

Tables

Table A3.1. Tephra petrographic description and maximum grain diameter for tephra observed in the Laguna La Trapananda core

Lake	Core	Section	Depth (cm)	Source	Max. grain size (mm)	Other tephra	Glass 1 (most abundant)						
							Color	Vesicles Abun.			Vesicle Morph	Microlites	
								High	Low	None		High	Low	None
LLT	0115A	T2	17-25	Mentolat	5.2	B2	C	X	-	-	Circ	-	-	X
LLT	0115A	T2	46-49	Macá	4.1	MAC1	Br	X	-	-	Circ	X	-	-
LLT	0115A	T2	52-55	Hudson	1.1	E2	D Or	X	-	-	Circ	-	-	X
LLT	0115A	T2	58.5-59	M/C/MEC	0.7	E3	Blk	-	-	X	-	-	-	X
LLT	0115A	T3	40-45	Hudson	3.6	H2	L Br	X	-	-	Elong	-	-	X
LLT	0115A	T3	49-49.5	Mentolat	0.5	I2	C	X	-	-	Circ	-	-	X
LLT	0115A	T3	56-56.5	Mentolat	0.9	L1n	C	X	-	-	Circ	-	-	X
LLT	0115A	T3	89-89.5	Mentolat	1	L4	C	X	-	-	Circ	-	-	X
LLT	0115A	T4	7-8	M/C/MEC	1.2	N2	Blk	-	-	X	-	-	-	X
LLT	0115A	T4	40-43	M/C/MEC	3	O2	Blk	-	-	X	-	-	-	X
LLT	0115A	T4	51-53	M/C/MEC	1.5	P1	Blk	-	-	X	-	-	-	X
LLT	0115A	T4	79-82.5	Mentolat	1.6	Q3	C	X	-	-	Circ	-	-	X
LLT	0115A	T5	24-25	Hudson	0.8	S3	D Or	-	X	-	Circ	X	-	-
LLT	0115A	T5	46	Mentolat	2.1	T	L P Br	X	-	-	Circ	-	-	X
LLT	0115A	T5	57	Hudson	0.6	U	D Or	-	X	-	Circ	X	-	-
LLT	0115A	T6	58	M/C/MEC	0.9	Y1	Blk	-	-	X	-	-	-	X
LLT	0115A	T6	79-81	Hudson	2.1	Z1	Br	-	X	-	Circ	X	-	-
LLT	0115A	T7	20-40	Hudson	7.5	Ho	L Br	X	-	-	Elong	-	-	X
LLT	0115A	T7	44-46	Mentolat	8.0	MENo	C	X	-	-	Circ	-	-	X

Color: Pale (P), Light (L), Dark (D), Brown (Br), Orange (Or), Colorless (C), Black (Blk), Green (G)
Phenocryst Morphology Euhedral (E) , Subhedral (S), Anhedral (A)
Abundance: >30% (High), <30% (Low), Trace (Tr<5%)
Vesicle Morphology: Circular (Circ), Elongate (Elong)

Source	Other tephra	Glass 2								Glass 3 (least abundant)							
		Color	Vesicles Abun.			Vesicle Morph	Microlites			Color	Vesicles Abun.			Vesicle Morph	Microlites		
			High	Low	None		High	Low	None		High	Low	None		High	Low	None
Mentolat	B2	-	-	-	-	-	-	-	-	-	-	-	-	-	-	-	-
Macá	MAC1	D Br	-	-	X	-	-	X	-	Blk	-	-	X	-	-	-	X
Hudson	E2	D Br	X	-	-	Circ	-	-	X	-	-	-	-	-	-	-	-
M/C/MEC	E3	D Br	-	X	-	Circ	X	-	-	-	-	-	-	-	-	-	-
Hudson	H2	D Br	-	X	-	Circ	-	X		-	-	-	-	-	-	-	-
Mentolat	I2	Br	-	X	-	Circ	-	-	X	Blk			X				X
Mentolat	L1n	D Br	-	-	-	-	-	-	-	-	-	-	-	-	-	-	-
Mentolat	L4	-	-	X	-	Circ		X	-	D Br		X	-	-	-	X	-
M/C/MEC	N2	Br	-	-	X	-	X	-	-	C			X	-	X	-	-
M/C/MEC	O2	P D Br	-	-	X	-	X	-	-	C	X	-	-	-		-	X
M/C/MEC	P1	D Br	-	-	X	-	X	-	-	C	X	-	-	-	-	-	X
Mentolat	Q3	D Br	-	-	X	-	X	-	-	C	X	-	-	-	-	-	X
Hudson	S3	-	-	-	-	-	-	-	-	-	-	-	-	-	-	-	-
Mentolat	T	Blk	-	-	X	-	-	X	-	-	-	-	-	-	-	-	-
Hudson	U	P D Br	-	X	-	Circ	X	-	-	-	-	-	-	-	-	-	-
M/C/MEC	Y1	Blk	-	-	X	-	-	X	-	-	-	-	-	-	-	-	-
Hudson	Z1	P Br	-	X	-	Circ	-	X	-	C	X	-	-	Circ	-	-	X
Hudson	Ho	P Br	-	X	-	Circ	-	X	-	-	-	-	-	-	-	-	-
Mentolat	MENo	Br	-	X	-	Circ	-	X	-	Blk	-	X	-	Circ	-	X	-
		-	-	-	-	-	-	-	-	-	-	-	-	-	-	-	-

Source	Other tephra	Plagioclase							Clinopyroxene				Orthopyroxene			
			Abundance			Inclusions				Abundance				Abundance		
Mentolat	B2	Morphology	High	Low	None	High	Low	None	Morphology	High	Low	None	Morphology	High	Low	None
Macá	MAC1	E, S	X	-	-	-	X	-	S, E	X	-	-	E, S	X	-	-
Hudson	E2	S, A	X	-	-	-	X	-	S, A		X	-	S	-	Tr	-
M/C/MEC	E3	E, S	X	-	-	-	X	-	S, A	X	-	-	S	-	X	-
Hudson	H2	S, A	X	-	-	X	-	-	S, A		Tr	-	S	-	X	-
Mentolat	I2	E, S	X	-	-	-	-	X	E, S	X	-	-	E, S	X	-	-
Mentolat	L1n	E, S	X	-	-	-	X	-	S, E	X	-	-	E, S	X	-	-
Mentolat	L4	E, S	X	-	-	-	X	-	S, E	X	-	-	E, S	X	-	-
M/C/MEC	N2	E, S	X	-	-	-	X	-	S, A	X	-	-	E, S	X	-	-
M/C/MEC	O2	E, S	-	X	-	X	-	-	S, A	X	-	-	S, A	-	X	-
M/C/MEC	P1	E, S	X	-	-	-	X	-	S, A	-	X	-	S, A	-	X	-
Mentolat	Q3	E, S	X	-	-	-	X	-	E, S	X	-	-	E, S	X	-	-
Hudson	S3	E, S	X	-	-	-	X	-	S, E	X	-	-	E, S	X	-	-
Mentolat	T	S, A	-	X	-	-	X	-	S, A	-	X	-	-	-	-	X
Hudson	U	S, A	-	X	-	-	X	-	S, A	-	X	-	E, S	-	X	-
M/C/MEC	Y1	S, A	-	X	-	-	-	X	-	-	-	X	-	-	-	X
Hudson	Z1	E, S	X	-	-	-	X	-	S, A	X	-	-	S, A	-	X	-
Hudson	Ho	E, S	X	-	-	-	X	-	S, A	-	X	-	E, S	-	X	-
Mentolat	MENo	E, S	X	-	-	-	-	X	E, S	X	-	-	E, S	X	-	-
		E, S	X	-	-	-	X	-	S, E	X	-	-	E, S	X	-	-

Source	Other tephra	Amphibole 1					Amphibole 2					Olivine			
			Color	Abundance				Color	Abundance				Abundance		
		Morphology		High	Low	None	Morphology		High	Low	None	Morphology	High	Low	None
Mentolat	B2	S	Br	X	-	-	-	-	-	-	X	S, A	-	X	-
Macá	MAC1	-	-	-	-	X	-	-	-	-	X	A	-	X	-
Hudson	E2	-	-	-	-	X	-	-	-	-	X	A	-	X	-
M/C/MEC	E3	-	-	-	-	X	-	-	-	-	X	A	-	X	-
Hudson	H2	-	-	-	-	X	-	-	-	-	X	A	-	X	-
Mentolat	I2	S	Br	X		-	-	-	-	-	X	S, A	-	X	-
Mentolat	L1n	S	Br	X	-	-	-	-	-	-	X	S, A	-	X	-
Mentolat	L4	S	Br	X	-	-	S	G	-	X	-	-	-	-	X
M/C/MEC	N2	S	G	-	X	-	S	B	-	X	-	-	-	-	X
M/C/MEC	O2	S	G	-	X	-	-	-	-	-	-	-	-	-	X
M/C/MEC	P1	S	Br	-	X	-	-	-	-	-	X	-	-	-	X
Mentolat	Q3	S	Br	X	-	-	-	-	-	-	X	S, A	-	X	-
Hudson	S3	-	-	-	-	-	-	-	-	-	X	-	-	-	X
Mentolat	T	-	-	-	-	X	-	-	-	-	X	-	-	-	X
Hudson	U	-	-	-	-	X	-	-	-	-	X	-	-	-	X
M/C/MEC	Y1	S	G	-	Tr	-	-	-	-	-	X	S, A	X	-	-
Hudson	Z1	S	G	-	X	-	-	-	-	-	X	A	-	Tr	X
Hudson	Ho	-	-	-	-	X	-	-	-	-	X	A	-	X	-
Mentolat	MENo	S	Br	X	-	-	-	-	-	-	X	S, A	-	X	-

Table A3.2. Calculated k value used in the OXCAL Bayesian age model

Lake	kest
Trapananda	17.6
Tranquilo	6.3
Unco	6.6
El Toro	10.8
Las Mellizas	16.0
Churrasco	15.0
Élida	11.5
Quijada	5.2
Espejo	7.5

Table A3.3a. Modeled ages in cal years BP for Laguna La Trapananda and the other lake cores from near Coyhaique (Weller et al., 2015)

Tephra	LE	LE	LQ	LQ	LC	LC	LEl	LEl	LT	LT	LM	LM	LU	LU	LTr	LTr	LLT	LLT	
	Median	1σ	Median	1σ	Median	1σ	Median	1σ	Median	1σ	Median	1σ	Median	1σ	Median	1σ	Median	1σ	**Average**
A1	521	1280	1067	853	-	-	-	-	590	1252	751	1052	729	1134	1097	616	-	-	793
A2	932	1031	1170	751	-	-	-	-	883	948	1102	663	854	1014	1184	514	-	-	1021
B1	1278	742	1428	371	989	1101	-	-	1438	236	1317	405	1415	351	1460	126	1397	81	1340
B2	1431	475	1458	248	1387	696	1368	895	1453	190	1413	255	-	-	1467	111	1433	63	1426
C1	1509	105	1500	129	1616	142	1512	101	1524	81	1534	90	1514	91	1548	129	-	-	1532
C2	1543	146	1527	197	1881	202	1552	143	1622	125	-	-	1537	114	1619	165	-	-	1612
D1	-	-	1725	315	-	-	1796	231	1810	171	1795	168	1743	194	-	-	-	-	1774
D2	-	-	-	-	2273	236	1881	249	1838	176	1858	179	1775	201	1849	230	1629	148	1872
D3	1966	278	-	-	2294	237	-	-	1841	176	1876	181	1839	215	1925	244	1715	173	1922
E1	2030	287	1764	328	-	-	1918	256	1855	179	1948	191	1949	234	1961	251	1777	187	1900
E2	-	-	1787	334	2356	238	-	-	1879	183	-	-	1979	239	1988	255	1801	191	1965
E3	-	-	-	-	-	-	1925	257	1891	184	-	-	2014	243	2000	256	1950	214	1956
E4	2157	301	1872	355	2423	237	1999	267	1913	188	-	-	2042	247	2032	261	2024	223	2058
F1	2270	309	1969	373	2505	236	2209	288	2041	204	-	-	2289	268	2231	282	2173	234	2211
F2	2329	312	2006	379	2536	234	-	-	2078	208	2141	208	2318	270	-	-	-	-	2235
F3	2649	312	2494	413	2768	216	2476	296	2229	221	2278	214	2563	274	-	-	-	-	2494
G1	3302	157	3337	241	3321	120	3291	138	3319	182	3369	150	3261	118	3316	203	3311	118	3314
G2	3516	213	3758	239	3484	161	3482	208	3702	214	3786	141	3699	219	3721	231	3377	146	3614
G3	3714	199	3834	188	3680	159	3684	204	3782	189	3854	104	3776	196	3846	149	3769	142	3771
H2	3869	83	3867	84	3868	84	3867	83	3868	84	3868	83	3868	84	3867	83	-	-	3868
I1	4257	440	4534	598	4789	461	4518	451	-	-	-	-	4540	393	-	-	-	-	4528
I2	-	-	-	-	-	-	-	-	-	-	-	-	-	-	5465	854	4120	337	4793
J	5550	699	5701	800	4966	489	5736	624	-	-	-	-	4730	431	-	-	-	-	5337
K	5632	707	5878	814	5070	503	5818	630	-	-	-	-	4771	439	-	-	-	-	5434

Table A3.3b. Modeled ages in cal years BP for Laguna La Trapananda and the other lake cores from near Coyhaique (Weller et al., 2015)

Tephra	LE	LE	LQ	LQ	LC	LC	LEl	LEl	LT	LT	LM	LM	LU	LU	LTr	LTr	LLT	LLT	
	Median	1σ	Median	1σ	Median	1σ	Median	1σ	Median	1σ	Median	1σ	Median	1σ	Median	1σ	Median	1σ	**Average**
L1n	-	-	-	-	-	-	-	-	-	-	-	-	5345	516	6175	909	4596	485	5372
Ls	-	-	-	-	5953	576	6946	645	-	-	-	-	-	-	-	-	-	-	6450
L4	-	-	-	-	-	-	-	-	-	-	-	-	-	-	-	-	6747	665	6747
M	8450	542	7946	715	7730	529	8382	494	-	-	-	-	8188	511	-	-	-	-	8139
N	8528	522	8091	689	7826	519	8502	469	-	-	-	-	8218	507	-	-	7855	583	8170
N2	-	-	-	-	-	-	-	-	-	-	-	-	8460	477	-	-	9268	216	8864
O1	9209	227	9158	133	9200	167	9245	348	9197	185	9238	184	9170	200	9157	106	9775	343	9261
O2	9235	256	9199	192	9286	229	9508	472	9313	274	9532	288	9216	288	9213	154	10253	363	9417
P1	10272	453	10593	395	10920	288	10294	542	10554	387	10599	323	10775	460	10896	254	-	-	10613
P2	10310	451	10623	390	11007	262	10365	538	10584	383	-	-	10840	445	10914	250	11148	164	10724
Q1	10975	332	11137	214	11166	183	11085	367	11130	211	11108	193	11148	294	11188	127	11347	311	11143
Q2	-	-	-	-	-	-	-	-	11278	171	-	-	11248	363	11208	102	11777	465	11378
Q3	11727	365	11475	273	11304	548	11299	237	11310	189	11395	313	11338	448	-	-	-	-	11407
R	13469	500	13627	459	12746	924	13109	540	-	-	-	-	14041	731	13380	520	14195	516	13510
S1	14832	281	14833	239	14582	707	-	-	14693	279	13801	544	14898	420	14893	233	-	-	14647
S2	-	-	14849	231	14811	566	14633	356	14717	271	13900	533	-	-	14913	221	-	-	14637
S3	14860	268	-	-	-	-	-	-	-	-	14253	479	-	-	-	-	-	-	14557
S4	14877	260	14871	221	-	-	-	-	14808	239	14775	326	-	-	-	-	-	-	14833
S5	14905	246	14910	201	-	-	-	-	14827	232	14817	305	-	-	-	-	-	-	14865
S6	14954	218	-	-	-	-	-	-	-	-	-	-	-	-	-	-	-	-	14954
S7	-	-	-	-	-	-	-	-	-	-	-	-	-	-	-	-	-	-	-
S8	-	-	14959	167	-	-	-	-	-	-	-	-	-	-	-	-	-	-	14959
S9	-	-	14978	151	-	-	-	-	-	-	-	-	14957	347	-	-	-	-	14968
S10	-	-	-	-	-	-	-	-	-	-	-	-	-	-	-	-	15196	172	-

Table A3.3c. Modeled ages in cal years BP for Laguna La Trapananda and the other lake cores from near Coyhaique (Weller et al., 2015)

Tephra	LE	LE	LQ	LQ	LC	LC	LEl	LEl	LT	LT	LM	LM	LU	LU	LTr	LTr	LLT	LLT	
	Median	1σ	Median	1σ	Median	1σ	Median	1σ	Median	1σ	Median	1σ	Median	1σ	Median	1σ	Median	1σ	**Average**
T	-	-	-	-	-	-	-	-	15090	176	15043	134	15114	384	15159	256	15380	195	15157
U1	15406	832	15591	329	15093	201	15195	222	15749	279	15603	205	15734	538	15507	339	-	-	15485
U2	15434	860	15626	332	15117	215	15252	238	-	-	15655	207	15836	541	-	-	-	-	15487
U3	-	-	15644	333	-	-	-	-	-	-	15680	208	15926	540	-	-	-	-	15750
V	15935	1304	16174	330	15430	298	15456	273	15928	280	16248	200	16322	507	16151	349	-	-	15956
Wn	-	-	-	-	-	-	-	-	16219	263	16592	163	16499	463	-	-	-	-	16437
Ws	16228	1548	16461	288	16048	324	16101	290	-	-	-	-	-	-	-	-	16582	163	16284
X1	-	-	-	-	16593	225	-	-	-	-	-	-	16623	394	-	-	16629	153	16615
X2	-	-	16693	204	16628	210	16619	195	16662	171	16703	142	16669	343	16677	206	-	-	16664
X3	-	-	16715	190	16685	178	16715	147	16703	152	16719	139	16701	293	16701	187	16887	192	16728
Y1	-	-	17000	378	16845	196	16929	159	16915	204	16815	183	16796	293	16838	206	-	-	16877
Y2	-	-	18044	403	-	-	-	-	17233	263	17125	288	-	-	-	-	17627	273	17507
Z1	-	-	18304	296	17268	300	-	-	17456	278	17397	319	16930	446	18049	293	18516	220	17703
Ho	-	-	18424	168	18435	195	18521	256	18425	113	18487	233	18417	183	18423	120	-	-	18447
Z3	-	-	18436	204	18494	312	-	-	18536	221	18509	261	18432	257	18573	291	18696	317	18525
MENo	-	-	-	-	-	-	-	-	18679	354	18733	476	18494	431	-	-	-	-	18635
Z5	-	-	-	-	-	-	-	-	18780	441	18908	607	-	-	-	-	19121	452	18936

A5 Chapter 5 Appendix

The appendix includes all of the supplementary files for which consists of X-ray images for Lake Baguales lake sediment core, the bulk trace element contents for the MAC1 and H2 tephras and the PEC and reverse crystallization modelling parameters

Figures

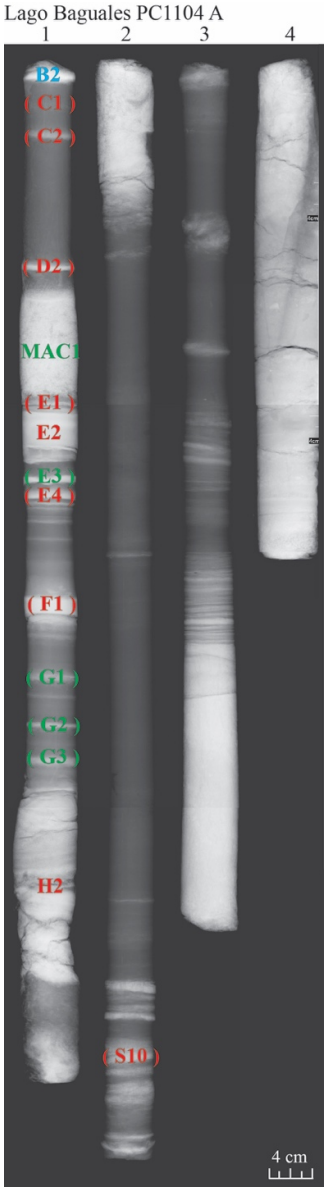

Figure A5.1. Transmitted x-ray photograph of a 4 meter long core taken from Lago Baguales (LB; Fig. 5.1). Each core section is ~1 meter in length and 4 cm in diameter and the youngest tephras and sediments occur at the top of core section 1. The dark material is the predominantly organic matter rich lacustrine material and the white layers are the denser lithologies which are often tephra deposits except in the deeper portions of the core where the dark lacustrine sediments transition to finely laminated glaciolacustrine clays and sands. The tephra are labeled with the corresponding tephra nomenclature developed by Weller et al. (2015) and are color-coded corresponding to the interpreted source volcano (Blue: Mentolat; Green: Macá; Red: Hudson). Tephras with parentheses were never collected but are correlated with the other cores based on the stratigraphic relations with the other cores taken from the region (Weller et al. 2015, 2017b). Olivines were hand-picked from the MAC1 eruption of Macá, and the H2 eruption of Hudson both occurring in core section 1 of LB core.

Table A5.1. Bulk trace elements contents (ppm) of MAC1 and H2 tephras

Reference	This Study	Weller et al. 2015	This Study	Weller et al. 2015
Lake	Baguales	Avg.	Baguales	Avg.
Section	AT1	-	AT1	-
Depth (cm)	21-30	-	66-74	-
Eruption	MAC1	D3=MAC1	H2	H2
Material	Bulk	Bulk	Bulk	Bulk
Lab #	CS0015	n=7	CS0016	n=10
Ti	6721	6820	7051	7221
V	249	222	166	146
Cr	66	102	21	13
Mn	977	1110	1072	1147
Co	31	45	18	20
Ni	43	84	21	26
Cu	42	92	32	55
Zn	97	98	103	110
Rb	21	19	41	54
Sr	667	580	522	368
Y	22	20	29	37
Zr	154	157	238	349
Nb	7	7	13	17
Cs	0.8	0.2	1.3	0.9
Ba	309	308	547	688
La	19.5	19.5	30.6	38.7
Ce	45.37	44.79	68.57	84.72
Pr	5.87	5.62	8.10	10.22
Nd	25.67	23.89	33.77	41.13
Sm	4.97	5.00	6.95	8.59
Eu	1.62	1.50	2.28	2.49
Gd	6.05	5.83	8.34	9.97
Tb	0.77	0.65	1.00	1.20
Dy	4.17	3.98	5.66	6.93
Ho	0.79	0.72	1.02	1.32
Er	2.50	2.28	3.22	4.27
Tm	0.27	0.22	0.44	0.50
Yb	2.17	2.03	3.06	3.95
Lu	0.27	0.17	0.39	0.49
Hf	3.5	3.7	5.3	8.0
Pb	4.8	5.3	8.1	11.2
Th	1.1	2.5	2.5	6.0
U	0.5	0.5	0.9	1.4

Table A5.2. Melt inclusion model input parameters and results

Volcano	Eruption	Inc.	Lab ID	FeO*	MgO Wt. % for Cpx	PEC % Oliv	Reverse Crystallization % Olv	% Cpx	Degassed?
Melimoyu	MEL2	a	MEL1	10.61	-	14.05	21.04	-	No
Melimoyu	MEL2	b	MEL1	10.46	-	19.31	20.59	-	No
Melimoyu	MEL2	a	MEL2	11.25	-	20.66	17.92	-	No
Mentolat	B2	a	MEN17	7.70	4.7	8.90	18.09	0.01	No
Mentolat	B2	a	MEN 21	7.70	4.7	5.54	19.31	0.01	No
Mentolat	B2	b	MEN21	7.70	4.7	8.64	19.08	0.01	No
Mentolat	B2	a	MEN22	7.70	4.7	5.28	16.50	0.01	No
Mentolat	D1	a	MEN3	7.60	4.7	1.20	21.50	4.90	No
Mentolat	D1	a	MEN19	7.70	4.7	8.43	18.94	0.01	No
Mentolat	D1	b	MEN19	7.70	4.7	12.84	18.36	0.01	No
Mentolat	D1	a	MEN20	7.70	4.7	6.14	19.13	0.01	No
Mentolat	I	b	MEN13	7.55	4.7	4.02	20.75	6.60	Yes
Mentolat	I	a	MEN14	7.94	4.7	2.50	23.94	4.82	No
Mentolat	I	a	MEN15	7.70	4.7	5.62	22.20	3.53	No
Mentolat	I	b	MEN15	7.70	4.7	2.78	19.20	6.20	Yes
Macá	MAC1	a	MAC1	9.32	5.3	5.08	22.65	0.01	No (Low Cl)
Macá	MAC1	a	MAC2	9.32	5.3	9.98	17.50	0.01	No
Macá	MAC1	b	MAC3	9.67	5.3	3.93	24.22	0.92	No
Macá	MAC1	a	MAC6	8.69	5.3	2.10	21.78	6.97	No
Macá	MAC1	a	MAC8	9.34	5.3	3.95	23.75	0.01	No
Macá	MAC1	c	MAC8	9.21	5.3	2.76	23.42	0.34	No
Macá	MAC1	a	MAC12	9.04	5.3	2.78	21.18	0.01	No
Macá	MAC1	b	MAC12	9.84	5.3	1.67	22.06	0.01	No
Macá	MAC1	a	MAC13	9.32	5.3	9.99	16.09	0.01	No (Low Cl)
Macá	MAC1	a	MAC14	9.43	5.3	1.15	23.76	7.64	No
Hudson	H2	a	HUD7	9.90	6.6	8.46	21.27	3.45	No
Hudson	H2	a	HUD8	9.90	6.6	14.91	19.72	0.01	Yes
Hudson	H1	a	HUD17	9.90	6.6	7.84	20.05	4.86	No
Hudson	H1	a	HUD18	9.90	6.6	11.08	16.22	0.01	No
Hudson	H1	b	HUD18	9.90	6.6	12.49	16.12	0.01	No
Hudson	H1	a	HUD21	9.90	6.6	20.72	16.14	0.01	No
Hudson	H1	b	HUD21	9.90	6.6	26.42	16.93	0.01	No
Hudson	Ho	a	HUD3	10.34	6.6	3.74	21.19	11.66	No
Hudson	Ho	a	HUD4	9.90	6.6	6.08	20.57	13.14	No
Hudson	Ho	a	HUD9	9.90	6.6	20.05	16.54	0.01	No
Hudson	Ho	a	HUD12	9.90	6.6	20.67	20.09	7.95	Yes
Hudson	Ho	a	HUD13	9.90	6.6	7.02	20.78	17.41	Yes
Hudson	Ho	b	HUD13	9.90	6.6	12.76	21.03	17.10	Yes
Hudson	Ho	a	HUD14	9.90	6.6	14.95	15.32	0.01	No
Hudson	Ho	a	HUD15	9.47	6.6	3.91	18.52	13.08	No
Hudson	Ho	b	HUD15	9.90	6.6	3.92	19.77	11.85	No
Hudson	Ho	a	HUD19	9.90	6.6	15.13	18.53	0.01	No
Hudson	Ho	a	HUD20	9.90	6.6	7.52	20.31	0.01	No
Hudson	Ho	a	HUD22	9.90	6.6	6.10	21.78	11.54	Yes
Hudson	Ho	b	HUD22	9.90	6.6	6.67	21.79	11.57	Yes
Hudson	Ho	a	HUD23	9.90	6.6	13.43	19.88	19.48	Yes
Hudson	Ho	b	HUD24	9.90	6.6	6.71	24.50	2.47	No
Hudson	Ho	a	HUD25	9.90	6.6	11.21	21.19	18.97	Yes